UNIVERSITY OF LIVERPOOL

Synthesis, structure and properties of bismuth based electroceramic perovskites

Thesis submitted in accordance with the requirements of the University of Liverpool for the degree of Doctor in Philosophy

by

Alicia Manjón Sanz

January 2015

Abstract

The work presented in this thesis focuses on the effect on structure and properties of the rhombohedral (R) perovskite system, $Bi(Ti_{3/8}Fe_{2/8}Mg_{3/8})O_3$ (BTFM), when solid solutions with $CaTiO_3$ (CTO) are made. Bismuth-based perovskites are established as candidates to replace the piezoelectric material $Pb(Zr_{1-x}Ti_x)O_3$ as they have high Curie and depolarisation temperatures which are necessary for applications and are not toxic. BTFM has a Curie temperature of ~730 °C; however it shows poor electromechanical properties.

In Chapter 3 of this thesis is shown that a range of xBTFM-(1-x)CTO compositions were synthesised successfully in the range $0.6 \leq x \leq 1$ obtaining the perovskite structure. They were proved to be polar by second harmonic generation measurements. Compositions in the range $0.6 \leq x \leq 0.825$ adopt an orthorhombic (O) structure. For $x \geq 0.95$ the R structure crystallises in the polar space group *R*3*c* with polarisation along $[111]_p$ as BTFM while in the range $0.837 \leq x \leq 0.925$ a mixed phase, O + R, region is achieved.

In Chapter 4 of this thesis, the study of the space group assignment for the O phase based on the reflection conditions and microscopy studies is shown. By using the Maximum Entrophy Method / Rietveld method a six sites disordered model for the A-site has been built based on the charge density distribution using synchrotron X-ray diffraction (SXRD) data. A joint refinement using SXRD and neutron data was performed on composition x = 0.8 and the structure of this new polar phase crystallising in $Pna2_1$ with polarisation along $[001]_p$ has been solved. However, the O phase despite of being polar displays poor physical properties being the maximum piezoelectric coefficient obtained of 2.8 pC/N for x = 0.835 .

In Chapter 5, preliminary structural analysis outcomes for the mixed phase, O + R, compositions with different polarisation directions along $[001]_p$ and $[111]_p$ respectively are shown along with their physical properties measurements results. By making solid solutions of BTFM and CTO, a maximum piezoelectric coefficient of 53 pC/N has been achieved for x = 0.835. This value is about two orders of magnitude greater than for BTFM (0.6 pC/N). A preliminary phase diagram of xBTFM-(1-x)CTO materials versus temperature has been built.

Acknowledgements

Firstly, I would like to thank my primary supervisor Prof Matthew Rosseinsky for giving me the opportunity to undertake my PhD in his research group. I would also like to thank my secondary supervisor Dr John Claridge for his help during my PhD and always being available for questions. During my stay in SPring-8 (Japan), I am very grateful to Takata-sensei for his support and countless lessons. Also special thanks go to Nishibori-sensei for guiding me through some of the structural analysis presented in this thesis and from whom I learnt about perseverance, writing skills and organization among others.

I am very thankful to Dr Michelle Dolgos, who taught me the secrets of synthesis whereas Dr Umut Adem helped me to develop my understanding in materials properties and for helping me to carry out some of the physical properties measurements presented in this work. They guided me through the initial stages of my project until they left. I wish to thank Dr Xinming Wang for performing piezoelectric measurements for me. I would like to express sincere thanks to Dr Phil Chapter, who really helped me to improve my Rietveld refinement skills. Lately, Dr Mike Pitcher has been on hand for refinement discussions and for valuable suggestions for the preparation of this manuscript.

Special thanks go to Dr Pranab Mandal for his great effort while performing the physical properties measurements for me and his very helpful suggestions. I am also grateful to Dr Alex Corkett for his input and fruitful discussions about refinements. I greatly appreciate the hard microscopy work by Mr Karl Dawson, Dr Simon Romani and Dr Marco Zanella.

I am also thankful to collaborators Dr Tim P. Stevenson, Dr Jim Bennet and Prof Andrew Bell at the Institute for Materials Research, University of Leeds for their help and input with physical properties measurements. I wish to thank Miss Thanth Thao Tran and Prof P Shiv Halasyamani at the Department of Chemistry, University of Houston for smoothly performing second harmonic generation measurements for me.

I would like to thank all previous and present members in the group for contributing to a pleasant working environment. Special thanks go to Mr Juan Carlos López and Dr Natasha Flack, who among those listed above, have spent a lot of their time reading my chapters and gave me valuable feedback.

Finally, I would like to express my gratitude to my family and friends, in Liverpool, Japan and back home for all their help and support during my PhD time.

Table of contents

CHAPTER 1 - Introduction

Piezoelectric ceramic materials are widely used in modern industry to transform electrical signals into mechanical strain and vice versa. Due to this dual nature piezoelectric materials can be used in electromechanical systems such as sensors and actuators [1], for example in automotive fuel injection, accelerometers, piezoelectric transformers and motors, micropositioning systems, vibration control, ultrasound sensors and generators, inkjet printers etc [2-4]. Currently, piezoceramic actuator materials in commercial use are based on lead titanate zirconate ($PbZrO_3$-$PbTiO_3$ or PZT) [5] and this will be explained in detail in Section 1.3.

1.1 Perovskite materials

Most technologically important ferroelectrics are oxides and adopt a perovskite structure [6]. Perovskites have the general formula ABO_3, with the A-site cations normally larger than the B-site cations and with a size similar to oxygen. The ideal perovskite-type structure adopts cubic symmetry with space group $Pm\bar{3}m$. As Figure 1.1 a) shows the A cations are surrounded by twelve anions in cubo-octahedral coordination and the B cations are surrounded by six anions in octahedral coordination (Figure 1.1 b)). The O anions are coordinated by two B-site cations and four A-site cations [7].

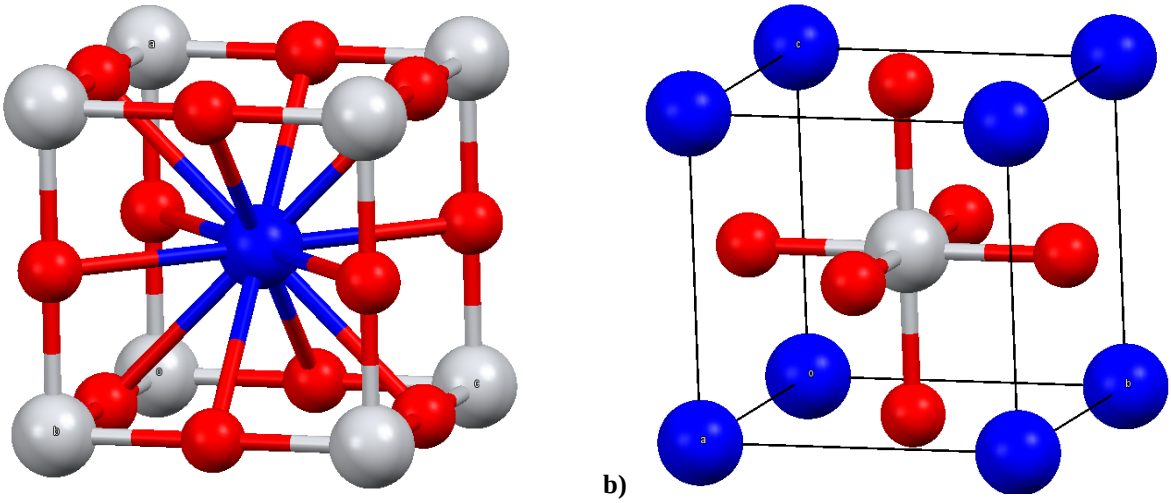

a) **b)**

Figure 1.1 The crystal structure of ideal perovskite $SrTiO_3$. The Sr^{2+} are marked in blue, the Ti^{4+} ions in grey and the O^{2-} in red: a) representation of the $SrTiO_3$ in the B-cell setting and b) representation of the $SrTiO_3$ in the A-cell setting.

In an idealised cubic perovskite constructed of rigid spheres, the A-site cation has the same size as the anions so the atoms are connected to each other. Therefore, for a unit cell drawn with the origin centred on the B-site cation (Figure 1.1b)) the following equation holds for the perfect cubic perovskite:

$$t = \frac{(r_A + r_O)}{\sqrt{2}(r_B + r_O)} = 1 \qquad \textit{Equation 1.1}$$

where t is the Goldschmidt tolerance factor and r_A, r_B and r_O are the ionic radii of A, B and O respectively. Although for ideal structures t is unity, it is still possible to obtain a stable perovskite of lower symmetry for values of t greater than 0.8. The tolerance factor can be used as a measure of the degree of distortion of a perovskite from ideal cubic and as a guide of whether a given assemblage of ions will adopt the perovskite structure at a particular temperature and pressure [7].

The versatility of the perovskite structure is in part due to the many different distortions of the unit cell. Thus, it can be distorted: a) along the cubic [001] direction, giving a tetragonal cell; b) along the [110] direction, resulting in an orthorhombic cell; c) along the [111] direction,

creating a rhombohedral cell, or d) along arbitrary [hk0] or [hkl] directions (monoclinic and triclinic cell, respectively) [8].

1.1.1 Distortion of the ideal perovskite structure

The ideal perovskite adopts a cubic structure with space group $Pm\bar{3}m$, however most perovskites have lower symmetry owing to distortions [9].

The most common type of distortion is the tilting of the BX_6 octahedra relative to one another as nearly rigid corner-linked units. This type of distortion arises when the size of the A-cation is too small for the 12-fold site within a BX_6 polyhedral framework [7]. Glazer in 1972 introduced a notation for tilt systems [10]. Using this notation a tilt system is described in terms of rotations of BX_6 polyhedra about any of three orthogonal Cartesian axes being these axes coincident with the three axes of the aristotype cubic unit cell. In the general case of unequal angles of rotation about the *x*, *y* and *z* axes, the rotation scheme is specified as *a*, *b* and *c* degrees. The sense of the rotations in successive layers of octahedra perpendicular to the rotation axis is given as superscripts. A positive superscript is used to represent tilt of octahedra in successive layers in the same direction (*in-phase* tilt) while a negative superscript indicates the rotation of neighbouring octahedra in the opposite sense (*anti-phase* tilt). Therefore, the symbol $a^+b^+c^+$ indicates three unequal angles of rotation about *x*, *y* and *z*, with octahedra in adjacent layers perpendicular to *x*, *y* and *z* rotating in the same sense. In the case where the angles of rotation were the same about each axis the notation would be $a^+a^+a^+$. If there are no rotations about an axis a zero superscript is used. Thus, for the cubic aristotype the tilt symbol $a^0a^0a^0$ is given [7].

Another common kind of perovskite distortion involves the displacement of the B cations within the octahedra, leading to either a ferroelectric or antiferroelectric structure [9].

The situation becomes more complicated when octahedral tilting and B-cation displacements are superimposed. Here, a modified Glazer notation where subscripts + and –

denote ferroelectric B-cation displacements along a given axis is introduced. For instance, the tetragonal ferroelectric structure of $BaTiO_3$ would be represented by $a^0a^0c^0_+$, where the single subscript + denotes B-cation displacements in the direction + along the *z* axis. Moreover, $a^0a^0c^0_-$ would represent a ferroelectric structure with B-cation displacements in the – direction along the *z* axis [9].

Aleksandrov in 1978 considered the superposition of ferroelectric B-cation displacements and octahedral tilting in perovskites and acquired a list of possible structures and their symmetries [11]. However, this work has been extended by Stokes *et al* [9] in 2002.

1.2 Properties associated with noncentrosymmetric materials

Materials that are crystallographically noncentrosymmetric (NCS) are of current interest because of their functional properties, including piezoelectricity, pyroelectricity, ferroelectricity and second-harmonic generation. An NCS compound must not have an inversion centre, that is, for example every atom on a site *x*, *y*, *z* in the unit cell there is an equivalent atom on a site -*x*, -*y*, -*z* [12]. Thus, net dipole moments cancel each other in the case of centrosymmetric materials. If we consider the 32 crystal classes into which all crystalline materials may be divided, 20 of the 21 which lack a centre of symmetry (the cubic class 432, even though lacking a centre of symmetry, cannot show piezoelectricity) are piezoelectric [2]. There are 11 centrosymmetric crystal classes called Laue classes. From these 20 non-centrosymmetric crystal classes just 10 of them are polar and have permanent dipole moment: 1, 2, 3, 4, 6, *m*, *mm*2, 3*m*, 4*mm* and 6*mm* [12].

1.2.1 Piezoelectricity

Piezoelectricity was discovered in 1880 by Jacques and Pierre Curie. The word piezoelectricity is derived from the Greek *piezo* or *piezen* which means to press [13]. Piezoelectric materials can be polarised, in addition to an electric field, also by application of a

mechanical stress. The linear relationship between an external stress σ_{jk} applied to a piezoelectric material and the change in polarisation, P_i, is known as the *direct* piezoelectric effect and may be written as [14]:

$$P_i = d_{ijk}\,\sigma_{jk} \qquad \textit{Equation 1.2}$$

where d_{ijk} (i, j, k = 1, 2, 3) is the piezoelectric charge coefficient, with units of coulombs per newton (C/N) .

Piezoelectric materials also have the property of changing their dimensions; they contract or expand, when an electric field E_i is applied to them. This is known as the *converse* piezoelectric effect and describes the strain, ε_{jk}, that results in a piezoelectric material because of the applied electric field, E_i, [14] and is formulated as:

$$\varepsilon_{jk} = d_{ijk}\,E_i = \frac{\Delta t}{V} \qquad \textit{Equation 1.3}$$

where d_{ijk} is the piezoelectric coefficient, Δt is the change in thickness and V is applied voltage. If strain is plotted versus electric field a butterfly loop is produced (Figure 1.2).

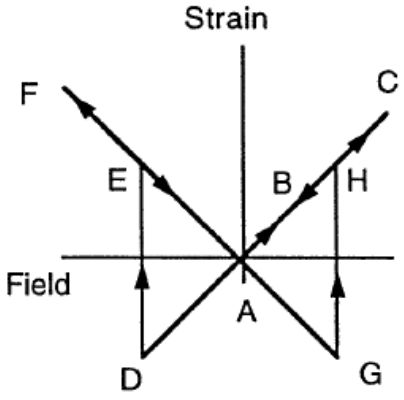

Figure 1.2 Strain-electric field hysteresis loop or butterfly loop in ferroelectrics. Figure taken from [14].

With the *direct* and *converse* piezoelectric effect, d_{ijk} is a third-rank tensor and its units when measuring both effects are equivalent, that is 1 C/N = 1 m/V. Therefore, both piezoelectric coefficients are identical *i.e.* $d_{direct} = d_{converse}$ [15].

The charge and strain piezoelectric constants, given as d_{ij}, are normally reported as one or more terms: d_{33}, d_{31} and/or d_{15}. The first subscript to d indicates the direction of the polarisation generated in the material when the electric field, E_i, is zero or, alternatively, is the direction of the applied field strength. The second subscript is the direction of the applied stress or the induced strain, respectively [12].

For d_{33} the induced polarisation (strain) is parallel to the applied stress (electric field), while for d_{31} and d_{15} the induced polarisations (strains) are perpendicular to the applied stresses (electric fields) as Figure 1.3 shows. For the piezoelectric coefficient measured in the direction of applied field it is common to call it the longitudinal coefficient, d_{33}, whereas for those measured in the direction perpendicular to the field it is typical to call these the transverse coefficients, d_{31} and d_{15} [12].

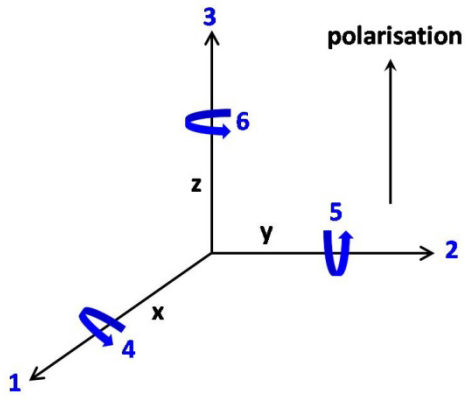

Figure 1.3 Directions of forces affecting a piezoelectric element. Figure adapted from [16].

The directions *x*, *y* and *z* are represented by the subscripts 1, 2 and 3 respectively and the shear about one of these axes is represented by the subscripts 4, 5 and 6 respectively. The direction of positive polarisation normally coincides with the *z*-axis. Thus, for the piezoelectric

constant d_{33} the induced polarisation is in direction 3 (parallel to direction in which the ceramic element is polarised) per unit and the stress applied in direction 3. For d_{31}, the induced polarisation is in direction 1 (perpendicular to the direction in which the ceramic element is polarised) and for d_{15} the induced polarisation is in direction 1 (perpendicular to the direction in which the ceramic element is polarised) per unit shear stress applied about direction 2 [16].

1.2.2 Pyroelectricity

The pyroelectric effect can be defined as the change in spontaneous polarisation, P_s, with temperature, T [12].

$$D_i = \Delta P_{s,i} = p_i \Delta T \qquad \textit{Equation 1.4}$$

where D_i is the surface charge density induced in the material by the temperature change ΔT and p_i is the vector of pyroelectric coefficients [14].

1.2.3 Ferroelectricity

Ferroelectricty is a property of certain materials which possess a spontaneous electric polarisation, below a certain temperature called Curie temperature, *Tc*, which can be reversed by the application of an external electric field. Therefore, for a material to be ferroelectric, the compound must be polar, *i.e.* must possess a permanent dipole moment, and must be able to have this moment reversed in the presence of an applied voltage. Moreover, due to the relatively large voltages applied for polarisation reversal, the material under study must be insulating so it does not degrade and become conducting [12]. Another advantageous characteristic is that the material exhibits low dielectric loss. This means that the amount of electrical energy lost as heat is minimised. Dielectric properties are defined by the behaviour of the material between two parallel plates. Nevertheless, first of all we need to consider when a vacuum is between the plates the capacitance of the material, C_o, is given by Equation 1.5.

$$C_o = \frac{\varepsilon_o A}{d} \qquad \textit{Equation 1.5}$$

where ε_o is the permittivity of free space (8.854 x 10^{-12} Fm^{-1}), *A* is the surface of the plates with units of m^2 and *d* is the distance between the two plates with units of m.

When a voltage, *V*, is applied across the two plates, a charge, *Q*, becomes stored in the material between the plates. In the case of the vacuum this is given by Equation 1.6.

$$Q_o = C_o V \qquad \textit{Equation 1.6}$$

When an actual dielectric material is located between the two plates the quantity of charge, Q_1, stored between the plates increases from the case of vacuum, Q_o. Thus, to determine the material's ability to hold a charge, how polarisable the material is, the ratio of the charge stored in the dielectric material in comparison to the vacuum can be used. This ratio is known as the dielectric constant, *ε'*, and is given by Equations 1.7 and 1.8.

$$\varepsilon' = \frac{Q1}{Qo} = \frac{C1}{Co} \qquad \textit{Equation 1.7}$$

If the equation for C_o (Equation 1.5) is substituted in Equation 1.7 this becomes:

$$\varepsilon' = \frac{C}{8.854x10-12} x \frac{d}{A} \qquad \textit{Equation 1.8}$$

As stated before, another important feature of dielectric materials is that they exhibit low dielectric loss. Dielectric measurements were performed over a range of frequencies with a superimposed AC field. At low frequencies the polarisation within the material can occur before the field reverses and consequently it creates an alternating current through the material. With increasing frequency, the polarisation in the material can no longer keep up with the alternating field. Accordingly, the current that is induced by the polarisation lags behind the applied voltage and the angle by which it lags is known as *δ*. As a result, there is dissipation of energy from the sample in the form of heat, also known as dielectric loss. Therefore, the polarisation can be

considered to have a real and imaginary part. Both real and imaginary values of the capacitance and charge can be measured. The dielectric loss is often reported with respect to the dielectric constant, it is given the term 'tan delta' and is calculated using Equation 1.9.

$$tan\delta = \frac{\varepsilon''}{\varepsilon'} \qquad \textit{Equation 1.9}$$

where ε' is the dielectric constant of the real part and ε'' the imaginary part.

One feature that can be observed in ferroelectric materials is a dielectric anomaly at the Curie temperature. This means that a maximum in the dielectric constant is normally observed at the Curie temperature. This temperature indicates a phase-change to a centrosymmetric, nonpolar, *i.e.* nonferroelectric, often called paraelectric structure [12].

Barium titanate $BaTiO_3$ was the first piezoelectric ceramic developed and adopts a perovskite structure with a TiO_6 octahedron surrounded by a cube of Ba^{2+} ions. At room temperature $BaTiO_3$ adopts a tetragonal structure crystallising in *P*4*mm* as Figure 1.4 a) shows. The titanium cations are displaced from the centre of the octahedron creating a dipole in the structure as represented with a blue arrow. Above 130 °C a phase transition takes place and the cubic structure is formed, $Pm\bar{3}m$ as shown in Figure 1.4 b). The paraelectric phase is then formed and the ionic charges cancel each other so the structure is un-polarised [2].

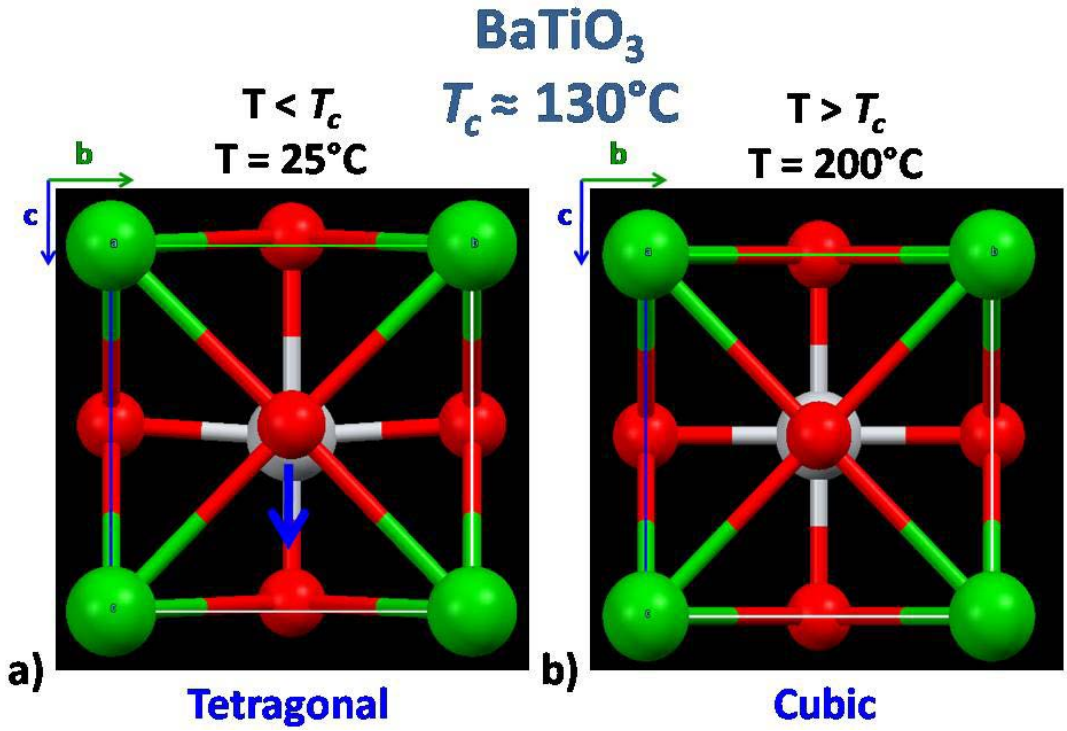

Figure 1.4 Structure of $BaTiO_3$ viewed along a: a) at 25 °C, below the Tc, the tetragonal structure is adopted. The blue arrow shows the displacement of the titanium cations along the c-axis; b) at 200 °C, above the Tc, the cubic structure is adopted. The crystallographic axis for b (green) and c (blue) are shown. Barium cations are shown in green, titanium in grey and oxygen anions in red.

The most important characteristic of ferroelectric materials is polarisation reversal or switching by an electric field. As a consequence of the domain wall switching, ferroelectric materials show a typical ferroelectric hysteresis loop as shown in Figure 1.5 for a $Pb(Zr_{0.45}Ti_{0.55})O_3$ thick film [14].

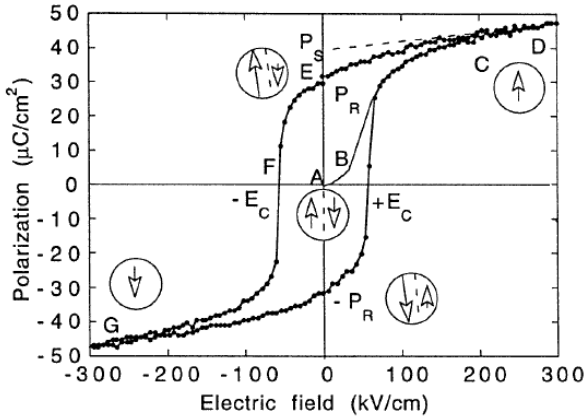

Figure 1.5 Ferroelectric polarisation-electric field (P(E)) hysteresis loop measured on a $Pb(Zr_{0.45}Ti_{0.55})O_3$ thick film. Circles with arrows represent the polarisation state of the material at the indicated fields. The symbols are explained in the text. This figure was taken from [14].

The polarisation, *y* axis, increases linearly with the field amplitude, *x* axis, according to Equation 1.10. This corresponds to segment AB in Figure 1.5. In this region, the field is not strong enough to switch domains with the unfavourable direction of the polarisation. With increasing field strength, the polarisation of domains with an unfavourable direction of the polarisation will start to switch in the direction of the field, rapidly increasing the measured charge density, segment BC. At point C all the domains are aligned. When the field strength starts to decrease, some domains will back-switch but at zero field the polarisation is non-zero, point E. To attain a zero polarisation state the field must be reversed, point F. If the field is further increased in the negative direction a new alignment of dipoles and saturation will be obtained, point G. The field strength is then reduced to zero and reversed to complete the cycle. The remanent polarisation, P_{rem} or P_R in Figure 1.5 is the value of polarisation at zero field, point E. The coercive field, E_c, is the field strength necessary to bring the polarisation to zero. The spontaneous polarisation, P_s, is usually taken as the intercept of the polarisation axis with the extrapolated linear segment CD [14].

The induced polarisation, P_i, is given by Equation 1.10:

$$P_i = X_{ij} E_j \qquad \textit{Equation 1.10}$$

where X_{ij} is the dielectric susceptibility of the material and E_j is the applied electric field [14].

In addition to the polarisation-electric field loop (Figure 1.5), polarisation switching by an electric field in ferroelectric materials leads to strain electric field hysteresis [14] as showed in Figure 1.2 .

This strain-field hysteresis loop is due to three kinds of effects. One is the normal converse piezoelectric effect to the lattice and the other two arise from the switching and movement of domain walls [14].

At zero field, point A in Figure 1.2, the strain of the crystal is taken to be zero. The electric field is then applied in the same direction as the spontaneous polarisation. As the field increases, the crystal expands through the piezoelectric effect, according to Equation 1.3 and the line A-B-C is traced by the strain. The expansion then continues until the maximum field is reached at point C. As the field starts to decrease, still parallel to P_s, the strain of the sample traces the same line but in the opposite direction, from C to A, with the strain again zero at point A. The field then changes its direction and is antiparallel to P_s. As the field strength increases in the negative direction, according to Equation 1.3, the crystal contracts with respect to point A. At point D, the field is large enough to switch the direction of polarisation and after switching, the polarisation becomes parallel to the field and the strain is positive again (point E). During further increase of the field in the negative direction, the strain increases to point F and then decreases back to point A as the field is decreased in accordance with Equation 1.3. At point G, the reversal of the polarisation and sudden change of strain happens again. The strain-field loop is linear, and this is evidence that the strain is purely piezoelectric except at the switching points D and G [14].

1.2.4 Second Harmonic Generation (SHG)

The Second Harmonic Generation (SHG) was discovered in 1961 by P. Franken [17] and at that time large crystals (several mm) were required to investigate the phenomenon. However, a technique described in 1968 [18] allowed one to determine the SHG efficiency of polycrystalline samples. SHG, also called frequency doubling, is a non-linear optical process and can be defined as the conversion of a specific wavelength of light into half its original, *i.e.* $\lambda_1 \rightarrow ½\ \lambda_1$ or with respect to frequency ω, $\omega_1 \rightarrow 2\omega_1$ [12].

A non-linear optical process occurs when some of the properties of the wave are modified (such as frequency doubling or summing of the frequencies) as a consequence of an interaction between the material and the electromagnetic wave, known as second order non-linear optical

phenomenon. However, sizeable non-linear optical effects, like SHG, could not be observed until the invention of the laser in 1960 by Maiman, who created the required high intensity monochromatic (6943 Å) light beams [19].

1.3 Lead ZirconateTitanate

Lead zirconate titanate, $Pb(Zr_{1-x}Ti_x)O_3$, (PZT) is a widely applied piezoelectric material that displays high dielectric and piezoelectric properties. The piezoelectric properties quantified by the piezoelectric coefficient, d_{33} range between 200-600 pC/N in commercial PZT [20]. These physical properties are enhanced at the morphotropic phase boundary (MPB) between two polar ferroelectric compositions of different symmetry around x ≈ 0.45-0.5 and with different polarisation directions. The PZT phase diagram is shown in Figure 1.6 a). Thus, at the morphotropic phase boundary, PZT is formed between $PbZrO_3$ and $PbTiO_3$ with rhombohedral (R) and tetragonal (T) structures respectively [2]. The PZT phases are untilted and the R and T structures are described crystallographically, using a modified Glazer notation, as $a_+^0 a_+^0 a_+^0$ and $a_0^0 a_0^0 c_+^0$ respectively where the subscript indicates ferroelectric displacement and the superscript the nature of the octahedral tilting with respect to the primitive unit cell axis [9]. In the tetragonal region of PZT the space group is *P*4*mm*, with the polar axis along [001], whereas in the rhombohedral region the space group is *R*3*m* with the polar axis along [111]. Other authors say that actually the MPB is formed at the boundary between the rhombohedral, tetragonal and a monoclinic phase [21]. They claimed that the monoclinic (M) phase crystallises in *Cm* with the mirror plane as the only symmetry element in common between the well-known R (space group *R*3*m*) and T (space group *P*4*mm*). Thus, this monoclinic phase can be viewed as a bridge between the R and T structures [22]. Figure 1.6 b) shows the PZT diagram around MPB including the monoclinic phase found based on synchrotron X-ray powder diffraction data [21]. The large piezoelectric response of PZT can be attributed to polarisation rotation at the MPB or in the

monoclinic phase and to a high contribution from the domain wall motion to the piezoelectric properties [20, 23].

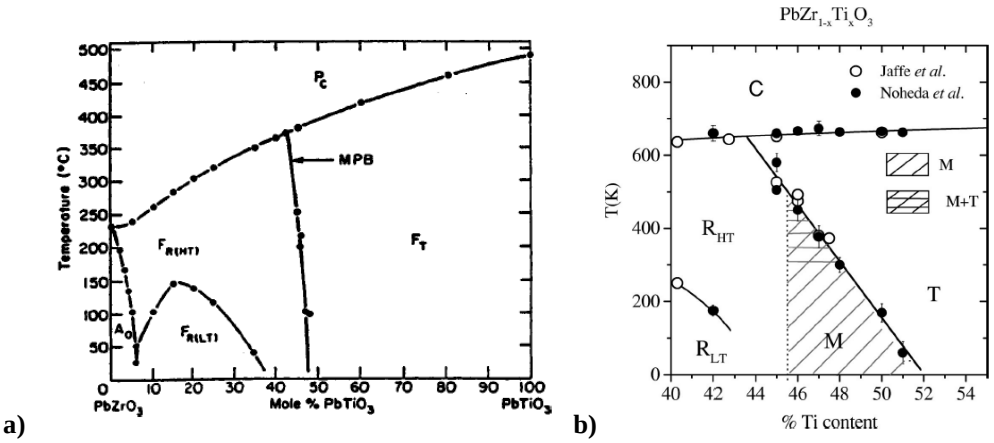

Figure 1.6 a) PZT phase diagram taken from [2]; b) PZT phase diagram around MPB including the monoclinic phase taken from [21].

Some of the large-volume applications of PZT require strain over an extended temperature range, which PZT can provide up to about 175 °C with little temperature dependence [24]. Therefore, due to the danger of thermal depoling associated with *Tc* of 300-400 °C and a significant increase in conductivity, its usage at higher temperature is limited [8]. Moreover, a wide variety of dopants can be used to manufacture a range of 'soft' and 'hard' PZT piezoelectrics tuned for distinct applications [2]. However, materials which offer higher *Tc* than PZT would be desirable for high temperature applications.

As a rule of thumb, piezoelectric materials can be safely used to nearly one half *Tc* without losing their piezoelectric activity considerably [25]. Lately, the depolarisation temperature (T_d) has been proposed to define the temperature at which a poled ferroelectric material completely or partially depolarises and can be determined from pyroelectric measurements [26]. T_d normally matches with the *Tc*, nevertheless in materials undergoing one or more polymorphic phase transitions below the *Tc* but above room temperature, T_d refers to the temperature of the lowest of these phase transitions [5].

1.3.1 Environmental context, toxicity of lead

It is well-known that lead is a toxic element [27]. During calcinations and sintering of PZT lead is released into the environment. Also, recycling and waste disposal of lead-containing devices could be dangerous for the environment and health [28]. Consequently, in the last decade legislation governing the use of lead containing compounds has been enforced in the European Union and the State of California including the draft Directives on Waste from Electrical and Electronic Equipment (WEEE), Restriction of Hazardous Substances (RoHS) and End-of-Life Vehicles (ELV) [29-32]. Therefore, there is a high interest in discovering lead-free piezoelectric materials which can afford MPB compositions and mimic the physical properties of PZT to replace it.

The exclusive dominance of lead-based piezoceramics, representatively PZT, over the piezoelectric market for more than fifty years is not just because of their excellent properties but also because of considerations of cost. PZT is based on relatively inexpensive raw materials [8]. Furthermore, the consolidation of raw materials with a density of more than 96% can be simply obtained even by non-high pressure sintering techniques [33]. Consequently, in the development of lead-free piezoceramics economical considerations are as important as excellent functional properties.

The striking ferroelectric properties of Pb-based systems are related to the $6s^2$ electronic configuration of Pb^{2+} [6]. It has been shown that the interaction of the *s*- and *p*- orbitals of the metal cation with the oxide anion *p*-states is critical for lone-pair formation resulting in a noncentrosymmetric coordination environment [6, 34-40]. Thus, the lone-pair 'pushes' the oxide ligands toward one side of the metal cation resulting in a noncentrosymmetric coordination environment [12, 36].

Bismuth has also the $6s^2$ inert pair of electrons. Moreover, it is an inexpensive and non-toxic heavy metal [8]. Actually, many studies have demonstrated that Bi^{3+} has practically no harmful effect on living organisms [41, 42] and therefore, it is a suitable candidate to replace Pb^{2+} ion.

1.4 Lead-free ferroelectric materials review

1.4.1 Titanate perovskites

Perovskite ferroelectrics in which the B-site is the Ti^{4+} ion make up a large fraction of the materials under consideration for lead-free piezoelectric. In Table 1.1, published piezoelectric coefficients and relevant phase transition temperatures for the titanate perovskites and their solid solutions are collected.

1.4.1.1 Barium titanate

$BaTiO_3$ (BTO) is the prototype polymorphic phase transition (PPT)-based high performance piezoceramic material [5] with a piezoelectric coefficient of 190 pC/N fabricated by conventional solid state processing [43]. BTO was used in naval sonar applications and phonograph needles before the discovery of PZT-based materials [5]. Nevertheless, due to its low Curie temperature (*Tc* = 120 °C [2]) extensive commercial application of BTO for piezoelectric actuators remains limited [5].

Lately, improvements on the piezoelectric response in BTO have been achieved by structural engineering as shown in Table 1.1 Large piezoelectric response (up to 460 pC/N in hydrothermal BTO [44]) has been obtained in optimally prepared ceramics. Furthermore, the piezoelectric properties of BTO have been enhanced up to ~ 800 pC/N in grain-oriented BTO [45].

1.4.1.2 Bismuth potassium titanate

Bismuth potassium titanate $(Bi_{1/2}K_{1/2})TiO_3$ (BKT) is another common lead-free ferroelectric ceramic material and adopts a tetragonal symmetry at room temperature. It undergoes a second phase transition to a pseudocubic structure at ~ 300 ºC. BKT was synthesised in 1957 [46] and its ferroelectricity and Curie temperature of 370 °C were confirmed later by Buhrer [47]. BKT shows a d_{33} = 70 pC/N when synthesised by hot pressing methods [48]. The piezoelectric coefficient for BKT has been improved when doping with bismuth and using sintering aids achieving a d_{33} = 100 pC/N [49].

1.4.1.3 Bismuth sodium titanate

Bismuth sodium titanate $(Bi_{1/2}Na_{1/2})TiO_3$ (BNT) is another important lead-free piezoelectric material and was reported by Smolenskii *et al.* in 1960 [50]. In BNT, a diffuse phase transformation in the temperature range 200-300 °C is observed corresponding to a transition from rhombohedral to tetragonal symmetry [51-53]. The synthesis of dense BNT ceramics is complicated as sintering temperatures above 1200 °C are required resulting in significant loss of bismuth. In conventional fabricated samples of BNT saturated loops are difficult to obtain due to high coercive field needed to apply. Nevertheless, dense ceramics have been achieved either using excess of Bi or hot pressing sintering methods, yielding samples with saturated polarisation loops [54]. BNT ceramics synthesised by these latter techniques show a d_{33} = 94-98 pC/N and a T_d = 200 °C [50, 54].

1.4.1.4 Bismuth potassium titanate-barium titanate solid solution

The binary system BKT-BTO has been studied in order to achieve a material with enhanced piezoelectric properties and higher *Tc* than pure BTO. A single phase ferroelectric perovskite is formed over the whole compositional range xBKT-(1-x)BTO and shows almost a linear

dependence of *Tc* on BKT concentration [55]. A transition from tetragonal to an intermediate pseudocubic phase is observed around 300 °C in compositions above x = 60 mol% BKT. Values of d_{33} do not vary significantly with composition and are in the range 60-70 pC/N. With the addition of manganese, the highest d_{33} of 100 pC/N has been achieved for x = 5 mol% BKT. However, the *Tc* for this composition is relatively low (168 °C). A considerably improved d_{33} value of 121 pC/N for x = 10 mol% BKT has been achieved using the templated grain growth technique [56, 57].

1.4.1.5 Bismuth sodium titanate-barium titanate solid solution

The binary system BNT-BTO was investigated by Takenaka *et al* .[58] to determine if an MPB between the rhombohedral ferroelectric BNT and the tetragonal BTO could be achieved as in the prototype PZT system. The existence of an MPB was confirmed at around 6-7 mol% BTO obtaining a d_{33} of 125 pC/N [59, 60]. d_{33} values in the range 122-176 pC/N at the MPB have been reported by various researchers [58, 61-63]. When modifying BNT-BTO with lithium d_{33} values of 208 pC/N were obtained [64, 65]. The system BNT-BTO at the MPB has a relatively high *Tc* of 288 °C while a low T_d of 150 °C has been reported [5]. As for the BNT end member, the T_d arises owing to a polymorphic phase transformation to an antiferroelectric (AFE) phase [58].

1.4.1.6 Bismuth sodium titanate-bismuth potassium titanate solid solution

The solid solution between BNT and BKT was synthesised by Elkechai *et al.* in 1996 [66]. An MPB was achieved in the compositional range 16-20 mol% BKT where the rhombohedral and tetragonal phases coexist [67]. The piezoelectric coefficients at the MPB are in the range of 140-190 pC/N [68-71]. The *Tc* of the MPB is of 280-300 °C and higher than that of pure BNT as expected. Nevertheless, the T_d is 140 °C and is due to a polymorphic phase transformation to the intermediate pseudocubic phase at the MPB.

1.4.1.7 Barium-titanate-bismuth sodium titanate-bismuth potassium titanate ternary solid solution

The ternary BTO-BNT-BKT solid solution has been widely investigating because of the relatively high Curie temperatures and high piezoelectric properties. BTO-BNT-BKT shows a tetragonal-rhombohedral MPB with a d_{33} of 170 pC/N and low T_d of ~110 °C [72-74]. The piezoelectric properties have been enhanced in Li-modified BTO-BNT-BKT showing a d_{33} of 205 pC/N and a T_d of 210 °C [75].

Table 1.1: Piezoelectric coefficients (d_{33}), depolarisation temperature (T_d) and Curie temperatures (Tc) for titanate perovskites at room temperature. Notes: Where available the measurement method used for determining the piezoelectric coefficient is indicated: refers to a Berlincourt-type meter and # to the IEEE resonance method. The type of polymorphic transition occurring at T_d is indicated as follows: O-T, orthorhombic-tetragonal or ?,unknown. Table adapted from [5].*

Titanates and solid solutions				
Material	d_{33} (pC/N)	T_d / °C	Tc / °C	Comment, reference
$BaTiO_3$	190*	0	120	[2]
$BaTiO_3$	350*	O-T / 0	120	Microwave sintered, [76]
$BaTiO_3$	460*	O-T / 24	126	Hydrothermal powders, [44]
$BaTiO_3$	788*	O-T / 0	120	Textured, [45]
BKT	70#	O-T / 315	410	[48]
BKT-Bi	100#	PC / 280 / AFE	391	[49]
$BaTiO_3$-BKT20 + Mn	76#	none	230	[55]
$BaTiO_3$-BKT5 + Mn	100#	none	168	[55]
BNT-BTO	122-176*	AFE / 150	288	[62]
BNT-BTO + Li	208	AFE / 85	260	[64]
BNT-BKT	140-190*	PC / 140	280-300	[66]
BNT-BKT-BTO	170*	PC / 162	262	[74]
BNT-BKT-BTO + Li	205*	AFE / 210	N/A	[75]

1.4.2 Alkaline niobates

The alkaline niobates and their solid solutions are another family of lead-free piezoelectric materials. In Table 1.2, published piezoelectric coefficients and relevant phase transition temperatures for the alkaline niobates and their solid solutions are compiled.

1.4.2.1 Potassium niobate

Ferroelectricity in potassium niobate, $KNbO_3$ (KNN), was discovered in 1951 and KNN has an orthorhombic structure at room temperature [77]. It undergoes the same sequence of symmetries as $BaTiO_3$ during cooling: cubic, tetragonal, orthorhombic and rhombohedral. However, the transitions take place at higher temperatures with the temperature of the second transition ~225 °C and *Tc* at ~ 435 °C [2]. Studies on bulk KNN ceramics report a d_{33} of 97 pC/N [78].

1.4.2.2 Sodium niobate

Sodium niobate, $NaNbO_3$, also adopts an orthorhombic structure at room temperature {Yuzyuk, 2005 #273} although Darlington et al have shown that the symmetry is monoclinic rather than orthorhombic {Darlington, 1999 #272}, transforming into another orthorhombic phase at 370 °C and with a *Tc* above 640 °C { #254;Darlington, 1999 #272;Jabarov, 2012 #276}. At room temperature, $NaNbO_3$ is antiferroelectric and does not exhibit piezoelectric activity in its pure form [2].

1.4.2.3 Potassium niobate-sodium niobate solid solution

The solid solutions between $KNbO_3$ and $NaNbO_3$, $(1-x)KNbO_3$-$xNaNbO_3$, possess an MPB at x ~ 0.5 separating the two ferroelectric phases. As for PZT, the properties were enhanced for compositions near to the MPB [80, 81]. The d_{33} value for $K_{0.5}Na_{0.5}NbO_3$ (KNN) is 80 pC/N and *Tc* at ~ 420 °C for an air-fired material [80]. Nevertheless, the major disadvantage of KNN ceramics is the need for special handling of the starting materials and difficulty during the densification process [82]. Sintering under normal conditions normally gives materials with low densities and therefore properties that are not optimised. To achieve high densities sintering aids

[83, 84] and hot pressing [81] have been used. However, these processing techniques are not suitable for industrial use [85].

In order to improve the physical properties of KNN, it has been modified with several materials. For instance, for KNN-$LiNbO_3$ (6mol%) has a piezoelectric constant d_{33} value reaching 235 pC/N with Tc = 460 °C [86], at least 100 °C higher than that of conventional PZT. KNN in combination with $LiSbO_3$ shifts the orthorhombic to tetragonal polymorphic phase transition down from 200 °C to almost room temperature (T_{OT} ~ 35 °C) and enhances the d_{33} up to 283 pC/N at approximately 5 mol% of $LiSbO_3$ with Tc = 392 °C [87-90]. The addition of $LiTaO_3$ into KNN exhibits an MPB between orthorhombic and tetragonal phases at 4-5 mol % of $LiTaO_3$. The piezoelectric properties at the MPB have been maximised and d_{33} in the range 200-259 pC/N have been reported [91-95]. The most successful modified KNN in terms of piezoelectric properties is the material $(K_{0.44}Na_{0.52}Li_{0.04})(Nb_{0.86}Ta_{0.10}Sb_{0.04})O_3$ synthesised by Saito *et al.* with a d_{33} value of 410 pC/N and Tc = 253 °C [96].

Table 1.2: Piezoelectric coefficients (d_{33}), depolarisation temperature (T_d) and Curie temperatures (Tc) for alkaline niobate perovskites at room temperature. Notes: Where available the measurement method used for determining the piezoelectric coefficient is indicated: refers to a Berlincourt-type meter and # to the IEEE resonance method. The type of polymorphic transition occurring at T_d is indicated as follows: O-T, orthorhombic-tetragonal or ?,unknown. Table adapted from [5].*

Titanates and solid solutions				
Material	d_{33} (pC/N)	T_d / °C	Tc / °C	Comment, reference
$KNbO_3$	97	O-T / 220	435	[78]
$(K,Na)NbO_3$	80	O-T / 195	420	[80]
$(K,Na)NbO_3$	127	O-T / 420	420	Hot pressed, [81]
$(K,Na)NbO_3$+ Sb	218*	O-T / 160	352	Textured, [97]
$(K,Na)NbO_3$+ Ag	186*	O-T / 170	355	[98]
$(K,Na)NbO_3$+ Li	240*	O-T / 20	460	[85]
$(K,Na)NbO_3$+ Li, Ta	190*	O-T / 50	210	[85]
$(K,Na)NbO_3$+ SrTiO3	200*	O-T / 27	277	[99]
$(K,Na)NbO_3$+ $LiTaO_3$	200*	O-T / 55	430	[91-95]
$(K,Na)NbO_3$+ $LiNbO_3$	235*	O-T / 70	452	[86]
$(K,Na)NbO_3$+ $LiSbO_3$	265#	O-T / 55	368	[87-90]
$(K,Na)NbO_3$+ Li, Sb, Ta (LF4)	410*	O-T / 25	253	Textured, [96]

1.4.3 Bismuth perovskites

Polar systems based on Bi^{3+} are being widely studied, but just few examples of perovskites with only Bi^{3+} ions at the A-site are stable under ambient pressure: $BiFeO_3$ [100], $Bi_2(Mn_{4/3}Ni_{2/3})O_6$ [101] and $Bi(Ti_{3/8}Fe_{2/8}Mg_{3/8})O_3$ [102]. The reason is because the size of Bi^{3+} is small and mismatch with the twelve coordinate A-site [102]. Other analogous Bi-based perovskites materials are just accessible via high pressure synthesis like $BiMnO_3$ [103] and $BiScO_3$ [104].

1.4.3.1 Bismuth ferrite

Bismuth ferrite $BiFeO_3$ (BFO) is the Bi-based perovskite material most studied so far because it is both magnetic and a strong ferroelectric at room temperature [105]. BFO has a rhombohedral structure and crystallises in *R*3*c* with a ferroelectric polarisation along [111] at room temperature. BFO undergoes two phase transitions. The first one is at around 825 °C and is a first-order transition to a high-temperature β phase. Although the exact symmetry of the β phase is not clear, most reports agree that it is centrosymmetric [106-111]. The orthorhombic *Pbnm* space group is the most favourable based on neutron diffraction experiments [111]. The second phase transition from the β phase to the γ phase occurs above 931 °C. It is proposed that the γ phase has a cubic structure with $Pm\bar{3}m$ symmetry [112]. However, another study suggests that actually the γ phase adopts an orthorhombic structure with space group *Pbnm.* Thus, it might undergo two further phase transitions to tetragonal and cubic at ~ 1020 °C and 1100 °C respectively although taking into account that BFO above ~ 950 °C decomposes to $Bi_2Fe_4O_9$ and liquid Bi_2O_3 [113].

As BFO is a room temperature ferroelectric, it is a clear candidate for applications and to replace PZT. Its remanent polarisation is very large, 100 $\mu C/cm^2$ along the polar [111] direction [114], and the d_{33} of BFO is 16 pC/N [25]. However, important impediments must be overcome,

such as: i) the higher conductivity (and therefore dielectric losses) of BFO in comparison with PZT, ii) its propensity to fatigue [115] and iii) the fact that it seems to decompose at voltages very close to the coercive field [116]. With the purpose to remove the above mentioned obstacles, BFO has been doped with many different rare-earth elements [117] such as: La [118-120], Nd, Sm [121, 122], or Gd. Partial substitution of Bi^{3+} ions by lanthanides has been shown to improve ferroelectric properties [119, 123, 124]. Furthermore, BFO has been doped with alkaline earth metals [24, 25].

Reported piezoelectric coefficients and transition temperatures for the lead-free bismuth perovskites and their solid solutions are listed in Table 1.3.

Table 1.3: Piezoelectric coefficients (d_{33}), depolarisation temperature (T_d) and Curie temperatures (Tc) for bismuth perovskites at room temperature. Notes: Where available the measurement method used for determining the piezoelectric coefficient is indicated: refers to a Berlincourt-type meter. The type of polymorphic transition occurring at T_d is indicated as follows: O-T, orthorhombic-tetragonal or ?,unknown. Table adapted from [5].*

Bismuth perovskites				
Material	d_{33} (pC/N)	T_d / °C	*Tc* / °C	Reference
$(K,Na)NbO_3$ $+SrTiO_3$, $BiFeO_3$, Li	155*	30	370	[125]
$(K,Na)NbO_3$ + $BiScO_3$	253*	O-T / 469	351	[126]
$BiFeO_3$-$BaTiO_3$	116*	? / 430	619	[127]

The low depolarisation temperatures associated with polymorphic phase transformations in both the titanate and alkaline niobate perovskites (Tables 1.1 and 1.2) are the main impediment in commercialization of lead-free piezoelectric actuators. However, bismuth–based perovskites offer high Curie and depolarisation temperatures (Table 1.3) which are required for demanding application environments [5, 128]. Furthermore, there are few examples of bismuth-based perovskites that can be synthesised at ambient pressure ($BiFeO_3$ [100], $Bi_2(Mn_{4/3}Ni_{2/3})O_6$ [101] and $Bi(Ti_{3/8}Fe_{2/8}Mg_{3/8})O_3$ [102]) so they could be suitable candidates to substitute PZT. The

compound $Bi(Ti_{3/8}Fe_{2/8}Mg_{3/8})O_3$ and their solid solutions will be explained in detail in Chapter 3 as they are the subject of study in this thesis.

1.5 References

1. Tressler, J. F., Alkoy, S., Dogan, A. and Newnham, R. E., *Composites Part a-Applied Science and Manufacturing*, 1999. **30**(4): p. 477-482.
2. Jaffe, B., Piezoelectric Ceramics, *Academic Press*: London, New York, 1971.
3. Randall, C. A., Kelnberger, A., Yang, G. Y., Eitel, R. E. and Shrout, T. R., *Journal of Electroceramics*, 2005. **14**(3): p. 177-191.
4. Uchinoin, K., Piezoelectric Actuators and Ultrasonic Motors (Boston, Ma: Kluwer), 1997.
5. Leontsev, S. O.and Eitel, R. E., *Science and Technology of Advanced Materials*, 2010. **11**(4).
6. Cohen, R. E., *Nature*, 1992. **358**.
7. Mitchell, R. H., Perovskites Modern and Ancient, *Almaz Press-Thunder Bay*, 2002**.**
8. Roedel, J., Jo, W., Seifert, K. T. P., Anton, E. M., Granzow, T. and Damjanovic, D., *Journal of the American Ceramic Society*, 2009. **92**(6): p. 1153-1177.
9. Stokes, H.T., Kisi, E. H., Hatch, D. M. and Howard, C. J., *Acta Crystallographica Section B-Structural Science*, 2002. **58**: p. 934-938.
10. Glazer, A. M., *Acta Crystallographica Section B-Structural Science*, 1972. **B28** p. 3384-3392.
11. Aleksandrov, K. S., *Ferroelectrics*, 1978. **20**(1-2): p. 61-67.
12. Halasyamani, P. S., *John Wiley & Sons*, Ltd., 2010.
13. Curie, J. and Curie, P., *Bulletin de la Societe Mineralogique de France*, 1880. **3**(90).
14. Damjanovic, D., *Reports on Progress in Physics* , 1998. **61**: p. 1267-1324.
15. Nye, J. F., *Oxford University Press*, Oxford, UK,, 1957.
16. https://www.americanpiezo.com/knowledge-center/piezo-theory/piezoelectric-constants.html.
17. Franken, P. A., Hill, A. E., Peters, C. W. and Weinreich, G., *Physical Review Letters*, 1961. **7**: p. 118-120.
18. Kurtz, S. K. and Perry., T. T., *Journal of Applied Physics*, 1968. **39**(8): p. 3798-3813.
19. Maiman, T. H., *Nature*, 1960. **187**: p. 493-494.
20. Damjanovic, D., Klein, N., Li, J. and Porokhonskyy, V., *Functional Materials Letters*, 2010. **3**(1): p. 5-13.
21. Noheda, B., Cox, D. E., Shirane, G., Guo, R., Jones, B. and Cross, L. E., *Physical Review B*, 2001. **63**(1): p.014103-1- 014103-8.
22. Noheda, B. and Cox, D. E., *Phase Transitions*, 2006. **79**(1-2): p. 5-20.
23. Damjanovic, D., *Applied Physics Letters*, 2010. **97**(6) : p. 062906-1-062906-3
24. Kungl, H. and Hoffmann., M. J., *Acta Materialia*, 2007. **55**(17): p. 5780-5791.
25. Zhang, S., Xia, R. and Shrout, T. R., *Journal of Electroceramics*, 2007. **19**(4): p. 251-257.
26. Shrout, T. R. and Zhang, S. J., *Journal of Electroceramics*, 2007. **19**(1): p. 113-126.
27. Safety data sheet, Lead (II) oxide".
28. Nevin, R., *Environmental Research Section A*, 2000. **83**: p. 1-22.
29. *EU-Directive 2002/95/EC:* . Official J. European Union, 2003. **46, (L37)**: p. 19-23.
30. *EU-Directive 2002/96/EC:* . Official J. European Union 2003. **46, (L37)**: p. 24-38.
31. *California Health and Safety Code* 2006: p. 25214.9-25214.10.2.
32. Official J. European Union, 2000. **269**: p. 34.
33. Haertling, G.H., *Journal of the American Ceramic Society*, 1999. **82**(4): p. 797-818.
34. Lefebvre, I., Lannoo, M., Allan, G., Ibanez, A., Fourcade, J., Jumas, J. C. and Beaurepaire, E., *Physical Review Letters*, 1987. **59**(21): p. 2471-2474.
35. Lefebvre, I., Szymanski, M. A., Olivier-Fourcade, J. and Jumas, J. C., *Physical Review B*, 1998. **58**(4): p. 1896-1906.

36. Seshadri, R. and Hill, N. A., *Chemistry of Materials*, 2001. **13**(9): p. 2892-2899.
37. Watson, G. W. and Parker, S. C., *Journal of Physical Chemistry B*, 1999. **103**(8): p. 1258-1262.
38. Watson, G. W., Parker, S. C. and Kresse, G., *Physical Review B*, 1999. **59**(13): p. 8481-8486.
39. Waghmare, U. V., Spaldin, N. A., Kandpal, H. C. and Seshadri, R., *Physical Review B*, 2003. **67**(12):p12501-1-12501-9.
40. Stoltzfus, M. W., Woodward, P. M., Seshadri, R., Klepeis, J. H. and Bursten, B., *Inorganic Chemistry*, 2007. **46**(10): p. 3839-3850.
41. Rodilla, V., Miles, A. T., Jenner, W. and Hawksworth, G. M., *Chemico-Biological Interactions*, 1998. **115**(1): p. 71-83.
42. Sano, Y., Satoh, H., Chiba, M., Okamoto, M., Serizawa, K., Nakashima, H. and Omae, K., *Journal of Occupational Health*, 2005. **47**(4): p. 293-298.
43. Bechmann, R., *Journal of the Acoustical Society of America*, 1956. **28**(3): p. 347-350.
44. Karaki, T., Yan, K. and Adachi, M. *Japanese Journal of Applied Physics Part 1-Regular Papers Brief Communications & Review Papers*, 2007. **46**(10B): p. 7035-7038.
45. Wada, S., Takeda, K., Muraishi, T., Kakemoto, H., Tsurumi, T. and Kimura, T., *Ferroelectrics*, 2008. **373**: p. 11-21.
46. Popper P., Ruddlesden S. N. and Ingles T. A., *Transactions British Ceramic Society*, 1957. **56**(9).
47. Buhrer, C. F., *Journal of Chemical Physics*, 1962. **36**(3): p. 798-803.
48. Hiruma, Y., Aoyagi, R., Nagata, H. and Takenaka, T., *Japanese Journal of Applied Physics Part 1-Regular Papers Brief Communications & Review Papers*, 2005. **44**(7A): p. 5040-5044.
49. Hiruma, Y., Nagata, H. and Takenaka, T., *Japanese Journal of Applied Physics Part 1-Regular Papers Brief Communications & Review Papers*, 2007. **46**(3A): p. 1081-1084.
50. Smolenskii, G. A., Isupov, V. A., Agranovskaya, A. I. and Krainik, N. N., *Soviet Physics-Solid State*, 1961. **2**(11): p. 2651-2654.
51. Jones, G. O. and Thomas, P. A., *Acta Crystallographica Section B-Structural Science*, 2002. **58**: p. 168-178.
52. Roleder, K., Suchanicz, J. and Kania, A., *Ferroelectrics*, 1989. **89**: p. 1-5.
53. Suchanicz, J., Roleder, K., Kania, A. and Handerek, J., *Ferroelectrics*, 1988. **77**: p. 107-110.
54. Nagata H, S. T., Hiruma Y. and Takenaka T., *Ceramic Transactions*, 2004. **167**(8).
55. Takenaka, T., Nagata, H. and Hiruma, Y., *Japanese Journal of Applied Physics*, 2008. **47**(5): p. 3787-3801.
56. Nemoto, M., Hiruma, Y., Nagata, H. and Takenaka, T., *Japanese Journal of Applied Physics*, 2008. **47**(5): p. 3829-3832.
57. Nemoto, M., Hiruma, Y., Nagata, H. and Takenaka, T., *Japanese Journal of Applied Physics*, 2009. **48**(7).
58. Takenaka, T., Maruyama, K. and Sakata, K., *Japanese Journal of Applied Physics Part 1-Regular Papers Short Notes & Review Papers*, 1991. **30**(9B): p. 2236-2239.
59. Takenaka, T., Sakata, K. and Toda, K., *Ferroelectrics*, 1990. **106**: p. 375-380.
60. Li, H. D., Feng, C. D. and Yao, W. L., *Materials Letters*, 2004. **58**(7-8): p. 1194-1198.
61. Chen, M., Xu, Q., Kim, B. H., Ahn, B. K., Ko, J. H., Kang, W. J. and Nam, O. J., *Journal of the European Ceramic Society*, 2008. **28**(4): p. 843-849.
62. Xu, C., Lin, D. and Kwok, K. W., *Solid State Sciences*, 2008. **10**(7): p. 934-940.
63. Oh, T. and Kim, M. H., *Materials Science and Engineering B-Solid State Materials for Advanced Technology*, 2006. **132**(3): p. 239-246.

64. Lin, D., Kwok, K. W. and Chan, H. L. W., *Solid State Ionics*, 2008. **178**(37-38): p. 1930-1937.
65. Lin, D., Xiao, D., Zhu, J. and Yu, P., *Journal of the European Ceramic Society*, 2006. **26**(15): p. 3247-3251.
66. Elkechai, O., Manier, M. and Mercurio, J. P., *Physica Status Solidi a-Applied Research*, 1996. **157**(2): p. 499-506.
67. Sasaki, A., Chiba, T., Mamiya, Y. and Otsuki, E., *Japanese Journal of Applied Physics Part 1-Regular Papers Short Notes & Review Papers*, 1999. **38**(9B): p. 5564-5567.
68. Yang, Z., Liu, B., Wei, L. and Hou, Y., *Materials Research Bulletin*, 2008. **43**(1): p. 81-89.
69. Yoshii, K., Hiruma, Y., Nagata, H. and Takenaka, T., *Japanese Journal of Applied Physics Part 1-Regular Papers Brief Communications & Review Papers*, 2006. **45**(5B): p. 4493-4496.
70. Oh, T., J*apanese Journal of Applied Physics Part 1-Regular Papers Brief Communications & Review Papers*, 2006. **45**(6A): p. 5138-5143.
71. Zhang, Y. R., Li, J. F. and Zhang, B. P., *Journal of the American Ceramic Society*, 2008. **91**(8): p. 2716-2719.
72. Hiruma, Y., Yoshii, K., Aoyagi, R., Nagata, H. and Takenaka, T., *Electroceramics in Japan Ix*, K. Katayama, et al., Editors. 2006. p. 23-26.
73. Nagata, H., Yoshida, M., Makiuchi, Y. and Takenaka, T., *Japanese Journal of Applied Physics Part 1-Regular Papers Short Notes & Review Papers*, 2003. **42**(12): p. 7401-7403.
74. Zhang, S., Shrout, T. R., Nagata, H., Hiruma, Y. and Takenaka, T. *Ieee Transactions on Ultrasonics Ferroelectrics and Frequency Control*, 2007. **54**(5): p. 910-917.
75. Lin, D. M., Xiao, D. Q., Zhu, J. G. and Yu, P., *Physica Status Solidi a-Applications and Materials Science*, 2005. **202**(9): p. R89-R91.
76. Takahashi, H., Numamoto, Y., Tani, J., Matsuta, K., Qiu, J. H. and Tsurekawa, S., *Japanese Journal of Applied Physics Part 2-Letters & Express Letters*, 2006. **45**(1-3): p. L30-L32.
77. Matthias, B. T. and Remeika, J. P., *Physical Review*, 1951. **82**(5): p. 727-729.
78. Nagata, H., Matsumoto, K., Hirosue, T., Hiruma, Y. and Takenaka, T., *Japanese Journal of Applied Physics Part 1-Regular Papers Brief Communications & Review Papers*, 2007. **46**(10B): p. 7084-7088.
79. Wood, E. A., *Acta Crystallographica*, 1951. **4**(4): p. 353-362.
80. Egerton, L. and Dillan, D. M., *Journal of the American Ceramic Society*, 1959. **42**(9): p. 438-442.
81. Jaeger, R. E.and Egerton, L., *Journal of the American Ceramic Society*, 1962. **45**(5): p. 209-213.
82. Kosec, M. and Kolar, D., *Materials Research Bulletin*, 1975. **10**(5): p. 335-339.
83. Matsubara, M., Yamaguchi, T., Sakamoto, W., Kikuta, K., Yogo, T. and Hirano, S., *Journal of the American Ceramic Society*, 2005. **88**(5): p. 1190-1196.
84. Matsubara, M., Kikuta, K. and Hirano, S., *Journal of Applied Physics*, 2005. **97**(11).
85. Hollenstein, E., Davis, M., Damjanovic, D. and Setter, N., *Applied Physics Letters*, 2005. **87**(18):p. 182905-1- 182905-4.
86. Guo, Y. P., Kakimoto, K. and Ohsato, H., *Applied Physics Letters*, 2004. **85**(18): p. 4121-4123.
87. Zang, G. Z., Wang, J. F., Chen, H. C., Su, W. B., Wang, C. M., Qi, P., Ming, B. Q., Du, J. and Zheng, L. M., *Applied Physics Letters*, 2006. **88**(21):p. 212908-1- 212908-4.
88. Yang, Z., Chang, Y., Liu, B. and Wei, L., *Materials Science and Engineering a-Structural Materials Properties Microstructure and Processing*, 2006. **432**(1-2): p. 292-298.

89. Wu, J., P., Ting, W., Yuanyu, X., Dingquan, Z., Jumu, J., Yong, Z., Jianguo, Y., Ping, W., L. and Jiang, Y., *Journal of the American Ceramic Society*, 2008. **91**(1): p. 319-321.
90. Zhang, S., Xia, Ru, Shrout, T. R., Zang, G. and Wang, J., *Journal of Applied Physics*, 2006. **100**(10):p. 104108-1- 104108-4.
91. Guo, Y. P., Kakimoto, K. and Ohsato, H., *Materials Letters*, 2005. **59**(2-3): p. 241-244.
92. Kim, M. S., Jeong, S. J. and Song, J. S., *Journal of the American Ceramic Society*, 2007. **90**(10): p. 3338-3340.
93. Rubio-Marcos, F., Ochoa, P. and Fernandez, J. F., *Journal of the European Ceramic Society*, 2007. **27**(13-15): p. 4125-4129.
94. Chang, Y., Yang, Z., Hou, Y., Liu, Z. and Wang, Z., *Applied Physics Letters*, 2007. **90**(23):p. 232905-1- 232905-3.
95. Saito, Y. and Takao, H., *Ferroelectrics*, 2006. **338**: p. 1433-1448.
96. Saito, Y., Takao, H., Tani, T., Nonoyama, T., Takatori, K., Homma, T., Nagaya, T. and Nakamura, M., *Nature*, 2004. **432**(7013): p. 84-87.
97. Chang, Y., Poterala, S. F., Yang, Z., Trolier-McKinstry, S. and Messing, G. L., *Applied Physics Letters*, 2009. **95**(23):p. 232905-1- 232905-4.
98. Lei, C. and Ye, Z. G., *Applied Physics Letters*, 2008. **93**(4):p. 042901-1-042901-4.
99. Wang, R. P., Xie, R. J., Hanada, K., Matsusaki, K., Bando, H. and Itoh, M., *Physica Status Solidi a-Applications and Materials Science*, 2005. **202**(6): p. R57-R59.
100. Filip'ev, V. S , Smol'yaninov, I. P, Fesenko, E. G and Belyaev, I. I, *Kristallografiya*, 1960. **5**: p. 958.
101. Hughes, H., Allix, M. M. B., Bridges, C. A., Claridge, J. B., Kuang, X. J., Niu, H. J., Taylor, S., Song, W. H. and Rosseinsky, M. J., *Journal of the American Chemical Society*, 2005. **127**(40): p. 13790-13791.
102. Craig, A. B., Allix, M., Suchomel, M. R. Xiaojun, K., Sterianou,I., Sinclair, D. C. and Rosseinsky M. J., *Angewandte Chemie-International Edition*, 2007. **46**: p. 8785 –8789.
103. Kimura, T., Kawamoto, S., Yamada, I., Azuma, M., Takano, M. and Tokura, Y., *Physical Review B*, 2003. **67**(18) : p. 180401-1-180401-4.
104. Belik, A. A., Iikubo, S., K., K., Igawa, N., Shamoto, S., Maie, M., Nagai, T., Matsui, Y., Stefanovich, S. Y., Lazoryak, B. I. and Takayama-Muromachi, E., *Journal of the American Chemical Society*, 2006. **128**(3): p. 706-707.
105. Catalan, G. and Scott., J. F., *Advanced Materials*, 2009. **21**(24): p. 2463-2485.
106. Haumont, R., Kreisel, J., Bouvier, P. and Hippert, F., *Physical Review B*, 2006. **73**(13):p. 132101-1-132101-4.
107. Haumont, R., Kreisel, J. and Bouvier, P., *Phase Transitions*, 2006. **79**(12): p. 1043-1064.
108. Kornev, I. A., Lisenkov, S., Haumont, R., Dkhil, B. and Bellaiche, L., *Physical Review Letters*, 2007. **99**(22):p. 227602-1227602-4.
109. Haumont, R., Kornev, Igor A., Lisenkov, S., Bellaiche, L., Kreisel, J. and Dkhil, B., *Physical Review B*, 2008. **78**(13):p. 134108-1-134108-8.
110. Selbach, S. M., Tybell, T., Einarsrud, M. A. and Grande, T., *Advanced Materials*, 2008. **20**(19): p. 3692-3696.
111. Arnold, D. C., Knight, K. S., Morrison, F. D. and Lightfoot, P., *Physical Review Letters*, 2009. **102**(2).
112. Palai, R., Katiyar, R. S., Schmid, H., Tissot, P., Clark, S. J., Robertson, J., Redfern, S. A. T., Catalan, G. and Scott, J. F., *Physical Review B*, 2008. **77**(1):p. 014110-1-014110-11.
113. Arnold, D. C., Knight, K. S., Catalan, G., Redfern, S. A. T., Scott, J. F., Lightfoot, P. and Morrison, F. D., *Advanced Functional Materials*, 2010. **20**(13): p. 2116-2123.
114. Shvartsman, V. V., Kleemann, W., Haumont, R. and Kreisel, J., *Applied Physics Letters*, 2007. **90**(17):p. 172115-1- 172115-15.

115. Jang, H. W., Baek, S. H., Ortiz, D., Folkman, C. M., Eom, C. B., Chu, Y. H., Shafer, P., Ramesh, R., Vaithyanathan, V. and Schlom, D. G., *Applied Physics Letters*, 2008. **92**(6):p. 062910-1- 062910-11.
116. Lou, X. J., Yang, C. X., Tang, T. A., Lin, Y. Y., Zhang, M. and Scott, J. F., *Applied Physics Letters*, 2007. **90**(26):p. 262908-1- 262908-4.
117. Karimi, S., Reaney, I. M., Han, Y., Pokorny, J. and Sterianou, I., *Journal of Materials Science*, 2009. **44**(19): p. 5102-5112.
118. Zhang, S. T., Zhang, Y., Lu, M. H., Du, C. L., Chen, Y. F., Liu, Z. G., Zhu, Y. Y., Ming, N. B. and Pan, X. Q., *Applied Physics Letters*, 2006. **88**(16):p. 162901-1-162901-4.
119. Lee, Y.H., Wu, J. M. and Lai, C. H., *Applied Physics Letters*, 2006. **88**(4):p. 042903-1-042903-4.
120. Das, S. R., Choudhary, R. N. P., Bhattacharya, P., Katiyar, R. S., Dutta, P., Manivannan, A. and Seehra, M. S., *Journal of Applied Physics*, 2007. **101**(3):p. 034104-1-034104-8.
121. Yuan, G. L. and Or, S. W., *Journal of Applied Physics*, 2006. **100**(2):p. 024109-1-024109-6.
122. Fujino, S., Murakami, M., Anbusathaiah, V., Lim, S. H., Nagarajan, V., Fennie, C. J., Wuttig, M., Salamanca-Riba, L. and Takeuchi, I., *Applied Physics Letters*, 2008. **92**(20) :p. 202904-1- 202904-4.
123. Zalesskii, A. V., Frolov, A. A., Khimich, T. A. and Bush, A. A., *Physics of the Solid State*, 2003. **45**(1): p. 141-145.
124. Nalwa, K. S., Garg, A. and Upadhyaya, A., *Materials Letters*, 2008. **62**(6-7): p. 878-881.
125. Li, E., Suzuki, R., Hoshina, T., Takeda, H. and Tsurumi, T., *Applied Physics Letters*, 2009. **94**(13):p. 132903-1- 132903-4.
126. Du, H., Zhou, W., Luo, F., Zhu, D., Qu, S., Li, Y. and Pei, Z., *Journal of Applied Physics*, 2008. **104**(4) :p. 044104-1- 044104-6.
127. Leontsev, S. O and Eitel, R. E. *Journal of the American Ceramic Society*, 2009. **92**: p. 2957-2961.
128. Zhang, S and Yu, F., *Journal of the American Ceramic Society*, 2011. **94**(10): p. 3153-3170.

CHAPTER 2 - Experimental techniques

2.1 Diffraction and crystal symmetry

Studying the structures of inorganic materials is essential to understand their physical properties. Powder diffraction is a powerful technique to gather information about the crystal structure of crystalline solids so it was widely used in this thesis.

2.1.1 Crystal systems and unit cells

Crystalline solids are distinguished by having long-range order in the arrangement of atoms in a fixed shape and size. A crystal is formed when a unit of atoms or molecules is repeated periodically in three dimensions. A lattice describes the periodic structure of an ideal crystal. In a lattice all elementary parallelepipeds, that is, unit cells have the same shape and content. The unit cell is the simplest repeating unit in a crystal lattice. If the exact arrangement of atoms within one unit cell is known, then the structure of the whole crystal can be built just by translating or shifting this unit cell along one, two or three directions independently [1]. The size and shape of the unit cell is determined by the lattice parameters, also called lattice constants, which are defined as the lengths of its three edges, a, b, c and the angles between them α, β, γ.

Table 2.1: The seven crystal systems and the lattice characteristics.

Crystal system	**Unit cell edges**	**Unit cell angles**
Cubic	a = b = c	α = β = γ = 90°
Tetragonal	a = b ≠ c	α = β = γ = 90°
Orthorhombic	a ≠ b ≠ c	α = β = γ = 90°
Monoclinic	a ≠ b ≠ c	α = γ = 90°; β ≠ 90°
Triclinic	a ≠ b ≠ c	α ≠ β ≠ γ ≠ 90°
Trigonal / Hexagonal	a = b ≠ c	α = β = 90°; γ = 120°

In Table 2.1, the 7 crystal/lattice systems are classified according to the relationship between the unit cell edges and the angles between them.

In order to illustrate the phenomenon of diffraction from ideal crystal lattices a geometrical concept is introduced, the crystallographic plane [1]. A family of crystallographic planes can be defined by the three Miller indices (*h*, *k* and *l*) which intersect the unit cell edges at *a/h*, *b/k* and *c/l* respectively. All planes in the same family have to be parallel to each other and equidistant. The interplanar distance or *d*-spacing is the distance between the neighboring planes.

A point group symmetry of an object is defined as all symmetry elements, passing by a point, describing the total symmetry of the object. The symmetry point group must be consistent with the crystalline periodicity and therefore just 32 point groups or crystal classes are allowed in the crystalline state of matter. Of these 32 crystal classes just 11 have operator centre of symmetry and are known as Laue groups. Furthermore, the way of repetition by translation in crystals must be compatible with the possible point groups, the 32 crystal classes. Only 14 types of translational lattices are compatible with the crystal classes and are known as Bravais lattices. If the 32 crystal classes are combined with possible translational symmetry elements such as: screw axis and glide planes or centering in the crystal lattice ,230 different ways to replicate a

finite object in three dimensional space are found. These 230 ways to repeat patterns in space are called space groups. Thus, the 32 crystal classes, the 14 Bravais lattices and the 230 space groups can be categorised, according to their hosted minimum symmetry, into the 7 crystal systems already defined in Table 2.1 [2].

As stated before, powder diffraction can give information about the space group that a crystalline solid adopts, and lattice characteristics, in particular the lattice constants and lattice angles.

2.1.2 Fundamentals of diffraction

If a radiation beam of wavelength, λ, impacts on a crystalline solid it will be scattered in various directions. Diffraction arises from the 'reflection' by the lattice planes within the crystal structure and can only be observed when the scattered beam from one lattice plane is *in phase* with the scattered beam from other lattice planes and they combine to form an enhanced scatter known as constructive interference. Constructive interference can occur when the λ of the radiation beam is comparable to the interplanar distance, d_{khl}. This condition can be expressed by Bragg´s law, Equation 2.1.

$$2d_{khl} \sin\theta = n\lambda \quad \text{Bragg's law} \qquad \textit{Equation 2.1}$$

where d_{khl} is the interplanar distance, θ is known as the Bragg angle and it is the angle between the incident beam and the scattering planes, *n* is the order of reflection and must be an integer and in general is taken as unity [3] and λ is the wavelength.

If the scattered beams are *out of phase*, then destructive interference occurs, where diffracted beams cancel each other.

Positions of Bragg peaks are determined from Bragg's law as a function of the wavelength and d_{khl} can be calculated if we know the lattice parameters by using the Equation 2.2 for the case of the cubic crystal system.

$$\frac{1}{d_{hkl}^2} = \frac{h^2}{a^2} + \frac{k^2}{b^2} + \frac{l^2}{c^2} = \frac{h^2+k^2+l^2}{a^2} \qquad \textit{Equation 2.2}$$

The Bragg peaks observed by diffraction for a material have different intensities. The main part defining the intensities of the individual diffraction is the structural part. Other factors such as: specimen factors or instrumental factors also play a role.

$$I_{hkl} = K p_{hkl} L_\theta P_\theta A_\theta T_{hkl} E_{hkl} |F_{hkl}|^2 \qquad \textit{Equation 2.3}$$

Equation 2.3 expresses the calculated integrated intensity in powder diffraction. Where *K* is the scale factor, p_{hkl} is the multiplicity factor, L_θ is the Lorentz multiplier and depends on the geometry of diffraction, P_θ is the polarisation factor, A_θ is the absorption multiplier, T_{hkl} is the preferred orientation factor, E_{hkl} is the extinction multiplier and $|F_{hkl}|^2$ is the structure factor [1].

The structure factor,$|F_{hkl}|^2$, is the square of the absolute value of the so-called structure amplitude, F_{hkl}. If in a unit cell there are many atoms with different scattering ability, the amplitude of the scattered wave is given by a complex function, the structure amplitude.

$$F_{hkl} = \sum_{j=1}^{n} g^j t^j(s) f^j(s) \exp\left[2\pi \mathbf{i}\left(hx^j + ky^j + lz^j\right)\right] \qquad \textit{Equation 2.4}$$

where each j represents the j^{th} atom, i = √-1, s = $\sin\theta_{hkl} / \lambda$, g^j is the occupation, t^j is the temperature factor and f^j is the atomic scattering factor and its fractional co-ordinates through hx^j, ky^j, lz^j. Both the atomic displacement and scattering factors depends on θ and λ.

When the temperature is higher than zero Kelvin the atoms in a crystal lattice are excited and in a continuous oscillation motion about their equilibrium positions, determined by

coordinate triplets, *x*, *y*, *z*. In order to take into account these vibrations, the temperature factor or atomic displacement is introduced into the general Equation 2.4 of the structure amplitude. The temperature factor of the j^{th} atom is represented as:

$$t^j = \exp\left(-B^j \frac{\sin^2\theta}{\lambda^2}\right) \qquad \textit{Equation 2.5}$$

where B^j is the displacement parameter of the j^{th} atom, defined in Equation 2.6. This is the so-called isotropic approximation. It assumes that an atom has equal probability to deviate in any direction despite of its environment; this means that atoms are considered as spheres.

$$B^j = 8\pi^2(\bar{u}^2)^j \qquad \textit{Equation 2.6}$$

where $\bar{u}^2$ is the root mean square deviation in $Å^2$ of the j^{th} atom from its equilibrium position, *x*, *y* , *z*.

The atomic scattering factor, f^j , is a measure of the scattering power of an isolated atom. It depends on the scattering amplitude of an individual atom and also the Bragg angle of scattering. The atomic scattering factor depends on the type of radiation involved and can be expressed as [4]:

$$f^j(s) = f_o^j(s) + \Delta f^{j\prime} + i\Delta f^{j\prime\prime} \qquad \textit{Equation 2.7}$$

where $s = \sin\theta/\lambda$, f_o^j is the normal atomic scattering factor, and $\Delta f^{j\prime}$ and $\Delta f^{j\prime\prime}$ are the real and imaginary components of the anomalous scattering factor.

2.1.3 Radiation sources for diffraction

2.1.3.1 X-ray sources

X-rays are electromagnetic radiation of $\lambda \sim 1$ Å and can be generated either by laboratory, the most common method, or by synchrotron sources through different processes. In both cases a single X-ray wavelength is desired for a diffraction experiment. This may be achieved using a crystal monochromator in which the X-ray beam emerging form the X-ray tube impinges on a single crystal at a chosen fixed orientation. Employing Bragg´s Law, Equation 2.1, and for a particular angle θ only one wavelength can be diffracted from the crystal. By adjusting θ it is possible to select one wavelength from the X-ray spectrum, normally the most intense $K_{\alpha 1}$ [3].

2.1.3.1.1 Laboratory diffractometers

The X-rays for laboratory diffractometers are generated by accelerating an electron from a cathode which bombards a target anode. When a beam of electrons hits a metal plate electrons are removed from one of the metal atom core orbitals leaving holes. Emission of radiation occurs when an electron from a higher energy orbital decays to fill a hole. X-rays can also be generated by the slowing down of the electrons as they enter the metal target, in a process called Bremsstrahlung. In the case of copper, core electron vacancies formed by bombardment with electrons can be filled by decay from various higher energy electrons. As a result, the spectrum of X-rays obtained contains a number of intense maxima corresponding to the energies of these various transitions. The filling of a vacant 1s orbital, principal quantum number one, is given a symbol K. In a copper atom, this may be achieved by electron decay from the 2p or 3p levels. The X-ray produced by the transitions from 2p to 1s and from 3p to 1s are called K_α and K_β respectively. Both these lines are actually close doublets because of the spin multiplicity in the p shells. In the copper spectrum the K_α line, $\lambda \sim 1.54$ Å, is formed of two lines at 1.5406 Å and

1.5444 Å called $K_{\alpha 1}$ and $K_{\alpha 2}$ respectively. A transition which fills a 2s or 2p shell, principal quantum number 2, is given the symbol L [3].

2.1.3.1.2 Synchrotron sources

Synchrotron sources are currently the most powerful X-ray radiation sources. The synchrotron output power exceeds that of the conventional X-ray tube by many orders of magnitude [1].

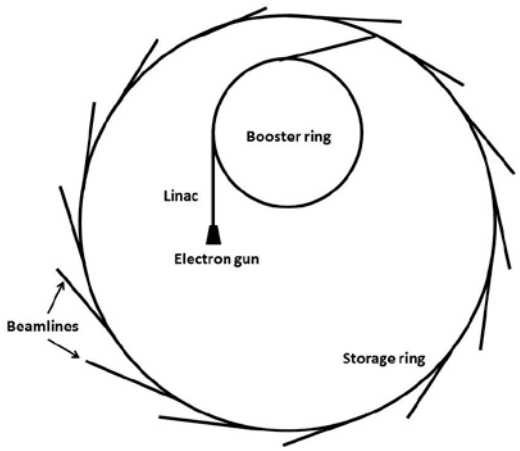

Figure 2.1 Schematic diagram of a synchrotron adapted from [5, 6].

Figure 2.1 shows a schematic diagram of a synchrotron. The electron gun produces the electrons under vacuum and they are then accelerated up to high energies in a series of particle accelerators. The linac which is linear is the first accelerator and feeds electrons into the second accelerator called a booster ring. The booster ring brings the electrons up to their final energy and transmits them to the third accelerator, the storage ring. These high-energy electrons circulate in the large storage ring in a vacuum environment, at a constant energy, for many hours. The storage ring consists of alternating straight and curved sections. The number of the sections depends on the size of the ring. In each curve section, two large bending magnets force the path of the electrons into the storage ring. In each straight section, several focusing magnets make sure that the electrons remain close to their ideal orbital path. When the electrons change direction the

synchrotron light is produced. The X-ray beams are directed toward the beam lines. The straight sections house the insertion devices or undulators. These insertion devices also create synchrotron light but in comparison with the bending magnets of the curved sections they produce more intense tuneable light [5].

In this thesis, synchrotron data were collected on the Super Photon ring-8, SPring-8, which is the largest third-generation synchrotron radiation facility in the world. It delivers the most powerful synchrotron radiation currently available [7]. The electrons are first accelerated in the linac at energy of 1 GeV. Then they are inserted into the booster ring and accelerated to the operating energy 8 GeV.

2.1.3.2 Neutron sources

Neutrons are tiny sub-atomic particles that make up around 50% of the mass of most atoms. Neutrons also possess a wavelength because of the principle of wave-particle duality. This can be described by the de Broglie equation.

$$\lambda = \frac{h}{p} = \frac{h}{mv}$$ de Broglie equation *Equation 2.8*

where λ is the wavelength, h is the Planck's constant (= $6.626*10^{-34}$ Js) , p is the momentum, m is the mass of the neutron (= $1.675*10^{-27}$ kg) and v the velocity of the neutron.

According to Equation 2.8, the velocity of the neutron is inversely proportional to its wavelength. The momentum can be expressed as the multiplication product of velocity and mass of nucleus [8].

The generation of intense neutron beams for diffraction cannot be produced in the laboratory; they are produced at specialised facilities. There are two methods for producing neutron beams: a nuclear reactor and a pulsed source. An example of producing neutron beams

with a nuclear reactor is found at the Institut Laue Langevin (ILL) in Grenoble, France. The nuclear reactor uses the fission reaction of ^{235}U in order to produce an intense flux of neutrons at the heart of the reactor. At the ISIS facility at the Rutherford-Appleton Laboratories in Oxfordshire, UK there is the most intense spallation source of pulsed neutrons. The production of neutron by spallation is based on the collision of a high energy proton beam into the nuclei of a heavy-metal target, at ISIS this is a tungsten target [9]. The result is the destruction of the metal nucleus into two or three smaller nuclei and several neutrons [9].

At ISIS, an 800 MeV proton accelerator produces an intense pulse of protons 50 times a second. It consists of an injector and a synchrotron. High energy neutrons are generated and slowed down by moderators to useful speeds for research and then directed to the different neutron beamlines. The detectors are fixed at 2θ scattering angles. The diffracted radiation is recorded as a function of neutron time-of-flight, TOF, which is defined as the time that a neutron needs to reach the detector from the specimen [9].

If Equation 2.8 is combined with Bragg's law, it is possible to relate the neutron time-of-flight to the interplanar distance:

$$\lambda = \frac{ht}{mL} = 2d_{hkl}sin\theta \qquad \textit{Equation 2.9}$$

where L is the path length and t is the time-of-flight. Thus, by using detectors at fixed 2θ positions and a fixed path length L, we can determine the values of interplanar spacing d_{hkl} by using neutron time-of-flight as the variable.

2.1.3.3 Electron sources

Electrons are produced by electron guns by heating a tungsten filament. Then electrons are accelerated through a high voltage, V, which is related to the wavelength, λ, of the resulting electron by:

$$\lambda = h(2meV)^{-1/2} \qquad \textit{Equation 2.10}$$

where *m* is the mass of an electron and *e* the charge of an electron.

2.1.4 Diffraction techniques

Radiation sources such as X-rays, neutrons and electrons have wavelengths in the order of the interplanar distance, d_{hkl}, and are then scattered by the lattice planes in crystalline materials.

Table 2.2 Comparison of three types of radiation used in powder diffraction. Table taken from [1].Z is the atomic number.

	X-rays (conventional/synchrotron)	Neutrons	Electrons
Nature	Wave	Particle	Particle
Scattered by	Electron density	Nuclei	Electrostatic potential
Scattered function	$f(s) \propto Z$	f is constant at all s	$f(s) \propto Z^{1/3}$
Wavelength range, λ	0.5-2.5/0.1-10 Å	~1 Å	0.02-0.05 Å

In Table 2.2, the properties of three types of radiation used in powder diffraction are compared: X-rays, neutrons and electrons.

Maximum flux of neutrons is usually obtained in the Angstrom range of wavelengths. There are some differences compared to X-rays, the main ones are as follows: (i) neutrons are scattered by nuclei which are much smaller than electron clouds so the scattering takes places on points; (ii) scattering factors of elements are independent of the Bragg angle; (iii) scattering functions are not proportional to the atomic number [1]. Therefore, because the scattering functions of neutrons are not proportional to the atomic number they are more adequate to distinguish atoms with similar atomic numbers and light elements, such as oxygens. Neutron

powder diffraction, NPD, is used as a complementary technique to X-ray powder diffraction, XRPD. The main disadvantage of neutron diffraction is that large samples of 1 to 5 cm^3 of material are needed. The reason for this is that the conventional (reactor-generated) neutron sources have relatively low neutron flux at useful energies and weak interactions of neutrons with matter occur [1].

2.2 Diffraction experiments

In this thesis, powder samples were synthesised and process into pellets to perform physical properties measurements as it will be described in Sections 3.7 and 3.8, Chapter 3.

Powder samples were initially characterised by laboratory X-ray diffraction to determine if the materials have impurities. Preliminary indications of the crystal structures were obtained and the promising samples were also measured by synchrotron radiation X-ray and neutron diffraction in order to get high quality data to perform structural analysis on them. Pellet samples were also characterised by laboratory X-ray diffraction to check their purity prior to physical properties measurements.

2.2.1 Instruments and experimental conditions

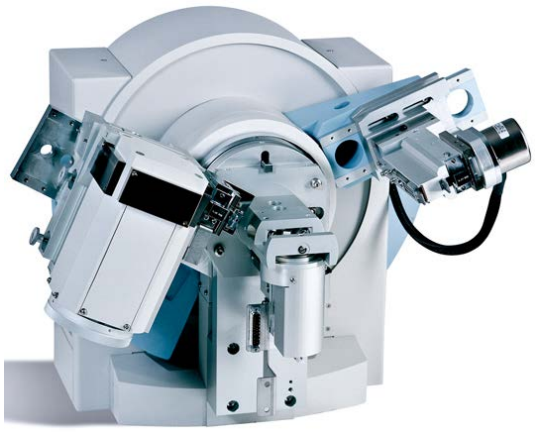

Figure 2.2 PANalytical X'Pert Pro diffractometer. This picture was taken from [10].

Laboratory diffraction data were measured on a PANalytical X'Pert Pro diffractometer in Bragg-Brentano geometry as shown in Figure 2.2. The metal of the target is cobalt with an X-ray wavelength of ~ 1.7890 Å. A mask was inserted in front of the detector, with the size of the mask chosen to alter the beam width depending on the sample. To measure powder samples, the width of the X-ray diffracted beam was 15 mm whereas for pellet samples, the width of the mask was 5 mm to avoid diffraction from the sample holder. The diameters of the pellets were around 7 mm so the width of the mask was smaller than the diameter. In all cases, the samples were rotated during the measurement in order to minimise the effect of preferred orientation.

Synchrotron X-ray diffraction data were collected on the powder diffraction beam line BL44B2 [11] at SPring-8. Figure 2.4 shows the experimental hutch II. The diffractometer is equipped with a Debye-Scherrer camera of radius 286.48 mm. It contains a 2D imaging plate, IP, as a detector. The station is equipped with an off-line IP reader and twenty data sets can be collected on one IP [12]. Data were recorded over a 2θ range from 2° to 75° every 0.01° and the wavelengths of the incident X-rays were ~0.45 and ~0.5 Å. A mask was inserted in front of the detector and the width of the X-ray diffracted beam in the left-right direction was 10 mm using this mask. The temperature of the sample was controlled by a N_2 gas flow device. Either an Ag or a Sn film was attached in front of the detector to reduce the background and be able to measure weak reflections as shown later in Figure 2.5. For the measurement of very weak reflections, a Pb-sheet was attached to the detector to avoid measuring the most intense reflections. Therefore the IP is not saturated. An example of data measured with a Pb-sheet is shown in Figure 2.6. For pellet diffraction measurements, Figure 2.3 shows a schematic illustration of a pellet attached to the aluminum sample holder. The holder was inserted into the gonio head and the sample was allowed to rock by 10° from the initial position using a spinner as marked with red arrows in Figure 2.3.

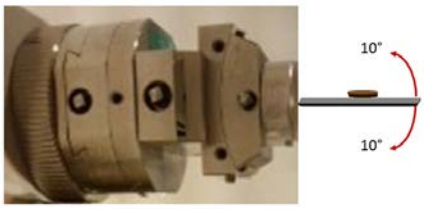

Figure 2.3 Schematic illustration of a pellet attached to the aluminium sample holder. The red arrows indicate that the sample was allowed to rock by 10° from the initial position using a spinner.

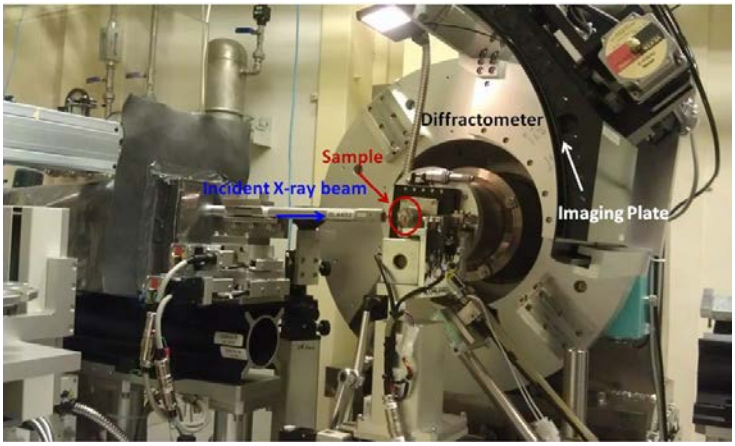

Figure 2.4 Experimental hutch II of the SPring-8 beam line BL44B2. The white arrow indicates the Imaging Plate, the red arrow indicates the goniometer with the sample and the blue arrow indicates the incident X-ray beam.

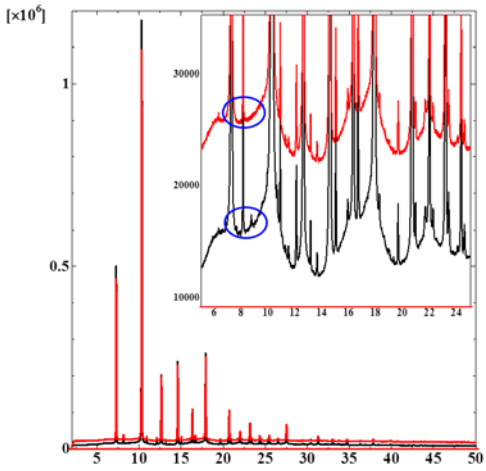

Figure 2.5 Comparison of synchrotron X-ray diffraction data of the solid solution x $Bi(Ti_{3/8}Fe_{2/8}Mg_{3/8})O_3$-(1-x)$CaTiO_3$ for x = 0.825 at 300 °C. The data in red were recorded without the Ag film. The data in black were recorded with the Ag film. The exposures times were 5 and 10 minutes respectively. The inset shows an enlargement comparing both data. The circles in blue indicate the region at the pattern where low intensity peaks are visible in the case of the data measured with the Ag film. It is observed that the background is clearly reduced using the Ag film.

Figure 2.5 shows synchrotron X-ray diffraction data of the solid solution $xBi(Ti_{3/8}Fe_{2/8}Mg_{3/8})O_3$-$(1-x)CaTiO_3$ for x = 0.825 at 300 °C measured with and without the Ag film attached in front of the detector. The data in red were recorded without the Ag film. The data in black were recorded with the Ag film. The exposures times were 5 minutes and 10 minutes respectively. The inset shows an enlargement comparing both data and the blue circles indicate the region at the pattern where low intensity peaks are visible in the case of the data measured with the Ag film. It is observed that the background is clearly reduced using the Ag film. The intensities of the reflections are also decreased so longer exposure time was needed to compensate. The background is due to the high X-ray fluorescence (phenomenon similar to the fluorescence in the visible spectrum and it originates from the fact that electrons in an atom can be excited and removed from their ground states by energy transfer from photons of sufficient energy. Electrons from higher energy levels produce fluorescent X-rays when they lower their energy by occupying the formed vacancies. Fluorescent radiation is dissipated in all directions, and it normally results in an increase of the background [1]) of Bi atoms interacting with the wavelength ~ 0.50028 Å. The anomalous scattering factor of Bismuth is ~ 0.92336 Å and therefore is higher than the wavelength used ~ 0.50028 Å so Bismuth scatters a lot. As a result of the high background, weak reflections cannot be distinguished clearly. To solve this problem an Ag film was attached to the detector as stated previously. The anomalous scattering factor of Silver is ~ 3.6983 Å so it is higher than the anomalous scattering factor for Bismuth. Therefore, the Ag film absorbs the energy and the contribution in the background due to the high X-ray fluorescence of Bi atoms is minimised.

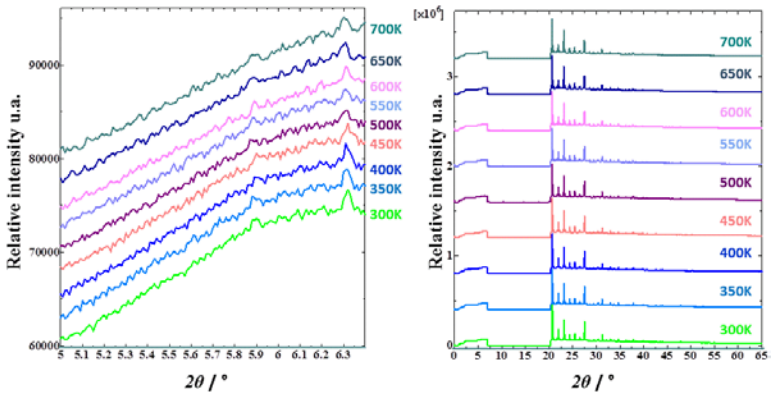

Figure 2.6 Synchrotron X-ray diffraction patterns for 0.825BTFM-0.175CTO from 300 K to 700K measured with a Pb-sheet attached to the IP. The data have been shifted up with temperature for better visualization. The left figure shows the 2θ region from 5° to 6.4°. The right figure shows the 2θ region from 0° to 65°. It is observed that the 2θ region from 7° to 20° was not measured due to the Pb-sheet.

Figure 2.6 shows synchrotron X-ray data diffraction patterns for synchrotron X-ray diffraction patterns for 0.825BTFM-0.175CTO from 300 K to 700K. The data were measured with a Pb-sheet attached to the detector at a specific position. The data have been shifted up with temperature for better visualization. It is observed that the 2θ region from 7° to 20° was not measured due to the Pb-sheet so the most intense peaks of the perovskite were not measured and the IP was not saturated. With this kind of measurement we were able to measure very weak reflections and collect high counting statistics data with exposure time of ~ 1 hour.

Neutron data were collected at the ISIS spallation neutron source at the Rutherford Appleton Laboratory on the High Resolution Powder Diffraction, HRPD beamline [13]. The experiments were carried out under the guidance of the instrument scientist Dr. Aziz Daoud-Aladine. HRPD has three fixed detectors banks at low angle (28-32°), 90° and the highest-resolution back-scattering at 168°. Therefore, three different data sets were recorded.

2.2.2 Sample preparation for diffraction experiments

To prepare the powder samples for laboratory X-ray diffraction a thin ring of grease was applied onto the centre of a semi-disposable cut glass slide. A well ground powder sample was

dispersed onto the glass and this was mounted on a metallic sample holder. Any excess of sample was removed by gently tapping the holder laterally onto the bench. For long exposure time measurements ≥ 4hours, the sample was well ground using a mortar and pestle. A small amount of acetone was added to the mortar to form a suspension. A few drops of the suspension were taken with a Pasteur pipette. They were released on the semi-disposable cut glass slide which was mounted on the metallic sample holder. The pellet samples were attached to the metallic sample holders with a re-usable adhesive making sure that they were at the same level as the sample holders.

For synchrotron X-ray diffraction experiments, the powder samples were prepared initially by placing a tiny quantity on weighing paper which was then crushed with a spatula. The powder sample was loaded into a capillary (Markröhrchen aus Glass Nr. 14, 80mm (long) × 0.1-0.2mm (diameter) × 0.01mm (thick), from Hilgenberg GmbH). The capillary was attached to the aluminium sample holder In the case of the pellets samples; they were attached to the aluminium sample holder with cellophane tape. Finally, the holders were inserted into the gonio heads.

For neutron diffraction experiments, well ground powder samples were loaded into Vanadium cans. For high temperature measurements, samples were firstly loaded into a silica tube which was then placed into the Vanadium cans. This is done because the Vanadium may react with the sample under study at T = 800 °C.

2.3 Structural analysis

2.3.1 Profile matching / Le Bail fitting

To carry out a Le Bail fitting [14] or profile matching of the diffraction patterns no structural information is needed and the intensities of the reflections are simply adjusted to the observed ones [15]. Just the space group, cell parameters, peak shape and background is fitted. In

this thesis a program developed at Prof. Takata's group and TOPAS ACADEMIC [16] were used to perform Le Bail analysis.

2.3.2 Rietveld method

The Rietveld method [17, 18] is a structure refinement method; consequently a reasonably good starting model is required. In the Rietveld method the least-squares refinements are performed until the best fit between the whole observed powder diffraction pattern and the whole calculated pattern is achieved. The calculated pattern is based on the simultaneous refinement of the crystal structure model, lattice parameters, profile and instrument parameters.

Diffraction patterns are collected in intensity, y_i at each increment, i in the pattern and, depending on the method; increments can be scattering angle 2θ, energy parameter, TOF, or wavelength. In the Rietveld method the quantity to minimise in the least-squares refinement is the residual, S_y:

$$S_y = \sum_i w_i [y_i(obs) - y_i(cal)]^2 \qquad \textit{Equation 2.11}$$

where w_i = 1 / $y_i(obs)$, $y_i(obs)$ = observed intensity at the i^{th} step and $y_i(cal)$, calculated intensity at the i^{th} step.

A powder diffraction pattern can be thought of as a collection of individual reflection profiles each with an individual peak height, a peak position and shape; the integrated area is proportional to the Bragg intensity, I_{hkl}. The intensity of the reflection, as discussed in Section 2.1.2, is proportional to the structure factor. Therefore, the calculated intensity is determined from the model summing together all contributions from the reflections and the background.

$$y_i(cal) = K \sum_{hkl} L_{hkl} |F_{hkl}|^2 \phi(2\theta_i - 2\theta_{hkl}) T_{hkl} A_\theta + y_{bi} \qquad \textit{Equation 2.12}$$

where L_{hkl} contains the Lorentz, polarisation and multiplicity factors, ϕ is the reflection profile function and y_{bi} is the background intensity at the i^{th} step. The other parameters such as: K, $|F_{hkl}|^2$, T_{hkl} and A_θ have already been defined in Section 2.1.2.

There are a number of parameters, R-values, which can be used as indicators to judge the agreement between the observed and calculated pattern.

$$R_{wp} = \left\{\frac{\sum_i w_i[y_i(obs)-y_i(calc)]^2}{\sum_i[y_i(obs)]^2}\right\}^{\frac{1}{2}} \quad \text{Weighted-profile } R \text{ value} \quad \textit{Equation 2.13}$$

$$R_{exp} = [(N-P)/\sum_i^N w^i\, y_i(obs)^2]^{\frac{1}{2}} \quad \text{Expected } R \text{ value} \quad \textit{Equation 2.14}$$

$$X^2 = R_{wp}/R_{exp} \quad \text{'Goodness of fit'} \quad \textit{Equation 2.15}$$

$$R_F = \frac{\sum_{hkl}|F_{hkl}(obs)-F_{hkl}(calc)|}{\sum_{hkl}|F_{hkl}(obs)|} \quad \text{Structure } R \text{ value} \quad \textit{Equation 2.16}$$

$$R_I = \frac{\sum_{hkl}|I_{hkl}(obs)-I_{hkl}(calc)|}{\sum_{hkl}|I_{hkl}(obs)|} \quad \text{Bragg-intensity } R \text{ value} \quad \textit{Equation 2.17}$$

where N is the number of observables and P the number of parameters.

The most reliable factor is the weighted-profile R value because it contains the residual which is actually being minimised in the least squares procedure; as a consequence it is a useful factor to judge the quality of the refinement.

During the process of refinement these fit parameters should be regularly checked to assess the refinement. Also, good care must be taken so all the refined parameters have reasonable values and the crystal structure stays sensible. Visual examination of the difference, $y_i(obs) - y_i(cal)$, normally gives an idea about which paramereter(s) needs to be refined [15]. Rietveld refinements were performed for SPring-8 data using a program developed at Prof. Takata's group

and for laboratory X-ray diffraction data and joint refinements (neutron and SPring-8 data) the program TOPAS ACADEMIC [16].

2.3.3 The Maximum Entropy Method (MEM) / Rietveld Method

The combination of Rietveld refinement [18] with Maximum Entropy Methods (MEM) enhances the extraction of accurate structural information using X-ray powder diffraction data. This MEM / Rietveld method [19] was developed by Prof. Takata's group and it is very effective for creating structural images at the charge density level. It has been successfully applied to structural studies of oxide metafullerenes [20-22], manganite [23], zeolite [24], α-boron [25], porous coordination polymers [26] etc. The MEM charge density maps can provide information about the atomic positions. At the beginning of the iteration, we need to have a primitive structural model. The MEM / Rietveld method consists of a repetitive procedure in which the features observed in the MEM electron density distribution at each step are incorporated into an improved structural model for the next step of Rietveld refinement. This procedure is repeated until the final distribution is compatible with the structural model developed. I used this method to build the structural model for a selected material under the supervision of Prof Nishibori at Prof Takata's group at SPring-8, Japan and the whole procedure is described in detail in Section 4.1.4, Chapter 4. The MEM study was performed using the program *ENIGMA* [27].

2.4 Physical properties measurements

2.4.1 Piezoelectric measurements

2.4.1.1 *Direct* piezoelectric measurements

The *direct* piezoelectric effect occurs when a mechanical force on a material results in a change of polarisation. As it was already stated in Section 1.2, Chapter 1, the resultant piezoelectric charge constant, *d*, is a third rank tensor, d_{ijk}, and is measured in C/N [28].

In this study, the longitudinal coefficient d_{33} has been measured by Dr Pranab Mandal and Dr Xinming Wan at the University of Liverpool to affirm the polar nature of the materials under study. Poling was performed on pellets and d_{33} was determined with a conventional Berlincourt piezometer (Piezotest PM300, London, UK), by applying an alternating force of 0.25 N at a frequency of 125 Hz. Before the measurement, the samples were poled in silicone oil at 200 °C (this is the maximum heating temperature of the silicone oil). The voltage was increased slowly up to attain 100 kV/cm and left for 15 minutes. Then samples were slowly cooled to room temperature in presence of electric field before, taking approximately three hours in total to perform the experiment.

2.4.1.2 *Converse* piezoelectric measurements

The *converse* piezoelectric effect occurs when an applied field on a material results in a strain [28] (Section 1.2.1, Chapter 1).

Strain-field measurements were performed at the Institute for Materials Research, University of Leeds with the assistance of Dr Pranab Mandal, Dr John Claridge and Dr T. P. Comyn. They were carried out using a Fotonic sensor MTI-2100 combined with a commercial Radiant Ferroelectric Tester Precision LC, in line with a Trek 5/80 high voltage amplifier and

Radiant high voltage interface using a frequency of 1 Hz. The electric field was applied until dielectric breakdown occurred.

2.4.1.3 Variable temperature piezoelectric measurements

To evaluate temperature dependence of piezoelectric coefficient d_{33}, ex-situ thermal depoling experiments were conducted on poled pellet. In this experiment, a poled pellet is short-circuited with a Pt wire clip and then heated slowly at a particular temperature for 1 hour and then cooled slowly. d_{33} was measured after 24 hours using the d_{33} piezometer. Variable temperature piezoelectric measurements were performed by Dr Pranab Mandal in the Deparment of Chemistry at the University of Liverpool using a Piezotest PM300, London, UK.

2.4.2 Pyroelectric current measurements

To confirm depolarisation temperature, the temperature at which the piezoelectric properties vanish [29], pyroelectric current measurements were performed. In this experiment, a poled pellet was heated at a uniform rate of 3 – 4 °C per minute and current was measured against time and temperature simultaneously using a Keithley 6430 remote sourcemeter. Current was integrated with respect to time to obtain charge and polarisation was calculated. An unpoled pellet was also measured to detect artifacts arising from loss at high temperature.

Pyroelectric current measurements were performed by Dr Pranab Mandal in the Deparment of Chemistry at the University of Liverpool. To carry out the experiment a pellet sample that has been electrically poled is placed on the sample holder as the inset at the top of Figure 2.8 a) shows. The sample was heated from room temperature above the depolarisation temperature at a rate of 3 °C per minute using a Lenton thermal designs furnace as indicated by a red arrow in Figure 2.8 a). The temperature was read from a thermocouple as shown in Figure 2.8 a) by a blue

arrow. The current was measured by a Keithley 6430 Sub-temtoamp remote sourcemeter; see Figure 2.8 b).

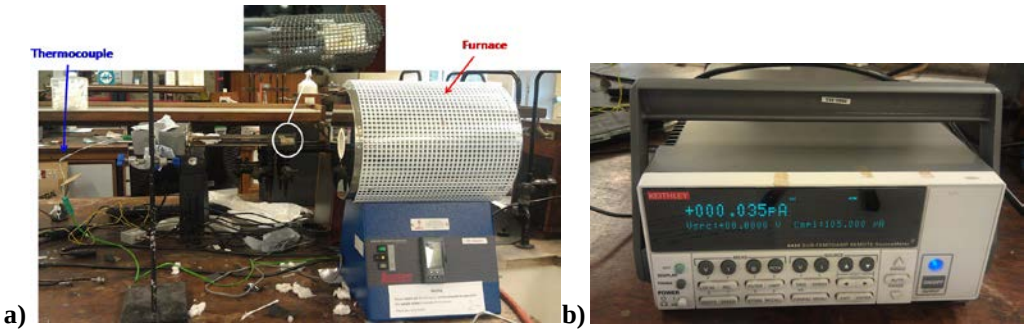

a) **b)**

Figure 2.8 Equipments to perform pyroelectric current measurements: a) Lenton thermal design furnace as shown by a red arrow. The blue arrow shows the thermocouple and the white circle and arrow the sample holder with an enlargement of it at the top; b) Keithley 6430 Sub-temtoamp remote sourcemeter to measure the current.

2.4.3 Ferroelectric measurements

Ferroelectric measurements were performed with the assistance of Dr Umut Adem and Dr Pranab Mandal in the Deparment of Chemistry at the University of Liverpool and in the Institute for Materials Research at the University of Leeds with the assistance of Dr Pranab Mandal and Dr T. P. Comyn. Ferroelectric measurements were carried out on a thin pellet with a Radiant Precision high voltage interface and a TRek 609B high voltage amplifier were used to measure the response as a function of voltage, at a frequency of 1 Hz. The electric field amplitude was increased in a stepwise way until dielectric breakdown occurs.

2.4.4 Dielectric measurements

Dielectric measurements were performed with the assistance of Dr Umut Adem and Dr Pranab Mandal in the Department of Chemistry at the University of Liverpool. These measurements were carried out by using a Solartron 1255B Frequency Response Analyzer and a Solartron 1296 dielectric interface. Also a HP4294A impedance analyser and Agilent E4980 LCR meter was used to perform measurements and they were taken over the frequency range of 1 Hz to 1 MHz from room temperature to 900 °C.

To perform the experiment, electrodes must be attached on both faces of the pellet sample under study separated by a distance *d*. Then the electrodes attached to the sample are connected to both the Frequency Response Analyzer and the dielectric interface. Then the sample was placed inside a tube furnace with a Eurotherm controller.

Impedance is the ratio of the voltage over current flowing through the sample because an AC voltage is being applied. The capacitance of the sample was measured during the experiment, this is a measure of the amount of electrical charged stored for a given voltage, again both real, *C'*, and imaginary, *C''*, capacitances were measured. The dielectric loss was also measured. The dielectric constant could then be calculated using these measured components by using Equation 1.8 in Chapter 1.

2.4.5 Positive-up negative-down (PUND) measurements

Positive-up negative-down (PUND) measurements $dP = P^* - P^{\wedge}$ were carried out to extract the remanent polarisation [30]. Where, P^* contains remanent and non-remanent polarisation and $P^{\wedge}$ contains non-remanent polarisation contributions.

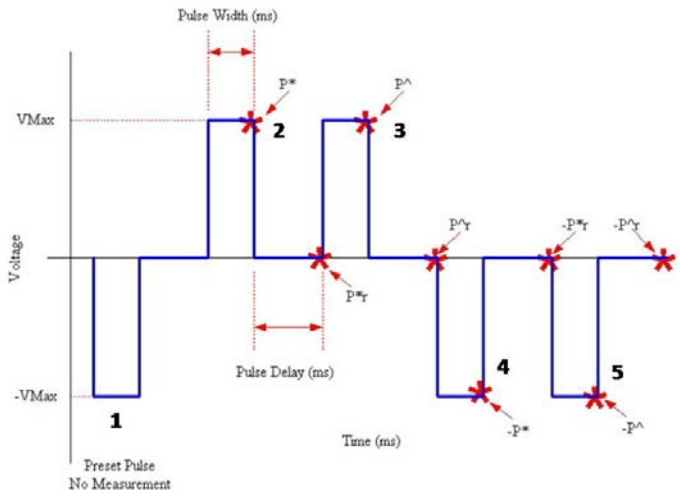

Figure 2.9 PUND waveform. Controlling parameters V_{max}, Pulse width and Pulse delay are shown. The serie of five pulses are indicated in black numbers. Figure adapted from [31].

Figure 2.9 shows PUND waverform over time. A PUND task is a measurement task that carries out a standard ferroelectric memory characterisation measurement based on a serie of five pulses [31]. They are indicated with numbers in black in Figure 2.9. The first pulse presets the sample to the polarisation state opposite the sign of V_{max}. As a result of this pulse no measurement is made. The second pulse switches the sign of the polarisation and measured the amount of polarisation switched. After the measurement, the sample is returned to zero volts and allowed to settle; therefore all-non remanent polarisation switching disappears. After this period, a second measurement is performed at 0.0 V. The third pulse is the same as the second and the same measurements are made. In this case, the sample is not being switched, so that the measured polarisation will represent the non-remanent content of the sample under study. The fourth and fifth measurements mirror the second and third but switching the sample in the $-V_{max}$ direction. Both the switching and non-switching measurements are performed in the same way described for pulses two and three.

PUND measurements were carried by Dr Pranab Mandal in the Deparment of Chemistry at the University of Liverpool. The disc under study was placed under silicone oil in a Radiant PVDF sample holder connected to a Radiant Ferroelectric Tester system coupled with a Fotonic sensor MTI-2100. The measurements were carried out with square pulses (pulse width = 1000 ms and pulse delay = 1000 ms).

2.5 Second Harmonic Generation (SHG) measurements

Powder SHG measurements were performed in order to prove the polarity of some selected materials. The SHG measurements were carried out by Miss Thanh Thao Tran under the supervision of Prof Halasyamani in the Department of Chemistry, University of Houston on a modified Kurtz-nonlinear optical (NLO) system using a pulsed Nd:YAG laser (λ = 1064 nm). Unsieved powders were placed in separate capillary tubes and no index matching fluid was used.

The SHG (532 nm radiation) was collected in reflection. A detailed description of the equipment and methodology has been published elsewhere [32].

2.6 Differential Thermal Analysis (DTA)

In a DTA experiment the temperature difference between the sample under study and an inert reference material is measured as a function of temperature. Thus, the substance under investigation and an inert reference are heated under the same conditions simultaneously in a furnace. Sample and reference are connected to thermocouples and these thermocouples are connected to each other. The differences of the voltages which are correlated to the differences of the temperatures are measured. In the case where there is an endothermic reaction in the sample, the sample temperature (T_s) increases slower as the reference temperature (T_i) so ($T_{s1} < T_{i1}$) and the gauge shows a thermovoltage according to a temperature difference $\Delta T_1 = T_{s1} - T_{i1}$which is negative. When there is an exothermic reaction in the sample, the sample temperature increases faster as the reference temperature ($T_{s2} < T_{i2}$) so the gauge shows a thermovoltage according to a temperature difference $\Delta T_2 = T_{s2} - T_{i2}$ which is positive.

This technique is widely used to study phase transitions, therefore DTA measurements were performed on selected materials.

DTA measurements were carried out using a SDT Q600 simultaneous TGA-DSC from TA [33] in the Department of Chemistry, University of Liverpool. In each case, the experiment was undertaken placing approximately 150 mg of hand ground sample in a Pt can. It was heated from room temperature to 900 °C and then kept constant at this temperature for 10 minutes. Heating and cooling rates of 10 °C per minute were used. A gas flow of air atmosphere of 100 ml per minute was used.

2.7 Electron Microscopy studies

Electron microscopy [34] is a useful technique because it only requires a tiny amount of sample. It was used in this study to provide information on the structure of the materials and the elemental composition of the phases present.

Because electrons have much smaller wavelengths than X-rays, see Table 2.2, their diffraction angles are much smaller, resulting in a narrow cone of diffraction centered around the electron beam. The result is a diffraction pattern consisting of a pattern of spots. The lattice constants and space group can be determined from this pattern.

In this thesis, selected area electron diffraction (SAED) and convergent beam electron diffraction (CBED) studies were carried out to confirm the symmetry of some materials.

SAED and CBED experiments were carried out using a JEOL 2000FX electron microscope by Mr Karl Dawson operating at 200 kV at the Nano Investigation Centre at Liverpool. Analysis was performed on a single crystal grain in thin lamella specimen by the lift out method [35]. A dual beam FEI focused ion beam instrument was used; final milling steps were performed using an 8 kV Ga ione beam. The samples were prepared by grinding the powder in acetone. Then the small crystallites in suspension were deposited onto a carbon file supported by a copper grid.

2.7.1 Energy dispersive X-ray spectroscopy (EDX)

This technique makes use of the X-ray spectrum emitted by the sample bombarded with the electron beam. Thus, the elements present in the sample can be detected [34]. The homogeneity of materials can be determined as each crystallite can be probed to establish which elements are present and in what ratio.

To perform the EDX analysis, sample powder was dispersed in acetone and deposited on a 300 Mesh copper TEM grid covered with a holey carbon film. EDX measurements were

performed by Dr Marco Zanella at the Nano Investigation Centre at Liverpool on a JEOL 2000FX equipped with an EDX detector. All measurements were performed at 200 KV.

2.8 References

1. Pecharsky, V. K. and Zavalij, P. Y., Fundamententals of Powder Diffraction and Structural Characterization of Materials, 2nd ed., *Springer*, New York, 2009.
2. Crystallography, *CSIC*. http://www.xtal.iqfr.csic.es/Cristalografia/index-en.html.
3. Weller, M. T., Inorganic Materials Chemistry, *Oxford Chemistry Primers*, 1994.
4. *http://reference.iucr.org/dictionary/Atomic_scattering_factor*.
5. *European Synchrotron Radiation Facility. What is a synchrotron?-ESRF*. http://www.esrf.eu/about/synchrotron-science/synchrotron.
6. *European Synchrotron Radiation Facility. What is a synchrotron?-ESRF*. http://www.esrf.eu/about/synchrotron-science/synchrotron-light-animation.
7. *What's SPring-8?* http://www.spring8.or.jp/en/about_us/whats_sp8/.
8. *Instrumentation III: Neutron Sources & Methods , School of Crystallography, Birkbeck College, University of London.* http://pd.chem.ucl.ac.uk/pdnn/inst3/neutronx.htm.
9. *How ISIS works. ISIS website, 2012.* http://www.isis.stfc.ac.uk/about-isis/how-isis-works6313.html.
10. http://www.panalytical.com/XPert-Powder/Gallery.htm.
11. Kato, K., Hirose, R., Takemoto, M., Ha, S., Kim, J., Higuchi, M., Matsuda, R., Kitagawa, S. and Takata, M., in *Sri 2009: The 10th International Conference on Synchrotron Radiation Instrumentation*, R. Garrett, et al., Editors. 2010. p. 875-878.
12. BL44B2, *Optical layout of RIKEN Materials Science Beamline* http://www.spring8.or.jp/wkg/BL44B2/instrument/lang-en/INS-0000000381/instrument_summary_view.
13. HRPD instrument. ISIS website, http://www.isis.stfc.ac.uk/instruments/hrpd/hrpd.html.
14. Le Bail, A., Duroy, H. and Fourquet, J. L., *Materials Research Bulletin*, 1988. **23**: p. 447-452.
15. McCusker, L. B., Von Dreele, R. B., Cox, D. E., Louër, D. and Scardi, P. *Journal of Applied Crystallography.*, 1999. **32**: p. 36-50.
16. Coelho, A. A., *Journal of Applied Crystallography*, 2000. **33**(2): p. 899-908.
17. Young, R. A., The Rietveld Method, *Oxford University Press*, Oxford, 1993.
18. Rietveld, H.M., *Journal of Applied Crystallography*, 1969. **2**: p. 65-71.
19. Takata, M., Umeda, B., Nishibori, E., Sakata, M., Saito, Y., Ohno, M. and Shinohara, H., *Nature*, 1995. **377**(6544): p. 46-49.
20. Nishibori, E., Takata, M., Sakata, M., Inakuma, M. and Shinohara, H., *Chemical Physics Letters*, 1998. **298**(1-3): p. 79-84.
21. Takata, M., Nishibori, E., Umeda, B., Sakata, M., Yamamoto, E. and Shinohara, H., *Physical Review Letters*, 1997. **78**(17): p. 3330-3333.
22. Takata, M., Nishibori, E., Sakata, M., Inakuma, M., Yamamoto, E. and Shinohara, H., *Physical Review Letters*, 1999. **83**(11): p. 2214-2217.
23. Takata, M., Nishibori, E., Kato, K., Sakata, M. and Moritoma, Y., *Journal of the Physical Society of Japan*, 1999. **68**(7): p. 2190-2193.
24. Hasegawa, K., Nishibori, E., Takata, M., Safata, M., Togashi, N., Yu, J. H. and Terasaki, O., *Japanese Journal of Applied Physics Part 1-Regular Papers Short Notes & Review Papers*, 1999. **38**: p. 65-68.
25. Fujimori, M., Nakata, T., Nakayama, T., Nishibori, E., Kimura, K., Takata, M. and Sakata, M., *Physical Review Letters*, 1999. **82**(22): p. 4452-4455.
26. Kubota, Y., Takata, M., Kitaura, R., Matsuda, R., Kobayashi, T. C. and Kitagawa, S., *Journal of Nanoscience and Nanotechnology*, 2009. **9**(1): p. 69-76.
27. Tanaka, H., et al., *Journal of Applied Crystallography*, 2002. **35**: p. 282-286.

28. Damjanovic, D., *Reports on Progress in Physics*, 1998. **61**: p.1267-1324
29. Shrout, T. R. and Zhang, S. J., *Journal of Electroceramics*, 2007. **19**(1): p. 113-126.
30. Yang, S. Y., Zavaliche, F., Mohaddes-Ardabili, L., Vaithyanathan, V., Schlom, D. G., Lee, Y. J., Chu, Y. H., Cruz, M. P., Zhan, Q., Zhao, T. and Ramesh, R., *Applied Physics Letters*, 2005. **87**(10).
31. *http://www.ferrodevices.com/1/297/software.asp*.
32. Ok, K.M., Chi, E. O. and Halasyamani, P. S., *Chemical Society Reviews*, 2006. **35**(8): p. 710-717.
33. http://www.tainstruments.com/pdf/brochure/sdt.pdf.
34. West, A. R., Solid State Chemistry and Its Applications, *2nd Edition*. John Wiley & Sons, Inc., 1996.
35. Giannuzzi, L. A. and Stevie, F. A., *Micron*, 1999. **30**(3): p. 197-204.

CHAPTER 3 - Synthesis and preliminary characterisation / results of bismuth-based electroceramic perovskites

Bismuth-based perovskites are established as potential candidates to replace $Pb(Zr_{1-x}Ti_x)O_3$ (PZT) [1-3]. They are also attractive because they can offer high Curie and depolarisation temperatures which are necessary for applications [4, 5]. However, bismuth-based perovskites normally are synthesised at high pressure (see Chapter 1, Section 1.4.3). An example of a Bi-based perovskite material synthesised at ambient pressure is $Bi(Ti_{3/8}Fe_{2/8}Mg_{3/8})O_3$ (BTFM) which has a high Curie temperature of 730 °C [6]. However, the piezoelectric and ferroelectric properties that this material displays are very poor as will be shown in Section 3.1. Thus, the aim of this thesis is to improve the electromechanical properties of BTFM by making solid solutions with other materials as will be explained in Section 3.3. In Section 3.2, the outcomes of a study of the solid solutions between BTFM and the classical piezoelectric material $BaTiO_3$ (BTO) [7] will be detailed. In this work, solid solutions between BTFM and $LaFeO_3$ (LFO) and $La(Mg_{1/2}Ti_{1/2})O_6$ (LMT) [8], $CaTiO_3$ (CTO) [9] and $NdFeO_3$ (NFO) have been synthesised and their results will be explained in Sections 3.4, 3.5 and 3.6 respectively. The goal is to have a morphotropic phase boundary (MPB) region formed by two polar phases with two different polarisation directions where the electromechanical properties will be enhanced as in PZT. The way of synthesising BTFM-CTO, BTFM-LMT-LFO and BTFM-NFO will be described in Section 3.7. The pellet

processing and sample preparation of BTFM-CTO materials to perform physical properties measurements will be explained in Sections 3.8 and 3.9 respectively.

3.1 Introduction to $Bi(Ti_{3/8}Fe_{2/8}Mg_{3/8})O_3$ (BTFM)

BTFM is a polar rhombohedral phase (space group *R*3*c*) with polarisation along $[111]_p$ that can be synthesised at ambient pressure thanks to a strategy developed on multiple B-site cations, the same as for $Bi_2Mn_{4/3}Ni_{2/3}O_6$ [10]. In BTFM, the Bi cations have locally correlated $[110]_p$ displacements [11] in addition to the long-range ordered $[111]_p$ displacements [6].

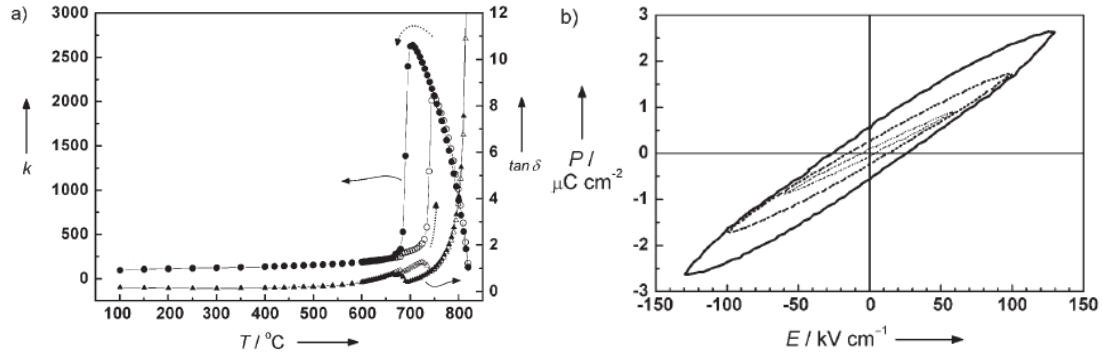

Figure 3.1 a) Temperature dependence of the relative permittivity (○,●, left axis) and dielectric loss (▲, Δ, right axis) measured at 1 MHz for BTFM. Open data points represent data collected on heating; filled points represent data collected on cooling. At 100 °C, tan δ = 0.20 (measured value). b) Room temperature hysteresis loops of polarisation versus applied electric field measured for increasing maximum applied fields on bulk BTFM. Figures taken from [6].

Figure 3.1 a) shows temperature dependence of the relative permittivity and dielectric loss measured at 1 MHz for BTFM. A sharp peak in permittivity around 730 °C is observed. This peak is characteristic of a ferroelectric Curie temperature transition to a non-polar structure which is confirmed by neutron powder diffraction data collected at 740 °C refined in the space group $Pm\bar{3}m$ [6]. Nevertheless, as Figure 3.1 b) shows, no indication of room temperature loop saturation was observed for BTFM. Also its remanent polarisation is very low ~0.5 $\mu C/cm^2$ along the polar $[111]_p$ direction. The d_{33} of BTFM is 0.6 pC/N [7]. This situation is similar as for $BiFeO_3$ (BFO), where in the initial studies saturated hysteresis loops were not obtained [12].

Only lately, with an improvement on the processing of the materials [13] and either doping or forming solid solutions improved hysteresis loops have been achieved in BFO [14].

3.2 Solid solutions $xBi(Ti_{3/8}Fe_{2/8}Mg_{3/8})O_3$ -(1-x)$BaTiO_3$

With the aim of improving the ferroelectric and piezoelectric properties of BTFM, solid solutions with the classical ferroelectric material $BaTiO_3$ (BTO) were synthesised by Dr Michelle Dolgos [7]. BTO crystallises in the *P*4*mm* tetragonal space group and the d_{33} value is 190 pC/N [15].

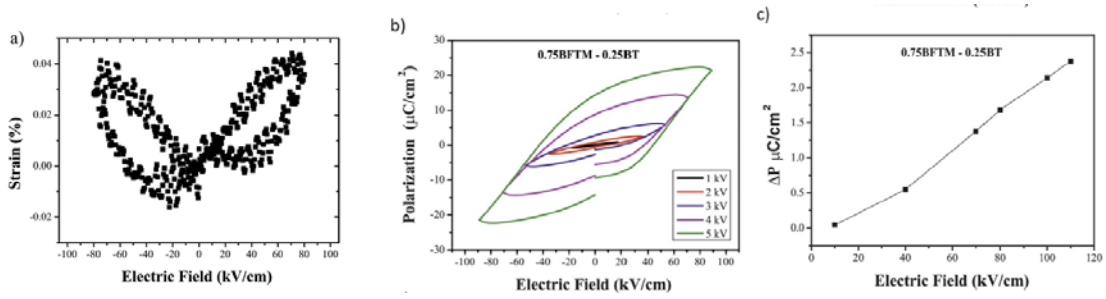

Figure 3.2 a) Butterfly loop from strain-electric field measurements of 0.75BTFM-0.25BTO. b) P(E) hysteresis loop of 0.75BTFM-0.25BTO and c) PUND data for 0.75BTFM-0.25BTO showing the true switched polarisation. Figures taken from [7].

Solid solutions between BTFM and BTO enhance the functional behaviour, especially for the composition 0.75BTFM-0.25BTO. Figure 3.2 a) shows strain-field measurements and the characteristic butterfly strain loop is displayed which is evidence for ferroelectric switching and bulk piezoelectricity. 0.75BTFM-0.25BTO shows nearly saturated ferroelectric hysteresis loops being the remanent polarisation 20 μC/cm^2 as Figure 3.2 b) shows. Although the real switched polarisation (ΔP) value obtained using PUND measurements [16] is small, 2.4 μC/cm^2, as shown in Figure 3.2 c). The d_{33} value for 0.75BTFM-0.25BTO is 16 pC/N, this value is considerably larger than for the parent material BTFM (d_{33} = 0.6 pC/N). This improvement of the physical properties is due to the substantial changes in the structure, where the rhombohedral distortion is reduced and transformed to a pseudo-cubic *R*3*m* space group. Substitution of the larger Ba^{2+} cation suppresses tilting of the BO_6 octahedra and allows for easier ferroelectric switching. For

0.75BTFM-0.25BTO, polar displacements were refined exclusively along the pseudo-cubic $[111]_p$ direction of the perovskite subcell [7].

3.3 Thesis aims

In order to improve the electromechanical properties of BTFM, firstly, solid solutions with $LaFeO_3$ (LFO) and $La(Mg_{1/2}Ti_{1/2})O_6$ (LMT) were studied (Section 3.4). The introduction of LFO into BTFM would modify the average structural asymmetry on the A-site as the aspherical Bi^{3+} and spherical La^{3+} cations are combined. The introduction of LMT, Mg^{2+} and Ti^{4+}, would decrease the dielectric loss caused due to the increase in Fe^{3+} content. With the introduction of LFO, the Bi cations which have locally correlated $[110]_p$ displacements can be converted into long-range polarisation along this direction [8]. Thus, motivated by the isostructural nature of LFO and $CaTiO_3$ (CTO) / $NdFeO_3$ (NFO) (all three materials crystallise in the space group *Pnma*) secondly, solid solutions between BTFM and CTO (Section 3.5) and thirdly, BTFM and NFO (Section 3.6) were synthesised.

3.4 Study of $Bi(Ti_{3/8}Fe_{2/8}Mg_{3/8})O_3$ – $La(Mg_{1/2}Ti_{1/2})O_6$ - $LaFeO_3$ materials and results

BTFM-LMT-LFO materials were studied with the purpose of improving the ferroelectric and piezoelectric performance of BTFM. LFO adopts the *Pnma* structure of $GdFeO_3$ with an $a^-b^+a^-$ tilt system and La^{3+} has antiferrodistortive displacements along the $[110]_p$ direction. LMT crystallises in $P2_1/a$ and has the same A-site displacements [17, 18]. Phases in the BTFM-LFO-LMT field were prepared by Dr Michelle Dolgos and the author following the protocol described in Section 3.7.2.

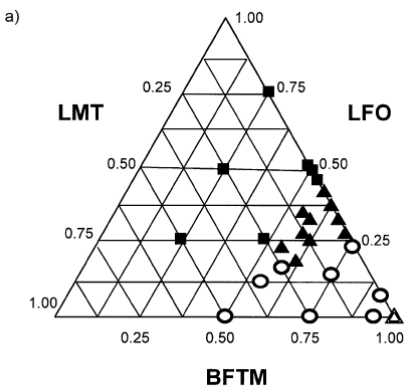

Figure 3.3 Phase diagram of the BTFM-LFO-LMT system. The four different categories of phase assemblage found in the system are shown (filled squares Pmna; filled triangles $Pmc2_1$; open circles two phase mixture and open triangle R3c). Figure taken from [8].

Figure 3.3 shows the phase diagram of the BTFM-LFO-LMT (BLTFM). Four different categories of phase assemblage were found in the system. Thus, BTFM represented with an open triangle crystallises in *R*3*c* and is surrounded by a two-phase region. At low LFO content and along the BTFM-LMT line an orthorhombic perovskite with Aurivillius phase as impurity appear represented with open circles (Figure 3.4 c) shows a X-ray diffraction pattern (XRD) for a selected composition). Nevertheless, single perovskite phases appear at higher substitution levels. These phases crystallise in the non polar *Pnma* structure at high LFO/LMT content as marked with filled squares and as expected in the case of high content of LFO because the end-member of the solid solution crystallises in *Pnma,* Figure 3.4 b) shows an XRD pattern for 0.25BTFM-0.5LFO-0.25LMT. However, a new orthorhombic appears between the *Pnma* and multiphase regions and adopt the polar space group $Pmc2_1$ as indicated with filled triangles, Figure 3.4 c) shows an XRD pattern as an example for a selected composition. The polarity of this phase was proved by SHG measurements.

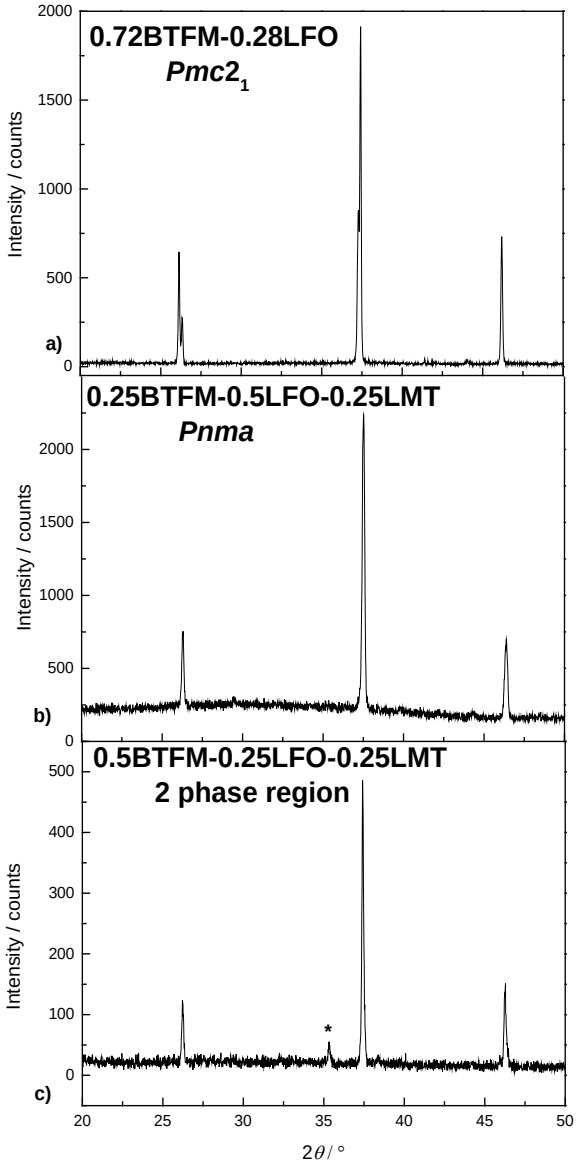

Figure 3.4 Laboratory XRD patterns on selected compositions of BTFM-LFO-LMT. a) 0.72BTFM-0.28 LFO ($Pmc2_1$), b) 0.25BTFM-0.5LFO-0.25LMT (Pnma) and c) 0.5BTFM-0.25LFO-0.25LMT (2-phase region), the Aurivillius impurity is marked with an asterisk.

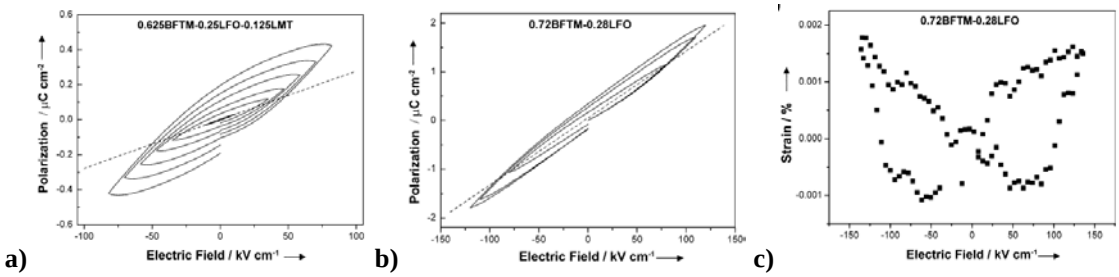

Figure 3.5 a) P(E) hysteresis loop for 0.625BTFM–0.25LFO–0.125LMT, b) P(E) hysteresis loop for 0.72BTFM–0.28LFO corresponding to c) the strain-field loop of the same composition. The dotted line in a) and b) represent the slope of the P(E) hysteresis loop at the lowest voltage and is used to demonstrate nonlinearity. Figures taken from [8].

As Figures 3.5 a) and b) show saturated loops were not obtained before dielectric breakdown for 0.625BTFM–0.25LFO–0.125LMT ($Pmc2_1$) and 0.72BTFM–0.28LFO ($Pmc2_1$) respectively. This is a common problem in BFO materials [19, 20]. The reason could be because of the high Curie temperature (Tc = 650 ± 5 °C) in the case of 0.72BTFM–0.28LFO, which undergoes a phase transition from the polar space group $Pmc2_1$ to the non-polar *Pmna*, and therefore the large coercive field needed to apply. However, electrical polarisation does not evolve as linear function of the driving field amplitude. This nonlinearity is a requisite for ferroelectrics and therefore domain wall motion [21]. A strain-field measurement on the polar 0.72BTFM–0.28LFO, Figure 3.5 c), displays a butterfly loop. The d_{33} for 0.72BTFM–0.28LFO is 0.25 pC/N. Thus, the polarity shown in the structure and SHG measurements was confirmed by measurements of piezoelectric behaviour [8].

To summarise, a Bi-based perovskite synthesised at ambient pressure with high Curie temperature has been synthesised. The electromechanical properties found are poor. Nevertheless, in the orthorhombic (O) $Pmc2_1$ structure found here the polarisation direction changes from $[111]_p$ in the parent phase BTFM rhombohedral (R) to $[110]_p$ for the (O) phase. This is due to the substitution of the La^{3+} onto the A-site of BTFM. This O phase is separated from R BTFM by a non-perovskite region of the phase diagram (Figure 3.3) and consequently a mixed phase region where the electromechanical properties would be maximised was not able to

be achieved. Nevertheless, this study opened the door to explore solid solutions between BTFM and CTO and NFO because of their isostructural nature with the aim of obtaining an MPB region.

3.5 Solid solutions x $Bi(Ti_{3/8}Fe_{2/8}Mg_{3/8})O_3$-(1-x)$CaTiO_3$

Solid solutions xBTFM-(1-x)CTO were synthesised successfully in the range $0.6 \geq x \geq 1$. Their protocol of synthesis will be detailed in Section 3.7.1

Table 3.1: Compositions of BTFM-CTO solid solutions synthesised in this thesis.

Calculated molecular formula	Abbreviated names
$Bi_{0.25}Ca_{0.75}(Ti_{0.8438}Mg_{0.09375}Fe_{0.0625})O_3$	0.25BTFM-0.75CTO
$Bi_{0.5}Ca_{0.5}(Ti_{0.6875}Mg_{0.1875}Fe_{0.125})O_3$	0.5BTFM-0.5CTO
$Bi_{0.55}Ca_{0.45}(Ti_{0.6563}Mg_{0.2063}Fe_{0.1375})O_3$	0.55BTFM-0.45BTFM
$Bi_{0.6}Ca_{0.4}(Ti_{0.625}Mg_{0.225}Fe_{0.15})O_3$	0.6BTFM-0.4CTO
$Bi_{0.65}Ca_{0.35}(Ti_{0.5938}Mg_{0.2438}Fe_{0.1625})O_3$	0.65BTFM-0.35CTO
$Bi_{0.7}Ca_{0.3}(Ti_{0.5625}Mg_{0.2625}Fe_{0.175})O_3$	0.7BTFM-0.3CTO
$Bi_{0.75}Ca_{0.25}(Ti_{0.531}Mg_{0.281}Fe_{0.188})O_3$	0.75BTFM-0.25CTO
$Bi_{0.8}Ca_{0.2}(Ti_{0.5}Mg_{0.3}Fe_{0.2})O_3$	0.8BTFM-0.2CTO
$Bi_{0.813}Ca_{0.187}(Ti_{0.4922}Mg_{0.3047}Fe_{0.2031})O_3$	0.813BTFM-0.187CTO
$Bi_{0.825}Ca_{0.175}(Ti_{0.4844}Mg_{0.3094}Fe_{0.2063})O_3$	0.825BTFM-0.175CTO
$Bi_{0.835}Ca_{0.165}(Ti_{0.4781}Mg_{0.3131}Fe_{0.2088})O_3$	0.835BTFM-0.165CTO
$Bi_{0.85}Ca_{0.15}(Ti_{0.4688}Mg_{0.3188}Fe_{0.2125})O_3$	0.85BTFM-0.15CTO
$Bi_{0.875}Ca_{0.125}(Ti_{0.4531}Mg_{0.3281}Fe_{0.2188})O_3$	0.875BTFM-0.125CTO
$Bi_{0.9}Ca_{0.1}(Ti_{0.438}Mg_{0.338}Fe_{0.225})O_3$	0.9BTFM-0.1CTO
$Bi_{0.925}Ca_{0.075}(Ti_{0.4219}Mg_{0.3469}Fe_{0.2313})O_3$	0.925BTFM-0.075CTO
$Bi_{0.95}Ca_{0.05}(Ti_{0.4063}Mg_{0.3563}Fe_{0.2375})O_3$	0.95BTFM-0.05CTO

Table 3.1 shows the list of the chemical compositions of BTFM-CTO synthesised in this study. The left column shows the calculated molecular formula of all the compositions and the right column shows their corresponding abbreviated names which were used throughout this thesis. The compositions 0.813BTFM-0.187CTO, 0.825BTFM-0.175CTO and 0.835BTFM-

0.165CTO were synthesised by Dr Alex Corkett at the University of Liverpool. EDX analysis matches with the expected compositions.

The tolerance factors for all the compositions of BTFM-CTO solid solutions synthesised in this thesis were calculated using Equation 1.1, Chapter 1. It is observed in Figure 3.6 that the tolerance factor decreases lineal with BTFM content (x).

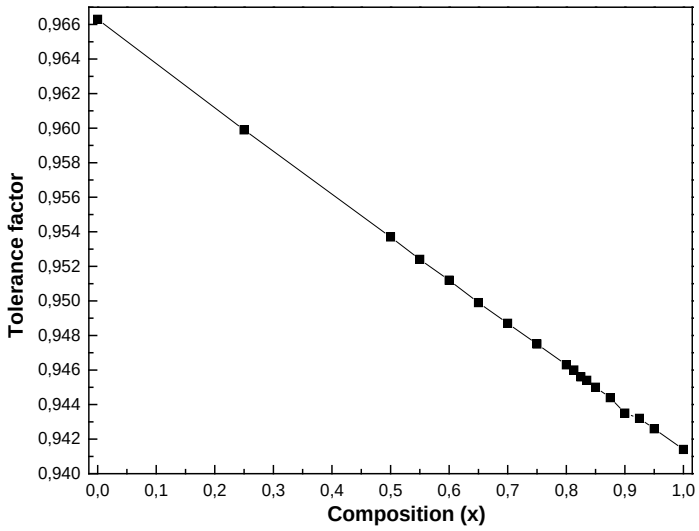

Figure 3.6 Tolerance factors versus composition for BTFM-CTO solid solutions where x is BTFM content. An ionic radius of 1.34 Å was used for a 12-coordinate Bi^{3+} ion [22].

Table 3.2: Values of the tolerance factors calculated for BTFM-CTO solid solutions.

Composition	**Tolerance factor**
CTO	0.9663
0.25BTFM-0.75CTO	0.9599
0.5BTFM-0.5CTO	0.9537
0.55BTFM-0.45BTFM	0.9524
0.6BTFM-0.4CTO	0.9512
0.65BTFM-0.35CTO	0.9499
0.7BTFM-0.3CTO	0.9487
0.75BTFM-0.25CTO	0.9475
0.8BTFM-0.2CTO	0.9463
0.813BTFM-0.187CTO	0.946
0.825BTFM-0.175CTO	0.9456
0.835BTFM-0.165CTO	0.9454
0.85BTFM-0.15CTO	0.945
0.875BTFM-0.125CTO	0.9444
0.9BTFM-0.1CTO	0.9435
0.925BTFM-0.075CTO	0.9432
0.95BTFM-0.05CTO	0.9426
BTFM	0.9414

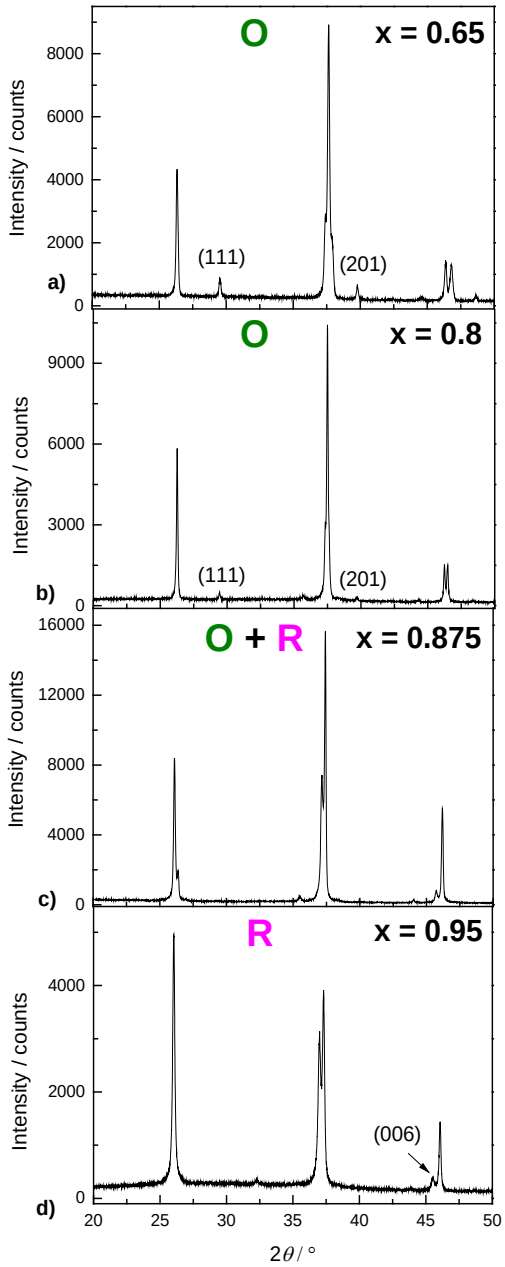

Figure 3.7 Laboratory XRD patterns on selected compositions of BTFM-CTO showing structural change. a) and b) show data for x = 0.65 and x = 0.8 respectively and the (111) and (201) reflections are shown which disappear on reaching the composition x = 0.875 (c). For x = 0.95 the reflection (006) appears but not for x = 0.65 and x = 0.8. Three different types of pattern are observed. x = 0.95 was indexed in a R unit cell, d); compositions in the range 0.6 ≤ x ≤ 0.825, a) and b) were indexed in an O unit cell and in the intermediate region 0.837 ≤ x ≤ 0.925 , c) as O + R.

Figure 3.7 shows laboratory XRD patterns on selected compositions of BTFM-CTO showing structural change. For Figure 3.7 a) and b) data for x = 0.65 and x = 0.8 respectively are shown. It is observed that the (111) and (201) reflections (which belong to an orthorhombic unit

cell) are shown and disappear on reaching the composition x = 0.875, Figure 3.7 c). For x = 0.95 the reflection (006) appears as Figure 3.7 d) shows but is absent for x = 0.65 and x = 0.8, Figures 3.6 a) and b) respectively. Thus, three different types of patterns are observed. x = 0.95 was indexed to an R unit cell, Figure 3.7 d); compositions in the range $0.6 \leq x \leq 0.825$, Figures 3.7 a) and b) were indexed in an O unit cell and in the intermediate region $0.837 \leq x \leq 0.925$, Figure 3.7 c) as O + R.

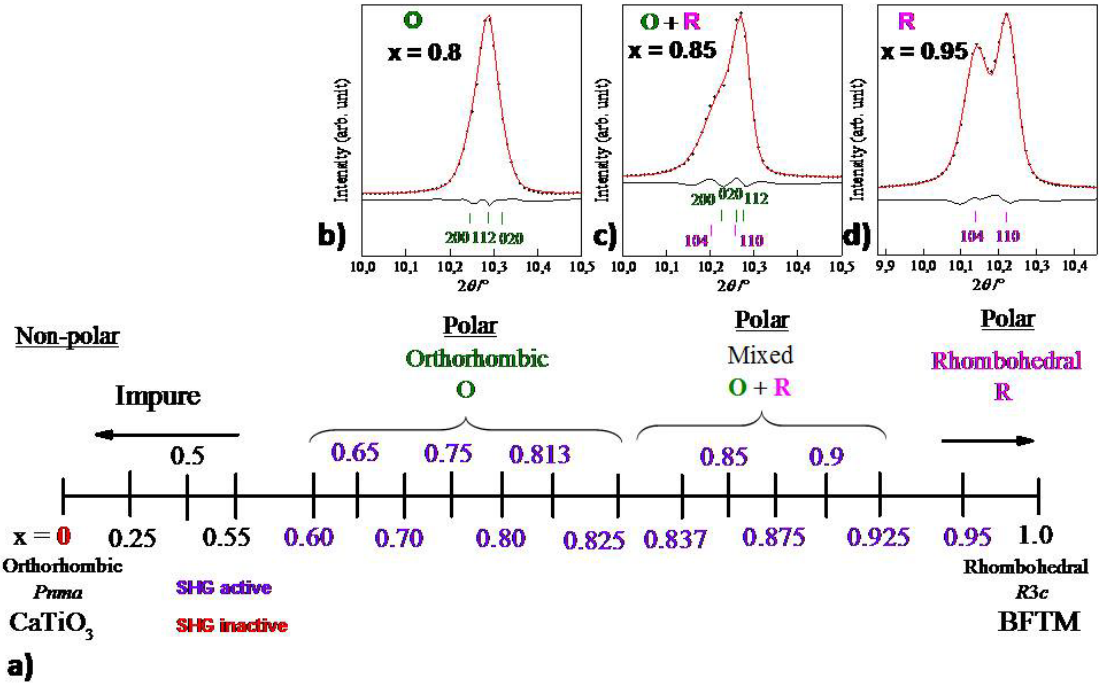

Figure 3.8 a) Phase diagram of BTFM-CTO solid solutions. At x = 0, lies $CaTiO_3$ which crystallises in the O non-polar space group Pnma. For $0.25 \leq x \leq 0.55$, the main perovskite phase is formed with Aurivillius phase impurities. For $0.6 \leq x \leq 0.825$, an O phase is formed. For $0.8375 \leq x \leq 0.925$, a mixture of the O and an R phase is formed. For x = 0.95 an R phase is formed. For x = 1, right side of the phase diagram the R polar phase BTFM with space group R3c and polarisation along $[111]_p$ is formed. The composition marked in red, x = 0 (CTO), indicates an SHG inactive sample. The compositions marked in purple are SHG active. The compositions marked in black were not measured (in the case of $x \leq 0.55$ because they are impure and BTFM because it is already known to be polar [6]).b) ,c) and d) show Le Bail fits to x = 0.8, (O) performed in $Pna2_1$, with the Miller indices in green; x = 0.85, (O+ R) performed in $Pna2_1$ and R3c, with the Miller indices of the O phase in green and of R phase in pink and x = 0.95, (R) performed in R3c, with the Miller indices in pink respectively.

As shown in Figure 3.8, when x = 0 the O non-polar phase CTO in the space group *Pnma* is formed. As expected CTO was not SHG active. When $0.25 \leq x \leq 0.55$, the main perovskite phase is formed along with Aurivillius phase impurities. For $0.6 \leq x \leq 0.825$, the XRD patterns are indexed to an O cell of dimensions $\sqrt{2}a_p \times \sqrt{2}a_p \times 2a_p$ (where a_p is the pseudocubic lattice

parameter). For $0.8375 \leq x \leq 0.925$, a mixed phase (O + R) is formed. Le Bail fits in this region $0.8375 \leq x \leq 0.925$ were performed in an O ($Pna2_1$) and an R ($R3c$) unit cell but a good fit was not achieved, see Figures 3.10 and 3.11 respectively for x = 0.85. Thus, they were performed in O + R ($Pna2_1$ + $R3c$) as it will be shown in Figure 3.12 for x = 0.85 and a good fit was achieved. For $x \geq 0.95$ an R phase is formed with space group $R3c$ as the parent compound BTFM. Compositions in the range $0.6 \leq x \leq 0.95$ were SHG active showing a polar nature. The perovskite structure is maintained over this composition range, in contrast to BTFM-LFO [8]. In the case of the system $Bi_{1-x}Ca_xFeO_3$, for $x \geq 0.2$ the R phase ($R3c$) is adopted whereas for x = 0.4 a tetragonal structure is formed and it crystallises in the non-polar space group $I4/mcm$ [23].

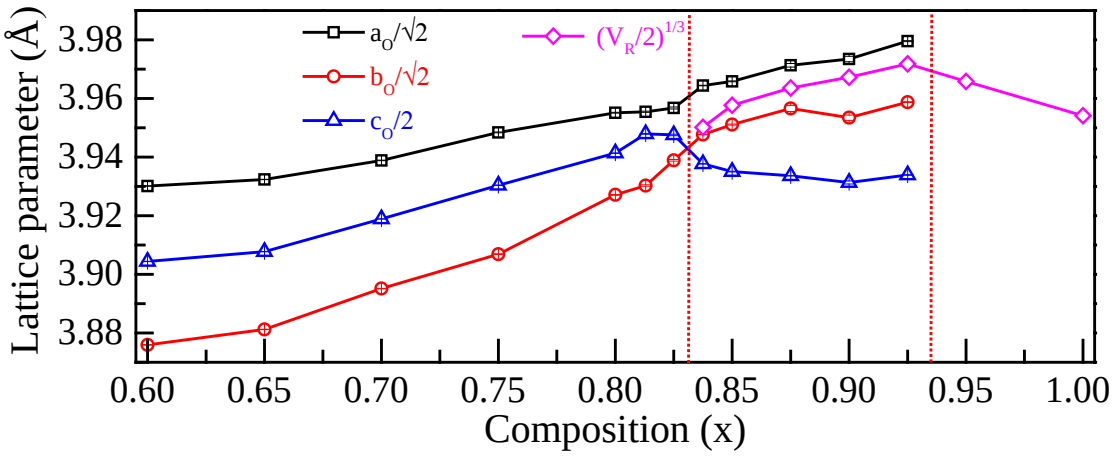

Figure 3.9 Lattice parameters determined from Le Bail fits to synchrotron XRD data plotted against composition at room temperature. $a_O/\sqrt{2}$, $b_O/\sqrt{2}$, $c_O/2$ are represented by open black squares, open red circles and blue open triangles respectively. The pink open rhombuses represent the volume of the rhombohedral primitive cell $\sqrt[3]{(V_R/2)}$

Figure 3.9 shows the reduced lattice parameters ($\sqrt[3]{(V_R/2)}$ for R and $a_O/\sqrt{2}$, $b_O/\sqrt{2}$, $c_O/2$ for O where V_R is the volume of the rhombohedral primitive cell and a_O, b_O, c_O are the lattice parameters of the orthorhombic unit cell) that correspond to pseudocubic cell dimensions and are plotted against BTFM content x for compositions in the range $0.6 \leq x \leq 1$. It is observed that from the lattice parameter variation the phase boundaries are clearly visible around $0.825 > x > 0.837$ and $0.925 > x > 0.95$ as indicated in Figure 3.9 with red short dot lines.

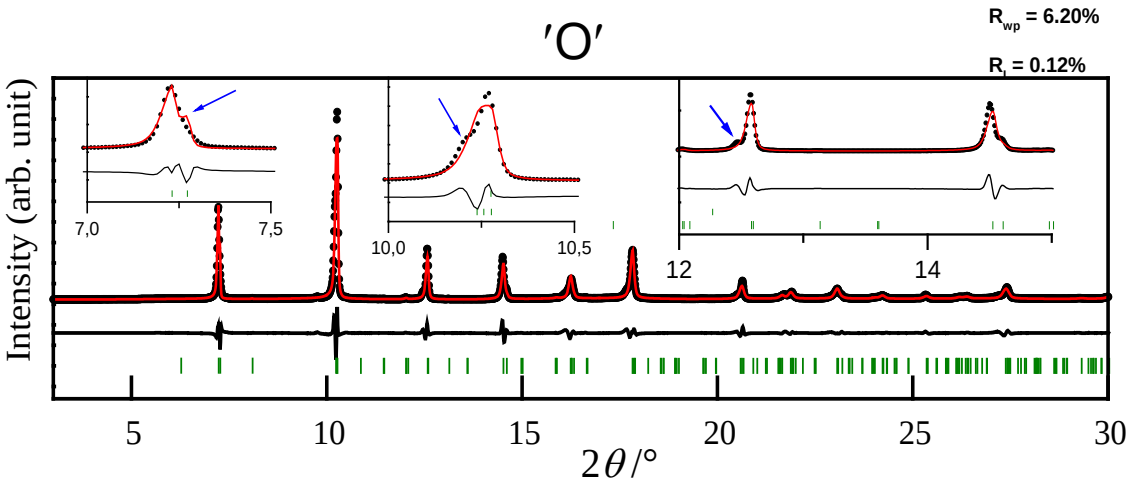

Figure 3.10 Le Bail fit on x = 0.85 in the O space group $Pna2_1$ at room temperature. The black points represent the observed data while the red solid line represents the model. The difference black curve is below. The green tics represent positions of Bragg reflections. The insets at the top show enlargements of the Le Bail fit and the blue arrows indicate the peaks with a poor fit.

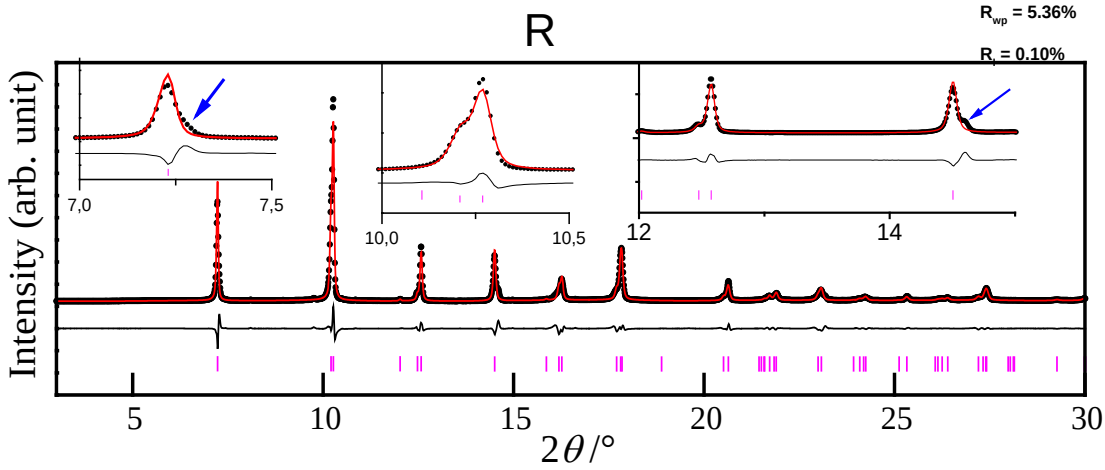

Figure 3.11 Le Bail fit on x = 0.85 in the R space group R3c at room temperature. The black points represent the observed data while the red solid line represents the model. The difference black curve is below. The pink tics represent positions of Bragg reflections. The insets at the top show enlargements of the Le Bail fit and the blue arrows indicate the peaks with a poor fit.

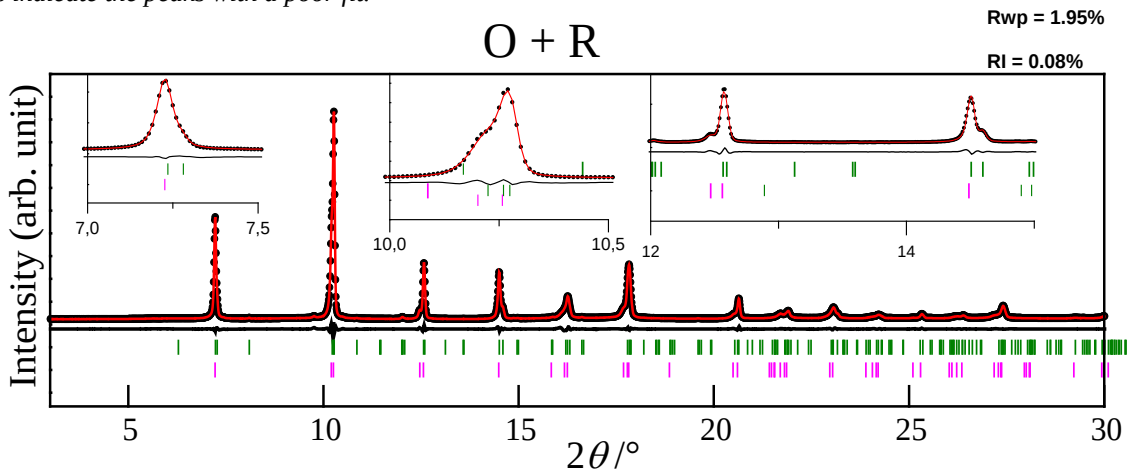

Figure 3.12 Le Bail fit on x = 0.85 with one O and one R phase in space groups $Pna2_1$ and R3c respectively at room temperature. The black points represent the observed data while the red solid line represents the model. The difference black curve is below. The green and pink tics represent positions of Bragg reflections of the O and R phase respectively.

The XRD patterns of the compositions in the range $0.8375 \leq x \leq 0.925$ could not be indexed in either O or R structures. Thus, poor Le Bail fits were obtained when they were performed in either an O or R unit cell. Figures 3.10 and 3.11 show poor Le Bail fits for x = 0.85 obtained when they were performed in the O space group $Pna2_1$ (R_{wp} = 6.20%) and in the R space group $R3c$ (R_{wp} = 5.36%) as indicated with blue arrows respectively. Therefore, a Le Bail fit in $Pna2_1$ and $R3c$, (O + R), (R_{wp} = 1.95%) was carried out and a good fit was achieved with all the peaks indexed as shown in Figure 3.12.

This BTFM-CTO system looked promising because there is a mixed phase (O+ R) between two polar phases in the range $0.8375 \leq x \leq 0.925$. Therefore, an MPB could be achieved where the electromechanical properties will be enhanced. The composition x = 0.95 has the same R structure as its parent compound BTFM, therefore attention was focused on solving the structure of the O polar phase. This study will be described in Chapter 4, Section 4.1. The structural analysis of (O+R) phase is expected to be challenging and some preliminary results will be showed in Chapter 5. The R phase will be discussed in Chapter 5.

3.6 Solid solutions $xBi(Ti_{3/8}Fe_{2/8}Mg_{3/8})O_3$-(1-x)$NdFeO_3$

Solid solutions xBTFM-(1-x)NFO were synthesised and the experimental conditions of synthesis will be described in Section 3.7.3 later on.

Table 3.3: Compositions of BTFM-NFO solid solutions synthesised in this thesis.

Calculated molecular formula	Abbreviated names
$Bi_{0.25}Nd_{0.75}(Ti_{0.09375}Mg_{0.09375}Fe_{0.8125})O_3$	0.25BTFM-0.75NFO
$Bi_{0.5}Nd_{0.5}(Ti_{0.1875}Mg_{0.1875}Fe_{0.625})O_3$	0.5BTFM-0.5NFO
$Bi_{0.65}Nd_{0.35}(Ti_{0.2438}Mg_{0.2438}Fe_{0.5125})O_3$	0.65BTFM-0.35NFO
$Bi_{0.7}Nd_{0.3}$ $(Ti_{0.475}Mg_{0.2625}Fe_{0.2625})O_3$	0.7BTFM-0.3NFO
$Bi_{0.75}Nd_{0.25}(Ti_{0.4375}Mg_{0.281}Fe_{0.281})O_3$	0.75BTFM-0.25NFO
$Bi_{0.85}Nd_{0.15}(Ti_{0.3625}Mg_{0.319}Fe_{0.319})O_3$	0.85BTFM-0.15NFO
$Bi_{0.9}Nd_{0.1}(Ti_{0.3375}Mg_{0.3375}Fe_{0.325})O_3$	0.9BTFM-0.1NFO

Table 3.3 shows the list of the chemical compositions of BTFM-NFO materials synthesised in this study. The left column shows the calculated molecular formula of all the compositions and the right column shows their corresponding abbreviated names. The compositions 0.25BTFM-0.75NFO, 0.5BTFM-0.5NFO, 0.65BTFM-0.35NFO and 0.9BTFM-0.1NFO were synthesised by Dr Michelle Dolgos and me while 0.7BTFM-0.3NFO, 0.75BTFM-0.25NFO and 0.85BTFM-0.15NFO by Dr Pranab Mandal at the University of Liverpool.

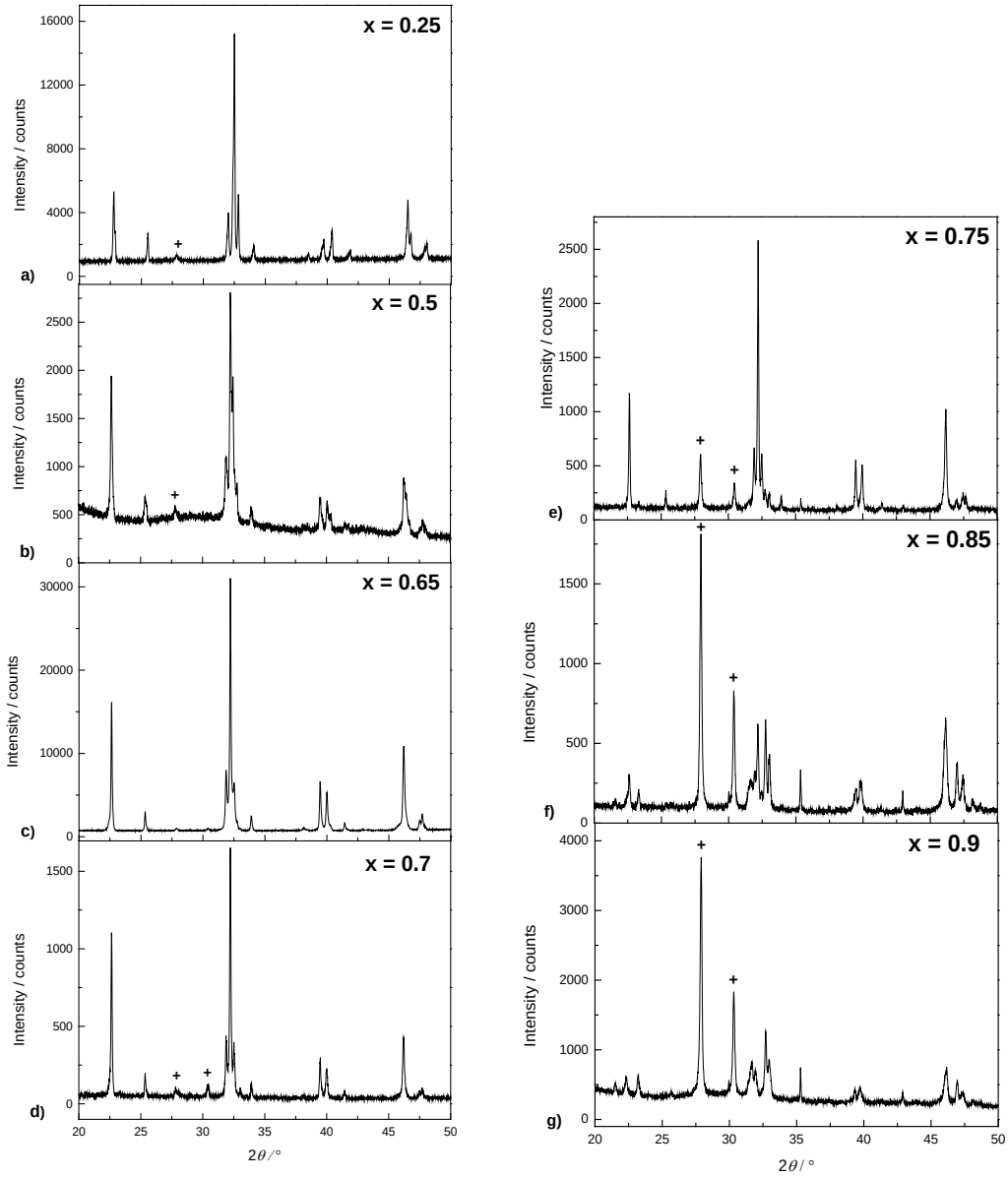

Figure 3.13 Laboratory XRD patterns of all the compositions of the BTFM-NFO materials synthesised. Impurities of sillenite-type $Bi_{25}FeO_{40}$ (+) appear especially for x ≥ 0.75.

Figure 3.13 a-g) show laboratory XRD patterns of all the compositions of BTFM-NFO synthesised in this work where x is the BTFM content. For compositions x ≤ 0.7 mainly the perovskite phase is formed and they were indexed in an orthorhombic unit cell. However, at x ≥ 0.75 the perovskite phase is formed along with sillenite-type $Bi_{25}FeO_{40}$ (+) as impurity.

The compositions 0.65BTFM-0.35NFO and 0.7BTFM-0.3NFO showed to be SHG active and therefore they are polar.

3.7 Synthesis of bismuth-based electroceramic perovskites

For the three systems studied in this work, the way of synthesising the materials is based on the protocol of BTFM [6]. It will be given in detail for BTFM-CTO in Section 3.7.1 as it is the main material studied in this thesis. In Section 3.7.2 the protocol of synthesis of BTFM-LFO-LMT [8] will be described and in Section 3.7.3 for BTFM-NFO. For the physical properties measurements presented in this work, the powder samples of BTFM-CTO were processed into pellets as explained in Section 3.8. Finally in Section 3.9, the sample preparation of BTFM-CTO materials to perform physical properties measurements will be explained.

3.7.1 Synthesis of solid solutions of $xBi(Ti_{3/8}Fe_{2/8}Mg_{3/8})O_3$-$(1-x)CaTiO_3$

3.7.1.1 Via hand-grinding

BTFM-CTO solid solutions were synthesised by the ceramic method [24] following two different ways of synthesis. The first method was carried out by hand-grinding with 7 steps as shown in Figure 3.14. The second way involved mechanical-grinding with 4 or 5 steps depending on the composition, as illustrated in Figure 3.15.

The solid state ceramic method consists of the mixture of solid reactants in the correct molar ratios and heating them up at high temperatures, typically around 1000 °C [24]. Normally, long reaction times (of the order of several days) are required; this is because the reaction takes place in the solid state so diffusion can be very slow. To overcome this, a good mixing of the starting materials plays a crucial role, whilst also having the benefit of improving sample homogeneity which is also critical for reaction completion.

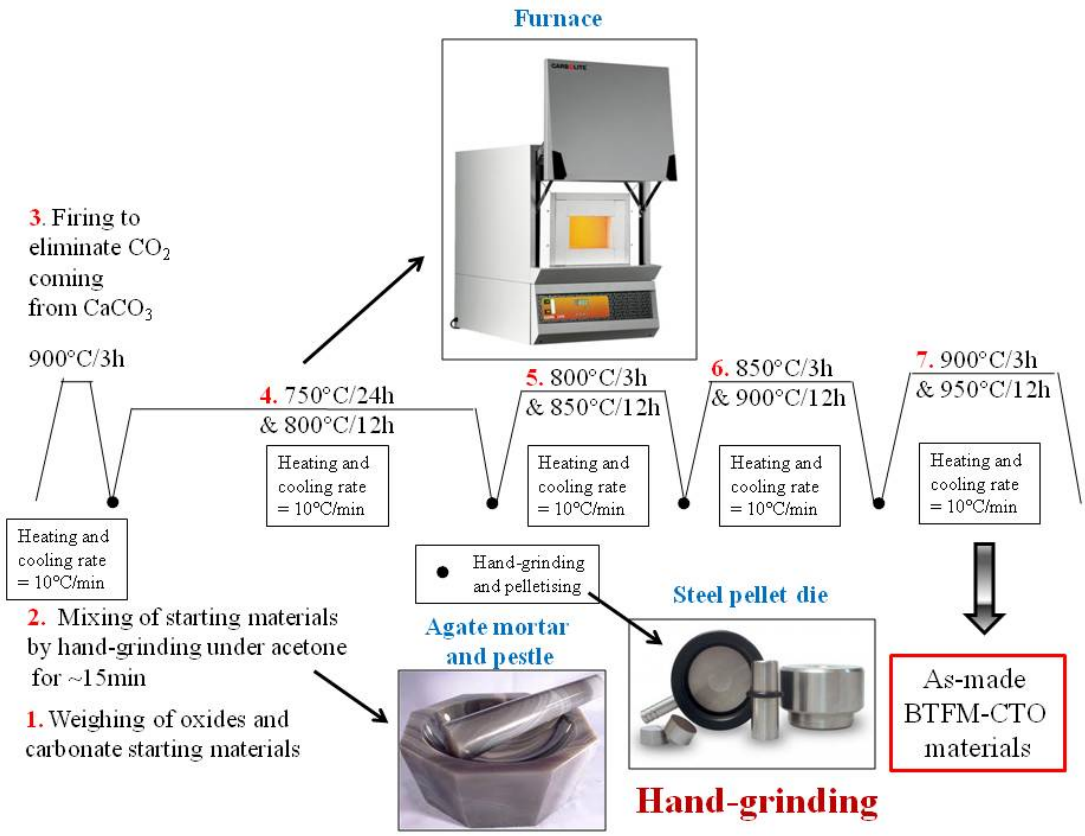

Figure 3.14 Schematic illustrations of the steps for the synthesis of BTFM-CTO solid solutions, with numbers in red indicating the 7 synthesis steps. The picture of the furnace was taken from [25].

Figure 3.14 shows a schematic illustration indicating one of the synthetic routes for BTFM-CTO solid solutions via hand-grinding, following the synthesis protocol of the parent compound BTFM [6]. The numbers in red indicate the 7 steps to achieve the synthesis. In step#1 starting materials of Bi_2O_3 (Alfa Aesar 99.99%), $CaCO_3$ (Alfa Aesar 99.95%), Fe_2O_3 (Alfa Aesar 99.945%), TiO_2 (Alfa Aesar 99.99%) and MgO (Alfa Aesar 99.95%) were weighed in stoichiometric ratios within ±0.0005 grams (g) using a Sartouris balance. For example, to synthesise 2 g of the composition 0.75BTFM-0.25CTO the weighed quantities were: 1.3573 g of Bi_2O_3, 0.1943 g of $CaCO_3$, 0.1163 g of Fe_2O_3, 0.3296 g of TiO_2 and 0.0881 g of MgO. In step#2 starting materials were hand-ground for ~15 minutes (min) under acetone in an agate mortar and pestle. In step#3 the mixed powder was placed in an alumina crucible and fired at 900 °C for 3 hours (h) in a Carbolite chamber furnace in order to eliminate the CO_2 of the $CaCO_3$. The lid of

the crucible was slightly opened to allow the CO_2 to escape. Heating and cooling rates of 10 °C per minute were used during all the processes. In step#4 the obtained powder was uniaxially pressed into pellets, using a 10 mm stainless steel pellet die in a hand pulled hydraulic piston press at 1 ton force. For 1 g of powder one pellet was made. The pellets were placed in an alumina crucible with Pt foil on the bottom to avoid reaction of the alumina and the material during the heating. The pellets were fired at 750 °C for 24 h and then at 800 °C for 12 h. In step#5, step#6 and step#7 the pellets were ground, repelletised and fired. The firing temperatures were: 800 °C 3 h / 850 °C 12 h in step #5, 850 °C 3 h / 900 °C 12 h in step #6 and 900 °C 3 h / 950 °C 12 h in step #7. The last heating step for the synthesis of the parent BTFM is at 875 °C / 12 h. In the case of BTFM-CTO the conditions had to be re-optimised in order to eliminate all the impurities.

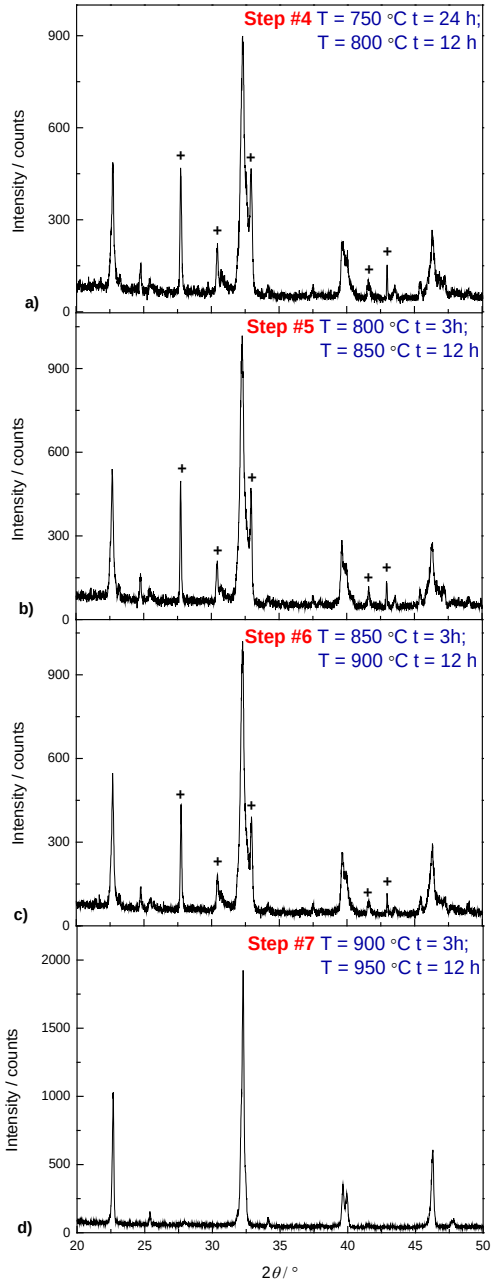

Figure 3.15 a-d) Laboratory XRD patterns on 0.75BTFM-0.25CTO synthesised via hand-grinding at step#4, step#5, step#6 and step#7 respectively.

Figure 3.15 a-d) shows laboratory XRD patterns on 0.75BTFM-0.25CTO synthesised via hand-grinding at step#4, step#5, step#6 and step#7 respectively. The formation of the perovskite phase and the decrease of impurities while heating is observed.

3.7.1.2 Via mechanical-grinding

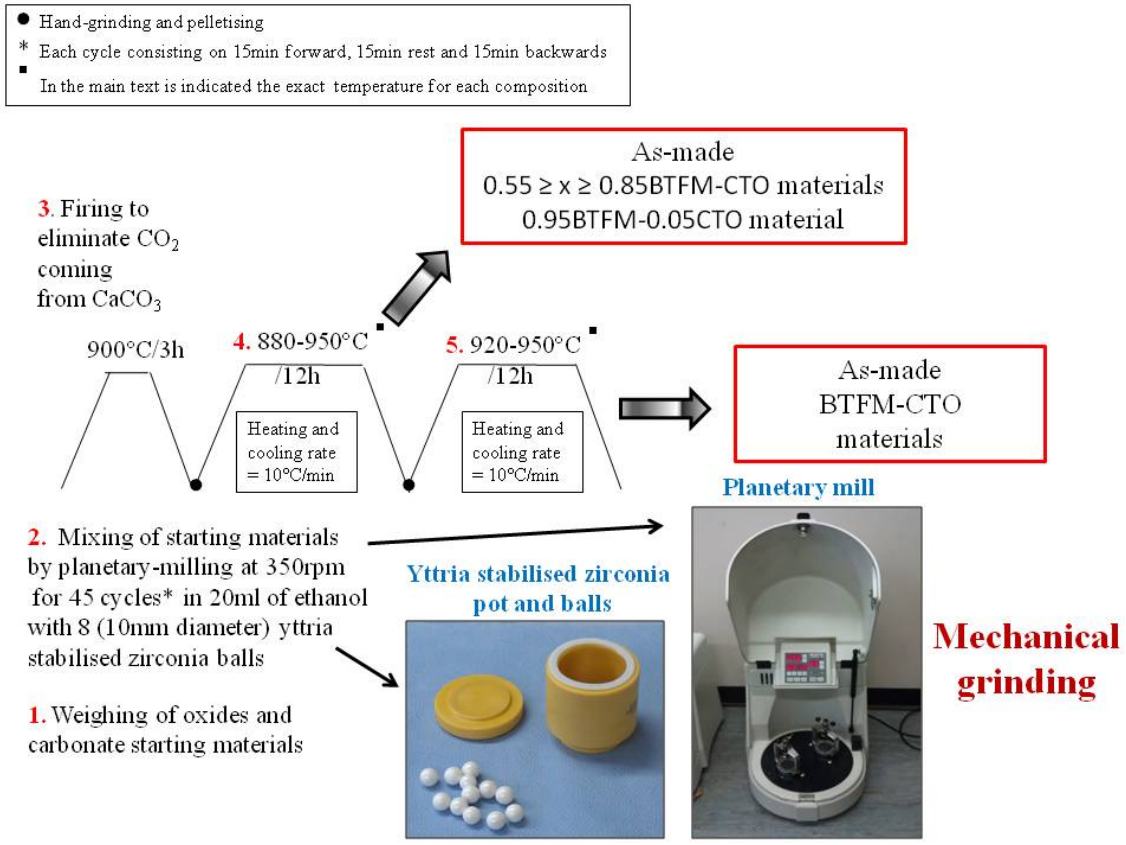

Figure 3.16 Schematic illustrations of the steps for the synthesis of BTFM-CTO solid solutions mixing the starting materials by planetary milling with numbers in red indicating the 5 synthesis steps.

Figure 3.16 shows a schematic illustration of the steps of synthesis of BTFM-CTO solid solutions via mechanical grinding. In this case, the starting materials were mixed in a Pulverisette planetary mill from Fritch. The numbers in red indicate the 4-5 steps required to achieve the synthesis. In step#1 starting materials of Bi_2O_3 (Alfa Aesar 99.99%), $CaCO_3$ (Alfa Aesar 99.95%), Fe_2O_3 (Alfa Aesar 99.945%), TiO_2 (Alfa Aesar 99.99%) and $4MgCO_3{\cdot}Mg(OH)_2{\cdot}4H_2O$ (Aldrich 99.99%) were mixed in stoichiometric amounts. $4MgCO_3{\cdot}Mg(OH)_2{\cdot}4H_2O$ was used instead of MgO as it reacts better with the other starting materials than MgO. In step#2 starting materials were ball milled in yttria stabilized zirconia (YSZ) pots with 8 YSZ balls. The diameters of the balls were 10 mm. 20 ml of ethanol was added to the pots. The milling was done at a rate of 350 revolutions per minute (rpm) for 45 cycles. The 45 cycles consisted of 15 min

forward, 15 min rest and 15 min backwards. The solvent was evaporated and the mixture was stirred in order to prevent the densest elements from falling to the bottom first. In step#3 the powder was heated at 900 °C / 3 h to eliminate the CO_2 of the $CaCO_3$. Then the powder was pressed into 10 mm pellets which were subsequently placed in an alumina crucible with Pt foil on the bottom to prevent the possibility of reaction between the alumina and the pellet material during heating. In step#4 the pellets were fired at 950 °C / 12 h for compositions in the range $0.55 \geq x \geq 0.85$ and the temperatures were 930 °C / 12 h for 0.875BTFM-0.125CTO, 900 °C / 12 h for 0.9BTFM-0.1CTO, 880 °C / 12 h for 0.925BTFM-0.075CTO and 900 °C / 12 h for 0.95BTFM-0.05CTO. In step#5 the pellets were fired at 950 °C / 12 h for 0.875BTFM-0.125CTO, 920 °C / 12 h for 0.9BTFM-0.1CTO and 920 °C / 12 h for 0.925BTFM-0.075CTO.

Figure 3.17 Powder sample of the composition 0.75BTFM-0.25CTO.

The photograph in Figure 3.17 shows a powder sample of the composition 0.75BTFM-0.25CTO, which is observed to be orange.

3.7.2 Synthesis of solid solutions of $Bi(Ti_{3/8}Fe_{2/8}Mg_{3/8})O_3$ – $La(Mg_{1/2}Ti_{1/2})O_6$ - $LaFeO_3$

Starting materials of Bi_2O_3 (Alfa Aesar, 99.9995%), La_2O_3 (Alfa Aesar, 99.999%; heated to 950 °C for several hours before use), Fe_2O_3 (Alfa Aesar, 99.998), TiO_2 (Alfa Aesar, 99.995%), and $4MgCO_3 \cdot Mg(OH)_2 \cdot 4H_2O$ (Aldrich 99.99%) were mixed in stoichiometric amounts and ball milled under the same conditions of BTFM-CTO materials already detailed in Section 3.7.1.2. The resulting homogenous mixture was pressed into pellets and placed in an alumina crucible lined with Pt foil on the bottom to avoid reaction with the alumina while heating. The pellets were then fired in air at 950 °C for 14 h to obtain a phase pure powder.

3.7.3 Synthesis of solid solutions of $xBi(Ti_{3/8}Fe_{2/8}Mg_{3/8})O_3$-$(1-x)NdFeO_3$

Starting materials of Bi_2O_3 (Alfa Aesar, 99.9995%), Nd_2O_3 (Alfa Aesar, 99.999%; heated to 950 °C for several hours before use), Fe_2O_3 (Alfa Aesar, 99.998), TiO_2 (Alfa Aesar, 99.995%), and MgO (Aldrich 99.99%) were weighed in stoichiometric ratios. The protocol of synthesis is the same as described for BTFM-CTO materials in Section 3.7.1.1 via hand-grinding. The only difference is that step#3, heating at 900 °C for 3 h in a furnace in order to eliminate the CO_2 of the $CaCO_3$, was not needed.

3.8 Pellet processing

Powder BTFM-CTO materials were processed into pellets for physical properties measurements. Compositions in the range $0.6 \geq x \geq 0.95$BTFM were ball milled with 0.2 wt% MnO_2 and 2-4 wt% Polyvinyl Butyral (Butvar 98) resin. The resin was used to increase the density whereas the MnO_2 to reduce the dielectric loss [8, 26]. In Appendix D a comparison of an impedance measurement performed on a sample with and without MnO_2 is shown. The conditions used for ball milling were the same as for the synthesis in Section 3.7.1.2. The powder was uniaxially pressed using an 8 mm stainless steel pellet die. A hand pulled hydraulic piston press at 1 ton pressure was used. The pellets were then isostatically pressed for 5 min using an Autoclave Engineers Cold Isostatic Press (CIP), under a pressure of 2000 bar. The pellets were sealed in waterproof bags to perform the CIP to prevent contamination. They were lowered into a hydraulic fluid, a mixture of oil and water. The pressure was released slowly and the sample bag recovered. The pellets were sintered under an O_2 atmosphere in a tube furnace to exceed a density of 95 %. The conditions of sintering change depending on the composition in order to prevent impurities. Compositions in the range $0.6 \geq x \geq 0.75$ were annealed three times at 960 °C 3 h / 900 °C 12 h. The compositions in the range $0.8 \geq x \geq 0.85$ were sintered three times at 930 °C 3 h / 900 °C 15 h. The compositions in the range $0.875 \geq x \geq 0.925$ were sintered three times at 900 °C / 12 h.

The mass of all the pellets was measured using an Archimedes balance. Firstly, the pellet under investigation was weighed before immersion into distilled water. Secondly, the pellet was submerged in water until its weight was constant, ensuring that the water fills in all the pores. Finally, the pellet was removed from the water. It was dried with a non-absorbing material to prevent the water in the pores from leaching out and weighed again. The sample density, ρ, was calculated using Equation 3.1.

$$\rho = \frac{m_1}{m_3 - m_2} \times \rho_{H2O} \qquad \textit{Equation 3.1}$$

where m_1 is the mass before immersion, m_2 is the mass during immersion, m_3 is the mass of the dried pellet after immersion and ρ_{H2O} is the density of water, 0.99826 g/cm^3 at 20 °C.

The pellets were polished on a semi-automatic polishing machine Tegramin-30 from Struers using silicon carbide papers of 20, 15 and 5 micron roughness to achieve a mirror finish. The diameter and thickness of the pellets were measured using a calliper. Their diameters were approximately 7 mm while the thickness was ranging from 0.10 – 0.20 mm.

3.9 Sample preparation for physical properties measurements

To measure the piezoelectric coefficient d_{33} and perform pyrocurrent experiments, the pellets were sputtered with Au electrodes on the parallel plane faces. In the case of ferroelectric measurements, the pellets were silver painted with a brush on both faces. Any silver paint remaining on the edges of the pellets was removed by polishing the edges gently in order to avoid shorting. To carry out impedance measurements Pt paste electrodes were applied to the pellets which were fired at 800 °C for 30 min. Pt wires were used to make electrical contact which were carefully attached to the Pt paste and heated again at 850 °C for 0.5 h to ensure their adhering.

3.10 References

1. Shrout, T. R. and Zhang, S. J., *Journal of Electroceramics*, 2007. **19**(1): p. 113-126.
2. Maeder, M. D., Damjanovic, D. and Setter, N., *Journal of Electroceramics*, 2004. **13**(1-3): p. 385-392.
3. Takenaka, T., Nagata, H. and Hiruma, Y., *Japanese Journal of Applied Physics*, 2008. **47**(5): p. 3787-3801.
4. Leontsev, S. O. and Richard E. E., *Science and Technology of Advanced Materials*, 2010. **11**(4): p. 2957-2961.
5. Zhang, S. and .Yu, F., *Journal of the American Ceramic Society*, 2011. **94**(10): p. 3153-3170.
6. Bridges, M. A., Suchomel, M. R., Kuang, X., Sterianou, I., Sinclair, D. C. and Rosseinsky, M. J., *Angewandte Chemie-International Edition*, 2007. **46**: p. 8785 –8789.
7. Dolgos, M., Adem, U., Wan, X., Xu, Z., Bell, A. J., Comyn, T. P., Stevenson, T., Bennett, J., Claridge, J. B. and Rosseinsky, M. J. *Chemical Science*, 2012. **3**: p. 1426-1435.
8. Dolgos, M. R., Adem, U., Manjon-Sanz, A., Wan, X., Comyn, T. P., Stevenson T., Bennett J., Bell, A. J., Tran, T. T., Halasyamani, P. S., Claridge, J. B. and Rosseinsky, M. J., *Angewandte Chemie-International Edition*, 2012. **51**: p. 10770-10775.
9. Mandal, P., Manjon-Sanz, A., Corkett, A. J., Comyn, T. P, Dawson, K., Stevenson T., Bennett J., Henrichs, L. F., Bell, A. J., Nishibori, E., Takata, M., Marco, Z., Dolgos, M. R., Adem, U., Wan, X., Pitcher, M. J., Romani, S., T. Tran, T. T., Halasyamani, P. S., Claridge, J. B. and Rosseinsky, M. J., *Submitted to Advanced Materials,* 2014.
10. Hughes, H., Allix, M. M. B., Bridges, C. A., Claridge, J. B., Kuang, X. J., Niu, H. J., Taylor, S., Song, W. H and Rosseinsky, M. J., *Journal of the American Chemical Society*, 2005. **127**(40): p. 13790-13791.
11. Chong, S. Y., Szczecinski, R. J., Bridges, C. A., Tucker, M. G., Claridge, J. B. and Rosseinsky M. J., *Journal of the American Chemical Society*, 2012. **134**(13): p. 5836-5849.
12. Teague, J. R., Gerson, R. and James, W. J., *Solid State Communications*, 1970. **8**(13): p. 1073-1074.
13. Wang, Y. P., Zhou, L., Zhang, M. F., Chen, X. Y., Liu, J. M. and Liu, Z. G., *Applied Physics Letters*, 2004. **84**(10): p. 1731-1733.
14. Rai, R., Bdikin, I., Valente, M. A. and Kholkin, A. L., *Materials Chemistry and Physics*, 2010. **119**(3): p. 539-545.
15. Jaffe, H., *Journal of the American Ceramic Society*, 1958. **41**(11): p. 494-498.
16. Yang, S. Y., Zavaliche, F., Mohaddes-Ardabili, L., Vaithyanathan, V., Schlom, D. G., Lee, Y. J., Chu, Y. H., Cruz, M. P., Zhan, Q., Zhao, T. and Ramesh, R., *Applied Physics Letters*, 2005. **87**(10).
17. Salak, A. N., Prokhnenko, O. and Ferreira, V. M., *Journal of Physics-Condensed Matter*, 2008. **20**(8): p. 85210-85219.
18. Lee, D. Y., Yoon, S. J., Yeo, J. H., Nahm, S., Paik, J. H., Whang, K. C. and Ahn, B. G., *Journal of Materials Science Letters*, 2000. **19**(2): p. 131-134.
19. Zhu, W. M., Guo, H. Y. and Ye, Z. G., *Journal of Materials Research*, 2007. **22**(8): p. 2136-2143.
20. Wei, J., Haumont, R., Jarrier, R., Berhtet, P. and Dkhil, B., *Applied Physics Letters,* 2010. **96**(10): p. 102509-102512.
21. Li, S. P., Cao, W. W. and Cross, L. E., *Journal of Applied Physics,* 1991. **69**(10): p. 7219-7224.

22. Eitel, R. E., Randall, C. A., Shrout, T. R., Rehrig, P. W., Hackenberger, W. and Park, S. E., *Japanese Journal of Applied Physics Part 1-Regular Papers Short Notes & Review Papers*, 2001. **40**(10): p. 5999-6002.
23. Troyanchuk, I. O., Karpinsky, D. V., Bushinskii, M. V., Prokhnenko, O., Kopcevicz, M., Szymczak, R. and Pietosa, J, *Journal of Experimental and Theoretical Physics*, 2008. **107**(1): p. 83-89.
24. Dann, S. E., *The Royal Society of Chemistry*, 2000.
25. *http://www.carbolite.com/products/furnaces/ashing-chamber-furnaces/gsm-specialist-ashing-furnaces/models/*.
26. Leontsev, S. O. and Richard, E. E., *Journal of the American Ceramic Society*, 2009. **92**: p. 2957-2961.

CHAPTER 4 - Structural analysis on the orthorhombic (O) phase and physical properties measurements

In this chapter, firstly the refinement strategy of the O phase using synchrotron radiation X-ray diffraction (SRXRD) data will be described in Sections from 4.1.1 to 4.1.4 and is as follows: first of all it was indexed to an orthorhombic cell and thus the lattice parameters were determined, Section 4.1.1. Secondly, published structural models of similar ABO_3 perovskite compounds were used to perform Rietveld analysis using the lattice parameters obtained previously but it was not possible to fit the data with any of them, Section 4.1.2. Therefore thirdly, Le Bail analysis were performed for all the non-centrosymmetric (because the O phase has shown to be polar by SHG measurements, see Section 3.5, Chapter 3) orthorhombic space groups in the six different settings and the space group was determined from the reflection conditions as $Pna2_1$, Section 4.1.3. Finally, in Section 4.1.4 a Maximum Entropy Method (MEM) study was carried out and a six sites disordered model for the A-site was built based on charge density maps using the Rietveld/MEM method [1], previously described in Section 2.3.3, Chapter 2. By studying the three-dimensional observed charge density distribution of the A-site it was concluded that this six sites disordered model for the A-site is equivalent to a three sites disordered model for the A-site but considering the anisotropic atomic displacement (Section 4.1.4.8). Nevertheless, as neutron powder diffraction (NPD) determines the atomic positions of light elements such as oxygens

more precisely, a joint refinement (NPD and SRXRD) was performed and the results will be presented in Section 4.1.5. The outcomes of microscopy studies carried out to support the assignment of the space group based on the analysis of the reflection conditions (Section 4.1.3) will be presented in Section 4.1.6. Finally, in Section 4.2, the results of physical properties measurements performed on the O phase will be presented and discussed.

4.1 Structural analysis of the orthorhombic (O) phase

For the structural analysis of the O phase using SRXRD (Sections from 4.1.1 to 4.1.4), the composition 0.825BTFM-0.175CTO was selected for structural analysis. As Figure 4.1 b) shows, the composition x = 0.825 is free of impurities. However, compositions x = 0.6, 0.7 and 0.8 have a weak impurity of Aurivillius-type $Bi_5FeTi_3O_{15}$ (*) and compositions x = 0.65, 0.7, 0.75 and 0.8 contain as impurity sillenite-type $Bi_{25}FeO_{40}$ (+). Also it was observed that the width of the peaks were very sharp indicating a single phase as Figure 4.1 a) shows.

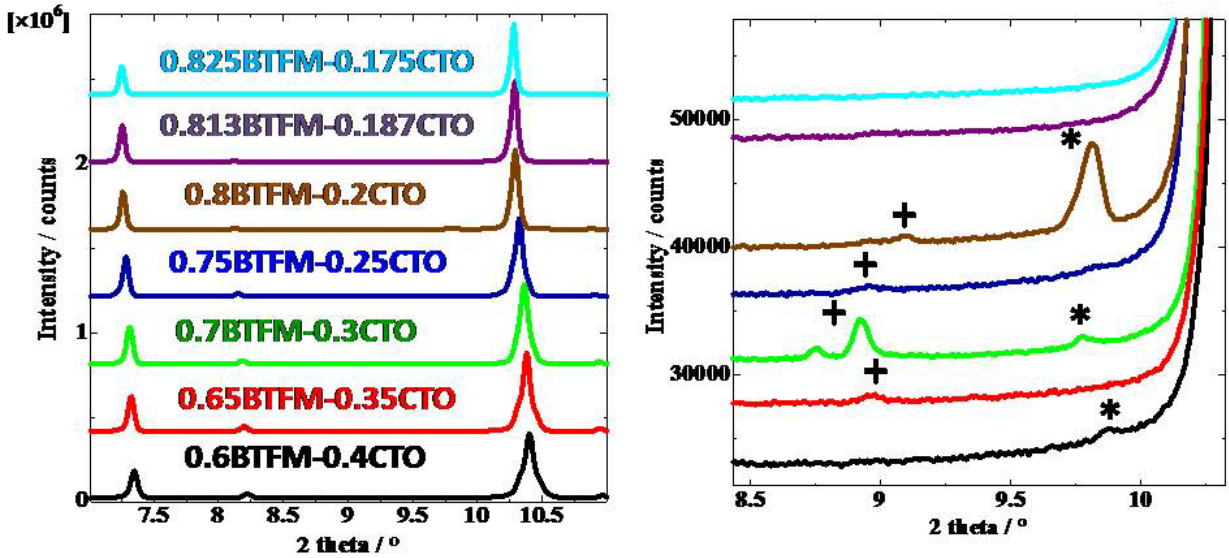

Figure 4.1 PXRD data of 0.6 ≤ x ≤ 0.825. Comparison of the compositions with orthorhombic structure for xBTFM-(1-x)CTO, the data have been normalised and shifted up as x increases: a) shows the 2θ range from 7° to 11°; b) shows the 2θ range from 8.5° to 10.5°.Note that weak impurity peaks corresponding to the most intense reflections of Aurivillius-type $Bi_5FeTi_3O_{15}$ (*) appear in x = 0.6, 0.7 and 0.8. Compositions x = 0.65, 0.7, 0.75 and 0.8 contain a weak impurity corresponding to the most intense reflection of sillenite-type $Bi_{25}FeO_{40}$ (+).

4.1.1 Indexing

Synchrotron X-ray data at -173 °C were used for the indexing process. The exposure time was 5 minutes. Thirty peak positions of isolated Bragg reflections in the data range from 3.00° to 28.60° were evaluated. The error of the peak positions is 0.010°. The lattice parameters were determined by the program *DICVOL06* [2] using the peak positions. The determined lattice constants are: a = 7.866(3) Å, b = 5.5920(8) Å and c = 5.5657(10) Å and the angles: $\alpha = \beta = \gamma$ = 90° which correspond to an orthorhombic structure.

4.1.2 Structural refinement using already published structural models

Published orthorhombic and monoclinic structural models of similar ABO_3 perovskite compounds were used for the analysis. Rietveld analysis was performed using synchrotron data at -173 °C. Data at this temperature was selected to perform the analysis on it because the atomic displacement of the atoms at low temperatures is smaller. As a consequence, the background is low and especially at high angle the quality of data is better. The 2θ range of analysis was from 3° to 42°. The lattice parameters obtained from the indexing were used as the initial values for the published orthorhombic structural models. In the case of the monoclinic structural model, the initial values of the lattice parameters were taken from the model. The initial atomic positions were taken from the published models. The initial values for the isotropic displacement factor, B, are for the A-site, B = 3.0, for the B-site, B = 1.0 and for the O, B = 3.0. The scale factor, peak shift, peak shape parameters, lattice parameters and atomic positions were refined.

Figures 4.2-4.10 show Rietveld refinements for 0.825BTFM-0.175CTO. For each figure, four different 2θ ranges are shown: a) from ~3° to ~13°, b) from ~13° to ~23°, c) from ~23° to ~33° and d) from ~33° to ~42°.

Figure 4.2 shows Rietveld refinements for 0.825BTFM-0.175CTO using the published orthorhombic structural model for $Bi_{0.72}La_{0.28}(Ti_{0.27}Fe_{0.46}Mg_{0.27})O_3$ [3]. The space group is $Pmc2_1$. The reliability factors based on the weighted profiles, R_{wp}, and Bragg intensities, R_I are 4.67% and 8.51%, respectively for the setting *abc* (being a = 7.866(3) Å , b = 5.5920(8) Å and c = 5.5657(10) Å). The black circles indicate the mismatches between the model and data either in terms of peak position and/or shape. The refined parameters are listed in Table 4.1.

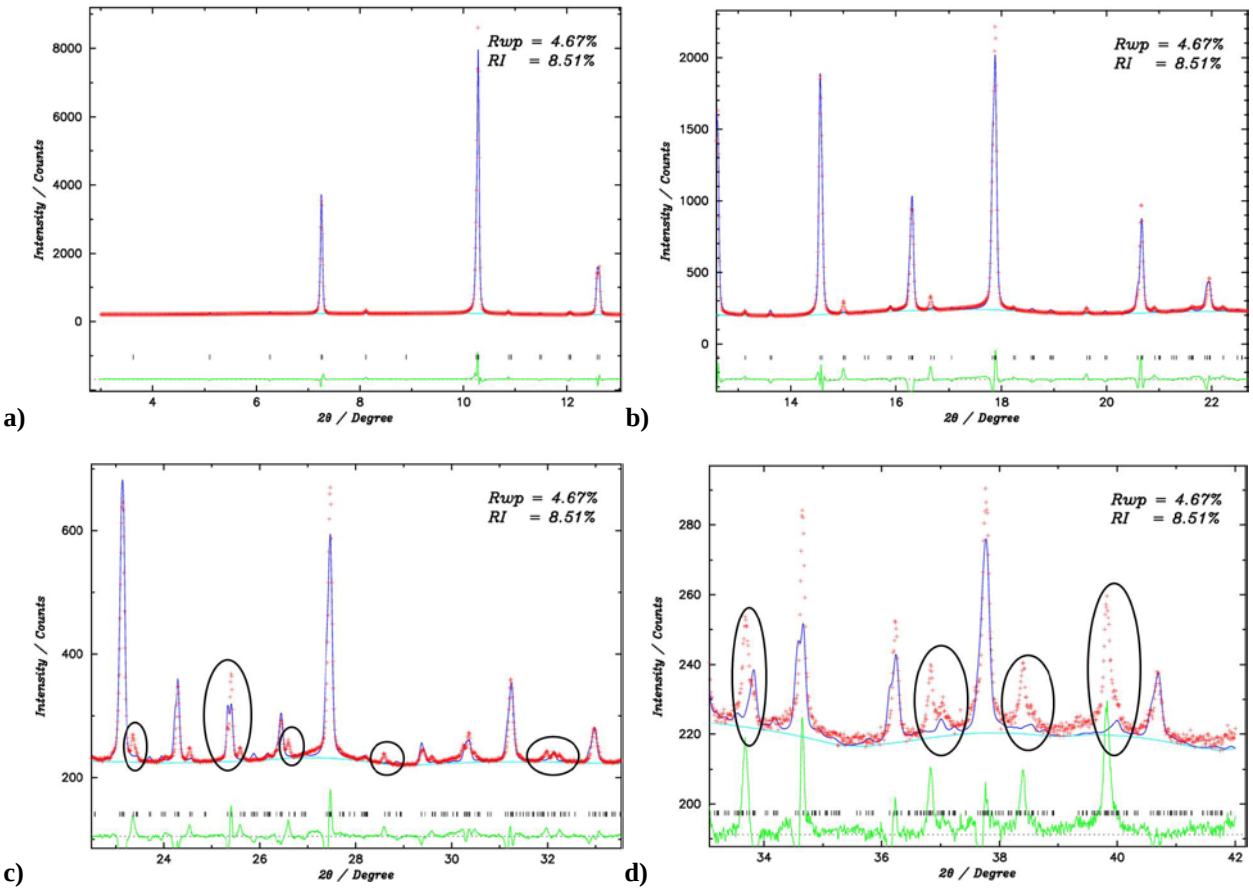

Figure 4.2 a) Rietveld refinement for 0.825BTFM-0.175CTO in $Pmc2_1$, setting abc. The black circles indicate the reflections missing in the model and the mismatches between the model and data either in terms of peak position and/or shape. The red crosses represent the observed data while the blue solid line represents the model. The difference green curve is below. The black tics represent positions of Bragg reflections.

Table 4.1: Atomic parameters for 0.825BTFM-0.175CTO from Rietveld refinement in $Pmc2_1$, setting abc. Lattice constants: a = 7.8632(2) Å, b = 5.5871(4) Å and c = 5.5621(1) Å.

Atoms	x	y	z	B	Occupancy
Bi1/Ca1	0	0.2696(6)	0.77160	3.0	0.825/0.175
Bi2/Ca2	0.5	0.2528(6)	0.78440	3.0	0.825/0.175
Ti/Fe/Mg	0.744(4)	0.751(4)	0.78(2)	1.0	0.4844/0.2063 /0.3094
O1	0	0.194(7)	0.36(1)	3.0	1
O2	0.5	0.305(7)	0.28(2)	3.0	1
O3	0.209(7)	0.51(2)	0.06(1)	3.0	1
O4	0.292(7)	0.021	0.56(1)	3.0	1

Figure 4.3 shows Rietveld refinements for 0.825BTFM-0.175CTO using the published orthorhombic structural model for $Bi_{0.72}La_{0.28}(Ti_{0.27}Fe_{0.46}Mg_{0.27})O_3$ [3]. The space group is $Pmc2_1$. The reliability factors based on the weighted profiles, R_{wp}, and Bragg intensities, R_I are 4.13% and 8.06% respectively for the setting *acb*. The black circles indicate the mismatches between the model and data either in terms of peak position and/or shape. The refined parameters are listed in Table 4.2.

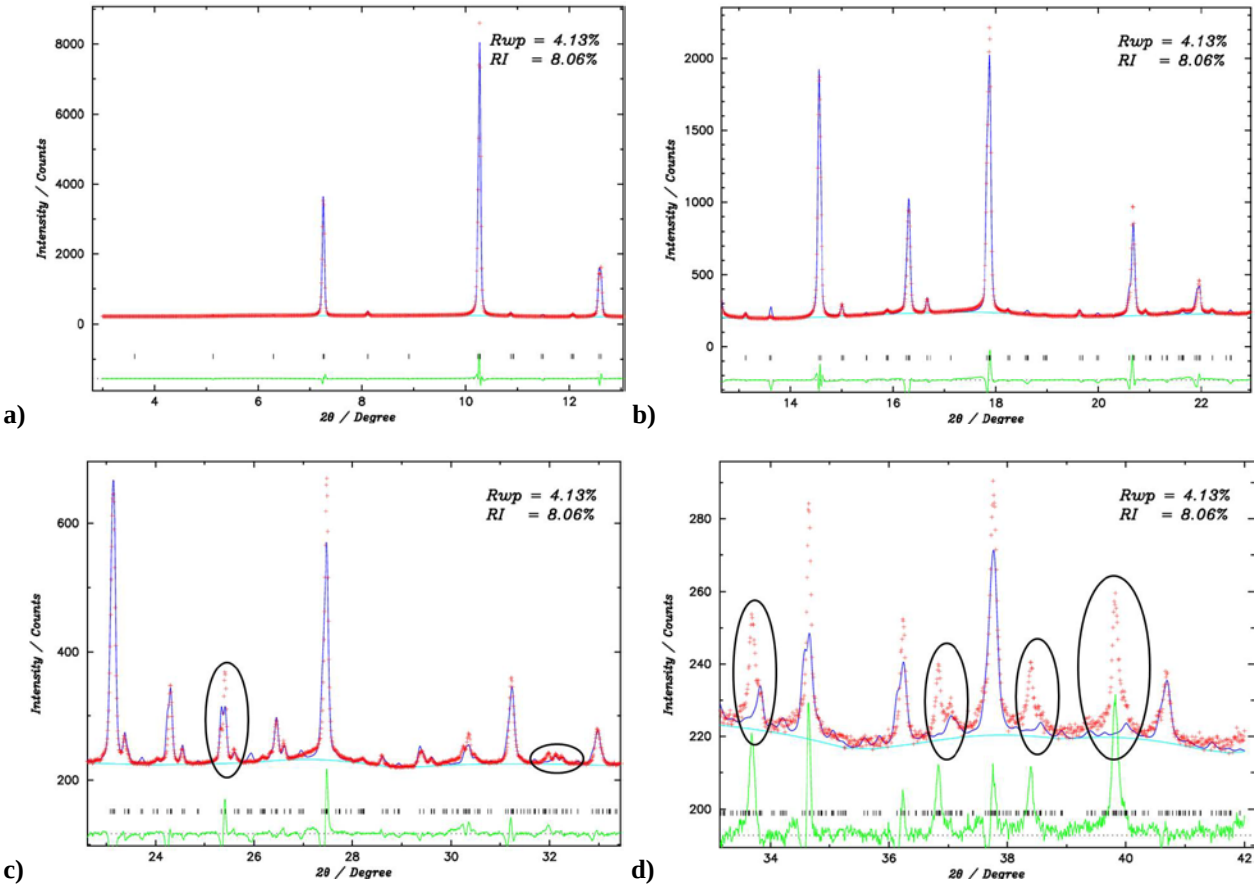

Figure 4.3 a) Rietveld refinement for 0.825BTFM-0.175CTO in $Pmc2_1$, setting acb. The black circles indicate the reflections missing in the model and the mismatches between the model and data either in terms of peak position and/or shape. The red crosses represent the observed data while the blue solid line represents the model. The difference green curve is below. The black tics represent positions of Bragg reflections.

Table 4.2: Atomic parameters for 0.825BTFM-0.175CTO from Rietveld refinement in $Pmc2_1$, setting acb. Lattice constants: a = 7.8637(2) Å, b = 5.5623(1) Å and c =5.5875(1) Å.

Atoms	x	y	z	B	Occupancy
Bi1/Ca1	0	-0.7575(8)	0.266(5)	3.0	0.825/0.175
Bi2/Ca2	0.5	-0.7689(7)	0.231(5)	3.0	0.825/0.175
Ti/Fe/Mg	0.75(2)	0.753(3)	0.74900	1.0	0.4844/0.2063 /0.3094
O1	0	-0.29(1)	0.218(9)	3.0	1
O2	0.5	-0.26(1)	0.241(9)	3.0	1
O3	0.193(5)	-0.049(6)	0.509(8)	3.0	1
O4	0.299(6)	-0.528(8)	0.021(9)	3.0	1

Figure 4.4 shows Rietveld refinements for 0.825BTFM-0.175CTO using the published orthorhombic structural model $(Bi_{0.8}Gd_{0.2})FeO_3$ [4]. The space group is $Pna2_1$. The reliability factors based on the weighted profiles, R_{wp}, and Bragg intensities, R_I are 4.97% and 10.66% respectively for the setting *bca*. The black circles indicate the mismatches between the model and data either in terms of peak position and/or shape. The refined parameters are listed in Table 4.3.

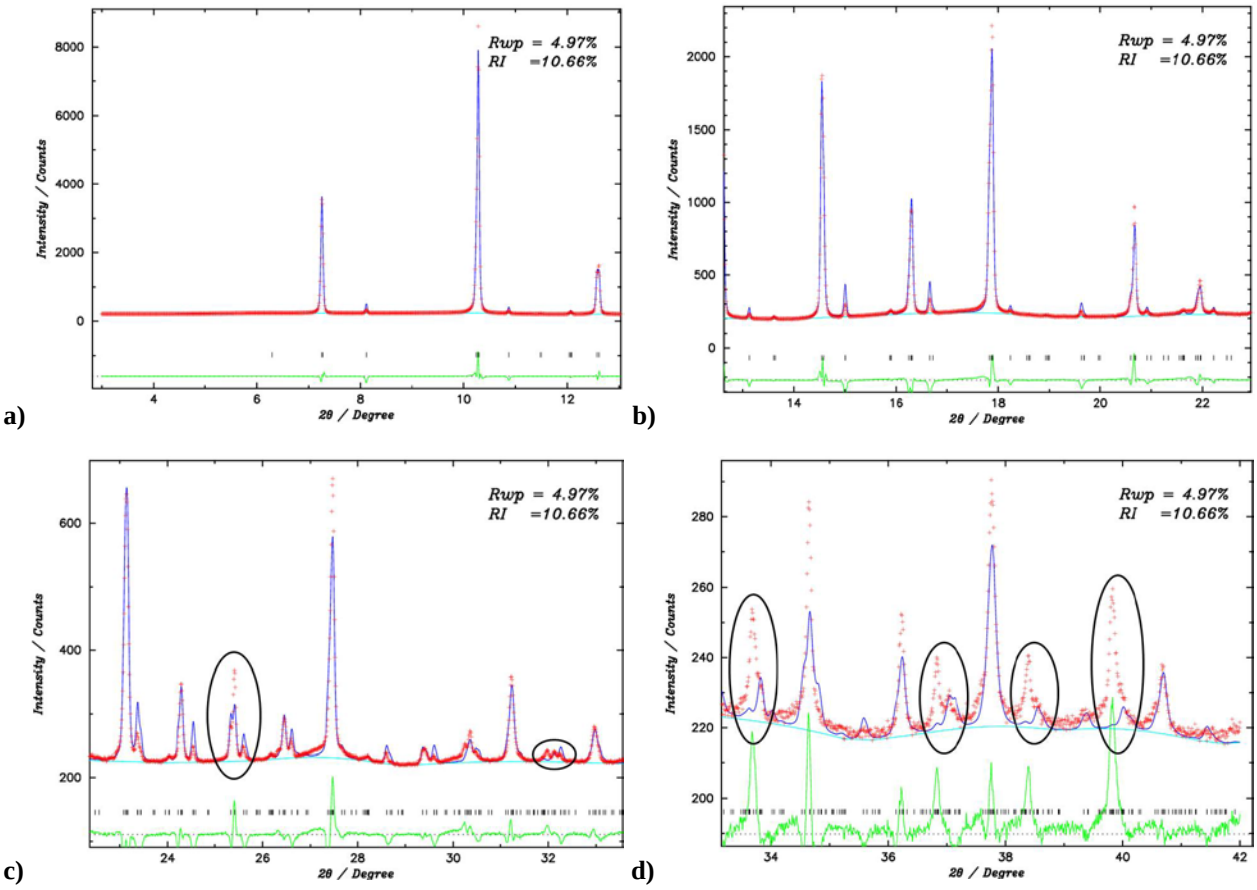

Figure 4.4 a) Rietveld refinement for 0.825BTFM-0.175CTO in $Pna2_1$, setting bca. The black circles indicate the reflections missing in the model and the mismatches between the model and data either in terms of peak position and/or shape. The red crosses represent the observed data while the blue solid line represents the model. The difference green curve is below. The black tics represent positions of Bragg reflections.

Table 4.3: Atomic parameters for 0.825BTFM-0.175CTO from Rietveld refinement in $Pna2_1$, setting bca. Lattice constants: a = 5.5883(1) Å, b = 5.5623(1) Å and c = 7.8645(2) Å.

Atoms	x	y	z	B	Occupancy
Bi/Ca	0.0269(2)	0.9923(5)	-0.254(5)	3.0	0.825/0.175
Ti/Fe/Mg	0.0065	0.49(4)	0	1.0	0.4844/0.2063 /0.3094
O1	0.487(2)	0.080(6)	-0.25(2)	3.0	1
O2	0.189(6)	0.24(1)	-0.54(1)	3.0	1
O3	0.262(8)	0.769(9)	-0.555(9)	3.0	1

Figure 4.5 shows Rietveld refinements for 0.825BTFM-0.175CTO using the published orthorhombic structural model for $(Bi_{0.8}Gd_{0.2})FeO_3$ [4]. The space group is $Pna2_1$. The reliability factors based on the weighted profiles, R_{wp}, and Bragg intensities, R_I are 9.03% and 16.70% respectively for the setting *cba*. The black circles indicate the mismatches between the model and data either in terms of peak position and/or shape. The refined parameters are listed in Table 4.4.

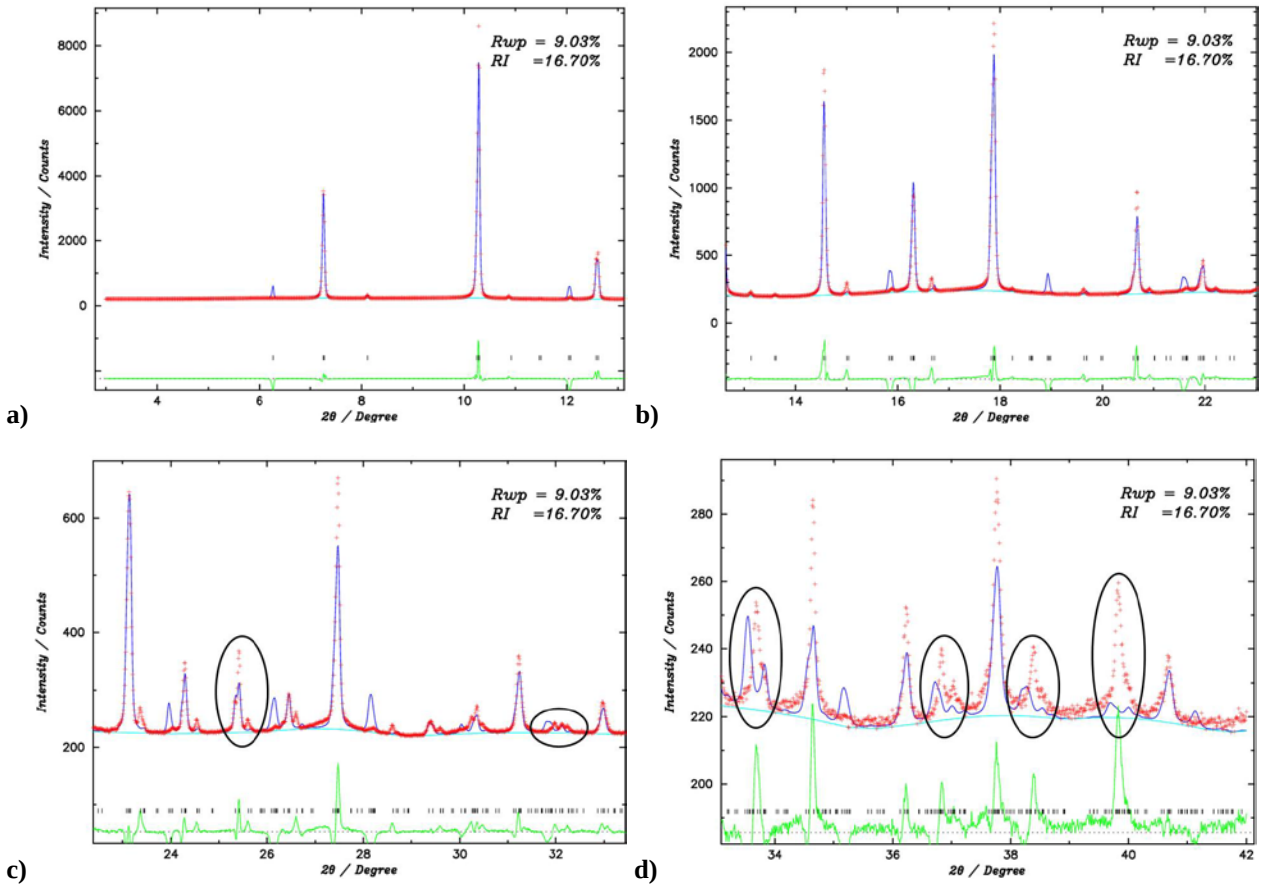

Figure 4.5 a) Rietveld refinement for 0.825BTFM-0.175CTO in $Pna2_1$, setting cba. The black circles indicate the reflections missing in the model and the mismatches between the model and data either in terms of peak position and/or shape. The red crosses represent the observed data while the blue solid line represents the model. The difference green curve is below. The black tics represent positions of Bragg reflections.

Table 4.4: Atomic parameters for 0.825BTFM-0.175CTO from Rietveld refinement in $Pna2_1$, setting cba. Lattice constants: a = 5.5627(3) Å, b = 5.5877(3) Å and c = 7.8641(4) Å.

Atoms	x	y	z	B	Occupancy
Bi/Ca	0.991(1)	0.0255(4)	0.244(7)	3.0	0.825/0.175
Ti/Fe/Mg	0.50(2)	0.015(7)	0	1.0	0.4844/0.2063 /0.3094
O1	0.05(1)	0.501(7)	0.25(4)	3.0	1
O2	0.24(1)	0.150(9)	0.52(1)	3.0	1
O3	0.83(1)	0.22(1)	0.57(1)	3.0	1

Figure 4.6 shows Rietveld refinements for 0.825BTFM-0.175CTO using the published orthorhombic structural model for $CaTiO_3$ [5]. The space group is *Pnma*. The reliability factors based on the weighted profiles, R_{wp}, and Bragg intensities, R_I are 11.06% and 28.61% respectively for the setting *cba*. The black circles indicate the mismatches between the model and data either in terms of position and/or shape. The refined parameters are listed in Table 4.5.

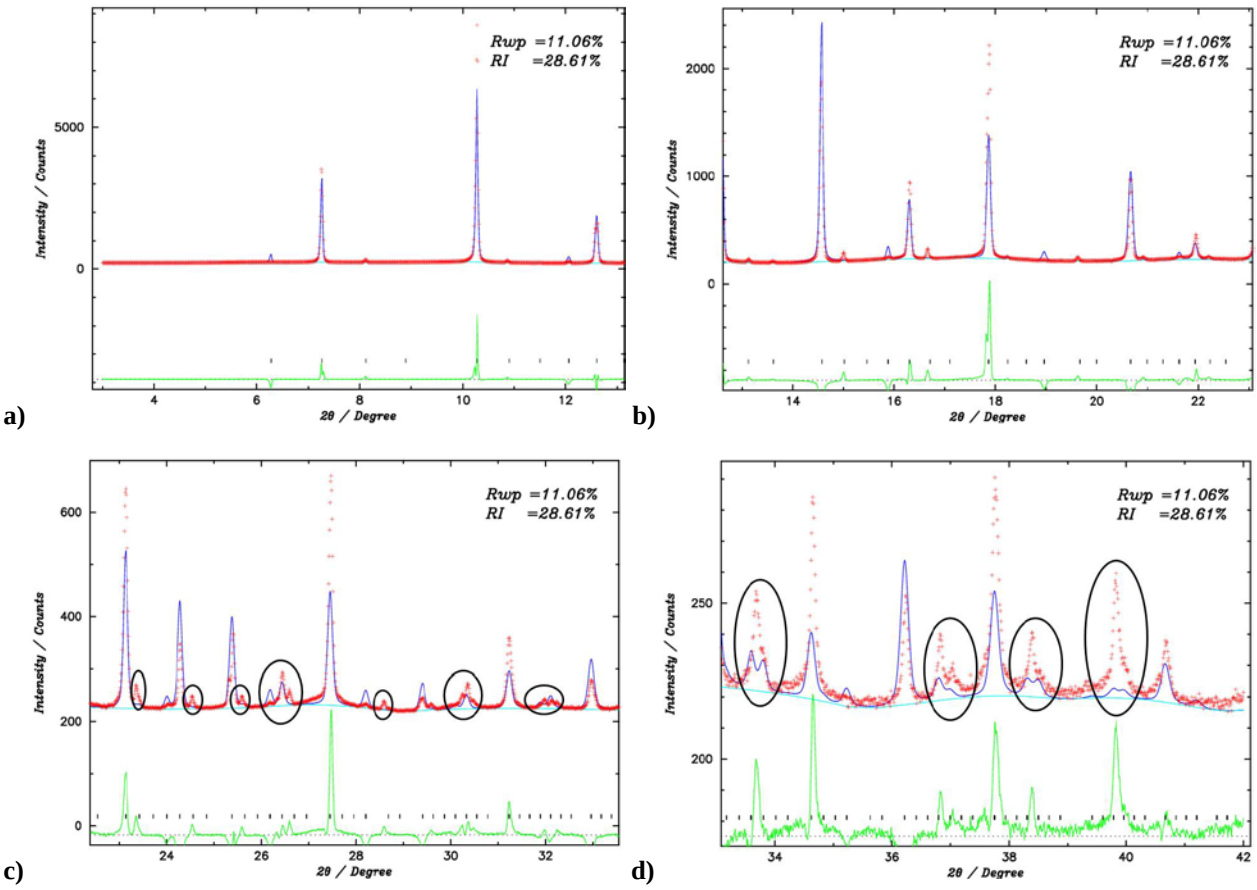

Figure 4.6 a) Rietveld refinement for 0.825BTFM-0.175CTO in Pnma, setting cba. The black circles indicate the reflections missing in the model and the mismatches between the model and data either in terms of peak position and/or shape. The red crosses represent the observed data while the blue solid line represents the model. The difference green curve is below. The black tics represent positions of Bragg reflections.

Table 4.5: Atomic parameters for 0.825BTFM-0.175CTO from Rietveld refinement in Pnma, setting cba. Lattice constants: a = 5.569(1) Å, b = 5.568(1) Å and c = 7.8729(4) Å.

Atoms	x	y	z	B	Occupancy
Bi/Ca	-0.002(2)	0.005(4)	0.25	3.0	0.825/0.175
Ti/Fe/Mg	0	0.5	0	1.0	0.4844/0.2063 /0.3094
O1	0.07140	0.56(2)	0.25	3.0	1
O2	0.603(7)	0.49(7)	0.087(5)	3.0	1

Figure 4.7 shows Rietveld refinements for 0.825BTFM-0.175CTO using the published orthorhombic structural model $CaTiO_3$ [5]. The space group is *Pnma*. The reliability factors based on the weighted profiles, R_{wp}, and Bragg intensities, R_I are 4.61% and 10.36% respectively for the setting *bac*. The black circles indicate the mismatches between the model and data either in terms of position and/or shape. The refined parameters are listed in Table 4.6.

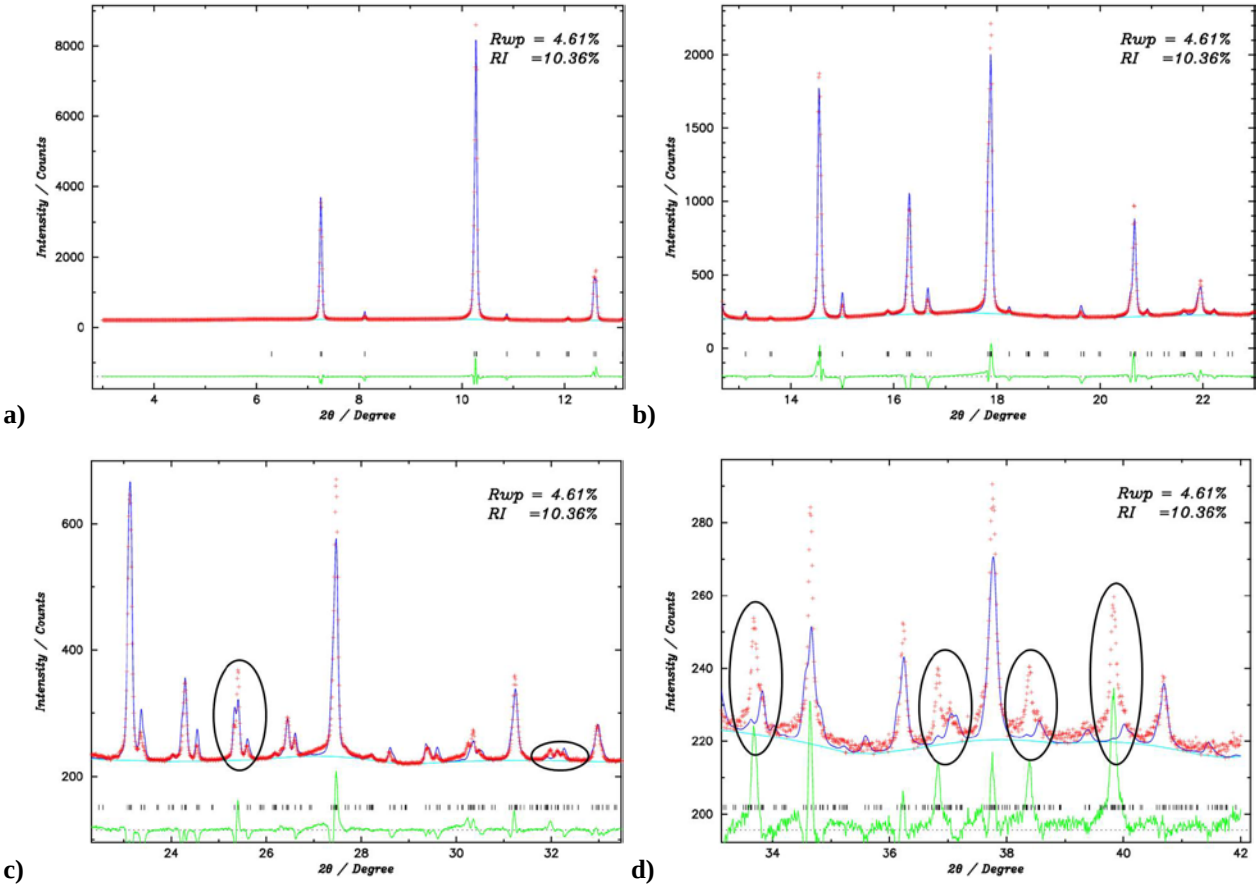

Figure 4.7 a) Rietveld refinement for 0.825BTFM-0.175CTO in Pnma, setting bac. The black circles indicate the reflections missing in the model and the mismatches between the model and data either in terms of peak position and/or shape. The red crosses represent the observed data while the blue solid line represents the model. The difference green curve is below. The black tics represent positions of Bragg reflections.

Table 4.6: Atomic parameters for 0.825BTFM-0.175CTO from Rietveld refinement in Pnma, setting bac. Lattice constants: a = 5.5876(1) Å, b = 7.8636(2) Å and c = 5.5622(1) Å.

Atoms	x	y	z	B	Occupancy
Bi/Ca	0.0243(2)	0.25	-0.0083(5)	3.0	0.825/0.175
Ti/Fe/Mg	0.5	0	0	1.0	0.4844/0.2063 /0.3094
O1	0.493(2)	0.25	0.045(5)	3.0	1
O2	0.26(1)	0.022(5)	0.74(2)	3.0	1

Figure 4.8 shows Rietveld refinements for 0.825BTFM-0.175CTO using the published orthorhombic structural model for $SrTiO_3$ [6]. The space group is *Ima*2. The reliability factors based on the weighted profiles, R_{wp}, and Bragg intensities, R_I are 5.04% and 8.75% respectively. The black circles indicate the mismatches between the model and data either in terms of peak position and/or shape. The refined parameters are listed in Table 4.7.

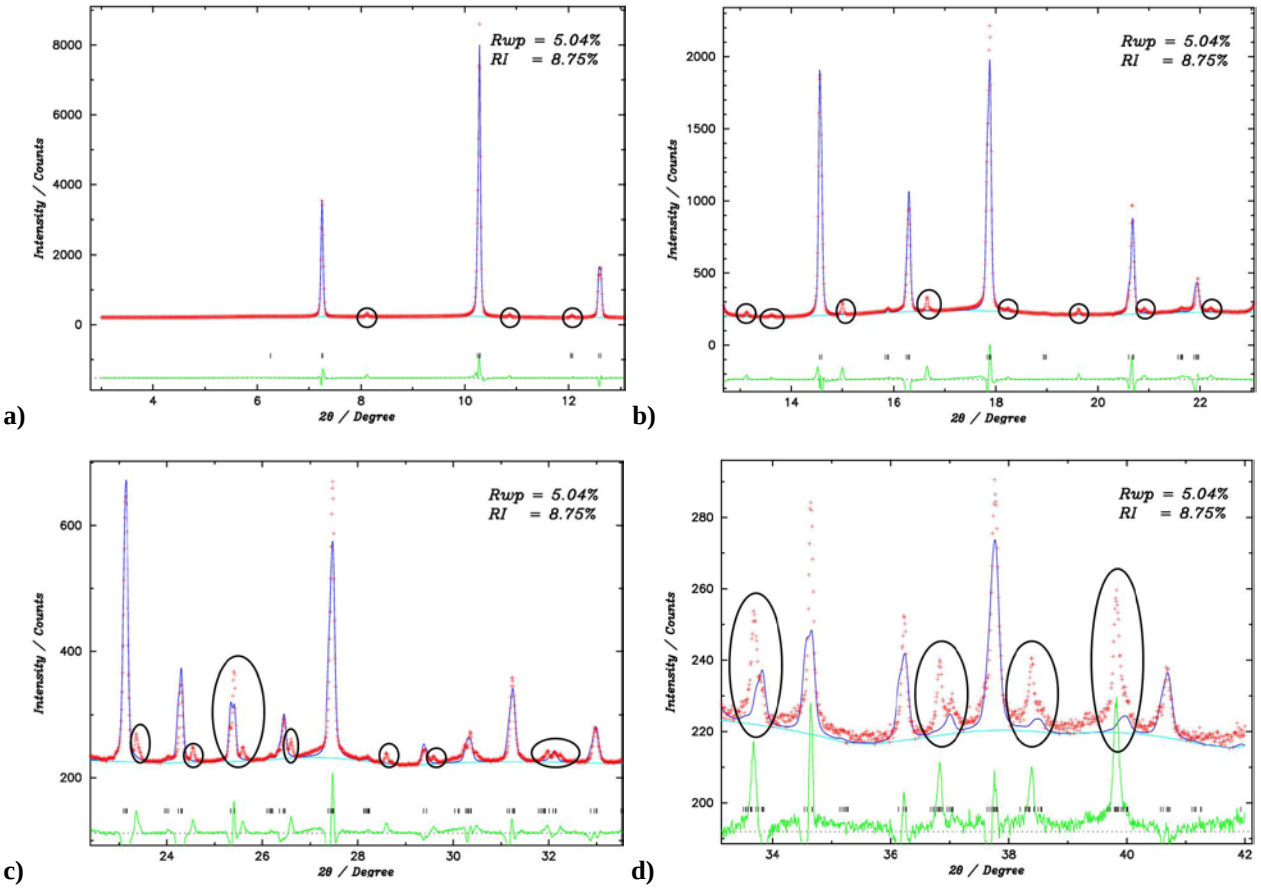

Figure 4.8 a) Rietveld refinement for 0.825BTFM-0.175CTO in Ima2. The black circles indicate the reflections missing in the model and the mismatches between the model and data either in terms of peak position and/or shape. The red crosses represent the observed data while the blue solid line represents the model. The difference green curve is below. The black tics represent positions of Bragg reflections.

Table 4.7: Atomic parameters for 0.825BTFM-0.175CTO from Rietveld refinement in Ima2. Lattice constants: a = 7.8618(2) Å, b = 5.5857(1) Å and c = 5.5606(1) Å.

Atoms	x	y	z	B	Occupancy
Bi/Ca	0.5	0.5	0.25(1)	3.0	0.825/0.175
Ti/Fe/Mg	0.25	0.012(4)	0.25224	1.0	0.4844/0.2063 /0.3094
O1	0.5	0	0.19(1)	3.0	1
O2	0.25	0.22(2)	0.96(3)	3.0	1
O3	0.75	0.19(1)	0.54(3)	3.0	1

Figure 4.9 shows Rietveld refinements for 0.825BTFM-0.175CTO using the published orthorhombic structural model for $NaNbO_3$ [7]. The space group is $Pnm2_1$. The reliability factors based on the weighted profiles, R_{wp}, and Bragg intensities, R_I are 10.74% and 30.02% respectively for the setting *abc*. The black circles indicate the mismatches between the model and data either in terms of peak position and/or shape. The refined parameters are listed in Table 4.8.

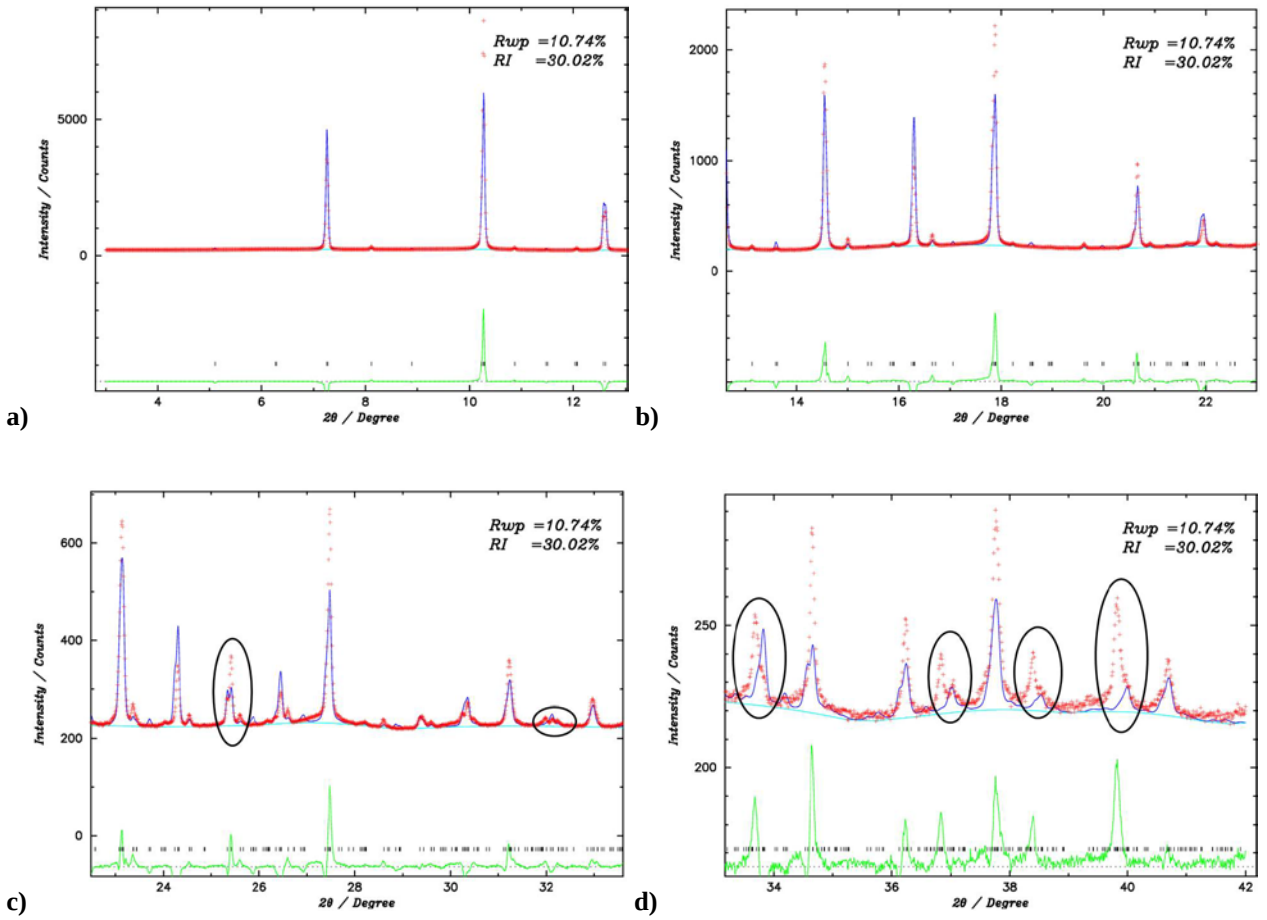

Figure 4.9 a) Rietveld refinement for 0.825BTFM-0.175CTO in Pnm2$_1$, setting abc. The black circles indicate the reflections missing in the model and the mismatches between the model and data either in terms of peak position and/or shape. The red crosses represent the observed data while the blue solid line represents the model. The difference green curve is below. The black tics represent positions of Bragg reflections.

Table 4.8: Atomic parameters for 0.825BTFM-0.175CTO from Rietveld refinement in Pnm2$_1$, setting abc. Lattice constants: a = 7.8647(4) Å, b = 5.5886(3) Å and c = 5.5624(3) Å.

Atoms	x	y	z	B	Occupancy
Bi/Ca	0.5	0.753(1)	0.0015	3.0	0.825/0.175
Ti/Fe/Mg	0	-0.224(1)	-0.00530	1.0	0.4844/0.2063 /0.3094
O1	0.5	0.76(1)	0.54(6)	3.0	1
O2	0	-0.26(2)	-0.58(5)	3.0	1
O3	0.28(2)	0.45(1)	0.27(2)	3.0	1
O4	0.22(2)	-0.02(3)	-0.27(2)	3.0	1

Figure 4.10 shows Rietveld refinements for 0.825BTFM-0.175CTO using the published orthorhombic structural model for $BaTiO_3$ [8]. The space group is *Amm*2. The reliability factors based on the weighted profiles, R_{wp}, and Bragg intensities, R_I are 5.56% and 10.83%, respectively. The black circles indicate the reflections missing in the model and the mismatches between the model and data either in terms of peak position and/or shape. It is observed that this orthorhombic model does not have all the necessary reflections to express the data. The refined parameters are listed in Table 4.9.

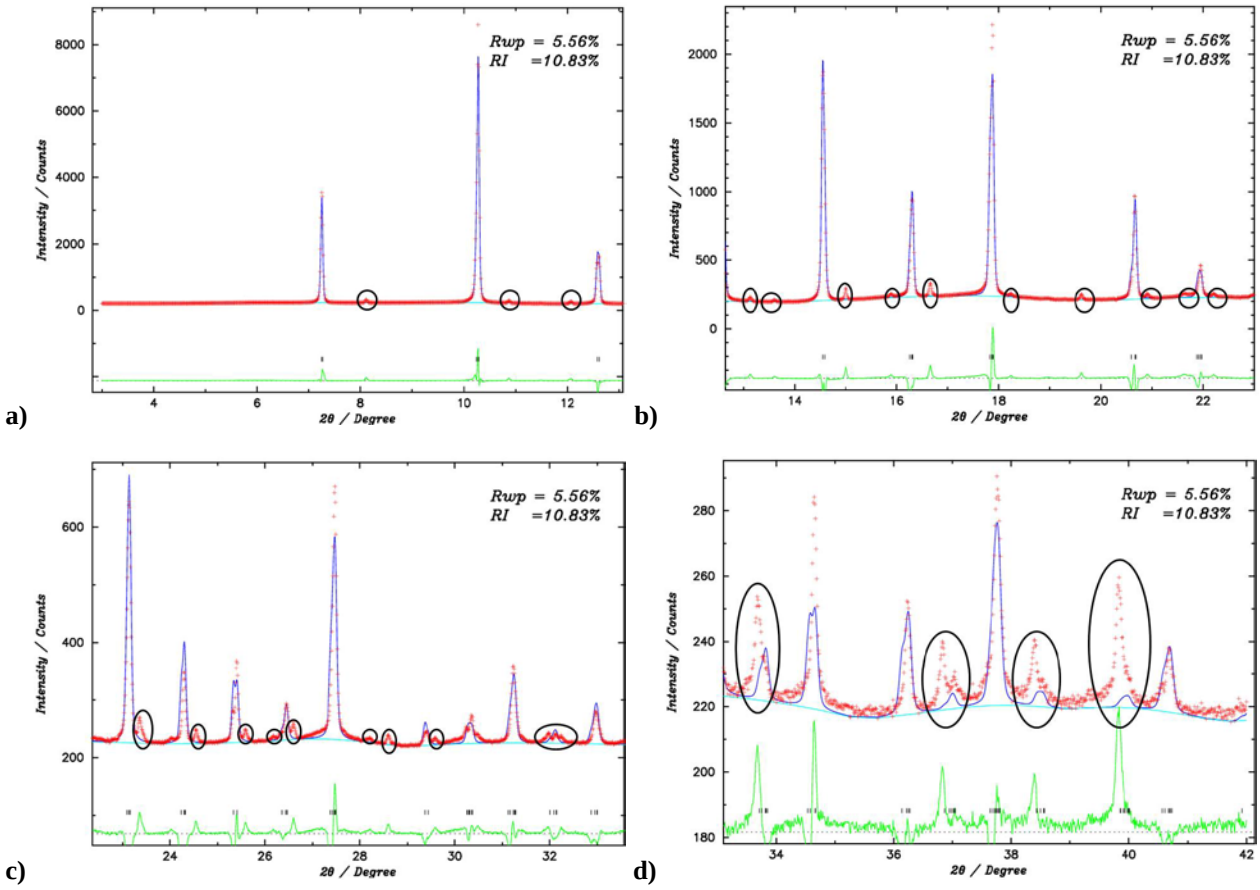

Figure 4.10 a) Rietveld refinement for 0.825BTFM-0.175CTO in Amm2. The black circles indicate the reflections missing in the model and the mismatches between the model and data either in terms of peak position and/or shape. The red crosses represent the observed data while the blue solid line represents the model. The difference green curve is below. The black tics represent positions of Bragg reflections.

Table 4.9: Atomic parameters for 0.825BTFM-0.175CTO from Rietveld refinement in Amm2. Lattice constants: a = 3.9315(1) Å, b = 5.5621(1) Å and c = 5.5868(1) Å .

Atoms	x	y	z	B	Occupancy
Bi/Ca	0	0	0	3.0	0.825/0.175
Ti/Fe/Mg	0.5	0	0.51(2)	1.0	0.4844/0.2063 /0.3094
O1	0	0	0.477(8)	3.0	1
O2	0.5	0.249(6)	0.225(5)	3.0	1

As shown in Figures 4.2-4.10, it was not possible to fit the 0.825BTFM-0.175CTO data using published orthorhombic structural models of similar ABO_3 perovskite compounds. Therefore, *ab initio* structure determination on the present material was carried out.

4.1.3 Space group determination from the reflection conditions

Le Bail analysis for the non-centrosymmetric orthorhombic space groups were performed at -173 °C in the six possible different settings: *abc*, *acb*, *bac*, *bca*, *cba* and *acb*. Just the non-centrosymmetric space groups were analysed. This is because this composition (the same as all the compositions that have an O unit cell) was SHG active so it means it is non-centrosymmetric (NCS). The lattice constants used for the analysis were previously determined by indexing in Section 4.1.1 and were not refined. The reflection conditions of all the non-centrosymmetric orthorhombic space groups in the six different settings were carefully investigated. The space group *P*222 was used as reference of the reflection conditions since it has no reflection conditions. The lattice is primitive. In Appendix B, Tables B1-B6 show the results of the Le Bail fits of all non-centrosymmetric space groups in the six different settings. Le Bail fits with R_{wp} < 2.4% performed for space groups with less than 408 allowed reflections were selected as potential candidates. Thus, *Pmc*2_1 (26) in setting *cba*, *Pmn*2_1 (31) in setting *cba*, *Pma*2 (28) in setting *abc*, *Pna*2_1 (33) in setting *bca*, *Pca*2_1 (29) in setting *bca*, *Pnc*2 (30) in setting *acb*, *Pnn*2 (34) in setting *abc* and *Pba*2 (32) in setting *bca* will be compared. A Le Bail fit for the space group $I2_12_12_1$ (24)

in setting *acb* with a R_{wp} > 2.4% (R_{wp} = 3.8% and number of allowed reflections 217) is shown in Figure 4.11 as evidence of a poor Le Bail fit. In black rectangles are shown reflections allowed in *P*222 but forbidden in $I2_12_12$, setting *acb*. A Le Bail fit for the for the space group $P2_12_12$ (18) in setting *acb* with more than 408 allowed reflections (426 and R_{wp} = 2.13%) is shown in Figure 4.12 as evidence that many of those allowed reflections are not necessary to fit the data.

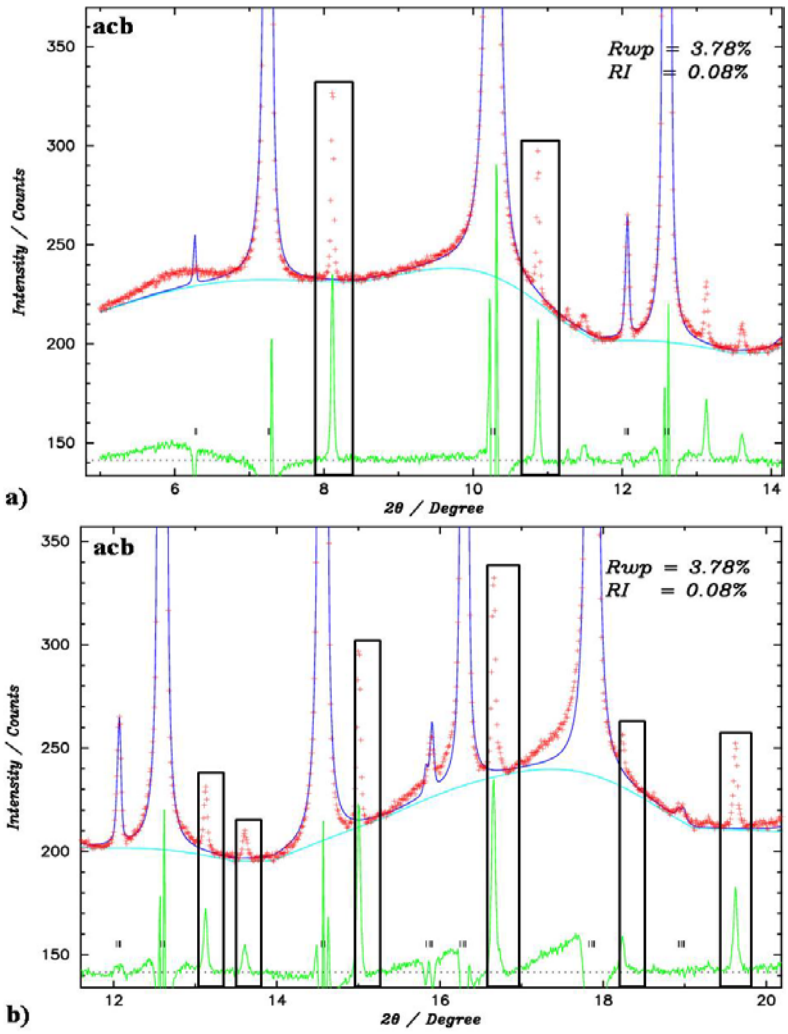

Figure 4.11 Fitting results of Le Bail analysis for 0.825BTFM-0.175CTO in $I2_12_12_1$, setting acb. The black rectangles at ~8°, ~10.9°, ~13.1°, ~13.6°, ~15, ~16.3°, ~18.2° and ~19.7° indicate reflections allowed in P222 but forbidden in $I2_12_12_1$, setting acb. The red crosses represent the observed data while the blue solid line represents the model. The difference green curve is below. The black tics represent positions of Bragg reflections.

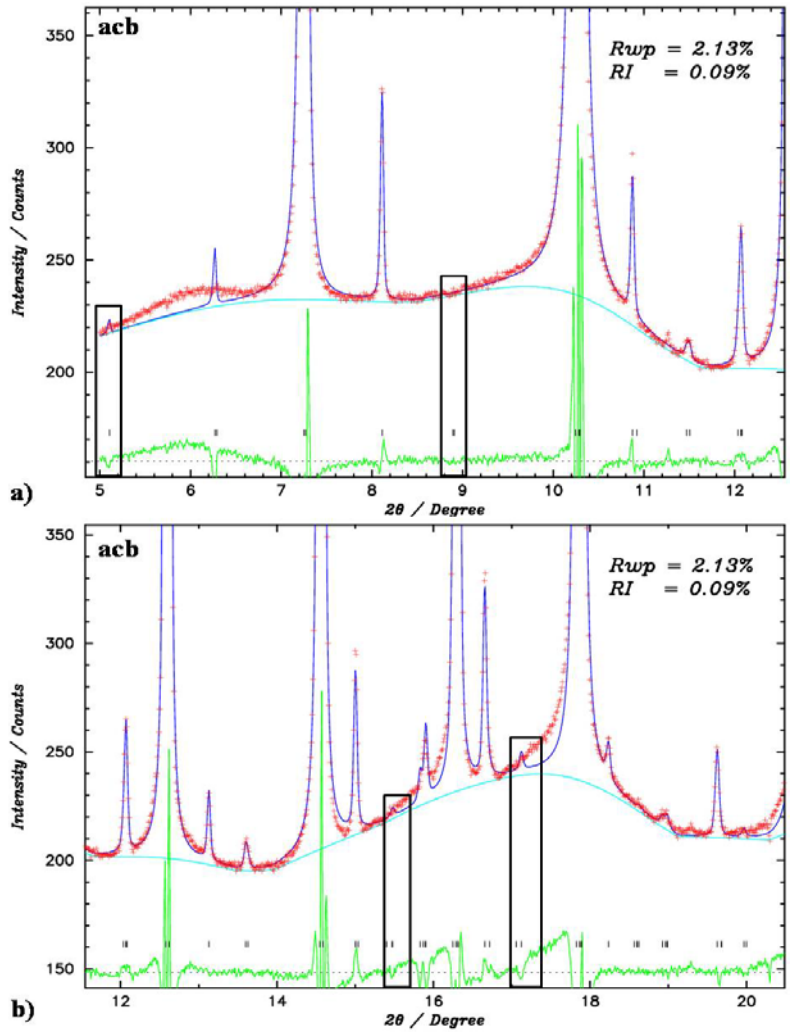

Figure 4.12 Fitting results of Le Bail analysis for 0.825BTFM-0.175CTO in $P2_12_12$, setting acb. The black rectangles at ~5.1°, ~8.9°, ~15.45° and ~17.1° indicate extra reflections not needed to fit the data. The red crosses represent the observed data while the blue solid line represents the model. The difference green curve is below. The black tics represent positions of Bragg reflections.

Table 4.10 Comparison of the 8 (NCS) orthorhombic potential space groups candidates.

Space group	Setting	R_{wp} (%)	Figure number	Number of reflections
Pmc2_1 (26)	*cba*	2.14	4.13	401
Pmn2_1 (31)	*cba*	2.14	4.14	397
*Pma*2 (28)	*abc*	2.14	4.15	401
Pna2_1 (33)	*bca*	2.15	4.16	361
Pca2_1 (29)	*bca*	2.15	4.17	365
*Pnc*2 (30)	*acb*	2.15	4.18	376
*Pnn*2 (34)	*abc*	2.16	4.19	375
*Pba*2 (32)	*bca*	2.17	4.20	362

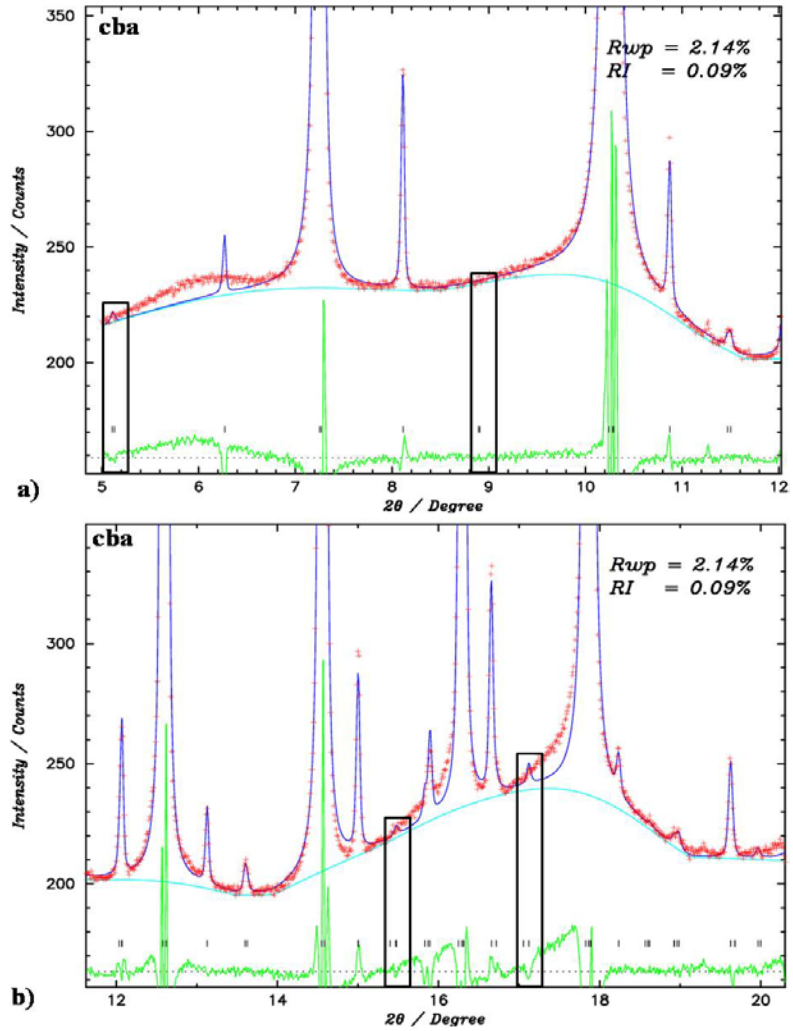

Figure 4.13 Fitting results of Le Bail analysis for 0.825BTFM-0.175CTO in $Pmc2_1$, setting cba. The black rectangles at ~5.1°, ~8.9°, ~15.45° and ~17.1° show extra reflections not needed to fit the data. The red crosses represent the observed data while the blue solid line represents the model. The difference green curve is below. The black tics represent positions of Bragg reflections.

Figure 4.13 a) and b) show fitting results of Le Bail analysis for 0.825BTFM-0.175CTO in *Pmc*2_1, setting *cba*. The black rectangles at ~5.1°, ~8.9°, ~15.45° and ~17.1° show extra reflections not needed to fit the data.

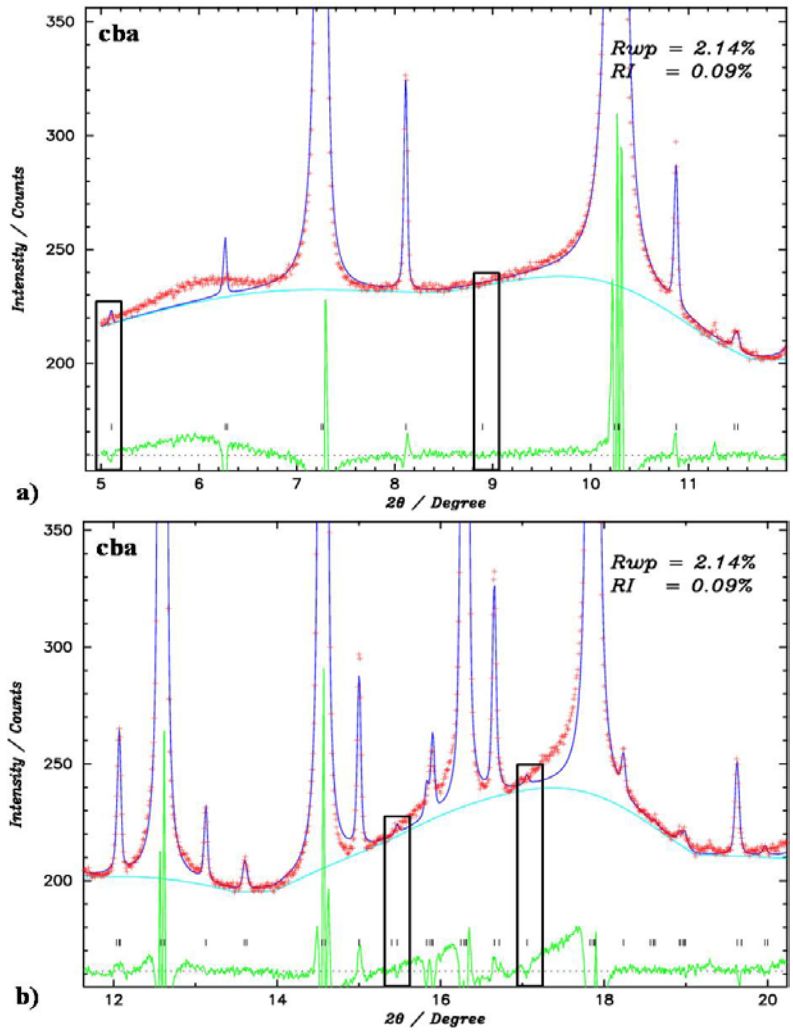

Figure 4.14 Fitting results of Le Bail analysis for 0.825BTFM-0.175CTO in $Pmn2_1$, setting cba. The black rectangles at ~5.1°, ~8.9°, ~15.45° and ~17.1° show extra reflections not needed to fit the data. The red crosses represent the observed data while the blue solid line represents the model. The difference green curve is below. The black tics represent positions of Bragg reflections.

Figure 4.14 a) and b) show fitting results of Le Bail analysis for 0.825BTFM-0.175CTO in $Pmn2_1$, setting *cba*. The black rectangles at ~5.1°, ~~8.9°, ~15.45° and ~17.1° show extra reflections not needed to fit the data.

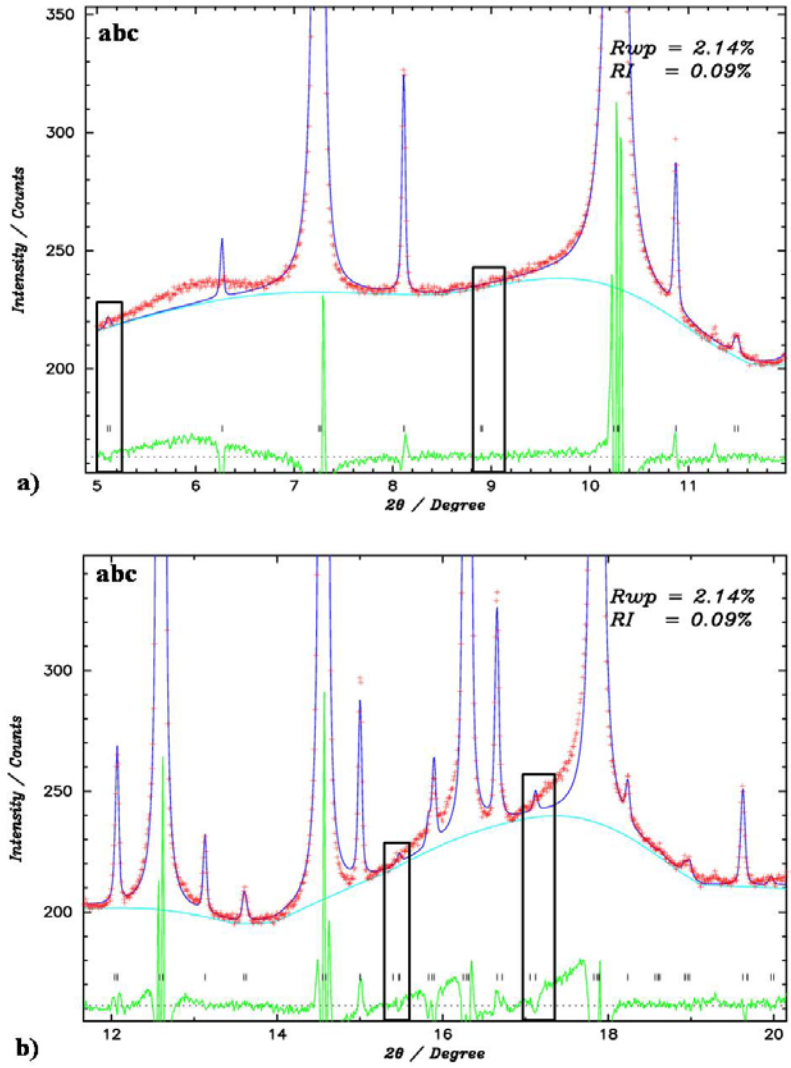

Figure 4.15 Fitting results of Le Bail analysis for 0.825BTFM-0.175CTO in Pma2, setting abc. The black rectangles at ~5.1°, ~8.9°, ~15.45° and ~17.1° show extra reflections not needed to fit the data. The red crosses represent the observed data while the blue solid line represents the model. The difference green curve is below. The black tics represent positions of Bragg reflections.

Figure 4.15 a) and b) show fitting results of Le Bail analysis for 0.825BTFM-0.175CTO in *Pma*2, setting *abc*. The black rectangles at ~5.1°, ~8.9°, ~15.45° and ~17.1° show extra reflections not needed to fit the data.

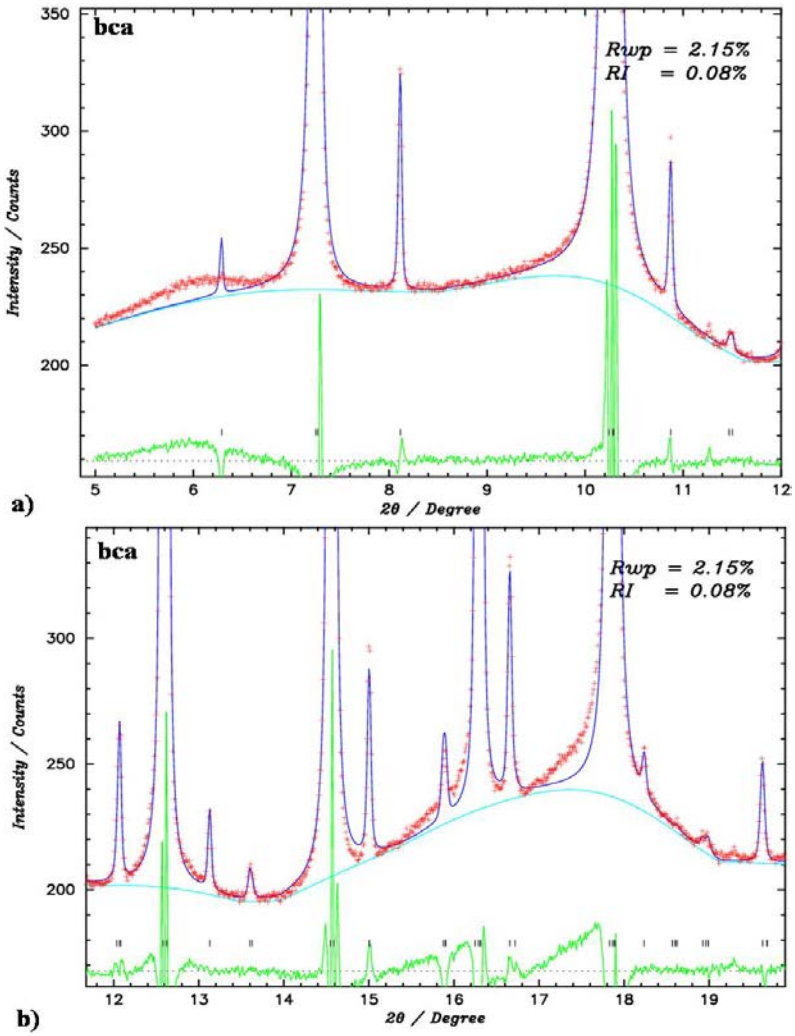

Figure 4.16 Fitting results of Le Bail analysis for 0.825BTFM-0.175CTO in $Pna2_1$, setting bca. The red crosses represent the observed data while the blue solid line represents the model. The difference green curve is below. The black tics represent positions of Bragg reflections.

Figure 4.16 a) and b) show fitting results of Le Bail analysis for 0.825BTFM-0.175CTO in *$Pna2_1$*, setting *bca*. It is observed that there are no extra reflections not needed to fit the data at ~5.1°, ~6.3°, ~8.9°, ~10.9°, ~15.45° and ~17.1° like occur in other space groups and all the reflections appear.

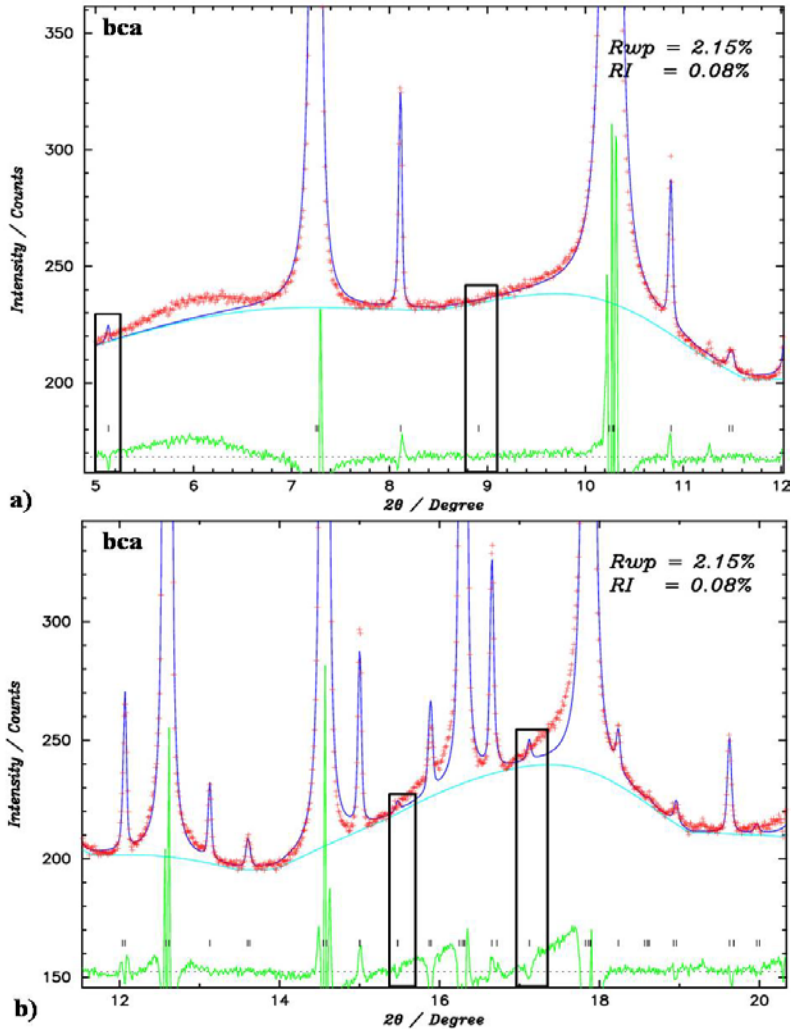

Figure 4.17 Fitting results of Le Bail analysis for 0.825BTFM-0.175CTO in $Pca2_1$, setting bca. The black rectangles at ~5.1, ~8.9°, ~15.45° and ~17.1° show some extra reflections not needed to fit the data. The red crosses represent the observed data while the blue solid line represents the model. The difference green curve is below. The black tics represent positions of Bragg reflections.

Figure 4.17 a) and b) show fitting results of Le Bail analysis for 0.825BTFM-0.175CTO in $Pca2_1$, setting *bca*. The black rectangles at ~5.1, ~8.9°, ~15.45° and ~17.1° show some extra reflections not needed to fit the data.

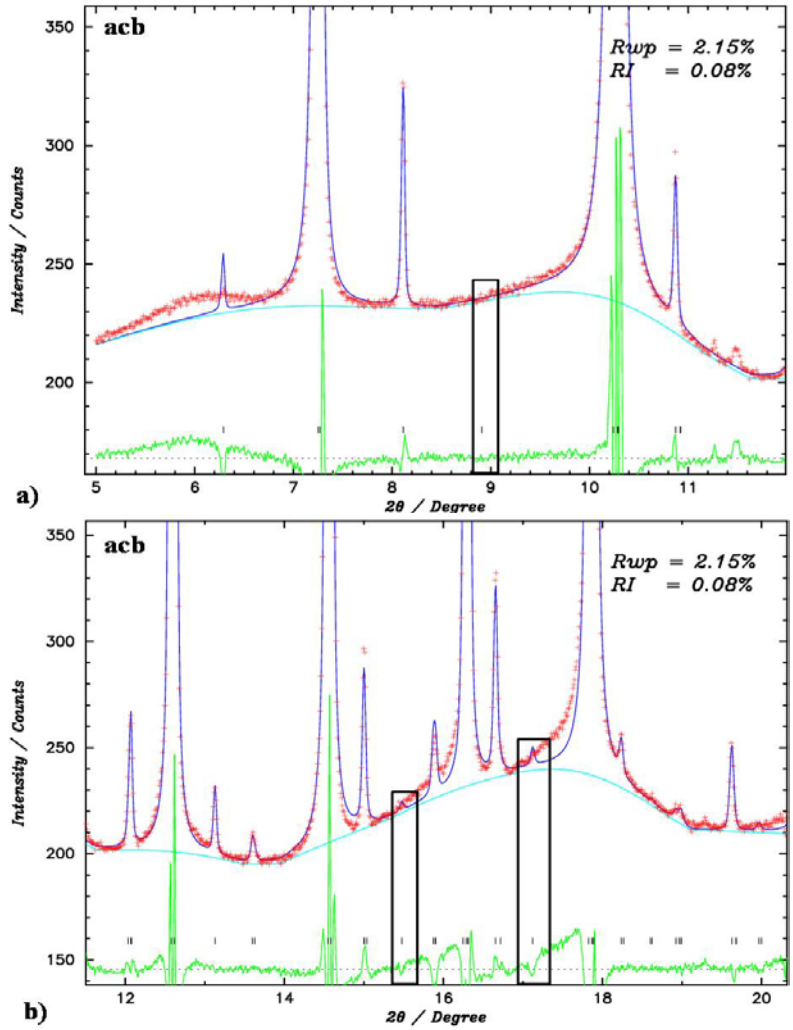

Figure 4.18 Fitting results of Le Bail analysis for 0.825BTFM-0.175CTO in Pnc2, setting acb. The black rectangles at ~8.9°, ~15.45° and ~17.1° show some extra reflections not needed to fit the data. The red crosses represent the observed data while the blue solid line represents the model. The difference green curve is below. The black tics represent positions of Bragg reflections.

Figure 4.18 a) and b) show fitting results of Le Bail analysis for 0.825BTFM-0.175CTO in $Pca2_1$, setting *bca*. The black rectangles at ~8.9°, ~15.45° and ~17.1° show some extra reflections not needed to fit the data.

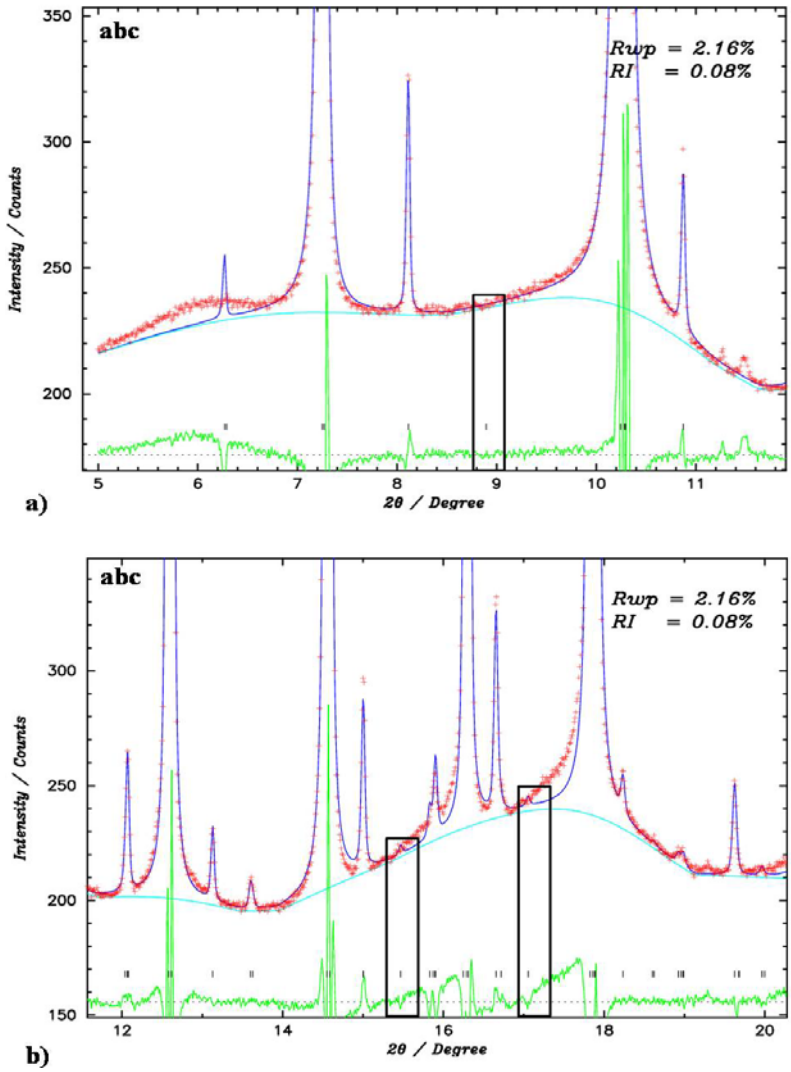

Figure 4.19 Fitting results of Le Bail analysis for 0.825BTFM-0.175CTO in Pnn2, setting abc. The black rectangles at ~6.3°,~8.9°,~12.1°, ~15.45° and ~17.1° show some extra reflections not needed to fit the data. The red crosses represent the observed data while the blue solid line represents the model. The difference green curve is below. The black tics represent positions of Bragg reflections.

Figure 4.19 a) and b) show fitting results of Le Bail analysis for 0.825BTFM-0.175CTO in $Pca2_1$, setting *bca*. The black rectangles at ~6.3°, ~8.9°, ~12.1°, ~15.45° and ~17.1° show some extra reflections not needed to fit the data.

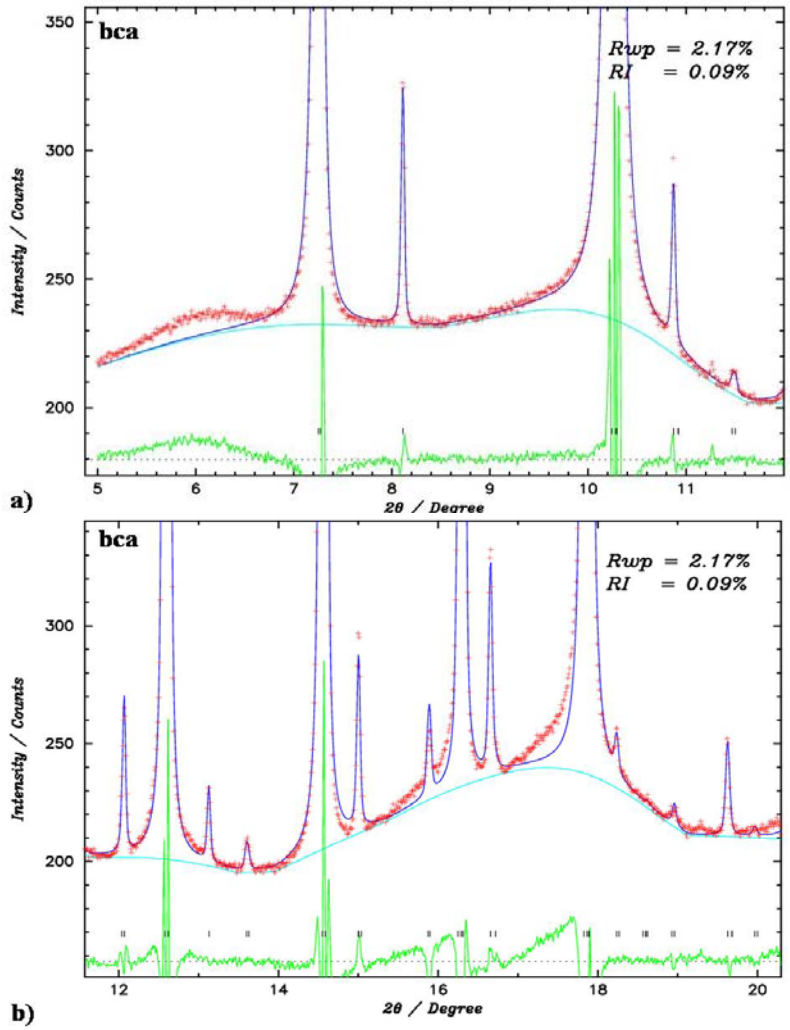

Figure 4.20 Fitting results of Le Bail analysis for 0.825BTFM-0.175CTO in Pba2, setting bca. The red crosses represent the observed data while the blue solid line represents the model. The difference green curve is below. The black tics represent positions of Bragg reflections.

Figure 4.20 a) and b) show fitting results of Le Bail analysis for 0.825BTFM-0.175CTO in *Pba2*, setting *bca*.

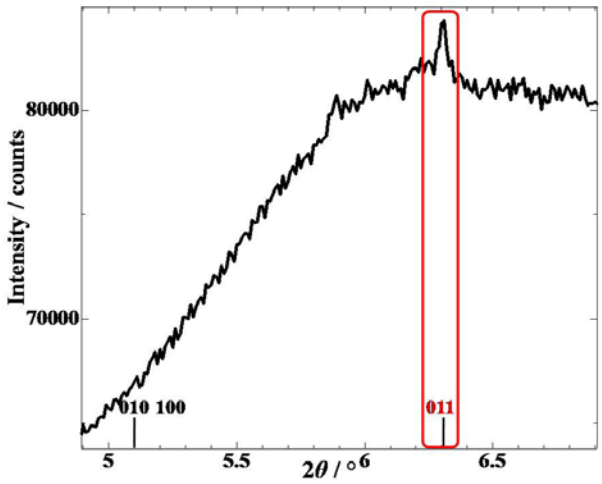

Figure 4.21 Synchrotron X-ray diffraction pattern for 0.825BTFM-0.175CTO at 27 °C. λ = 0.5002527(9) Å at the 2θ range from 4.9° to 6.9°. The red rectangle shows that the only reflection observed at low angle region at ~6.3° can be indexed in the (011) reflection.

Figure 4.21 shows the 2θ range from 4.9° to 6.9° for high counting statistics synchrotron data for 0.825BTFM-0.175CTO. At ~5.1°, there is a black tic showing the position of the (010) and (100) reflections in black colour. At ~ 6.3°, there is a black tic showing the position of the (011) reflection in red colour. It is observed in the raw data that there is a peak at ~6.3°. The red rectangle shows that this peak indexes in the (011) reflection.

In Figure 4.13 a) it is observed that for the space group *Pmc*2_1 in the setting *cba* the reflections (010) and (100) appear at ~5.1°. In Figure 4.14 a) it is observed that for *Pmn*2_1 in the setting *cba* the reflection (010) appear at ~5.1°. In Figure 4.15 a) it is observed that for *Pma*2 in the setting *abc* the reflections (010) and (100) appear at ~5.1°. In Figure 4.17 a) it is observed that for the space group *Pca*2_1 in the setting *bca* the reflection (010) appears at ~5.1°. Therefore, these four space groups (*Pmc*2_1, setting *cba*; *Pmn*2_1, setting *cba; Pma*2, setting *abc* and *Pca*2_1, setting *bca*) were discarded. Also as marked in black rectangles in Figures 4.13, Figure 4.14, Figure 4.15 and Figure 4.17 they have reflections not needed to fit the data. In Figure 4.20 a) it is observed that for the space group *Pba*2 in the setting *bca* there are not reflections at low angle region so it was discarded. If the three space groups left are compared (*Pna*2_1, setting *bca* (Figure 4.16 a);

*Pnc*2, setting *acb* (Figure 4.18 a) and *Pnn*2, setting *abc* (Figure 4.19 a)) it is observed that they have the (011) reflection al low angle region at ~ 6.3°. However, *Pnc*2, setting *acb* and *Pnn*2, setting *abc* have reflections not needed to fit the data as the black rectangles indicate in Figures 4.18 a- b) and Figure 4.19 a- b) respectively. Just the space group $Pna2_1$, setting *bca* does not have extra reflections not needed to fit the data as Figures 4.16 a- b) show. Therefore, the space group for 0.825BTFM-0.175CTO is $Pna2_1$ in the setting *bca.* Although, we need to take into account that some of these extra reflections could have zero intensity by coincidence *i.e.* if the structure factor is zero for these hkls. This assignment of the space group of O phase has been corroborated by CBED analysis in Section 4.1.6.2.

4.1.4 The construction of the structural model

4.1.4.1 Rietveld analysis of the initial structural model

A structural analysis using a combination of the maximum entrophy method (MEM) [9] and Rietveld refinement was carried out.

Rietveld analysis was performed using synchrotron data at -173 °C on 0.825BTFM-0.175CTO, in $Pna2_1$, setting *bca*. The 2θ range of analysis was from 3° to 74°. The lattice parameters obtained from the indexing were used as the initial values. The initial values for the isotropic displacement factor, B, are: for the A-site, B = 1.0, for the B-site, B = 1.0 and for the O, B = 1.0. The scale factor, peak shape parameters and atomic positions were refined. The initial atomic positions taken are shown in Table 4.11.

Table 4.11: Initial atomic positions taken to perform the Rietveld analysis.

Atoms	x	y	z
Bi/Ca	0.5	0.5	0.5
Ti/Fe/Mg	0.5	0	0.75
O1	0.5	0	0.5
O2	0.25	0.25	0.25
O3	0.25	0.75	0.25

Figures 4.22, 4.24, 4.26, 4.28, 4.30, 4.32, 4.34, 4.36 and 4.38 show Rietveld refinements for 0.825BTFM-0.175CTO. For each figure, eight different 2θ ranges are shown: a) from ~6° to ~12.4°, b) from ~12.2° to ~17°, c) from ~17.2° to ~23.8°, d) from ~23.8° to ~30° ,e) from ~28.8° to ~35.4°, f) from ~35.8° to ~42°, g) from ~41.8° to ~46.8° and h) from ~46° to ~50°. The red crosses represent the observed data while the blue solid line represents the model. The difference green curve is below. The black tics represent positions of Bragg reflections.

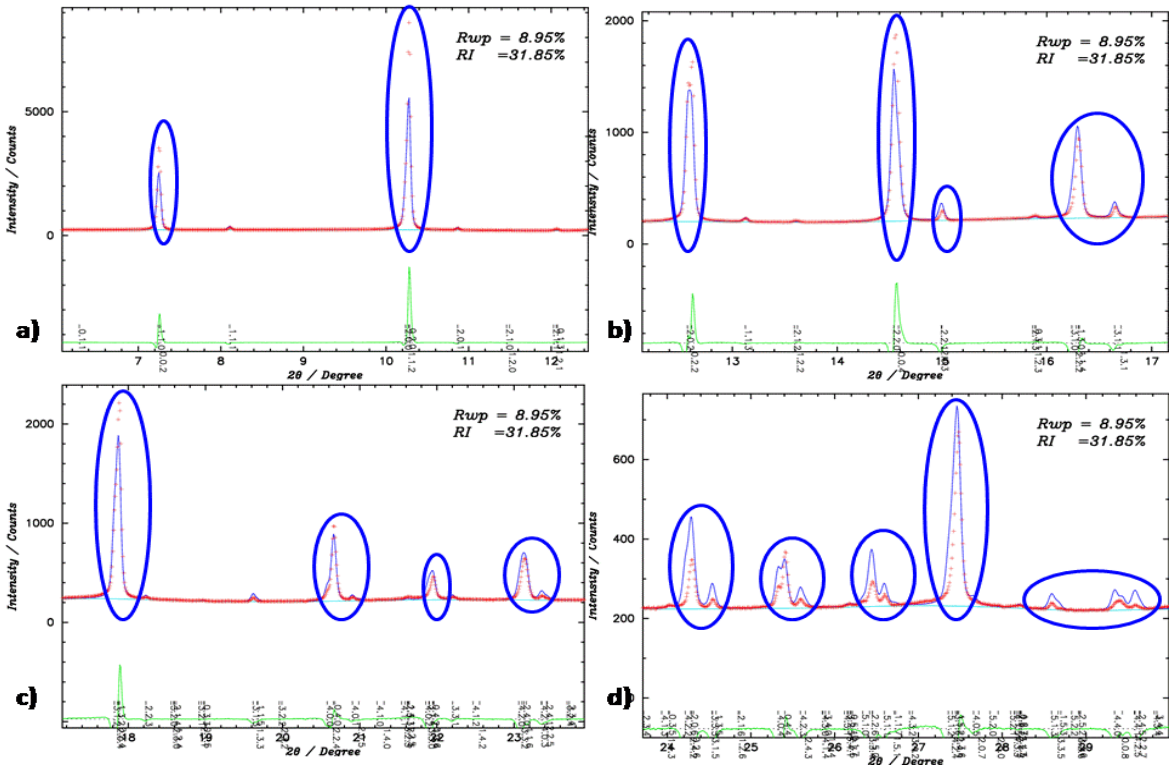

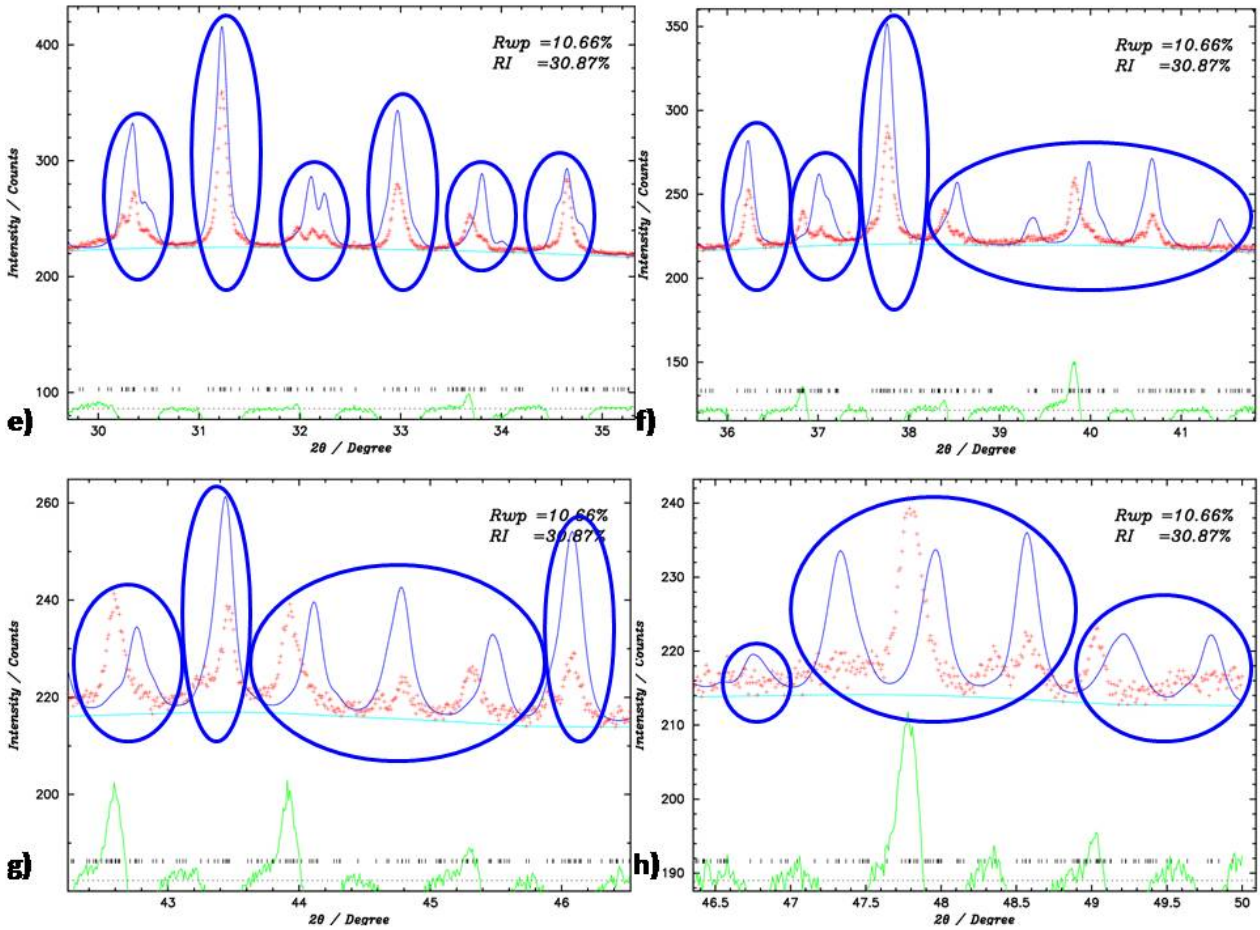

Figure 4.22 Rietveld refinement for 0.825BTFM-0.175CTO in $Pna2_1$, setting bca. The blue circles indicate the mismatches between the model and data in terms of peak position and/or shape and intensity.. The red crosses represent the observed data while the blue solid line represents the model. The difference green curve is below. The black tics represent positions of Bragg reflections.

Figure 4.22 shows the Rietveld refinement for 0.825BTFM-0.175CTO in $Pna2_1$, setting *bca*. The reliability factors based on the weighted profiles, R_{wp}, and Bragg intensities, R_I are 10.66% and 30.87%, respectively. The blue circles indicate the mismatches between the model and data in terms of peak position and/or shape and intensity. The refined parameters are listed in Table 4.12. As it is observed in Figures 4.22 a–c) the model fits the data quite well until ~25° but as Figures 4.22 d–h) show the model offers a poor fit over ~25°.

Table 4.12: Atomic parameters for 0.825BTFM-0.175CTO from Rietveld refinement in $Pna2_1$, setting bca.

Atoms	x	y	z	B	Occupancy
Bi/Ca	0.4778(5)	0.495	0.5	1.0	0.825/0.175
Ti/Fe/Mg	0.50(3)	0.005	0.75 (2)	1.0	0.4844/0.2063 /0.3094
O1	0.503(4)	0.005	0.51(2)	1.0	1
O2	0.294(9)	0.245	0.161(6	1.0	1
O3	0.23(1)	0.745	0.223(7)	1.0	1

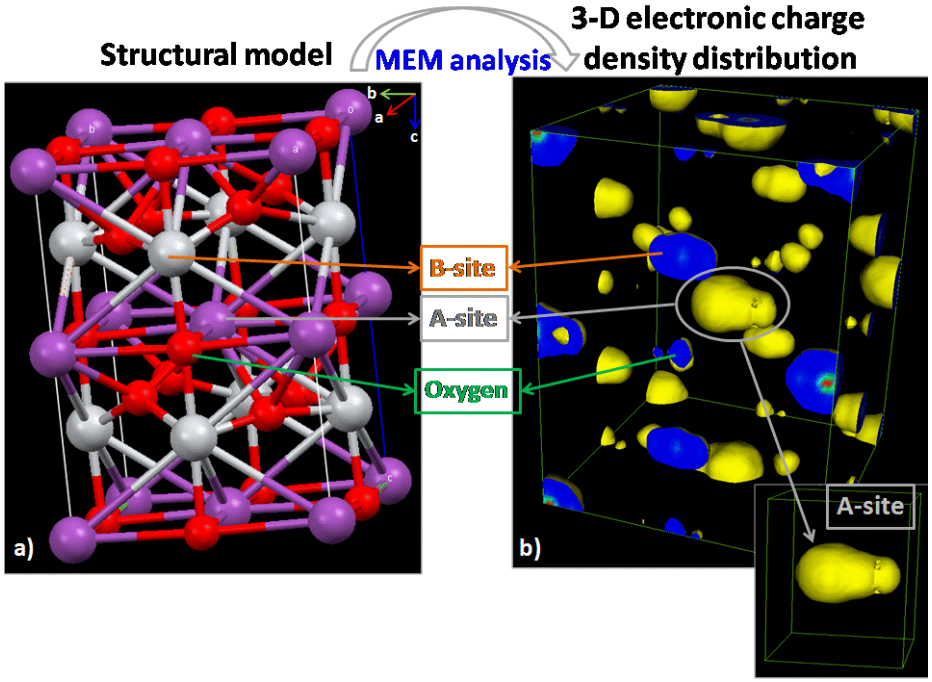

Figure 4.23 a) Structural model, A-site cations are represented in purple, B-site cations in grey and oxygen atoms in red. b) 3-D electronic charge density distribution for 0.825BTFM-0.175CTO. The orange, grey and green arrows indicate the location of the B-site, A-site and oxygens respectively at the structural model and the 3 dimensional electronic charge density distribution. The grey circle shows the A-site, the inset at the right bottom shows an enlargement of it.

Figure 4.23 a) shows the structural model for 0.825BTFM-0.175CTO after the refinement in $Pna2_1$, setting *bca*. A-site cations are represented in purple, B-site cations in grey and oxygen atoms in red. Figure 4.23 b) shows the 3 dimensional electronic charge density distribution for 0.825BTFM-0.175CTO. The orange, grey and green arrows indicate the location of the B-site, A-site and oxygens respectively at the structural model and the 3 dimensional electronic charge

density distribution. The grey circle shows the A-site, the inset at the right bottom shows an enlargement of it. It is observed that the A-site is clearly expanded so the analysis was firstly performed using anisotropic atomic displacement.

4.1.4.2 Rietveld analysis using anisotropic atomic displacement for the A-site

Rietveld analysis was performed using synchrotron data at -173 °C on 0.825BTFM-0.175CTO, in *Pna*2_1, setting *bca*. Anisotropic atomic displacement was used just for the A-site. Two data sets were used for the analysis: normal and high counting statistics data. The 2θ range of analysis for the normal counting statistics data was from 3° to 50° and for the high counting statistics data was from 21.3° to 70°. The lattice parameters obtained from the indexing were used as the initial values. Six parameters are used to describe anisotropic atomic displacement, U_{11}, U_{22}, U_{33}, U_{12}, U_{23} and U_{13}. The initial values used were as follows: U_{11} = 0.1, U_{22} = 0.1, U_{33} = 0.1, U_{12} = 0, U_{23} = 0 and U_{13} = 0. The scale factor, atomic positions and anisotropic displacement parameters for the A-site were refined. Bond-distance and bond-angle restraints were applied between the B-site and the oxygen in order to keep a reasonable structure during the process of refinement.

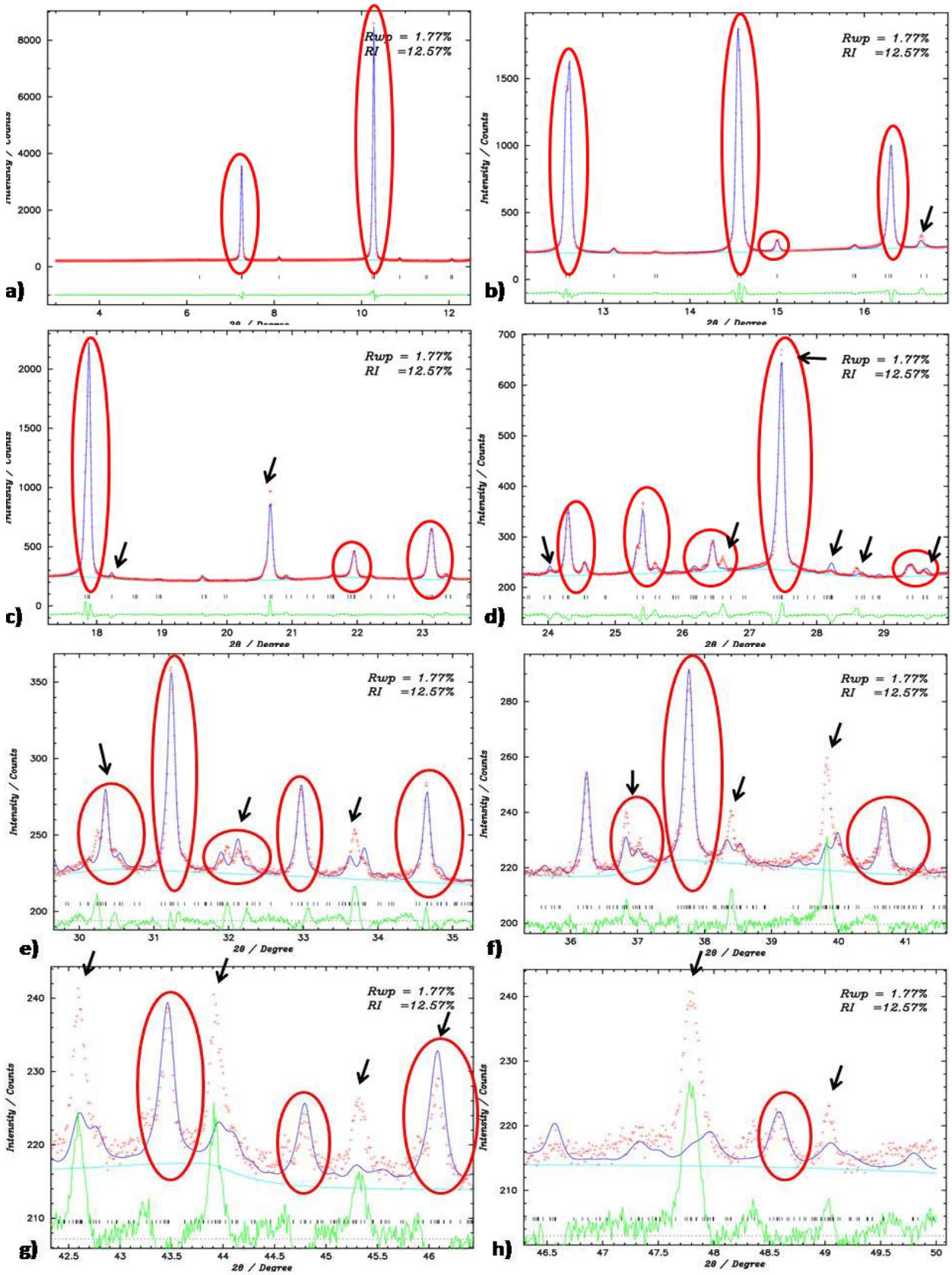

Figure 4.24 Rietveld refinement for 0.825BTFM-0.175CTO in $Pna2_1$, setting bca using anisotropic atomic displacement. The red circles indicate the peaks that improve the fitting in comparison with the Rietveld refinement using isotropic atomic displacement, Figure 4.22. The black arrows indicate the mismatches between the model and data in terms of peak position and/or shape and intensity. The red crosses represent the observed data while the blue solid line represents the model. The difference green curve is below. The black tics represent positions of Bragg reflections.

Figure 4.24 shows the Rietveld refinement for 0.825BTFM-0.175CTO in *Pna*2_1, setting *bca* using anisotropic atomic displacement. The reliability factors based on the weighted profiles, R_{wp}, and Bragg intensities, R_I are 1.77% and 12.57%, respectively. The red circles indicate the peaks that improve the fitting in comparison with the Rietveld refinement using isotropic atomic displacement, Figure 4.22. The black arrows indicate the mismatches between the model and data in terms of peak position and/or shape and intensity. In Table 4.13 and Table 4.14 are listed the refined parameters. B-site cations and oxygens were treated as isotropic atomic displacement model.

Table 4.13: Atomic parameters for 0.825BTFM-0.175CTO from Rietveld refinement in Pna2_1, setting bca considering anisotropic atomic displacement. The column one shows the different atoms; in columns two, three and four the atomic coordinates of each atom being x, y and z respectively; in column five the isotropic displacement parameters, B, and in column six the occupancy of each atom.

Atoms	x	y	z	B	Occupancy
Bi/Ca	0.481(2)	0.5017(6)	0.5050(3)	-	0.825/0.175
Ti/Fe/Mg	-0.508(2)	0.001(1)	0.7685	0.19286	0.4844/0.2063 /0.3094
O1	0.497(2)	0.098(2)	0.5107(9)	2.5(2)	1
O2	0.244(3)	0.263(2)	0.216(2)	2.5(2)	1
O3	0.223(3)	0.766(2)	0.231(3)	2.5(2)	1

Table 4.14: Anisotropic atomic displacement parameters for 0.825BTFM-0.175CTO from Rietveld refinement in Pna2_1, setting bca for the A-site. The column one shows the different atoms of the A-site and in the columns from two to six the six different anisotropic atomic displacement parameters for each atom.

Atoms	U_{11}	U_{22}	U_{33}	U_{12}	U_{23}	U_{12}
Bi/Ca	0.1149(9)	0.0275(5)	0.0349(6)	-0.017(1)	0.0214(4)	0.023(1)

As shown in Figure 4.24, the Rietveld refinement for the 0.825BTFM-0.175CTO using anisotropic atomic displacement for the A-site does not lead to a satisfactory fit. Therefore, we investigated the electronic charge density distribution of the A-site in detail using the MEM method.

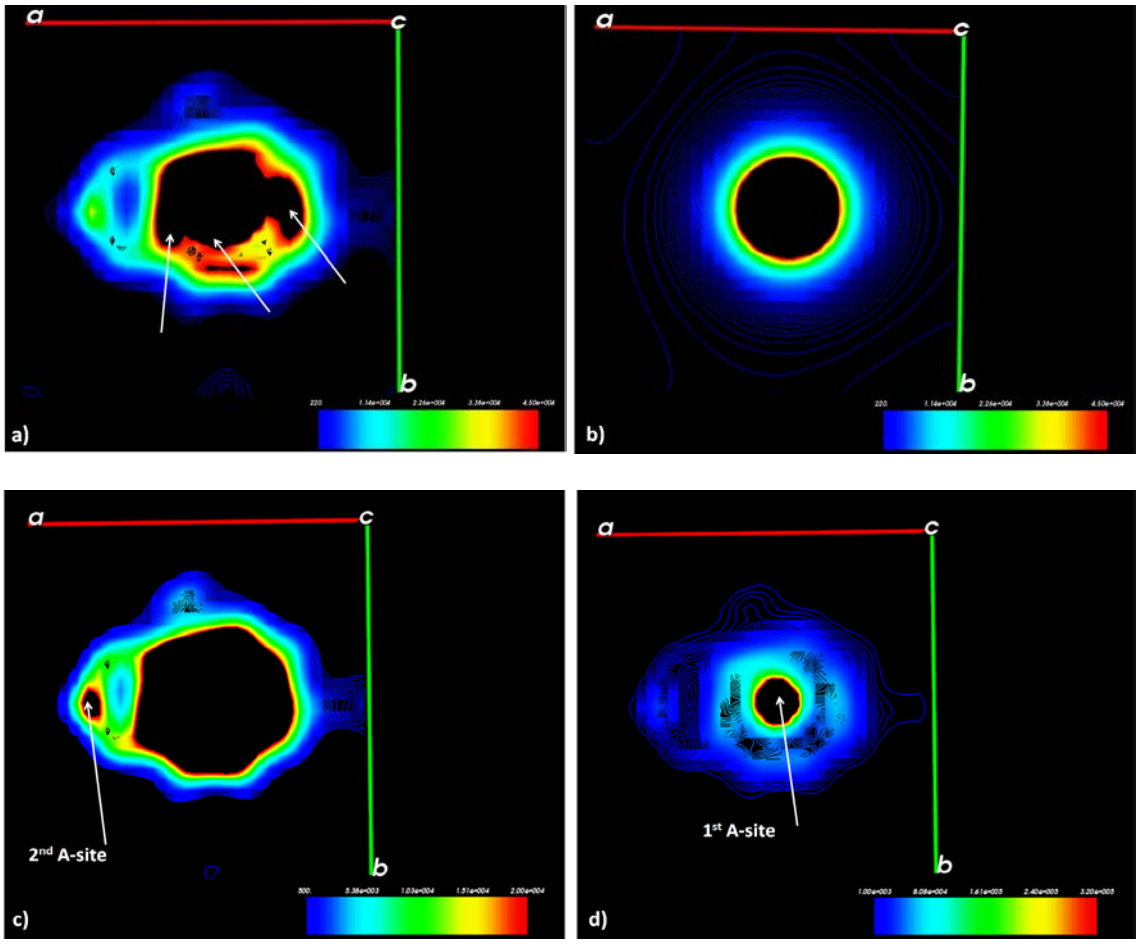

Figure 4.25 Charge density distribution maps of the A-site for the (002) plane. The crystallographic axis are marked in red for a and in green for b. The bars at the right bottom of the pictures show the charge density, the units are me/Å^3. The values of charge density increase from blue to red. a) observed charge density map of the A-site. The white arrows indicate the location of several possible atoms. b) simulated charge density map of the A-site. c) observed charge density map of the A-site. The white arrow indicates the location of the second atom. d) simulated charge density map of the A-site. The white arrow indicates the location of the first atom.

Figure 4.25 a), c) and d) show the observed charge density map of the A-site for the (002) plane while Figure 4.25 b) shows the simulated charge density map of the A-site for the (002) plane. The crystallographic axis are marked in red for *a* and in green for *b*. The bars at the right bottom of the pictures show the charge density, the units are milielectron/Å^3. The values of

charge density increase from blue to red. The maxima of electronic charge density, black area inside the red circle, tell us the location of the atoms. Figure 4.25 a) shows that several possible atoms are located on the map as indicated by the white arrows. In Figure 4.25 b) it is observed that the shape of the simulated charge density distribution of the A-site is very different from the observed charge density distribution in Figure 4.25 a). Figure 4.25 c) shows the location of the second A-site selected by a white arrow. Figure 4.25 d) shows the location of the first A-site.

4.1.4.3 Two sites disordered model for the A-site

Rietveld refinement was performed using synchrotron data at -173 °C on 0.825BTFM-0.175CTO, in $Pna2_1$, setting *bca*. The 2θ range of analysis was from 3° to 74°. A two sites disordered model for the A-site was used. The initial atomic positions for the second atom were estimated from the observed charge density map of the A-site in Figure 4.25 c). The ratio of occupancy between the first and the second A-site was initially estimated as 5:1 from the peak values of charge densities. The scale factor, peak shape parameters, occupancy of the bismuth and atomic positions for the B-site and oxygens were refined.

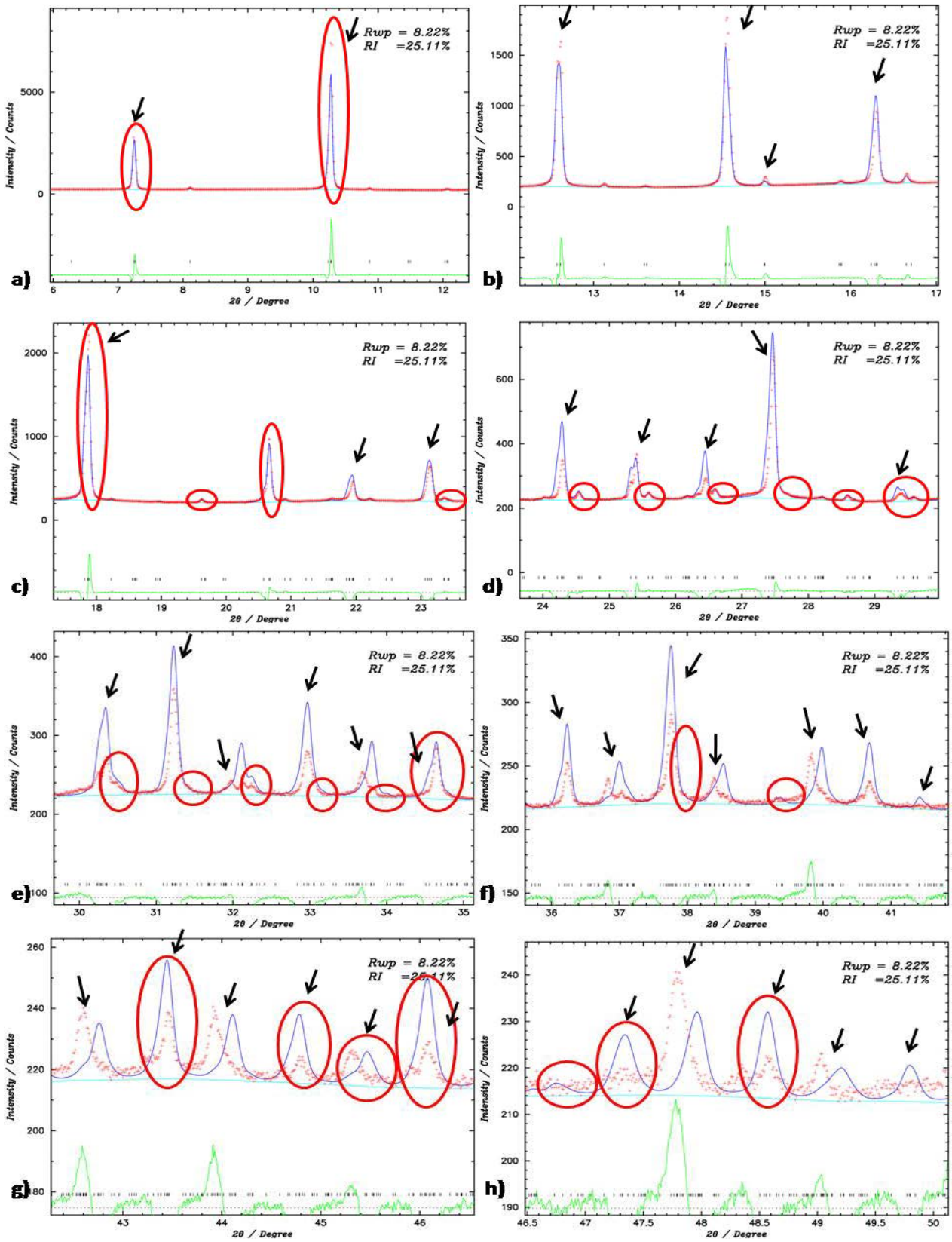

Figure 4.26 Rietveld refinement for 0.825BTFM-0.175CTO in $Pna2_1$, setting bca considering a two sites disordered model for the A-site. The red circles indicate the peaks that improve the fitting in comparison with the Rietveld refinement using isotropic atomic displacement, Figure 4.22. The black arrows indicate the mismatches between the model and data in terms of peak position and/or shape and intensity. The red crosses represent the observed data while the blue solid line represents the model. The difference green curve is below. The black tics represent positions of Bragg reflections.

Figure 4.26 shows the Rietveld refinement for 0.825BTFM-0.175CTO in $Pna2_1$, setting *bca* using a two sites disordered model for the A-site. The reliability factors based on the weighted profiles, R_{wp}, and Bragg intensities, R_I are 8.22% and 25.11%, respectively. The red circles indicate the peaks that improve the fitting in comparison with the Rietveld refinement using a one site model for the A-site, Figure 4.24. The black arrows indicate the mismatches between the model and data in terms of peak position and/or shape and intensity. The refined parameters are listed in Table 4.15.

Table 4.15: Atomic parameters for 0.825BTFM-0.175CTO from Rietveld refinement in $Pna2_1$, setting bca using a two sites disordered model for the A-site. The column one shows the different atoms; in columns two, three and four the atomic coordinates of each atom being x, y and z respectively; in column five the isotropic displacement parameters, B, and in column six the occupancy of each atom.

Atoms	x	y	z	B	Occupancy
Bi1/Ca1	0.4778(5)	0.495	0.5	1.0	0.67(1) /0.14583
Bi2/Ca2	0.54	0.495	0.5	1.0	0.142(8) /0.02917
Ti/Fe/Mg	0.525(5)	0.005	0.75(2)	1.0	0.4844 /0.2063 /0.3094
O1	0.536(6)	0.005	0.51(3)	1.0	1
O2	0.320(7)	0.245	0.150(5)	1.0	1
O3	0.26(1)	0.745	0.226(6)	1.0	1

As shown in Figure 4.26, the Rietveld refinement for the 0.825BTFM-0.175CTO using a two sites disordered model for the A-site should be improved. Therefore, the electronic charge density distribution of the A-site was investigated in detail using the MEM method.

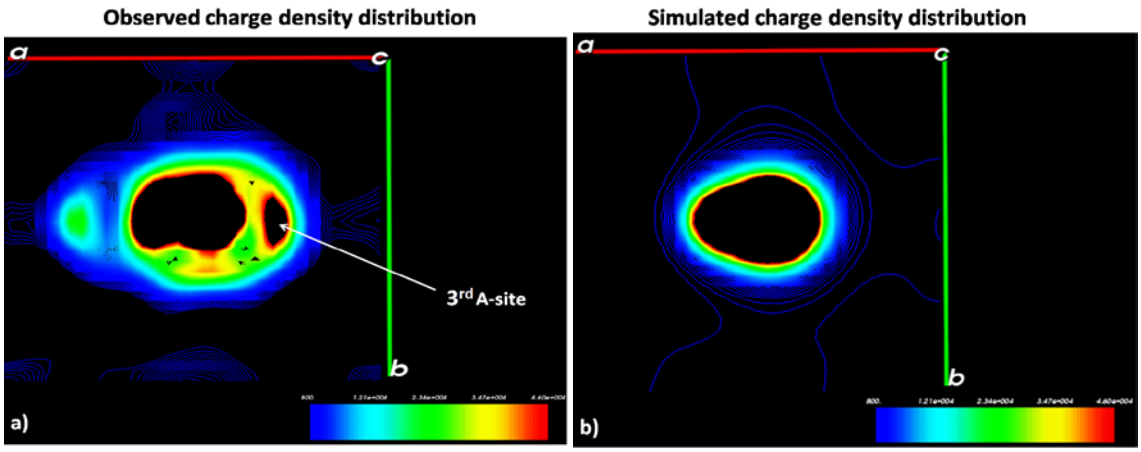

Figure 4.27 Charge density distribution maps of the A-site for the (002) plane a) observed charge density distribution. The white arrow indicates the location of the third atom selected, b) simulated charge density distribution map of the A-site. The crystallographic axis are marked in red for a and in green for b. The bars at the right bottom of the pictures show the charge density, the units are me/Å^3. The values of charge density increase from blue to red.

Figure 4.27 a) shows the observed charge density map of the A-site for the (002) plane. Figure 4.27 b) shows the simulated charge density map of the A-site for the (002) plane. Figure 4.27 a) shows with a white arrow the location of the third A-site selected. It is observed that the shape of the observed and simulated charge density distribution is very similar. Therefore, the selection of the second A-site was correct.

4.1.4.4 Three sites disordered model for the A-site

Rietveld refinement was performed using synchrotron data at -173 °C on 0.825BTFM-0.175CTO, in *Pna*2_1, setting *bca*. The 2θ range of analysis was from 3° to 74°. A three sites disordered model for the A-site was used. The initial atomic positions for the third atom were estimated from the observed charge density map of the A-site, Figure 4.27 a). The ratio of occupancy between the first, second and third A-site was initially estimated as 3:1:2 from the peak values of charge density. The scale factor, peak shape parameters, atomic positions and displacement parameters were refined.

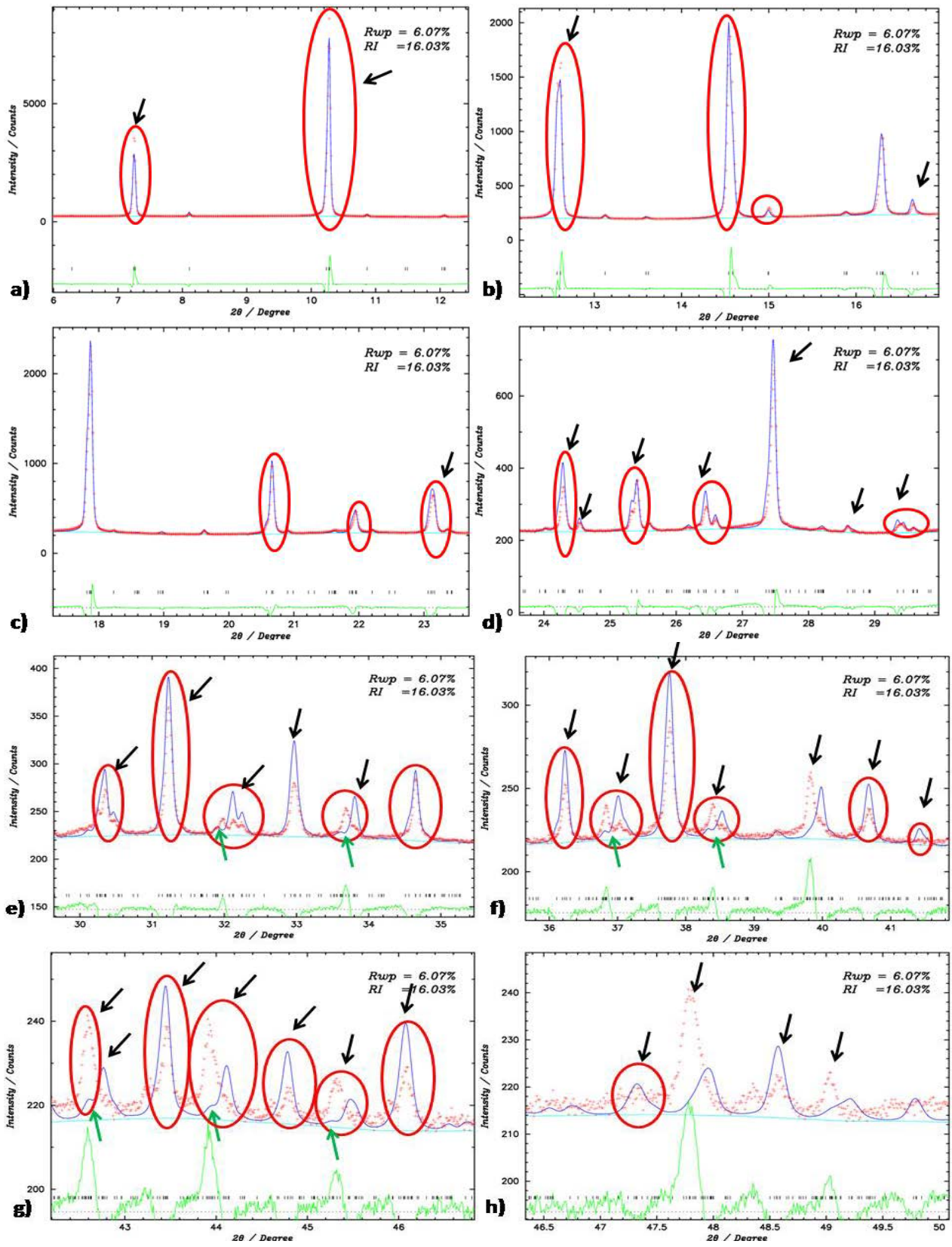

Figure 4.28 Rietveld refinement for 0.825BTFM-0.175CTO in $Pna2_1$, setting bca considering a three sites disordered model for the A-site. The red circles indicate the peaks that improve the fitting in comparison with the Rietveld refinement using a two sites model for the A-site, Figure 4.26. The black arrows indicate the mismatches between the model and data in terms of peak position and/or shape and intensity. The green arrows indicate appearance of the new reflections. The red crosses represent the observed data while the blue solid line represents the model. The difference green curve is below. The black tics represent positions of Bragg reflections.

Figure 4.28 shows the Rietveld refinement for 0.825BTFM-0.175CTO in $Pna2_1$, setting *bca* using a three sites disordered model for the A-site. The reliability factors based on the weighted profiles, R_{wp}, and Bragg intensities, R_I are 6.07% and 16.03%, respectively. The red circles indicate the peaks that improve the fitting in comparison with the Rietveld refinement using a two sites model for the A-site, Figure 4.26. The green arrows indicate appearance of new reflections. The black arrows indicate the mismatches between the model and data in terms of peak position and/or shape and intensity. The refined parameters are listed in Table 4.16.

Table 4.16: Atomic parameters for 0.825BTFM-0.175CTO from Rietveld refinement in $Pna2_1$, setting bca using a three sites disordered model for the A-site. In the column one the different atoms; in columns two, three and four the atomic coordinates of each atom being x, y and z respectively; in column five the isotropic displacement parameters, B, and in column six the occupancy of each atom.

Atoms	x	y	z	B	Occupancy
Bi1/Ca1	0.476(1)	0.494(3)	0.518(3)	1.05(6)	0.4125/0.0875
Bi2/Ca2	0.552(2)	0.49(1)	0.501(7)	1.05(6)	0.1375/0.02916
Bi3/Ca3	0.442(8)	0.49(2)	0.472(9)	1.05(6)	0.2750/0.05833
Ti/Fe/Mg	0.526(4)	0.006(1)	0.75240	1.1(4)	0.4844/0.2063 /0.3094
O1	0.551(3)	0.003(1)	0.526(7)	1.3(5)	1
O2	0.331(4)	0.249(5)	0.139(6)	1.3(5)	1
O3	0.253(8)	0.741(9)	0.219(5)	1.3(5)	1

As shown in Figure 4.28, the Rietveld refinement for the 0.825BTFM-0.175CTO using a three sites disordered model for the A-site should be improved. Therefore, the electronic charge density distribution of the A-site was further investigated in detail.

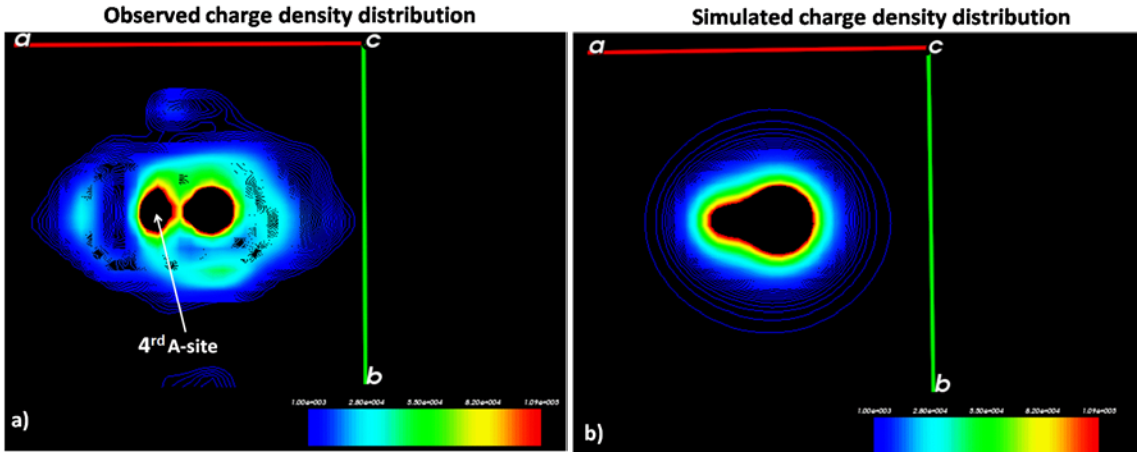

Figure 4.29 Charge density distribution maps of the A-site for the (002) plane: a) observed charge density distribution b) simulated charge density distribution map of the A-site. The white arrow indicates the location of the forth atom selected, b) simulated charge density distribution map of the A-site. The crystallographic axis are marked in red for a and in green for b. The bars at the right bottom of the pictures show the charge density, the units are me/Å^3. The values of charge density increase from blue to red.

Figure 4.29 a) shows the observed charge density map of the A-site for the (002) plane. Figure 4.29 b) shows the simulated charge density map of the A-site for the (002) plane. Figure 4.29 a) shows with a white arrow the location of the forth A-site selected. We can see that the shape of the observed and simulated charge density distribution is similar. Therefore, the selection of the third A-site was correct.

4.1.4.5 Four sites disordered model for the A-site

Rietveld refinement was performed using synchrotron data at -173 °C on 0.825BTFM-0.175CTO, in *Pna*2$_1$, setting *bca*. The 2θ range of analysis was from 3° to 74°. A four sites disordered model for the A-site was used. The initial atomic positions for the four atoms were accurately estimated from the observed charge density map of the A-site, Figure 4.29 a). The ratio of occupancy between the first, second, third and forth A-site was initially estimated as 3:1:2:2.5 from the peak values of charge density. The scale factor, peak shape parameters, atomic positions and displacement parameters were refined.

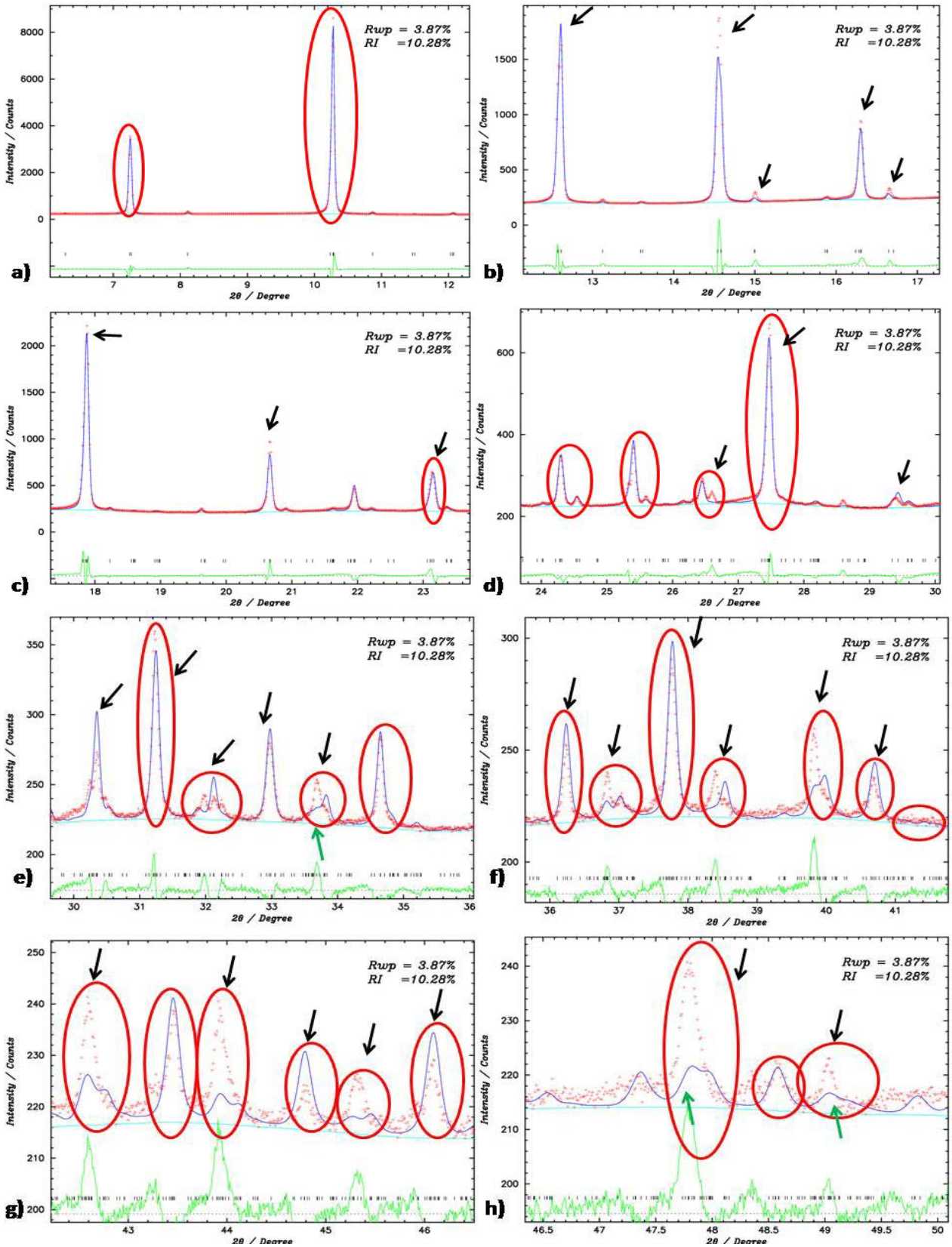

Figure 4.30 Rietveld refinement for 0.825BTFM-0.175CTO in $Pna2_1$, setting bca considering a four sites disordered model for the A-site. The red circles indicate the peaks that improve the fitting in comparison with the Rietveld refinement using a three sites model for the A-site, Figure 4.28. The black arrows indicate the mismatches between the model and data in terms of peak position and/or shape and intensity. The green arrows indicate appearance of new reflections. The red crosses represent the observed data while the blue solid line represents the model. The difference green curve is below. The black tics represent positions of Bragg reflections.

Figure 4.30 shows the Rietveld refinement for 0.825BTFM-0.175CTO in $Pna2_1$, setting *bca* using a four sites disordered model for the A-site. The reliability factors based on the weighted profiles, R_{wp}, and Bragg intensities, R_I are 3.87% and 10.28%, respectively. The red circles indicate the peaks that improve the fitting in comparison with the Rietveld refinement using a three sites model for the A-site, Figure 4.28. The green arrows indicate the appearance of the new reflections. The black arrows indicate the mismatches between the model and data in terms of peak position and/or shape and intensity. The refined parameters are listed in Table 4.17.

Table 4.17: Atomic parameters for 0.825BTFM-0.175CTO from Rietveld refinement in $Pna2_1$, setting bca using a four sites disordered model for the A-site. The column one shows the different atoms; in columns two, three and four the atomic coordinates of each atom being x, y and z respectively; in column five the isotropic displacement parameters, B, and in column six the occupancy of each atom.

Atoms	x	y	z	B	Occupancy
Bi1/Ca1	0.532(1)	0.512(2)	0.509(3)	1.0 (1)	0.291/0.0617
Bi2/Ca2	0.319(3)	0.512(2)	0.509(3)	1.0 (1)	0.097/0.0206
Bi3/Ca3	0.596(2)	0.482(2)	0.496(3)	1.0 (1)	0.194/0.0412
Bi4/Ca4	0.448(2)	0.508(3)	0.504(3)	1.0 (1)	0.2426/0.0517
Ti/Fe/Mg	0.510(6)	0.002(8)	0.75427	0.7(1)	0.4844/0.2063 /0.3094
O1	0.522(4)	0.020(4)	0.487(4)	0.9(6)	1
O2	0.279(5)	0.210(5)	0.162(4)	0.9(6)	1
O3	0.239(8)	0.736(8)	0.229(4)	0.9(6)	1

As shown in Figure 4.30, the Rietveld refinement for the 0.825BTFM-0.175CTO using a four sites disordered model for the A-site needs to be improved. Therefore, the electronic charge density distribution of the A-site was further investigated in detail.

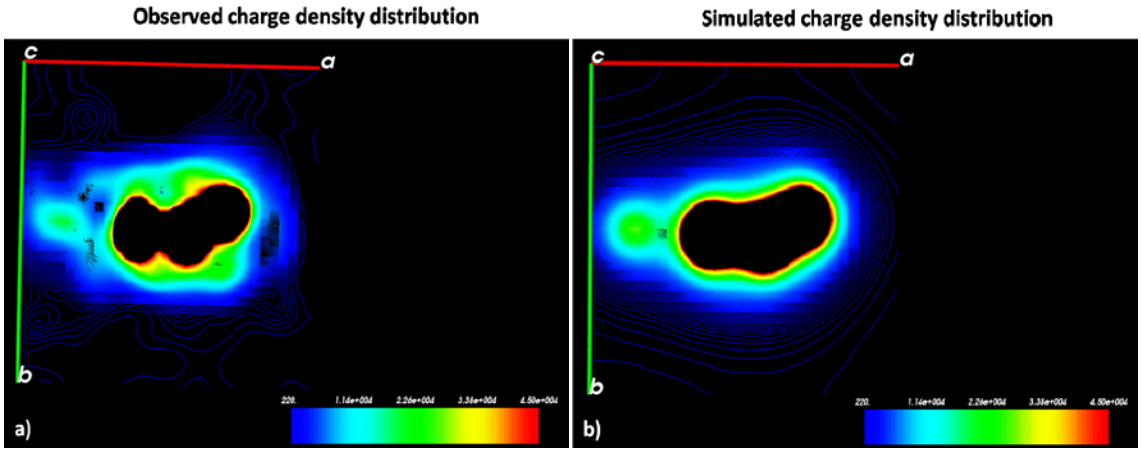

Figure 4.31 Charge density distribution maps of the A-site for the (002) plane: a) Observed charge density distribution; b) Simulated charge density distribution map of the A-site. The crystallographic axis are marked in red for a and in green for b. The bars at the right bottom of the pictures show the charge density, the units are me/Å^3. The values of charge density increase from blue to red.

Figure 4.31 a) shows the observed charge density map of the A-site for the (002) plane. Figure 4.31 b) shows the simulated charge density map of the A-site for the (002) plane. The origin was taken from the top left. We can see that the shape of the observed and simulated charge density distribution is similar. Therefore, the selection of the forth A-site was correct.

Up to twenty cycles of refinement were performed until the R_{wp} and R_I were almost constant using a four sites disordered model for the A-site. Synchrotron data at -173 °C on 0.825BTFM-0.175CTO, in *Pna*2_1, setting *bca* were used. The 2θ range of analysis was from 3° to 65°. Each cycle of refinement consisted of: 1st step, refinement of the occupancy for the A-site and 2nd step, refinement of the atomic positions and displacement parameters. Before the 2nd step the occupancy was recalculated so the total sum was 1. The atomic positions, *x* and *y*, were recalculated in the cases where they were different between the simulated and observed charge density maps.

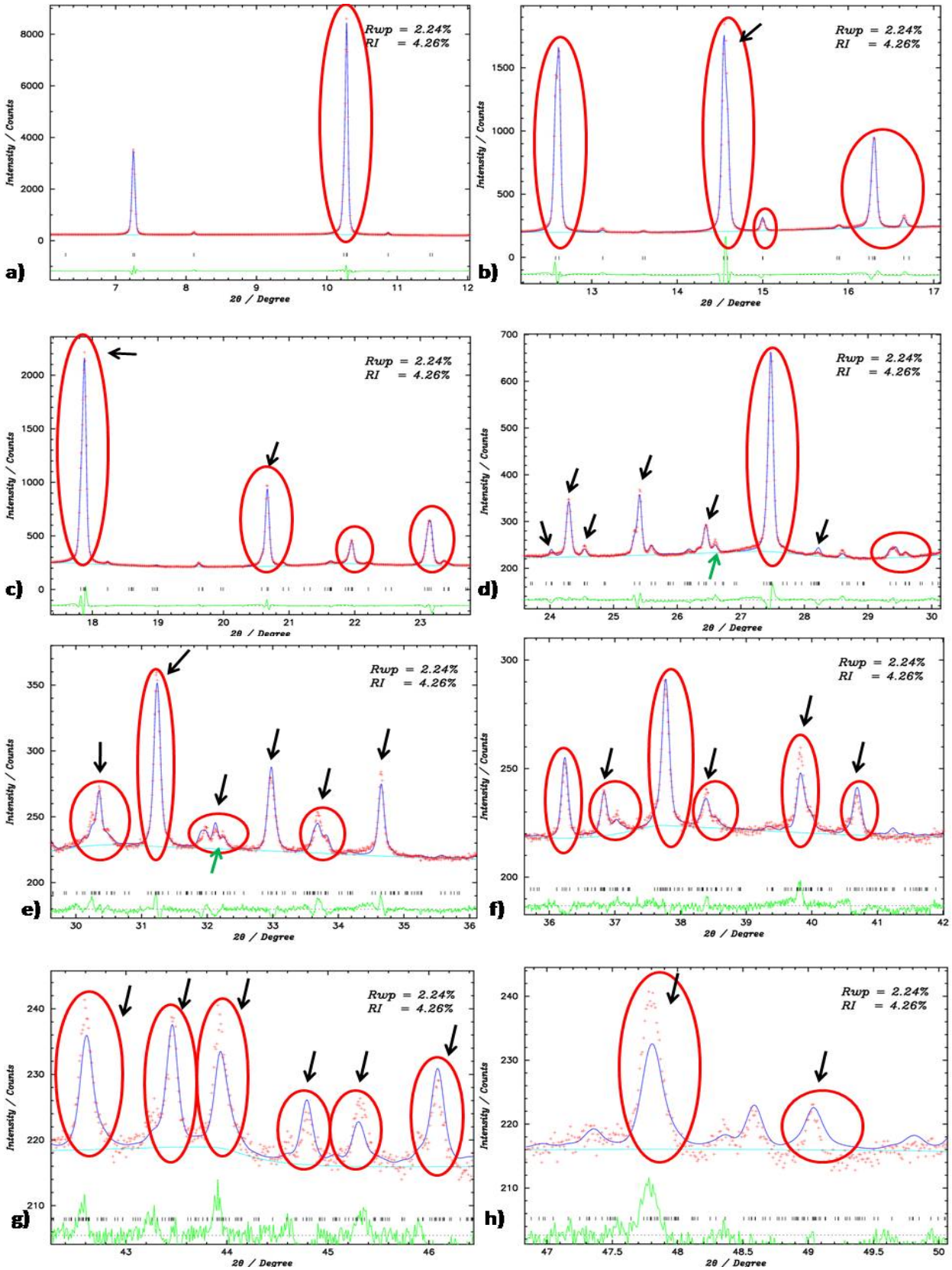

Figure 4.32 Rietveld refinement for 0.825BTFM-0.175CTO in $Pna2_1$, setting bca considering a four sites disordered model for the A-site. The red circles indicate the peaks that improve the fitting in comparison with the Rietveld refinement using a three sites model for the A-site, Figure 4.30. The black arrows indicate the mismatches between the model and data in terms of peak position and/or shape and intensity. The green arrows indicate appearance of the new reflections. The red crosses represent the observed data while the blue solid line represents the model. The difference green curve is below. The black tics represent positions of Bragg reflections.

Figure 4.32 shows the Rietveld refinement for 0.825BTFM-0.175CTO in $Pna2_1$, setting *bca* using a four sites disordered model for the A-site after twenty cycles of refinement. The reliability factors based on the weighted profiles, R_{wp}, and Bragg intensities, R_I are 2.24% and 4.26% respectively. The red circles indicate the peaks improve the fitting in comparison with the Rietveld refinement using a four sites model for the A-site, Figure 4.30 but before performing the twenty cycles of refinement. The green arrows indicate the appearance of the new reflections. The black arrows indicate the mismatches between the model and data in terms of peak position and/or shape and intensity. The refined parameters are listed in Table 4.18.

Table 4.18: Atomic parameters for 0.825BTFM-0.175CTO from Rietveld refinement in $Pna2_1$, setting bca using a four sites disordered model for the A-site. The column one shows the different atoms; in columns two, three and four the atomic coordinates of each atom being x, y and z respectively; in column five the isotropic displacement parameters, B, and in column six the occupancy of each atom.

Atoms	x	y	z	B	Occupancy
Bi1/Ca1	0.553(2)	0.522(1)	0.517(1)	1.18(6)	0.32023/ 0.06793
Bi2/Ca2	0.29(1)	0.49(3)	0.584(7)	1.18(6)	0.01439/0.00305
Bi3/Ca3	0.546(4)	0.484(1)	0.4772(10)	1.18(6)	0.21882/ 0.04641
Bi4/Ca4	0.4479(5)	0.508(2)	0.512(1)	1.18(6)	0.27156/0.05760
Ti/Fe/Mg	0.504(4)	0.0002(3)	0.75427	0.37(5)	0.4844/0.2063 /0.3094
O1	0.51695	0.02757	0.49500	3.9(2)	1
O2	0.20562	0.23880	0.23390	3.9(2)	1
O3	0.23153	0.74321	0.19483	3.9(2)	1

As shown in Figure 4.32, the Rietveld refinement for the 0.825BTFM-0.175CTO using a four sites disordered model for the A-site after performing the twenty cycles of refinement needs to be improved. Therefore, the electronic charge density distribution of the A-site was further investigated in detail.

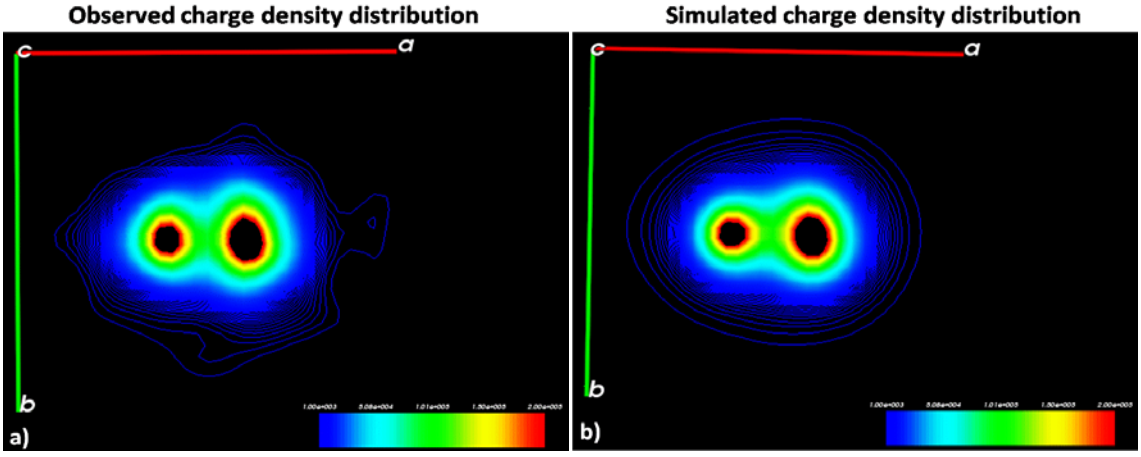

Figure 4.33 Charge density distribution maps of the A-site for the (002) plane: a) Observed charge density distribution; b) Simulated charge density distribution map of the A-site. The crystallographic axis are marked in red for a and in green for b. The bars at the right bottom of the pictures show the charge density, the units are me/Å^3. The values of charge density increase from blue to red.

Figure 4.33 a) shows the observed charge density map of the A-site for the (002) plane. Figure 4.33 b) shows the simulated charge density map of the A-site for the (002) plane. We can see that the shape of the observed and simulated charge density distribution is similar. Also, we can observe that the first atom has been merged with the third atom.

As shown in Table 4.18, the occupancy of the second atom has decreased considerably after twenty cycles of refinement being its value very close to zero. For this reason, the second atom was not included as a site in the next analysis.

4.1.4.6 Three sites disordered model for the A-site

Up to four cycles of refinement were performed until the R_{wp} and R_I were constant using a three sites disordered model for the A-site. Synchrotron data at -173 °C on 0.825BTFM-0.175CTO, in *Pna*2$_1$, setting *bca* was used. The 2θ range of analysis was from 3° to 65°. Each cycle of refinement consisted of: 1st step, refinement of the occupancy for the A-site and 2nd step, refinement of the atomic positions and displacement parameters. Care was taken so the distances between the B-site and oxygens were between the values: ~1.95 - ~2.05 Å. The distances were checked often and in the cases where they were smaller than ~1.95 Å or bigger than ~2.05 Å, the

atomic positions were readjusted manually. The occupancy of the three sites was fixed to be the same after the four cycles.

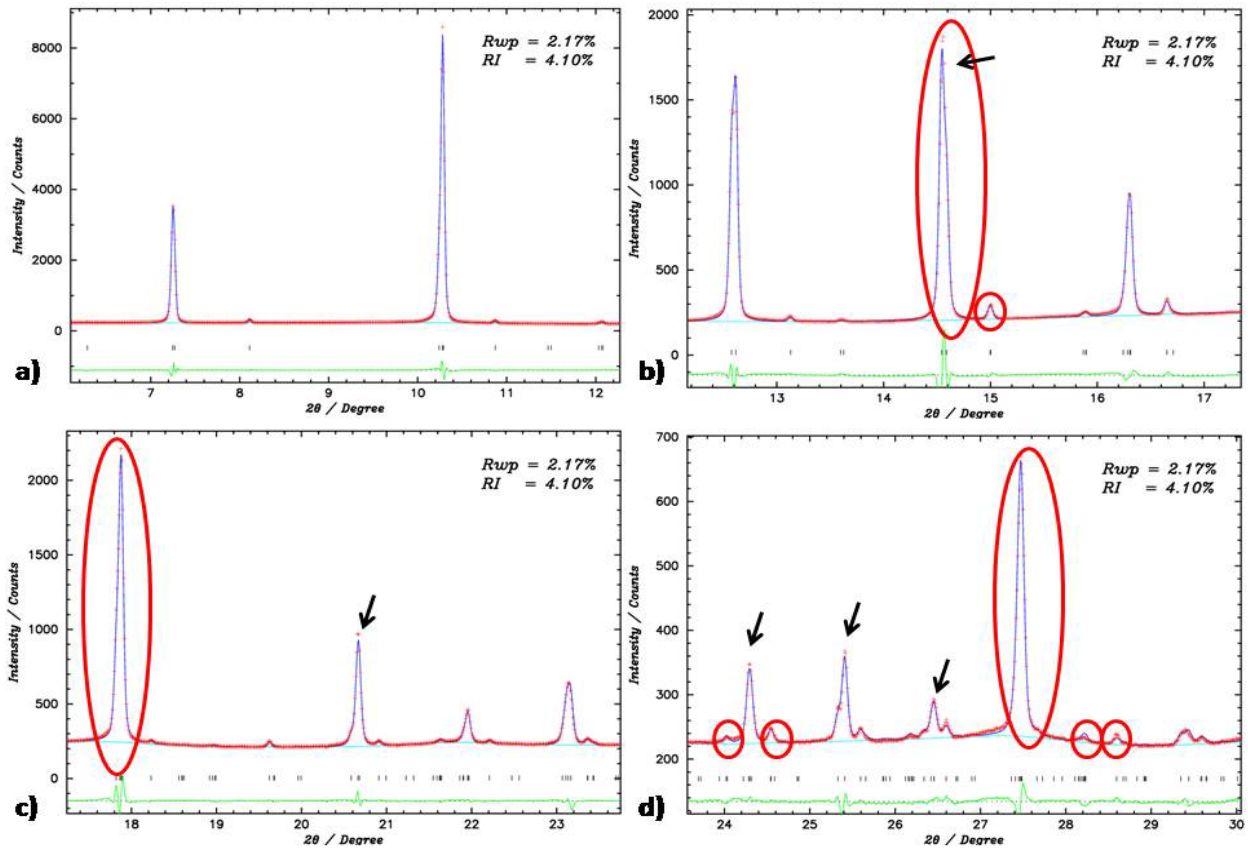

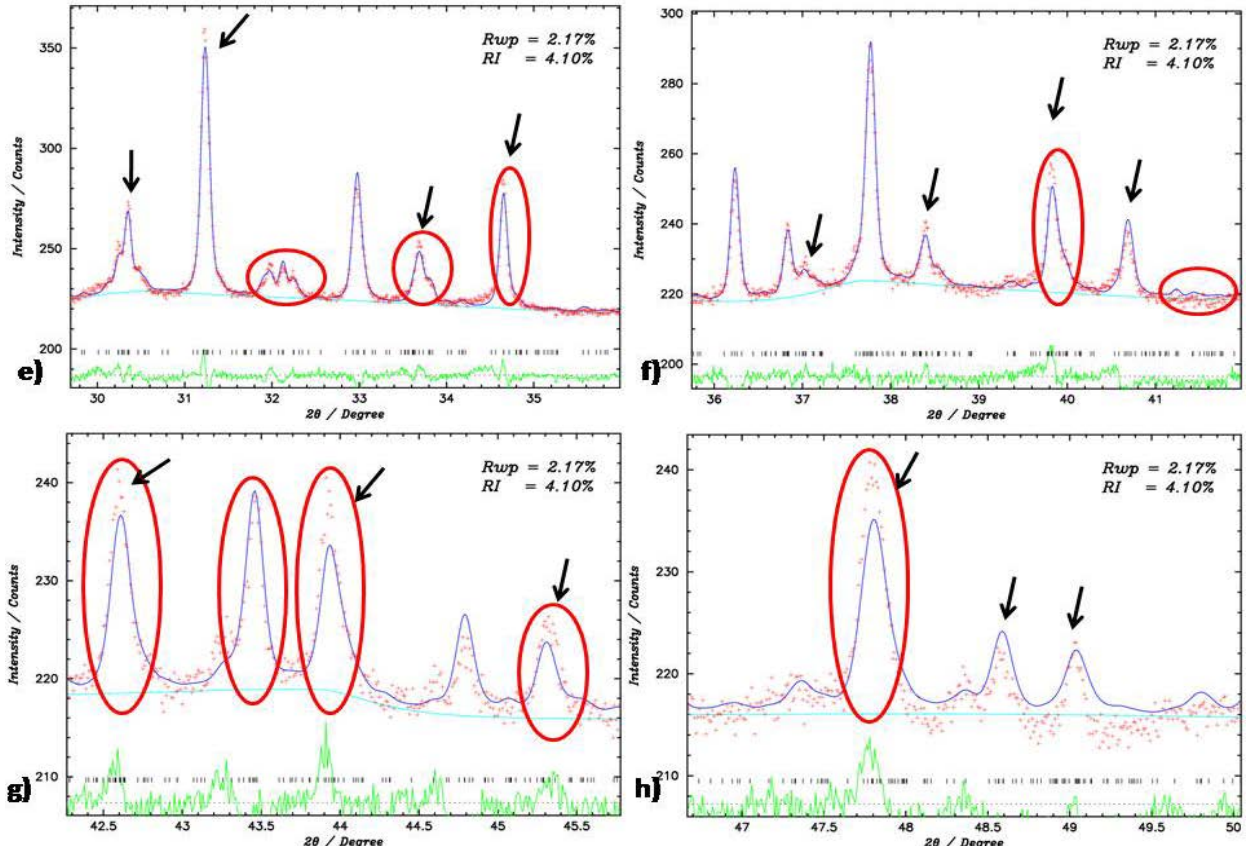

Figure 4.34 Rietveld refinement for 0.825BTFM-0.175CTO in Pna2$_1$, setting bca using athree sites disordered model for the A-site. The red circles indicate the peaks that improve the fitting in comparison with the Rietveld refinement using a four sites model for the A-site, Figure 4.32. The black arrows indicate the mismatches between the model and data in terms of peak position and/or shape and intensity. The red crosses represent the observed data while the blue solid line represents the model. The difference green curve is below. The black tics represent positions of Bragg reflections.

Figure 4.34 shows the Rietveld refinement for 0.825BTFM-0.175CTO in *Pna*2$_1$, setting *bca* using a three sites disordered model for the A-site after the four cycles of refinement. The reliability factors based on the weighted profiles, R_{wp}, and Bragg intensities, R_I are 2.17% and 4.10%, respectively. The red circles indicate the peaks that improve the fitting in comparison with the Rietveld refinement using a four sites model for the A-site, Figure 4.32. The green arrows indicate appearance of the new reflections. The black arrows indicate the mismatches between the model and data in terms of peak position and/or shape and intensity. The refined parameters are listed in Table 4.19.

Table 4.19: Atomic parameters for 0.825BTFM-0.175CTO from Rietveld refinement in $Pna2_1$, setting bca using a three sites disordered model for the A-site. The column one shows the different atoms; in columns two, three and four the atomic coordinates of each atom being x, y and z respectively; in column five the isotropic displacement parameters, B, and in column six the occupancy of each atom.

Atoms	x	y	z	B	Occupancy
Bi1/Ca1	0.552(3)	0.525(1)	0.5226(9)	1.17(7)	0.275/0.05833
Bi2/Ca2	0.549(3)	0.489(1)	0.4815(8)	1.17(7)	0.275/0.05833
Bi3/Ca3	0.446(4)	0.504(2)	0.514(1)	1.17(7)	0.275/0.05833
Ti/Fe/Mg	0.500(5)	0.0009(3)	0.75427	0.19(5)	0.4844/0.2063 /0.3094
O1	0.50273	0.05191	0.50656	3.6(2)	1
O2	0.23898	0.24457	0.24293	3.6(2)	1
O3	0.24088	0.76629	0.19789	3.6(2)	1

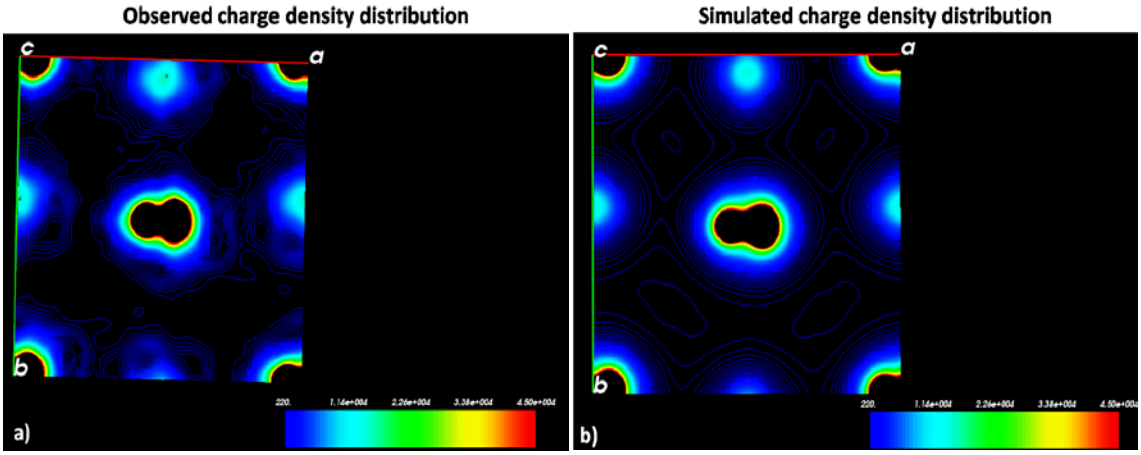

Figure 4.35 Charge density distribution maps of the A-site for the (002) plane: a) Observed charge density distribution; b) Simulated charge density distribution map of the A-site. The crystallographic axis are marked in red for a and in green for b. The bars at the right bottom of the pictures show the charge density, the units are me/Å^3. The values of charge density increase from blue to red.

Figure 4.35 a) shows the observed charge density map of the A-site for the (002) plane. Figure 4.35 b) shows the simulated charge density map of the A-site for the (002) plane. We can see that the shape of the observed and simulated charge density distribution is very similar.

As shown in Figure 4.34, the Rietveld refinement for the 0.825BTFM-0.175CTO using a three sites disordered model for the A-site after performing the four cycles of refinement fits well

until ~30°. However, especially over ~40° there is a mismatch in intensity between the observed and calculated data.

This three sites disordered model for the A-site built based on the electronic charge density gives a better fit than the one site disordered model for the A-site explained in Section 4.1.4.1, the two sites disordered model for the A-site explained in Section 4.1.4.3, the three sites disordered model for the A-site explained in Section 4.1.4.4 and the four sites disordered model for the A-site explained in Section 4.1.4.5.

Attempts to modify the ratio of occupancy between the first, second and third A-site did not improve the fit over ~40°. Therefore, in order to further improve the model the difference between the observed and calculated charge density distributions were investigated.

4.1.4.7 Model building based on the difference charge density distribution

With the aim of enhancing any small difference between the model and observation, the difference between the observed and calculated charge density distributions were investigated. The goal was to minimise the residual density distribution as much as possible. In order to carry out this study, it is necessary to achieve a high quality fit. Normal and high counting statistics data were used for the analysis and the background of both data sets were carefully adjusted manually.

A Rietveld refinement was performed using synchrotron data at 27 °C on 0.825BTFM-0.175CTO in $Pna2_1$, setting *bca*. The 2θ range of analysis for the normal counting statistics data was from 6 to 65° and for the high counting statistics data was from 21.3 to 65°.

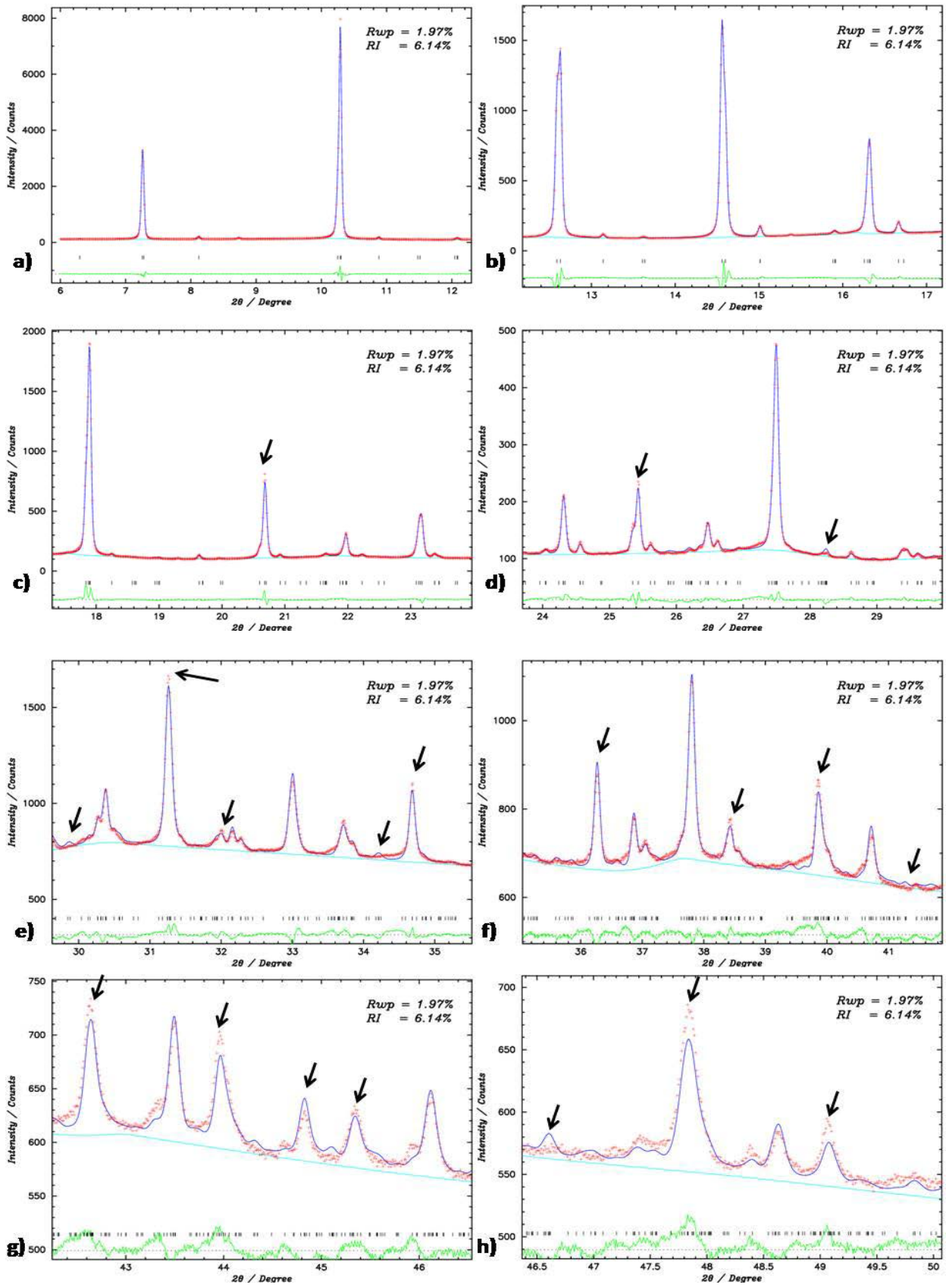

Figure 4.36 Rietveld refinement for 0.825BTFM-0.175CTO in $Pna2_1$, setting bca using a three sites disordered model for the A-site. The black arrows indicate the mismatches between the model and data in terms of peak position and/or shape and intensity. The red crosses represent the observed data while the blue solid line represents the model. The difference green curve is below. The black tics represent positions of Bragg reflections.

Figure 4.36 shows the Rietveld refinement for 0.825BTFM-0.175CTO in $Pna2_1$, setting *bca* using a three sites disordered model for the A-site at 27 °C. The reliability factors based on the weighted profiles, R_{wp}, and Bragg intensities, R_I are 1.97% and 6.14%, respectively. The black arrows indicate the mismatches between the model and data in terms of peak position and/or shape and intensity. The atomic parameters are listed in Table 4.20.

Table 4.20: Atomic parameters for 0.825BTFM-0.175CTO from Rietveld refinement in $Pna2_1$, setting bca using a three sites disordered model for the A-site. The column one shows the different atoms; in columns two, three and four the atomic coordinates of each atom being x, y and z respectively; in column five the isotropic displacement parameters, B, and in column six the occupancy of each atom. Lattice constants: a = 5.59242 Å, b = 5.56521 Å and c = 7.86742 Å.

Atoms	x	y	z	B	Occupancy
Bi1/Ca1	0.54814	0.52662	0.52926	1. 4188	0.275/0.05833
Bi2/Ca2	0.55301	0.49308	0.48343	1. 4188	0.275/0.05833
Bi3/Ca3	0.4469	0.49958	0.51768	1. 4188	0.275/0.05833
Ti/Fe/Mg	0.50001	0.00380	0.75452	0.4803	0.4844/0.2063 /0.3094
O1	0.49770	0.05898	0.50675	3.54157	1
O2	0.23940	0.24550	0.24212	3.54157	1
O3	0.24112	0.76800	0.20515	3.54157	1

As shown in Figure 4.36, the Rietveld refinement for the 0.825BTFM-0.175CTO using a three sites disordered model for the A-site needs to be improved especially over 30°. Consequently, the difference between the observed and simulated charge density distribution map of A-site for the (001) plane was studied in order to reduce the residual charge.

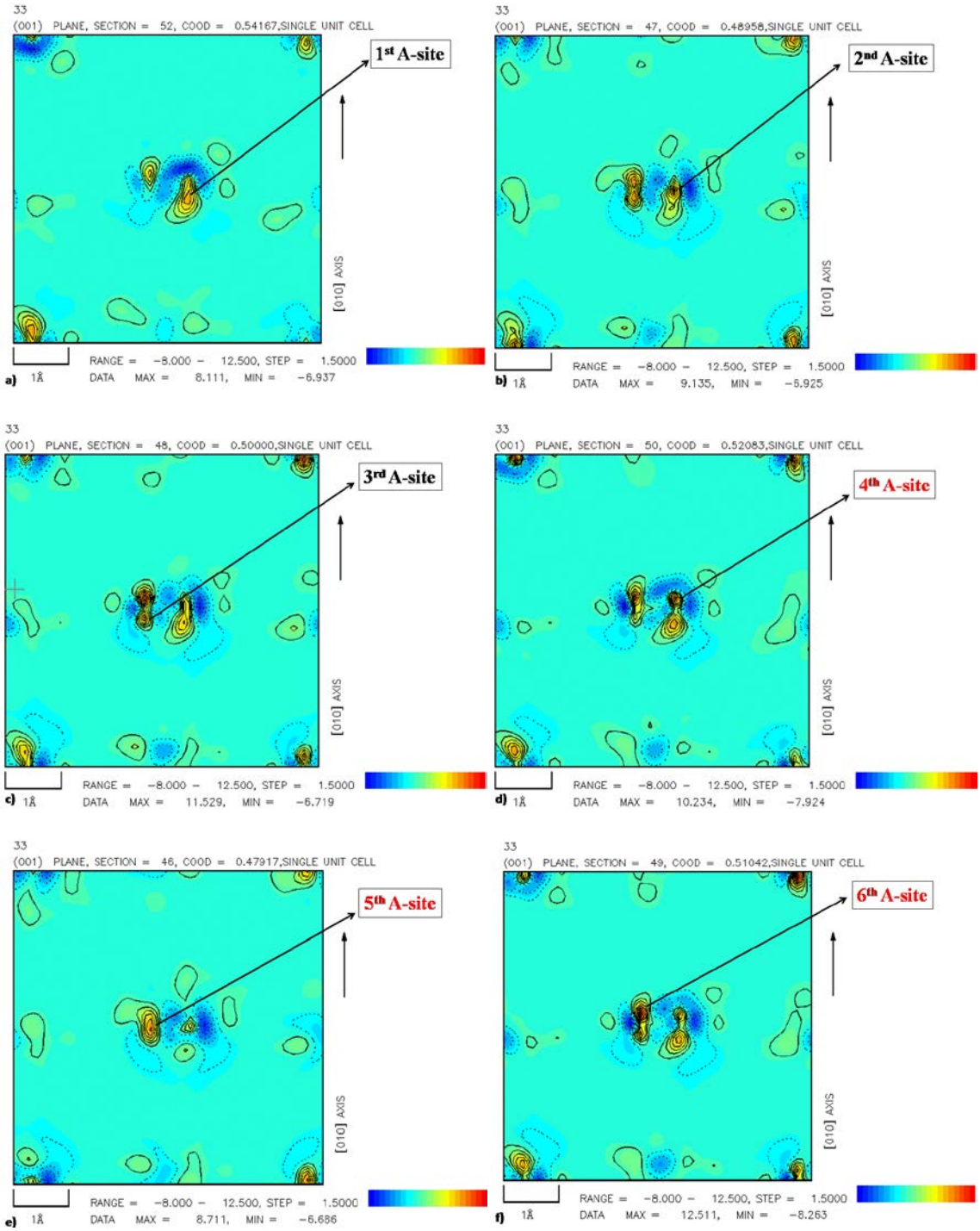

Figure 4.37 Difference between observed and simulated charge density distribution map of A-site for the (001) plane. The black arrows point out the location of the atoms. The bars at the right bottom of the pictures show the charge density, the units are me/Å^3. The values of charge density increase from blue to red.

Figure 4.37 a-f) show the difference between observed and simulated charge density distribution map of A-site for the (001) plane. The *c*-axis is divided into 96 sections. The black arrows point out the location of the atoms. The value of the *z* position can be known from the figures. For instance, the maxima of electronic charge density distribution for the first A-site

appears at section 52 and it is 0.54167, as shown in Figure 4.37 a). Figures 4.67 a- f) show the location of the first, second, third, forth, fifth and sixth A-site respectively. Six different maxima of electronic charge density distribution were observed so the analysis was performed using a six sites disordered model for the A-site.

4.1.4.8 Six atoms disordered model for the A-site

A Rietveld refinement was perfomed using synchrotron data at 27 °C on 0.825BTFM-0.175CTO in $Pna2_1$, setting *bca*. A six sites disordered model for the A-site was used. The initial atomic positions for the forth, fifth and sixth sites were estimated from the Figures 4.37 d), e) and f) respectively. Two data sets, normal and high counting statistics data, were used for the analysis. The 2θ range of analysis for the normal counting statistics data was from 6 to 46.7° and for the high counting statistics data was from 21.3 to 65°. The occupancy was the same for all the atoms. The scale factor, peak shift, lattice constants, peak shape parameters, atomic positions and displacement parameters were refined.

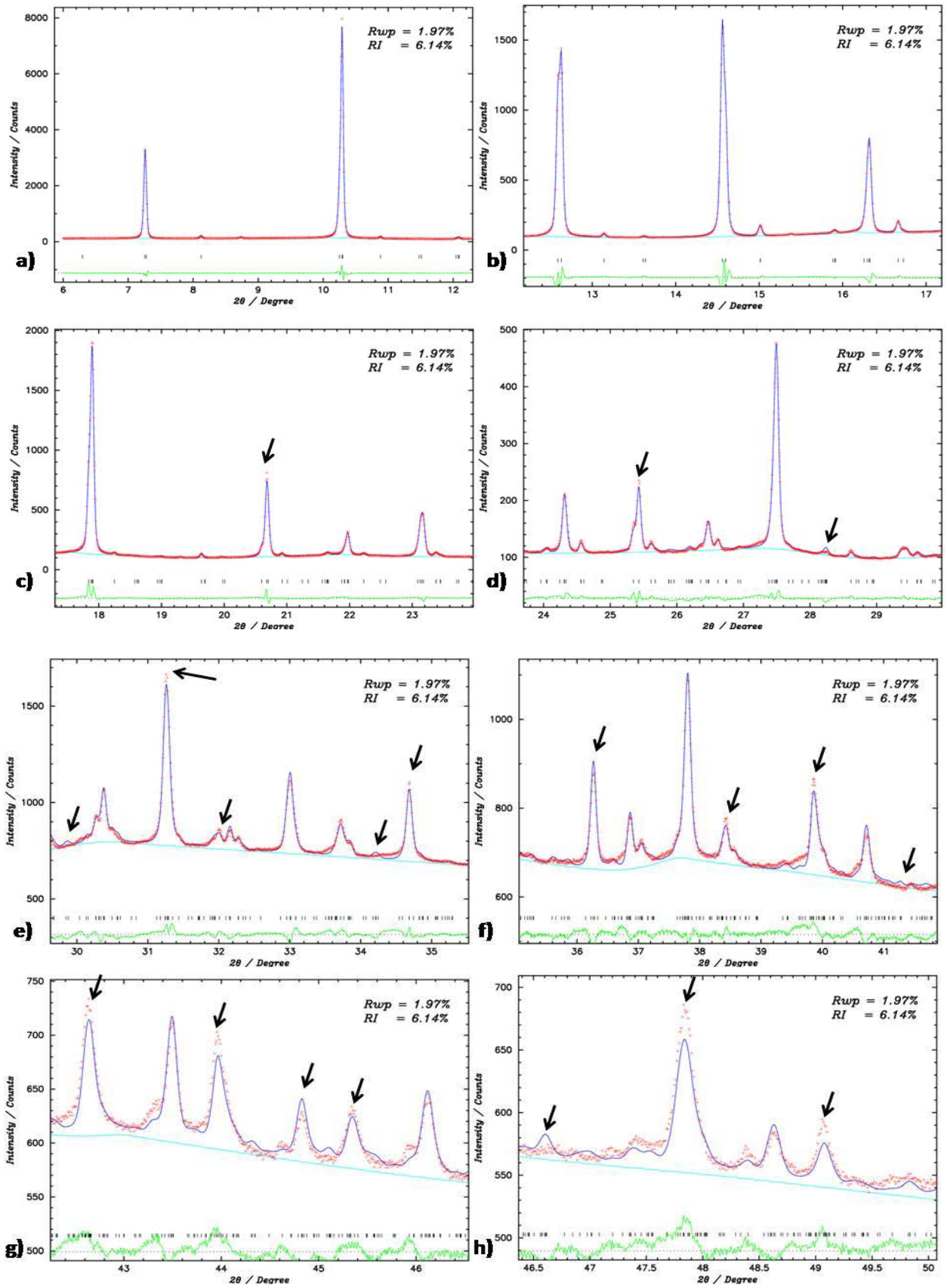

Figure 4.38 Rietveld refinement for 0.825BTFM-0.175CTO in $Pna2_1$, setting bca using a six sites disordered model for the A-site. The red circles indicate the peaks that improve the fitting in comparison with the Rietveld refinement using a three sites model for the A-site, Figure 4.36. The red crosses represent the observed data while the blue solid line represents the model. The difference green curve is below. The black tics represent positions of Bragg reflections.

Figure 4.38 shows the Rietveld refinement for 0.825BTFM-0.175CTO in $Pna2_1$, setting *bca* using a six sites disordered model for the A-site. The reliability factors based on the weighted profiles, R_{wp}, and Bragg intensities, R_I are 1.14% and 2.15%, respectively. The red circles indicate the peaks that improve the fitting in comparison with the Rietveld refinement using a three sites disordered model for the A-site, Figure 4.36. The atomic parameters are listed in Table 4.21.

Table 4.21: Atomic parameters for 0.825BTFM-0.175CTO from Rietveld refinement in $Pna2_1$, setting bca using a six sites disordered model for the A-site. The column one shows the different atoms; in columns two, three and four the atomic coordinates of each atom being x, y and z respectively; in column five the isotropic displacement parameters, B, and in column six the occupancy of each atom.
Lattice constants: a = 5.59249(5) Å, b = 5.56431(4) Å and c = 7.86869(7) Å

Atoms	x	y	z	B	Occupancy
Bi1/Ca1	0.444(1)	0.518(1)	0.5376(9)	0.72(7)	0.1375/0.02917
Bi2/Ca2	0.5667(4)	0.513(1)	0.4889(6)	0.72(7)	0.1375/0.02917
Bi3/Ca3	0.465(1)	0.4619(8)	0.523(1)	0.72(7)	0.1375/0.02917
Bi4/Ca4	0.5386(3)	0.509(2)	0.5166(9)	0.72(7)	0.1375/0.02917
Bi5/Ca5	0.457(1)	0.537(1)	0.486(1)	0.72(7)	0.1375/0.02917
Bi6/Ca6	0.434(1)	0.487(1)	0.4857(9)	0.72(7)	0.1375/0.02917
Ti/Fe/Mg	0.500(1)	0.000(2)	0.75452	0.49(2)	0.4844/0.2063 /0.3094
O1	0.5075(7)	0.0864(9)	0.503(2)	1.67(9)	1
O2	0.244(1)	0.262(2)	0.217(1)	1.67(9)	1
O3	0.315(1)	0.719(2)	0.229(1)	1.67(9)	1

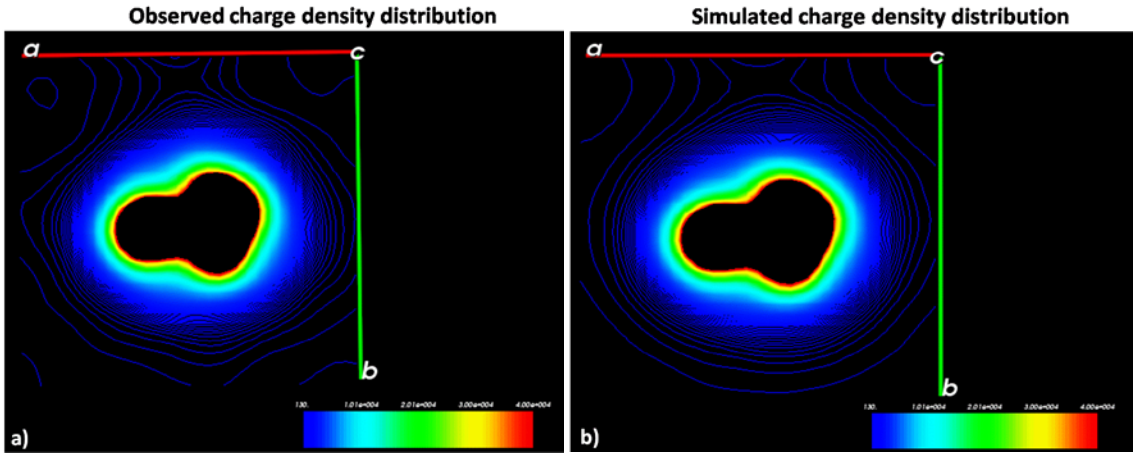

Figure 4.39 a) Observed charge density distribution; b) Simulated charge density distribution map of the A-site.

Figure 4.39 a) shows the observed charge density map of the A-site for the (002) plane. Figure 4.39 b) shows the simulated charge density map of the A-site for the (002) plane. It is observed that the shape of the observed and simulated charge density distribution is almost identical.

As shown in Figure 4.38, a good fit was achieved for the 0.825BTFM-0.175CTO using a six sites disordered model for the A-site. The fit is better than for the three sites disordered model for the A-site shown in Figure 4.36. In comparison with the fit using anisotropic displacement motion for the A-site (Section 4.1.4.2, Figure 4.24), this six sites disordered model for the A-site built fit the data much better. Furthermore, the shape of the observed and simulated charge density distribution is almost identical as Figures 4.39 a) and 4.39 b) show. Therefore, this six sites disordered model for the A-site was concluded as the final model using synchrotron X-ray powder diffraction data.

The comparison of R-factors for the different models used through section 4.1.4 to perform Rietveld analysis for 0.825BTFM-0.175CTO in $Pna2_1$, setting *bca* are compiled in Table 4.22.

Table 4.22: Comparison of the different models used in section 4.1.4 to perform Rietveld analysis for 0.825BTFM-0.175CTO in $Pna2_1$, setting bca.

Model	T (°C)	R_{wp} / R_I (%)	Figure number
Initial model	-173	8.95 / 31.85	4.22
Initial model (anisotropic atomic displacement)	-173	1.77 / 12.57	4.24
Two sites disordered model for the A-site	-173	8.22 / 25.11	4.26
Three sites disordered model for the A-site	-173	6.07 / 16.03	4.28
Four sites disordered model for the A-site	-173	3.87 / 10.28	4.30
Four sites disordered model for the A-site (after 20 cycles of refinement)	-173	2.24 / 4.26	4.32
Three sites disordered model for the A-site	-173	2.17 / 4.10	4.34
Three sites disordered model for the A-site	27	1.97 / 6.14	4.36
Six sites disordered model for the A-site	27	1.14 / 2.15	4.38

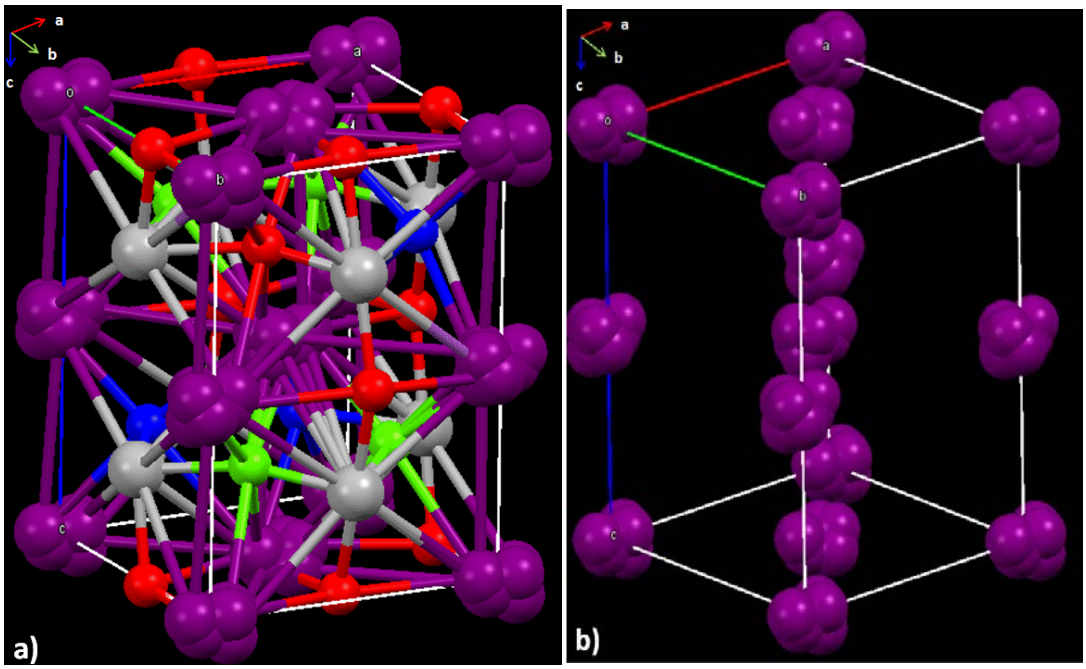

Figure 4.40 a) Structural model and b) A-sites structural model of 0.825BTFM-0.175CTO in $Pna2_1$ at 27 °C for the final six sites disordered model for the A-site. A-site cations represented in purple, B-site cations in grey, and oxygen atoms 1, 2 and 3 in red, green and blue respectively.

Figure 4.40 a) shows the structural model of 0.825BTFM-0.175CTO in $Pna2_1$ at 27 °C using a six sites disordered model for the A-site. A-site cations represented in purple, B-site cations in grey, and oxygen atoms 1, 2 and 3 in red, green and blue respectively. Figure 4.40 b) shows the A-sites structural model for the final structure using synchrotron X-ray powder diffraction data.

In order to know the origin of the polarisation in this six sites disordered model for the A-site, the atomic displacements of the $Pna2_1$ structure with respect to this idealised *Pnma* configuration were calculated using the program *PSEUDO [10]*. This program is designed to detect pseudosymmetry in a given structure (the $Pna2_1$ structure in this case) and derive a virtual parent high-symmetry structure (the *Pnma* structure in this case). The atomic coordinates of the six different A-sites were treated individually and thus the atomic displacements with respect to each A-site were obtained.

Thus, the maximum atomic displacement between the two structures when inputting just the atomic coordinates of the first A-site is of the order of 0.3752 Å and it comes from the O2 and O3 as shown in Table 4.23.

Table 4.23: Displacements of the $Pna2_1$ structure (when inputting just the atomic coordinates of the first A-site) with respect to the idealised structure Pnma. Note: u_x, u_y and u_z are given in relative units. $|u|$ is the absolute displacement given in Å.

Atom	Idealised coordinates	u_x	u_y	u_z	$\|u\|$
Bi/Ca	(0.4438, 0.5176, 0.2500)	0.000000	0.000000	0.024481	0.1926
Ti/Fe/Mg	(0.5000, 0.0000, 0.5000)	0.000029	0.000296	-0.008638	0.0680
O1	(0.5075, 0.0864, 0.2500)	0.000000	0.000000	-0.010473	0.0824
O2	(0.2148, 0.2404, 0.9942)	0.029670	0.021590	-0.039947	0.3752
O3	(0.2852, 0.7404, 0.0058)	0.029670	-0.021590	-0.039947	0.3752

The maximum atomic displacement between the two structures when inputting just the atomic coordinates of the second A-site is of the order of 0.2312 Å and it comes from the O2 and O3 as shown in Table 4.24.

Table 4.24: Displacements of the $Pna2_1$ structure (when inputting just the atomic coordinates of the second A-site) with respect to the idealised structure Pnma. Note: u_x, u_y and u_z are given in relative units. $|u|$ is the absolute displacement given in Å

Atom	Idealised coordinates	u_x	u_y	u_z	$\|u\|$
Bi/Ca	(0.5667, 0.5127, 0.7500)	0.000000	0.000000	0.002032	0.0160
Ti/Fe/Mg	(0.5000, 0.0000, 0.0000)	0.000029	0.000296	0.017678	0.1391
O1	(0.5075, 0.0864, 0.7500)	0.000000	0.000000	0.015843	0.1247
O2	(0.2148, 0.2404, 0.4942)	0.029670	0.021590	-0.013631	0.2312
O3	(0.2852, 0.7404, 0.5058)	0.029670	-0.021590	-0.013631	0.2312

The maximum atomic displacement between the two structures when inputting just the atomic coordinates of the third A-site is of the order of 0.2877 Å and it comes from the A-site as shown in Table 4.25.

Table 4.25: Displacements of the $Pna2_1$ structure (when inputting just the atomic coordinates of the third A-site) with respect to the idealised structure Pnma. Note: u_x, u_y and u_z are given in relative units. $|u|$ is the absolute displacement given in Å

Atom	Idealised coordinates	u_x	u_y	u_z	$\|u\|$
Bi/Ca	(0.4654, 0.4619, 0.7500)	0.000000	0.000000	0.036563	0.2877
Ti/Fe/Mg	(0.5000, 0.0000, 0.0000)	0.000029	0.000296	0.017678	0.1391
O1	(0.5075, 0.0864, 0.7500)	0.000000	0.000000	0.015843	0.1247
O2	(0.2148, 0.2404, 0.4942)	0.029670	0.021590	-0.013631	0.2312
O3	(0.2852, 0.7404, 0.5058)	0.029670	-0.021590	-0.013631	0.2312

The maximum atomic displacement between the two structures when inputting just the atomic coordinates of the fourth A-site is of the order of 0.2343 Å and it comes from the A-site as shown in Table 4.26.

Table 4.26: Displacements of the $Pna2_1$ structure (when inputting just the atomic coordinates of the fourth A-site) with respect to the idealised structure Pnma. Note: u_x, u_y and u_z are given in relative units. $|u|$ is the absolute displacement given in Å

Atom	Idealised coordinates	u_x	u_y	u_z	$\|u\|$
Bi/Ca	(0.5386, 0.5100, 0.7500)	0.000000	0.000000	0.029775	0.2343
Ti/Fe/Mg	(0.5000, 0.0000, 0.0000)	0.000029	0.000296	0.017678	0.1391
O1	(0.5075, 0.0864, 0.7500)	0.000000	0.000000	0.015843	0.1247
O2	(0.2148, 0.2404, 0.4942)	0.029670	0.021590	-0.013631	0.2312
O3	(0.2852, 0.7404, 0.5058)	0.029670	-0.021590	-0.013631	0.2312

The maximum atomic displacement between the two structures when inputting just the atomic coordinates of the fifth A-site is of the order of 0.2312 Å and it comes from the O2 and O3 as shown in Table 4.27.

Table 4.27: Displacements of the $Pna2_1$ structure (when inputting just the atomic coordinates of the fifth A-site) with respect to the idealised structure Pnma. Note: u_x, u_y and u_z are given in relative units. $|u|$ is the absolute displacement given in Å

Atom	Idealised coordinates	u_x	u_y	u_z	$\|u\|$
Bi/Ca	(0.4571, 0.5372, 0.7500)	0.000000	0.000000	-0.000804	0.0063
Ti/Fe/Mg	(0.5000, 0.0000, 0.0000)	0.000029	0.000296	0.017678	0.1391
O1	(0.5075, 0.0864, 0.7500)	0.000000	0.000000	0.015843	0.1247
O2	(0.2148, 0.2404, 0.4942)	0.029670	0.021590	-0.013631	0.2312
O3	(0.2852, 0.7404, 0.5058)	0.029670	-0.021590	-0.013631	0.2312

The maximum atomic displacement between the two structures when inputting just the atomic coordinates of the sixth A-site is of the order of 0.2312 Å and it comes from the O2 and O3 as shown in Table 4.28.

Table 4.28: Displacements of the $Pna2_1$ structure (when inputting just the atomic coordinates of the sixth A-site) with respect to the idealised structure Pnma. Note: u_x, u_y and u_z are given in relative units. $|u|$ is the absolute displacement given in Å

Atom	Idealised coordinates	u_x	u_y	u_z	$\|u\|$
Bi/Ca	(0.4571, 0.5372, 0.7500)	0.000000	0.000000	-0.000804	0.0063
Ti/Fe/Mg	(0.5000, 0.0000, 0.0000)	0.000029	0.000296	0.017678	0.1391
O1	(0.5075, 0.0864, 0.7500)	0.000000	0.000000	0.015843	0.1247
O2	(0.2148, 0.2404, 0.4942)	0.029670	0.021590	-0.013631	0.2312
O3	(0.2852, 0.7404, 0.5058)	0.029670	-0.021590	-0.013631	0.2312

To summarise, the maximum atomic displacement of *Pna*2_1 structure with respect to *Pnma* is as follows: 0.3752 Å (O2 and O3) when inputting the structure data for the first A-site atom, 0.2312 Å (O2 and O3) when inputting the structure data for the second, fifth and the sixth A-site atoms, 0.2877 Å (A-site) when inputting the structure data for the third A-site atom, 0.2343 Å (A-site) when inputting the structure data for the fourth A-site atom. Thus, this study suggests that the polarisation in this six sites disordered model for the A-site crystallising in *Pna*2_1 is driven mainly by the A-site and O2 and O3.

The three dimensional observed charge density distribution of the A-site for 0.825BTFM-0.175CTO in *Pna*2_1 at 27 °C using a six sites disordered model for the A-site was studied as shown in Figure 4.41 a) and b).

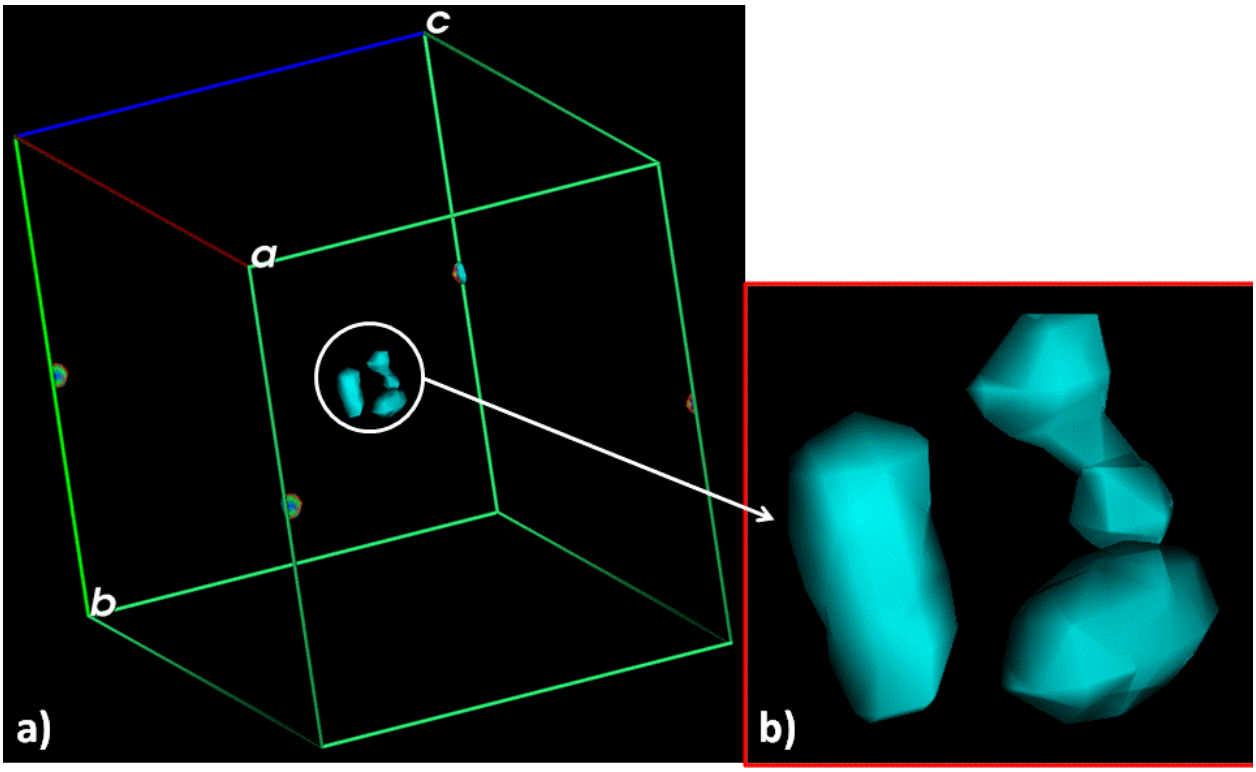

Figure 4.41 Three-dimensional observed charge density distribution of the A-site for 0.825BTFM-0.175CTO in Pna2_1 at 27 °C using a six sites disordered model for the A-site. The white circle in a) shows the A-site and the whitearrow points out an enlargement of it, as shown in b).

It is observed in Figure 4.41 that for the A-site there are three pairs of atoms. Therefore, it is concluded that this six sites disordered model for the A-site built based on the electronic charge density distribution for 0.825BTFM-0.175CTO is equivalent to a three sites disordered model using anisotropic atomic displacement for the A-site.

However, the composition 0.825BTFM-0.175CTO is very close to the phase boundary between pure O and the mixed region (O + R) as shown in the phase diagram (Figure 3.8, Chapter 3) and in the graph lattice parameters versus composition (Figure 3.9,Chapter 3). Therefore, it is complicated to synthesise it pure O phase and a small quantity of R phase has been found in some batches of 0.825BTFM-0.175CTO as shown in Figure 4.42. Consequently, the composition 0.8BTFM-0.2CTO (pure O) was selected to continue performing structural analysis on it.

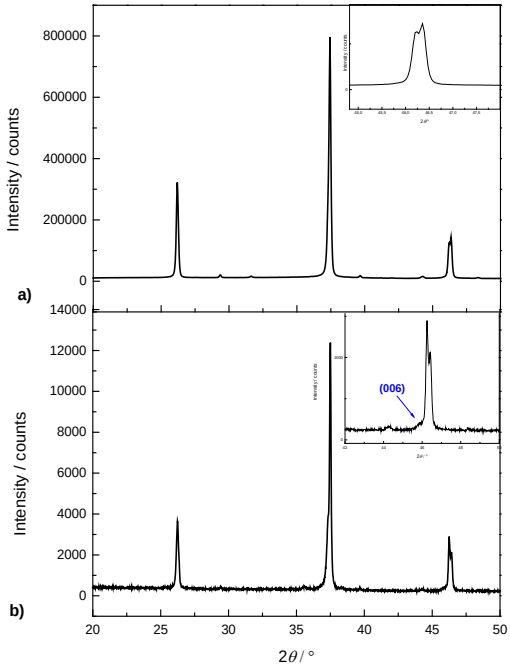

Figure 4.42 XRD patterns of 0.825BTFM-0.175CTO. a) O phase; b) O phase and small quantity of R phase, the blue arrow points out the appearance of the (006) reflection which belongs to the R phase.

Neutron powder diffraction (NPD) is used as a complementary technique to X-ray powder diffraction (XRPD) because it determines the atomic positions of light elements such as oxygens more accurately (see Section 2.1.4, Chapter 2). Thus, a joint refinement (XRPD and NPD) was performed on the composition 0.8BTFM-0.2CTO at 27 °C. The three sites disordered model for the A-site built based on the charge density distribution was used considering anisotropic atomic displacement for the A-site.

4.1.5 Joint refinement considering anisotropic atomic displacement for the three sites disordered model for the A-site

Rietveld refinement was performed using SRXRD and NPD data at 27 °C on 0.8BTFM-0.2CTO in $Pna2_1$, setting *bca*. In the case of NPD, just data collected on bank 1 and bank 2 were used. The three sites disordered model for the A-site built in Section 4.1.4.6 was used and anisotropic atomic displacement was considered for the A-site. The scale factor, peak shape parameters, lattice constants, atomic positions and displacement parameters were refined. This joint Rietveld refinement was carried out by Dr Alex Corkett and the author.

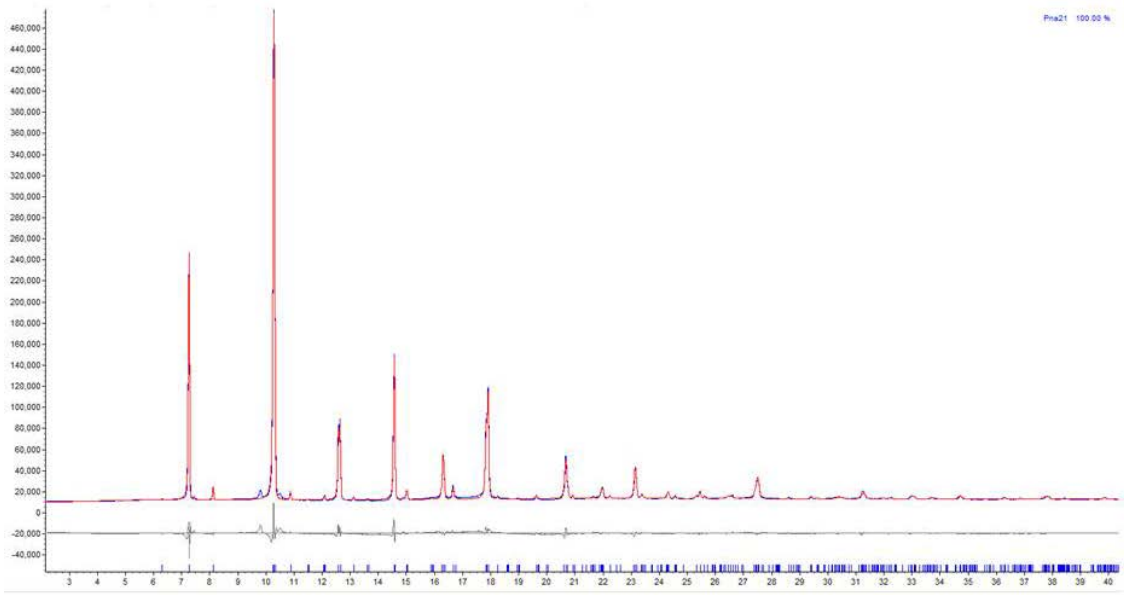

a)

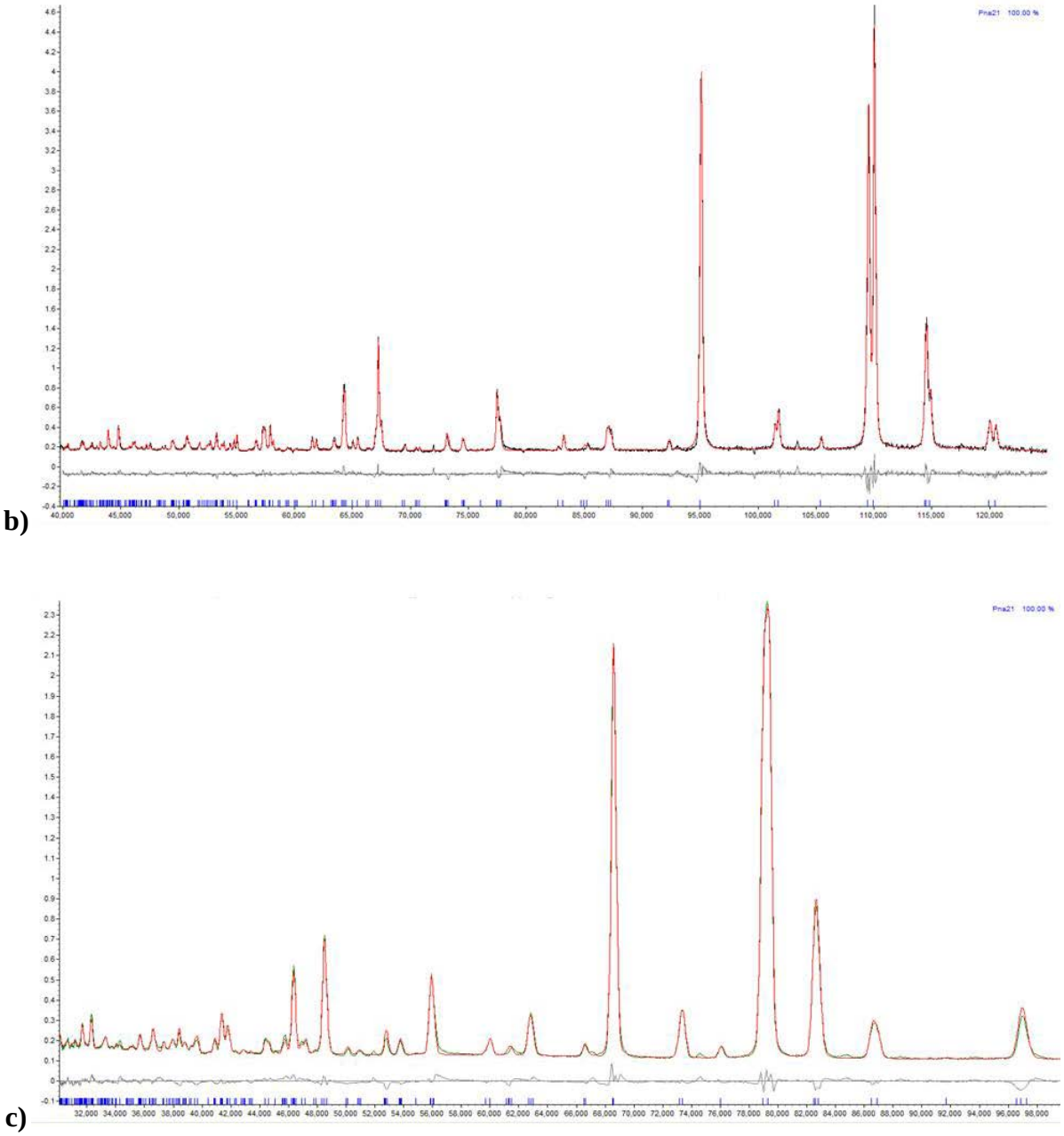

Figure 4.43 Rietveld refinement for 0.8BTFM-0.2CTO in $Pna2_1$, setting bca using a three sites disordered model for the A-site and considering anisotropic atomic displacement for the A-site: a) SRXRD data; b) NPD data (bank 1) and c) NPD data (bank 2). The blue solid line represents the observed data while the red solid line represents the model. The difference grey curve is below. The black tics represent positions of Bragg reflections.

Rietveld refinements of SRXRD, NPD (bank 1) and NPD (bank 2) are shown in Figures 4.43 a-c) respectively. The reliability factor based on the weighted profiles, R_{wp} is 5.03% and χ^2 = 4.84%. In Tables 4.29 and 4.30 are listed the refined parameters. B-site cations and oxygens were treated as isotropically.

Table 4.29: Atomic parameters for 0.8BTFM-0.2CTO from joint Rietveld refinement in $Pna2_1$, setting bca using a three sites disordered model for the A-site considering anisotropic atomic displacement for the A-site. The column one shows the different atoms; in columns two, three and four the atomic coordinates of each atom being x, y and z respectively; in column five the isotropic displacement parameters, B, and in column six the occupancy of each atom.
Lattice constants: a = 5.5908(1) Å, b = 5.5514(1) Å and c = 7.8763(2) Å.

Atoms	x	y	z	B	Occupancy
Bi1/Ca1	0.447(2)	-0.012(2)	0.228(2)	-	0.266/0.066
Bi2/Ca2	0.5448(6)	-0.0001(1)	0.246(2)	-	0.266/0.066
Bi3/Ca3	0.442(2)	0.0019(2)	0.283(2)	-	0.266/0.066
Ti/Fe/Mg	-0.020(2)	-0.009(3)	0	0.12(8)	0.4844/0.2063 /0.3094
O1	0.219(1)	0.717(1)	0.054(2)	0.9(1)	1
O2	0.210(1)	0.714(2)	0.489(2)	3.8(2)	1
O3	0.0136(5)	0.0695(6)	0.253(2)	1.50(8)	1

Table 4.30: Anisotropic atomic displacement parameters for 0.8BTFM-0.2CTO from joint Rietveld refinement in $Pna2_1$, setting bca using a three sites disordered model for the A-site considering anisotropic atomic displacement for the A-site. The column one shows the different atoms of the A-site and in the columns from two to six the six different anisotropic atomic displacement parameters for each atom.

Atoms	U_{11}	U_{22}	U_{33}	U_{12}	U_{23}	U_{12}
Bi/Ca	0.0046(8)	0.022(1)	0.006(2)	0	0	0

Figure 4.44 a-c) show the structural model of 0.8BTFM-0.2CTO at 27 °C on 0.8BTFM-0.2CTO in *Pna*2_1, setting *bca*, Figure 4.44 d) B-site environment and Figure 4.44 e-g) A-site environment for the three different sites (Bi/Ca1, Bi/Ca2 and Bi/Ca3) respectively.

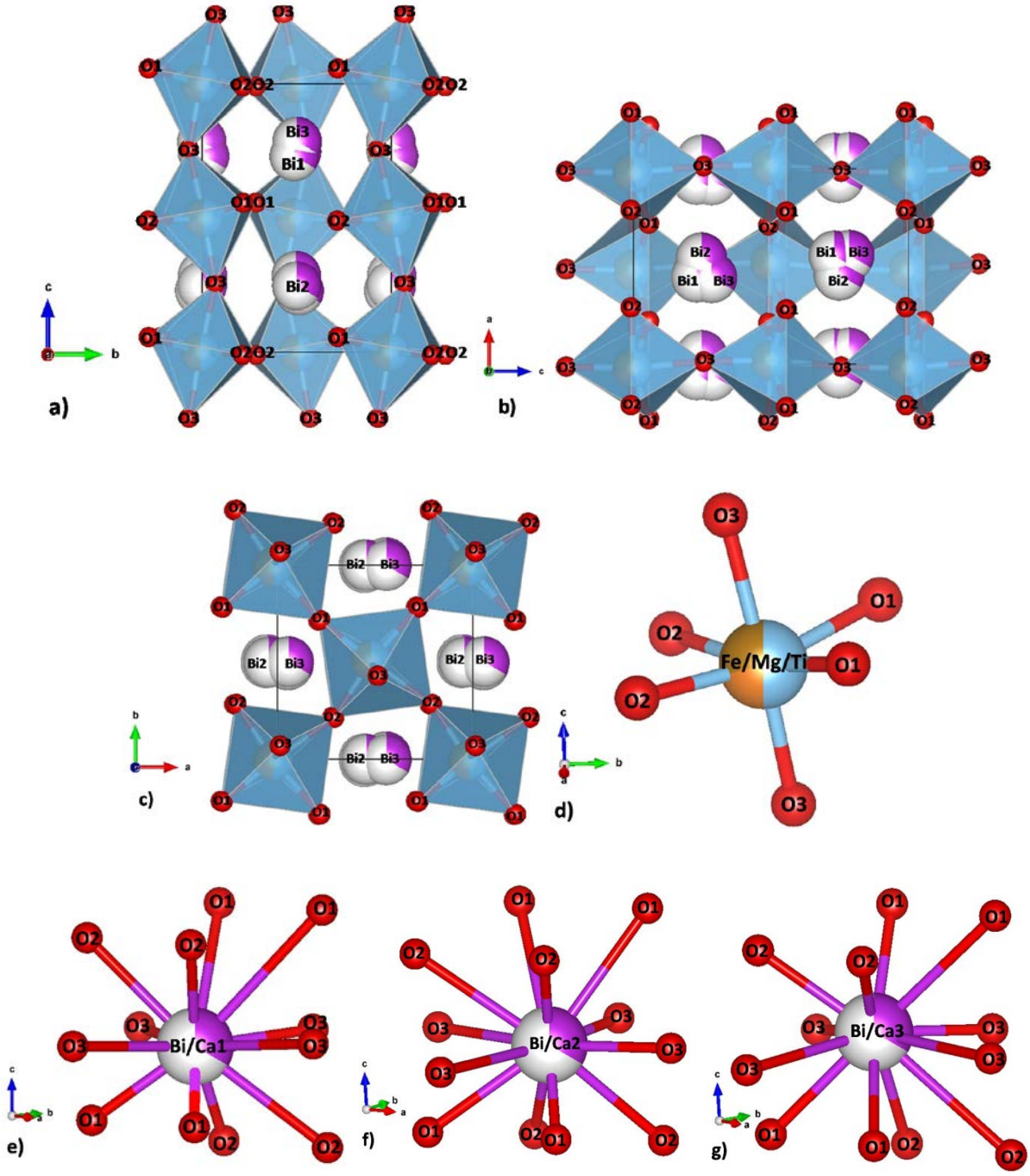

Figure 4.44 Structure of 0.8BTFM-0.2CTO at 27 °C from joint Rietveld refinement in $Pna2_1$, setting bca using a three sites disordered model for the A-site considering anisotropic atomic displacement for the A-site. A-site cations represented in purple and white, B-site cations in brown, blue and orange and oxygens in red a-c) viewed along a, b and c respectively, d) B-site environment and e-g) A-site environment for the three different sites (Bi/Ca1, Bi/Ca2 and Bi/Ca3) respectively.

As shown in Table 4.29 the displacement parameter for O2 is large (B = 3.8(2)). This fact may be consequence of the three sites disordered model for the A-site. Thus, the charge density distribution was studied and Figure 4.45 shows the Fourier map. A-site cations are represented in

blue, B-sites in grey and oxygens in red. The white balls represent the maxima of charge density. The red circle indicates the O2 and it is observed that there is a white ball at the top of the O2 and another one at the bottom. This fact suggests that the O2 may be split along the c-axis.

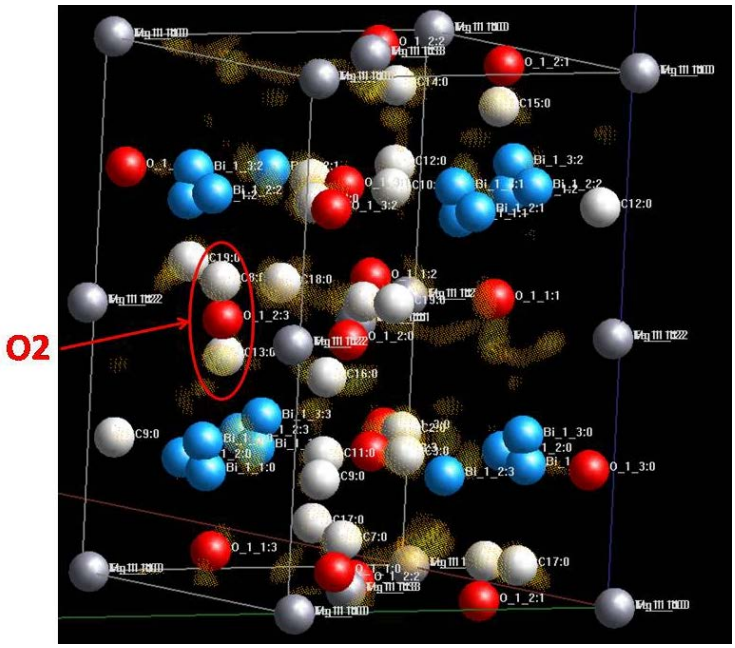

Figure 4.45 Fourier map corresponding to the joint Rietveld refinement for 0.8BTFM-0.2CTO in $Pna2_1$, setting bca at 27 °C using a three sites disordered model for the A-site and considering anisotropic atomic displacement for the A-site. A-site cations are represented in blue, B-sites in grey while oxygens in red. The white balls represent the maxima of charge density. The red circle indicates the O2.

4.1.5.1 Joint refinement considering anisotropic atomic displacement for the three sites disordered model for the A-site and the O2 split along the c-axis

Rietveld refinement was performed using SRXRD and NPD data at 27 °C on 0.8BTFM-0.2CTO in *Pna*2_1, setting *bca*. In the case of NPD, just data collected on bank 1 and bank 2 were used. The previous three sites disordered model for the A-site considering anisotropic atomic displacement for the A-site was used. The O2 was split along the c-axis. The scale factor, peak shape parameters, lattice constants, atomic positions and displacement parameters were refined.

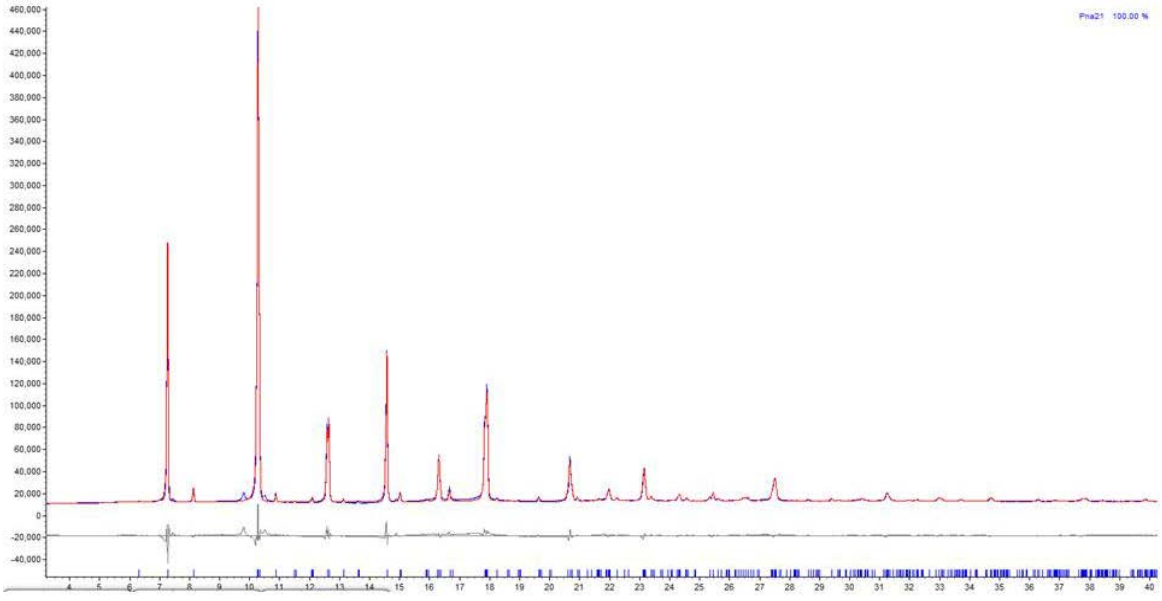

a)

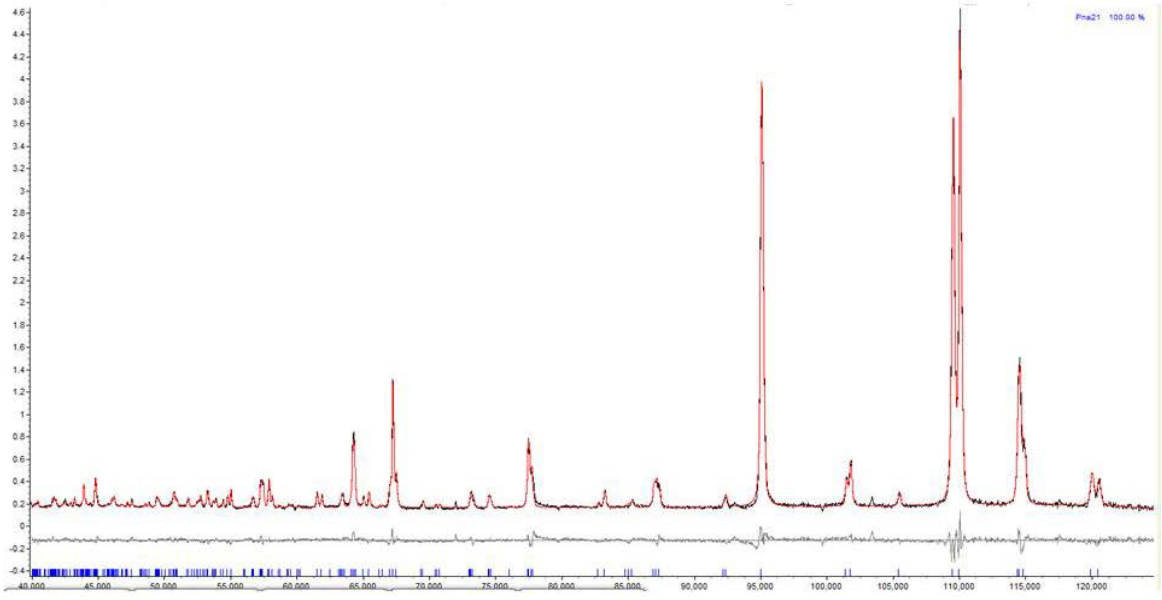

b)

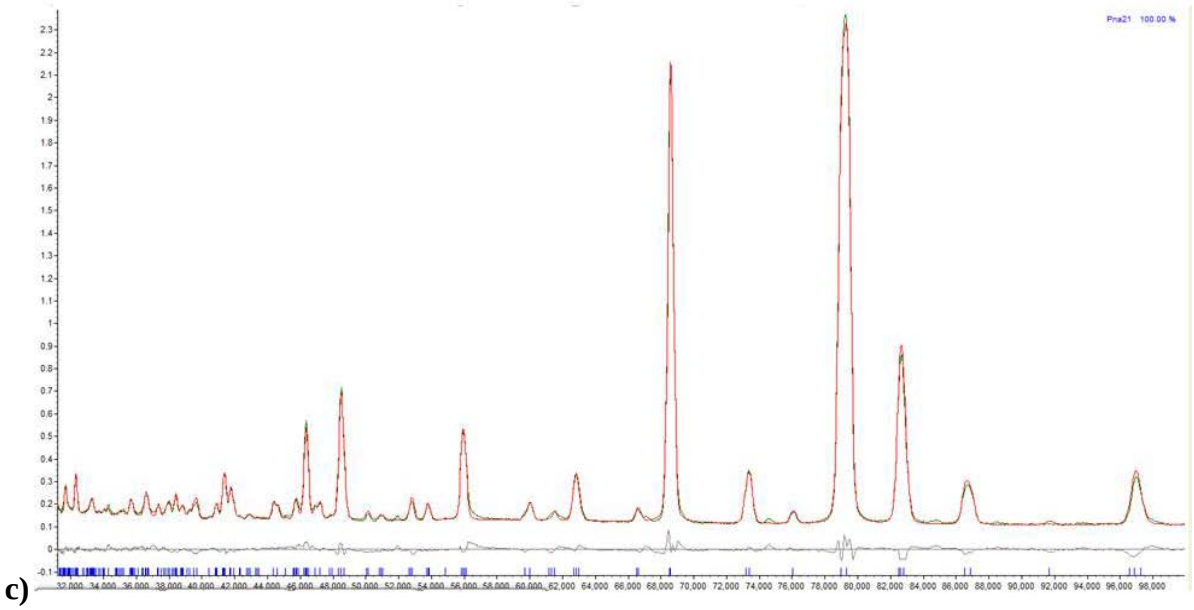

Figure 4.46 Rietveld refinement for 0.8BTFM-0.2CTO in $Pna2_1$, setting bca using a three sites disordered model for the A-site and considering anisotropic atomic displacement for the A-site and the O2 split along the c-axis: a) SRXRD data; b) NPD data (bank 1) and c) NPD data (bank 2). The blue solid line represents the observed data while the red solid line represents the model. The difference grey curve is below. The black tics represent positions of Bragg reflections.

Rietveld refinements of SRXRD, NPD (bank 1) and NPD (bank 2) are shown in Figures 4.46 a-c) respectively. The reliablility factor based on the weighted profiles, R_{wp} is 4.95% and χ^2 = 4.76%. In Tables 4.31 and 4.32 are listed the refined parameters. B-site cations and oxygens were treated as isotropic atomic displacement model.

Table 4.31: Atomic parameters for 0.8BTFM-0.2CTO from joint Rietveld refinement in $Pna2_1$, setting bca using a three sites disordered model for the A-site considering anisotropic atomic displacement for the A-site and the O2 split along the c-axis. The column one shows the different atoms; in columns two, three and four the atomic coordinates of each atom being x, y and z respectively; in column five the isotropic displacement parameters, B, and in column six the occupancy of each atom.
Lattice constants: a = 5.5908(1) Å, b = 5.5514(1) Å and c = 7.8766(2) Å.

Atoms	x	y	z	B	Occupancy
Bi1/Ca1	0.447(2)	0.010(3)	0.227(2)	-	0.266/0.066
Bi2/Ca2	0.5453(6)	0.0003(1)	0.247(2)	-	0.266/0.066
Bi3/Ca3	0.442(2)	0.0002(2)	0.282(2)	-	0.266/0.066
Ti/Fe/Mg	-0.022(1)	0.011(2)	0	0.03(8)	0.4844/0.2063 /0.3094
O1	0.222(1)	0.719(1)	0.050(2)	1.3(1)	1
O2a	0.208(1)	0.712(2)	0.513(2)	1.7(2)	0.5
O2b	0.208(1)	0.712(2)	0.448(2)	1.7(2)	0.5
O3	0.0128(5)	0.0688(6)	0.253(2)	1.29(8)	1

Table 4.32: Anisotropic atomic displacement parameters for 0.8BTFM-0.1CTO from joint Rietveld refinement in $Pna2_1$, setting bca using a three sites disordered model for the A-site considering anisotropic atomic displacement for the A-site and the O2 split along the c-axis. The column one shows the different atoms of the A-site and in the columns from two to six the six different anisotropic atomic displacement parameters for each atom.

Atoms	U_{11}	U_{22}	U_{33}	U_{12}	U_{23}	U_{12}
Bi/Ca	0.0046(8)	0.0228(9)	0.007(2)	0	0	0

Figure 4.47 a-c) show the structural model of 0.8BTFM-0.2CTO at 27 °C on 0.8BTFM-0.2CTO in *Pna*2_1, setting *bca*, Figure 4.47 d) B-site environment and Figure 4.47 e-g) A-site environment for the three different sites (Bi/Ca1, Bi/Ca2 and Bi/Ca3) respectively.

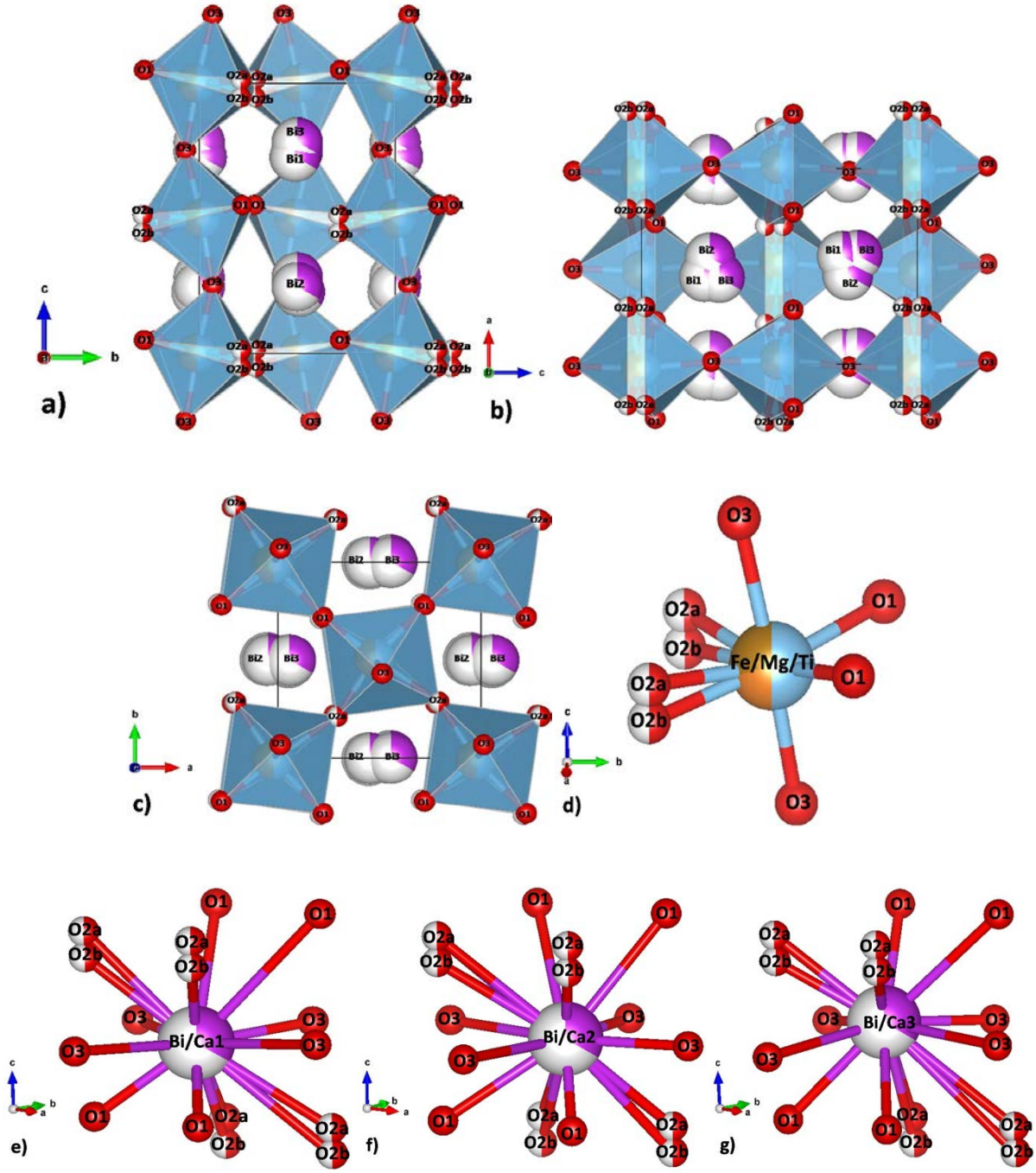

Figure 4.47 Structure of 0.8BTFM-0.2CTO at 27 °C from joint Rietveld refinement in $Pna2_1$, setting bca using a three sites disordered model for the A-site considering anisotropic atomic displacement for the A-site and the O2 split along the c-axis. A-site cations represented in purple and white, B-site cations in brown, blue and orange and oxygens in red a-c) viewed along a, b and c respectively, d) B-site environment and e-g) A-site environment for the three different sites (Bi/Ca1, Bi/Ca2 and Bi/Ca3) respectively.

As shown in Table 4.31, the displacement parameter for O2 obtained is more reasonable (B = 1.7(2)) when this oxygen is split along the c-axis as the Fourier map in Figure 4.45 suggested. Thus, this three sites disordered model for the A-site considering anisotropic atomic displacement

and the O2 split along the c-axis was considered the final structure. The final charge density distribution was studied and Figure 4.48 shows the Fourier map. A-site cations are represented in blue, B-sites in grey and oxygens in red. The white balls represent the maxima of charge density. The red circle indicates the O2 and it is observed that it is split along the c-axis.

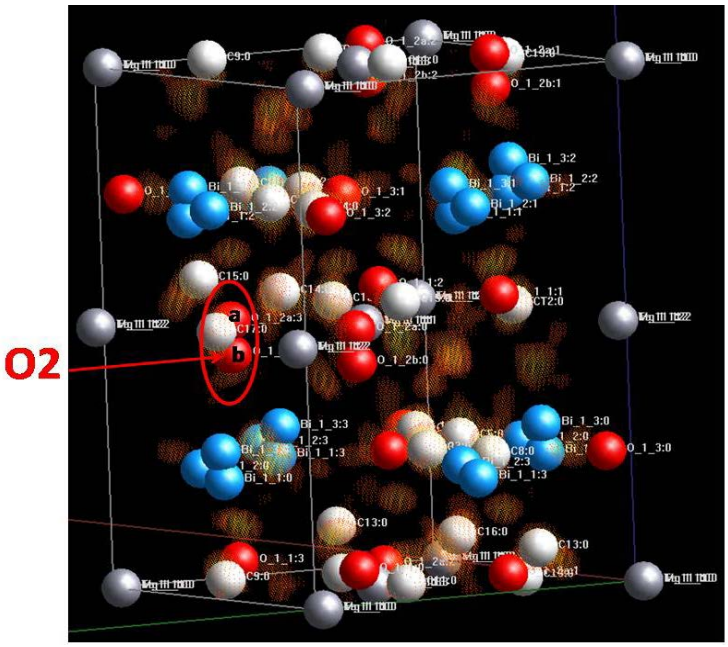

Figure 4.48 Fourier map corresponding to the joint Rietveld refinement for 0.8BTFM-0.2CTO in $Pna2_1$, setting bca at 27 °C using a three sites disordered model for the A-site and considering anisotropic atomic displacement for the A-site and the O2 split along the c-axis. A-site cations are represented in blue, B-sites in grey while oxygens in red. The white balls represent the maxima of charge density. The red circle indicates the O2.

The three sites disorder model for the A-site could affect to the oxygens and this may be the reason of the big displacement parameter obtained in the case of O2 (B = 3.8(2)), Table 4.29 before splitting this oxygen along the c-axis. Therefore, the distances between the three different A-sites and the oxygens, the B-site and the oxygens and the angles between the B-site and oxygens were studied and compared for both models.

Table 4.33: Bond lengths for 0.8BTFM-0.2CTO in $Pna2_1$, setting bca at 27 °C: using a three sites disordered model for the A-site and considering anisotropic atomic displacement for the A-site (left) and using a three sites disordered model for the A-site and considering anisotropic atomic displacement for the A-site and the O2 split along the c-axis (right).

Bond	Bond length (Å)	Bond	Bond length (Å)
Bi/Ca1-O1	2.343(17)	Bi/Ca1-O1	2.380(18)
	2.398(17)		2.403(19)
	3.01(2)		3.00(2)
	3.573(18)		3.53(2)
Bi/Ca1-O2	2.43(2)	Bi/Ca1-O2a / Bi/Ca1-O2b	2.27(2) / 2.53(2)
	2.762(19)		2.91(2) / 2.67(2)
	2.872(19)		3.03(2) / 2.68(2)
	3.157(18)		3.050(19) / 3.359(19)
Bi/Ca1-O3	2.474(13)	Bi/Ca1-O3	2.476(13)
	2.496(14)		2.489(16)
	3.120(14)		3.126(16)
	3.207(12)		3.200(12)
Bi/Ca2-O1	2.166(17)	Bi/Ca2-O1	2.211(19)
	2.839(14)		2.848(15)
	3.086(18)		3.07(2)
	3.174(18)		3.13(2)
Bi/Ca2-O2	2.434(19)	Bi/Ca2-O2a / Bi/Ca2-O2b	2.57(2) / 2.18(2)
	2.751(18)		2.61(2) / 2.934(16)
	2.915(18)		2.800(19) / 2.99(2)
	3.107(16)		3.239(7) / 3.16(2)
Bi/Ca2-O3	2.398(7)	Bi/Ca2-O3	2.399(7)
	2.650(5)		2.642(2)
	2.996(4)		3.002(4)
	3.166(8)		3.165(7)
Bi/Ca3-O1	2.61(2)	Bi/Ca3-O1	2.60(2)
	2.671(18)		2.700(19)
	2.704(18)		2.700(19)
	3.249(18)		3.220(19)
Bi/Ca3-O2	2.512(18)	Bi/Ca3-O2a / Bi/Ca3-O2b	2.57(2) / 2.306(19)
	2.616(18)		2.63(2) / 2.442(19)
	2.74(18)		2.75(2) / 3.00(2)
	3.413(19)		3.294(19) / 3.64(2)
Bi/Ca3-O3	2.423(3)	Bi/Ca3-O3	2.437(15)
	2.438(12)		2.441(13)
	3.207(12)		3.191(15)
	3.226(12)		3.223(12)

Table 4.34: Bond lengths and angles for 0.8BTFM-0.2CTO in $Pna2_1$, setting bca at 27 °C: using a three sites disordered model for the A-site and considering anisotropic atomic displacement for the A-site (left) and using a three sites disordered model for the A-site and considering anisotropic atomic displacement for the A-site and the O2 split along the c-axis (right). Where M is the B-site.

Bond	Bond length (Å)	Bond	Bond length (Å)
M-O1	1.906(14) 2.069(14)	M-O1	1.880(13) 2.065(13)
M-O2	1.953(16) 2.135(14)	M-O2a / M-O2b	1.957(14) / 1.995(14) 2.155(12) / 2.190(12)
M-O3	1.967(17) 2.056(16)	M-O3	1.97(2) 2.054(19)
Bond	Angles / °	Bond	Angles / °
O3-M-O1	84.0(3)	O3-M-O1	84.7(4)
O1-M-O1	90.3(3)	O1-M-O1	91.0(3)
O1-M-O3	97.8(4)	O1-M-O3	97.3(4)
O3-M-O2	96.2(3)	O3-M-O2a / O3-M-O2b	102.0(4) / 87.2(4)
O2-M-O2	87.1(3)	O2b-M-O2b / O2b-M-O2a O2a-M-O2b / O2a-M-O2a	84.8(3) / 87.5(3) 87.5(3) / 86.7(3)
O2-M-O3	80.8(3)	O2a-M-O3 / O2b-M-O3	75.4(3) / 88.8(3)

Table 4.35: Average of bond lengths for 0.8BTFM-0.2CTO in $Pna2_1$, setting bca at 27 °C listed in Table 4.33: using a three sites disordered model for the A-site and considering anisotropic atomic displacement for the A-site (left) and using a three sites disordered model for the A-site and considering anisotropic atomic displacement for the A-site and the O2 split along the c-axis (right).

Bond	Average bond length (Å)	Bond	Average bond length (Å)
Bi/Ca1-O1	2.831	Bi/Ca1-O1	2.828
Bi/Ca1-O2	2.805	Bi/Ca1-O2a / Bi/Ca1-O2b	2.812
Bi/Ca1-O3	2.824	Bi/Ca1-O3	2.823
Bi/Ca2-O1	2.816	Bi/Ca2-O1	2.815
Bi/Ca2-O2	2.802	Bi/Ca2-O2a / Bi/Ca2-O2b	2.810
Bi/Ca2-O3	2.802	Bi/Ca2-O3	2.802
Bi/Ca3-O1	2.808	Bi/Ca3-O1	2.805
Bi/Ca3-O2	2.820	Bi/Ca3-O2a / Bi/Ca3-O2b	2.829
Bi/Ca3-O3	2.823	Bi/Ca3-O3	2.823

Table 4.36: Average of bond lengths for 0.8BTFM-0.2CTO in $Pna2_1$, setting bca at 27 °C listed in Table 4.34: using a three sites disordered model for the A-site and considering anisotropic atomic displacement for the A-site (left) and using a three sites disordered model for the A-site and considering anisotropic atomic displacement for the A-site and the O2 split along the c-axis (right). Where M is the B-site.

Bond	Average bond length (Å)	Bond	Average bond length (Å)
M-O1	1.988	M-O1	1.973
M-O2	2.044	M-O2a / M-O2b	2.074
M-O3	2.011	M-O3	2.012

The bond valence sums (BVS) have been calculated using the Equation 4.1 for all the atoms as Table 4.37 shows.

$$bond\ valence = \exp\left(\frac{(R_o - R)}{B}\right) \qquad \textit{Equation 4.1}$$

where the bond valence is a measure of the strength of the bond, R is the length of a bond between the two given atoms, R_o is a tabulated parameter expressing the (ideal) bond length when the element has exactly valence 1, and B is an empirical constant. The sum of the bond valence around each atom in a compound is equal to the valence (oxidation state) of that atom. The bond valence is given in valence units (v.u) which represent the number of electron pairs that form the bond [11].

Table 4.37: Bond valence sums (BVS) for 0.8BTFM-0.2CTO in $Pna2_1$, setting bca at 27 °C: using a three sites disordered model for the A-site and considering anisotropic atomic displacement for the A-site (second column) and using a three sites disordered model for the A-site and considering anisotropic atomic displacement for the A-site and the O2 split along the c-axis (third column). Calculated BVS for BTFM in the fourth column. BVS are given in valence units (v.u). Values in green and red indicate underbonding and overbonding respectively for an atom.

BVS			
	Model with O2 non split	Model with O2 split along the c-axis	BTFM
$BVS_{Bi1/Ca1}$	2.79 / 1.84	(O2a) 2.85 / 1.92 (O2b) 2.78 / 1.82 (O2a-b) 2.92 / 1.97 (O2a-b) 2.71 / 1.77	2.75
$BVS_{Bi2/Ca2}$	2.78 / 1.86	(O2a) 2.72 / 1.78 (O2b) 2.91 / 2.01 (O2a-b) 2.67 / 1.75 (O2a-b) 2.96 / 2.05	
$BVS_{Bi3/Ca3}$	2.64 / 1.68	(O2a) 2.59 / 1.63 (O2b) 2.82 / 1.87 (O2a-b) 2.47 / 1.55 (O2a-b) 2.94 / 1.94	
$BVS_{Ti/Fe/Mg}$	3.58 / 2.88 / 2.57	(O2a) 3.61 / 2.90 /2.60 (O2b) 3.51 / 2.82 / 2.52 (O2a-b) 4.26 / 2.87 / 2.72 (O2a-b) 4.22 / 2.85 / 2.69	3.38 / 2.71 / 2.43

In Table 4.37 is shown the comparison of the BVS for all the atoms for the model 0.8BTFM-0.2CTO in $Pna2_1$, setting *bca* at 27 °C: using a three sites disordered model for the A-site and considering anisotropic atomic displacement for the A-site (second column) and using a three sites disordered model for the A-site and considering anisotropic atomic displacement for the A-site and the O2 split along the c-axis (third column). The BVS was calculated for BTFM using the same parameters as for the other two models for comparison (fourth column). The A-site is occupied by Bi^{3+} and Ca^{2+} in the case of 0.8BTFM-0.2CTO and just Bi^{3+} in BTFM. The BVS show underbonding for Bi^{3+} for the three cases and underbonding for Ca^{2+} for the model of 0.8BTFM-0.2CTO using a three sites disordered model for the A-site and considering anisotropic atomic displacement parameter (second column). However, for the model using a three sites disordered model for the A-site and considering anisotropic atomic displacement for the A-site and the O2 split along the c-axis (third column) it is observed that the BVS for Bi^{3+} and Ca^{2+} when using distances O2a-b are very close to the ideal values proving that this model is chemically more sensible. The octahedral B-site is occupied by Ti^{4+}, Fe^{3+} and Mg^{2+}. The BVS show underbonding for Ti^{4+} in the case of the model using a three sites disordered model for the A-site and considering anisotropic atomic displacement for the A-site (second column) and BTFM (fourth column). In the case of the model using a three sites disordered model for the A-site and considering anisotropic atomic displacement for the A-site and the O2 split along the c-axis (third column), the BVS show underbonding for Ti^{4+} except for two cases as indicated in red values where the BVS show overbonding. The BVS show underbonding for Fe^{3+} and overbonding for Mg^{2+} for the three different cases.

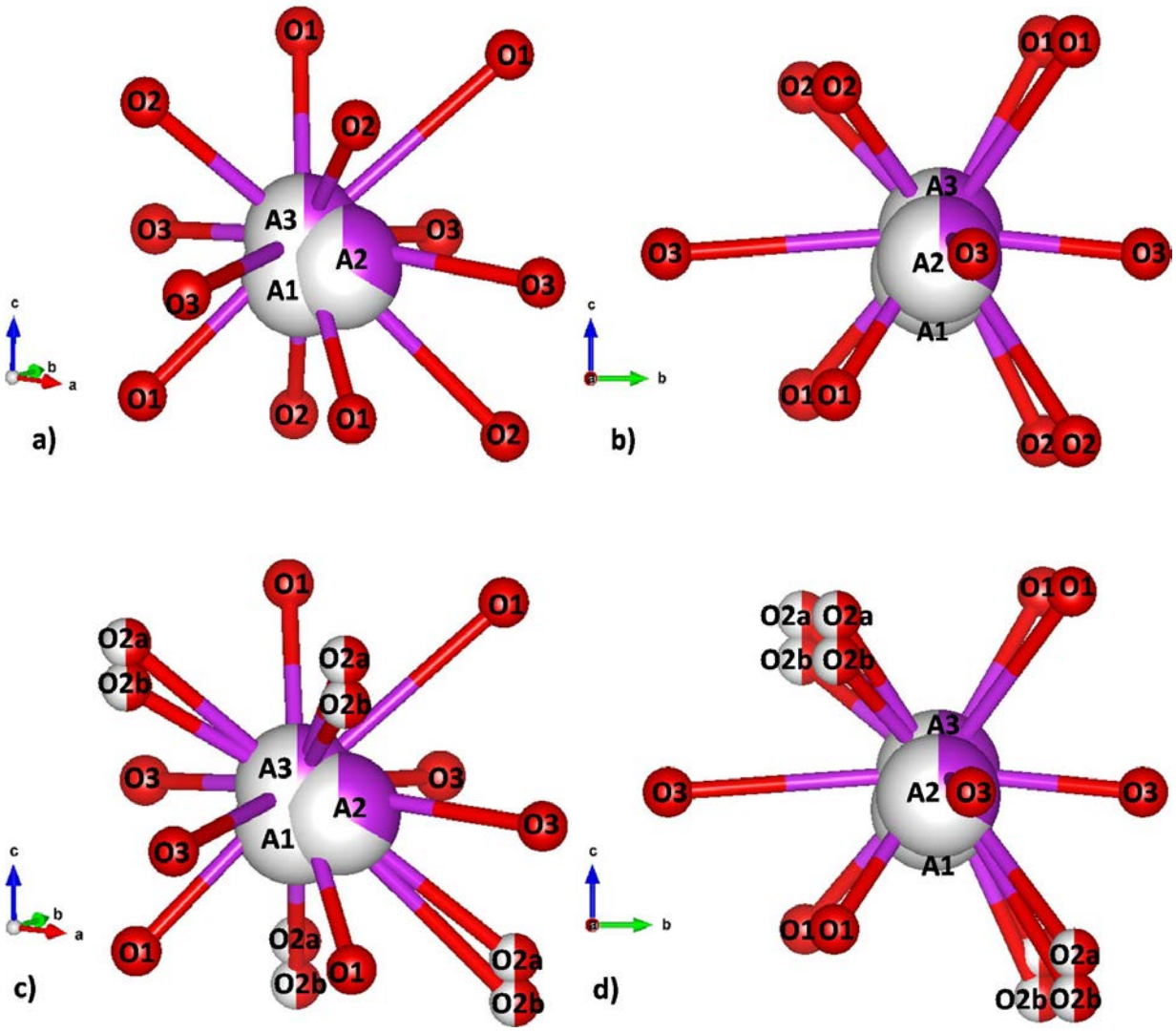

Figure 4.49 A-site environment of 0.8BTFM-0.2CTO at 27 °C from Rietveld refinement in Pna2$_1$, setting bca: a-b) using a three sites disordered model for the A-site considering anisotropic atomic displacement for the A-site and c-d) using a three sites disordered model for the A-site and considering anisotropic atomic displacement for the A-site and the O2 split along the c-axis. A-site cations represented in purple and white whereas oxygens in red and in the case of the split O2 in red and white.

As it is observed in Figure 4.49 b) and Figure 4.49 d) the three different A-sites are oriented along the c-axis. The O3 is at the same plane as the A-sites whereas the O1 and O2 are at a different plane. Thus, it can be expected that the O3 might be not so affected by them. This fact is affirmed by observing the bond lengths averages obtained between the three A-sites and O3 and the B-site and O3 (Tables 4.35 and 4.36 respectively) which are practically the same. Thus, splitting the O2 along the c-axis just affect to the distances between the three A-sites and O1 and O2 and the B-site and O1 and O2. Moreover, reasonable displacement parameters are obtained

for all the atoms so the structure with the O2 along the c-axis is more relaxed than without splitting it.

4.1.6 Microscopy studies

4.1.6.1 Selected area electron diffraction (SAED) on 0.8BTFM-0.2CTO

In order to confirm the symmetry of the O phase a SAED experiment was carried out on a single crystal grain on 0.8BTFM-0.2CTO along the [010] zone axis as Figure 4.48 shows.

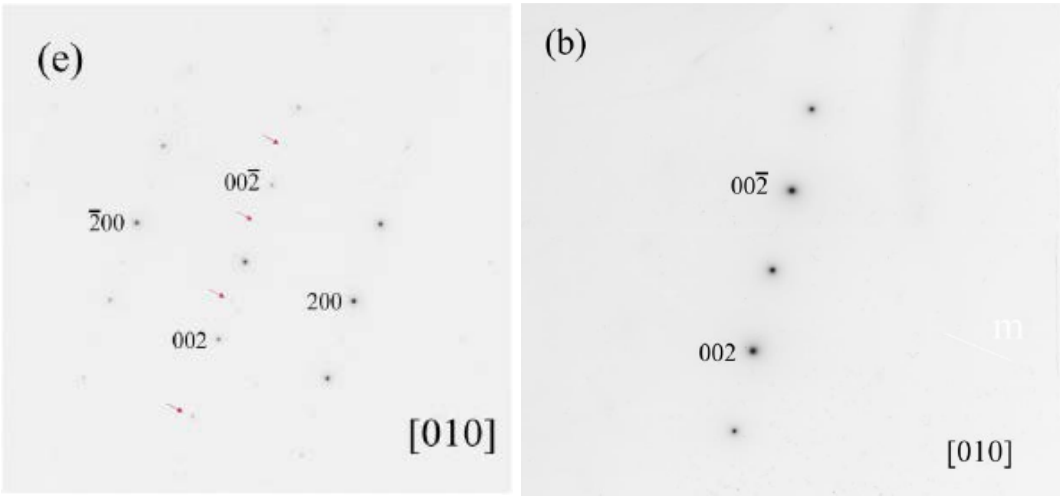

Figure 4.48 a) SAED pattern for the O composition 0.8BTFM-0.2CTO along the [010] axis. The weak l = odd reflections are shown by red arrows. However, they are result of double diffraction and disappeared upon tilting along [200] and [$\bar{2}$00] directions as shown in b). This is consistent with the space groups Pnam and Pna2$_1$. Figures taken from [12].

SAED experiments can not differentiate between the non-polar space group *Pnam* and the polar *Pna*2$_1$ as they have the same reflection conditions. Thus, a convergent beam electron diffraction (CBED) experiment was performed.

4.1.6.2 Convergent beam electron diffraction (CBED) on 0.8BTFM-0.2CTO

CBED is a powerful and conclusive tool for point symmetry determination. Consequently, a CBED experiment was carried out along the [010] axis. *Pnam* belongs to the point symmetry *mmm* and *Pna*2_1 to *mm*2 so in this zone axis, two mirror planes are expected for *Pnam* while only one mirror plane for *Pna*2_1 [13].

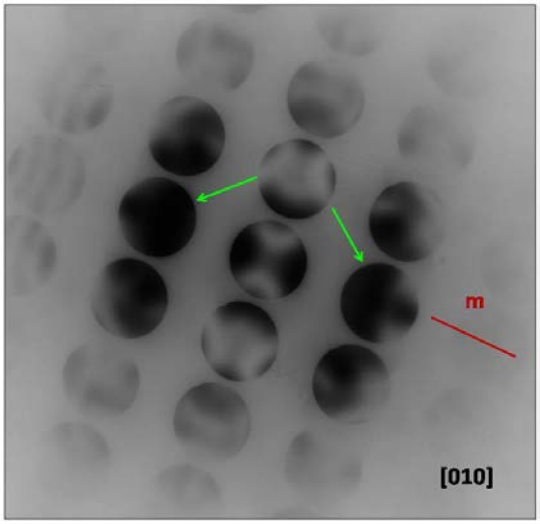

Figure 4.49 CBED pattern along the [010] axis for 0.8BTFM-0.2CTO. The green arrows point out the (200 *) and* $(\bar{2}00)$ *discs whereas the dark red line indicates a mirror plane (m).*

In Figure 4.49 it is observed that there is just one mirror plane (m) as shown with a dark red line. This fact confirms that the space group is *Pna*2_1. This is also corroborated by the absence of inversion symmetry by the non-identical structures in the (200) and $(\bar{2}00)$ discs as shown by the green arrows.

Accordingly, the space group assignment of the O phase based on the reflection conditions in Section 4.1.3 is verified by the results of the CBED experiment. Therefore, the symmetry of the O phase is uniquely confirmed to be *Pna*2_1 and described in terms of tilts and displacements as $a_0^- a_0^- c_+^+$ [14]. After concluding the space group of the O phase it will be designated as $O_{[001]}$ from now on as the space group *Pna*2_1 requires the polarisation to lie along

the [001] cell edge direction. As stated in Section 3.5, Chapter 3 all the compositions with orthorhombic structure are SHG active. It was therefore concluded that the compositions in the range $0.6 \leq x \leq 0.825$ adopt a polar orthorhombic structure with *Pna*2_1 symmetry and with polarisation along $[001]_p$ as shown in Figure 4.50. The polarisation of the $O_{[001]}$ phase is therefore in the same direction as for one of the end-member of PZT, $PbTiO_3$ ($T_{[001]}$) [15] with respect to the primitive perovskite cell but the BO_6 octahedra are tilted to cause the expanded orthorhombic cell.

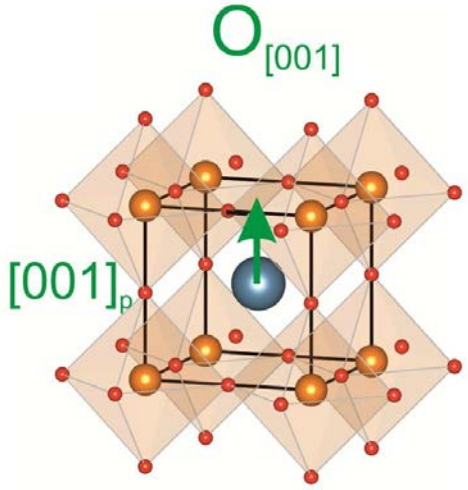

Figure 4.50 Schematic unit cell diagram showing the polarisation direction present in $O_{[001]}$ structure in the cubic perovskite sub cell, where the green arrow indicates the polarisation direction of A-site cations (blue atoms) and B-site cations (orange atoms), with the oxide sublattice (red atoms) defining the shaded BO_6 octahedra. Figure adapted from [12].

4.2 Physical properties measurements on the $O_{[001]}$ phase

The piezoelectric behaviour of compositions on the $O_{[001]}$ phase was explored. Discs were poled and longitudinal piezoelectric coefficients (d_{33}) were measured over the range $0.65 \leq x \leq 0.825$ and their values are listed in Table 4.38.

Table 4.38: Longitudinal piezoelectric coefficient (d_{33}) values for selected compositions with $O_{[001]}$ structure.

COMPOSITION	d_{33} **(pC/N)**
0.65BTFM-0.35CTO	0.1
0.7BTFM-0.3CTO	1.1
0.75BTFM-0.25CTO	1.3
0.8BTFM-0.2CTO	2.2
0.813BTFM-0.187CTO	2.8
0.825BTFM-0.175CTO	49

It is observed in Table 4.38 that d_{33} increases with composition moderately from 0.65BTFM-0.35CTO (d_{33} = 0.1 pC/N) to 0.813BTFM-0.187CTO (d_{33} = 2.8 pC/N) which is higher than for the parent compound BTFM (d_{33} = 0.6 pC/N [16]). However, when reaching the composition 0.825BTFM-0.175CTO which is close to the mixed phase region (O+R) as shown in Figures 3.8 and 3.9, Chapter 3, the piezoelectric coefficient increases sharply (d_{33} = 49 pC/N). This may be due to polarisation rotation [12, 17] as it is observed at the PXRD pattern of a poled pellet for 0.825BTFM-0.175CTO (top panel) with the increase in the intensity of the rhombohedral (104) reflection.

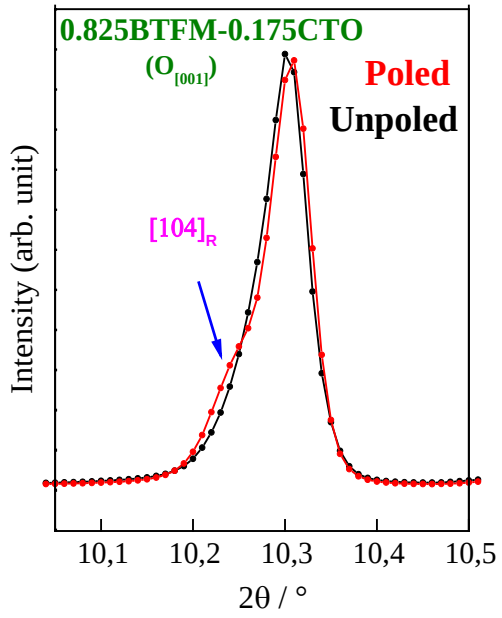

Figure 4.51 XRD patterns for 0.825BTFM-0.175CTO showing the main perovskite peak collected on poled (red data) and unpoled black data pellets (λ ~ 0.45 Å). The blue arrow in the top panel corresponding to the poled pellet points out the intensity of the rhombohedral (104) reflection. Figure adapted from [12].

In order to investigate the behaviour of the piezoelectric coefficient versus temperature an ex-situ d_{33} measurement from 25 °C to 900 °C was carried out on the selected composition 0.8BTFM-0.2CTO.

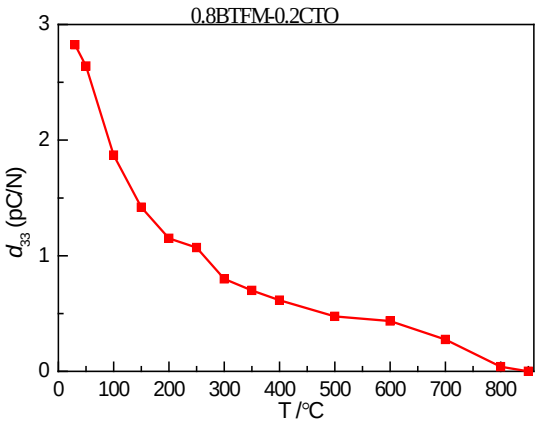

Figure 4.52 Ex-situ d_{33} measurement from 25 °C to 900 °C on 0.8BTFM-0.2CTO.

As observed in Figure 4.52 the piezoelectric coefficient vanishes at T ~ 850 °C for the composition 0.8BTFM-0.2CTO. The disappearance of ex-site d_{33} indicates a Curie temperature (Tc) of 850 °C.

Differential thermal analysis (DTA) were performed on compositions with $O_{[001]}$ structure to detect any phase transitions from 25 °C to 900 °C. However, as shown on Figure 4.53 a) for the selected composition 0.8BTFM-0.2CTO it was not possible to detect any phase transitions from 25 °C to 900 °C. DTA measurements on more compositions with $O_{[001]}$ structure are shown in Appendix C.

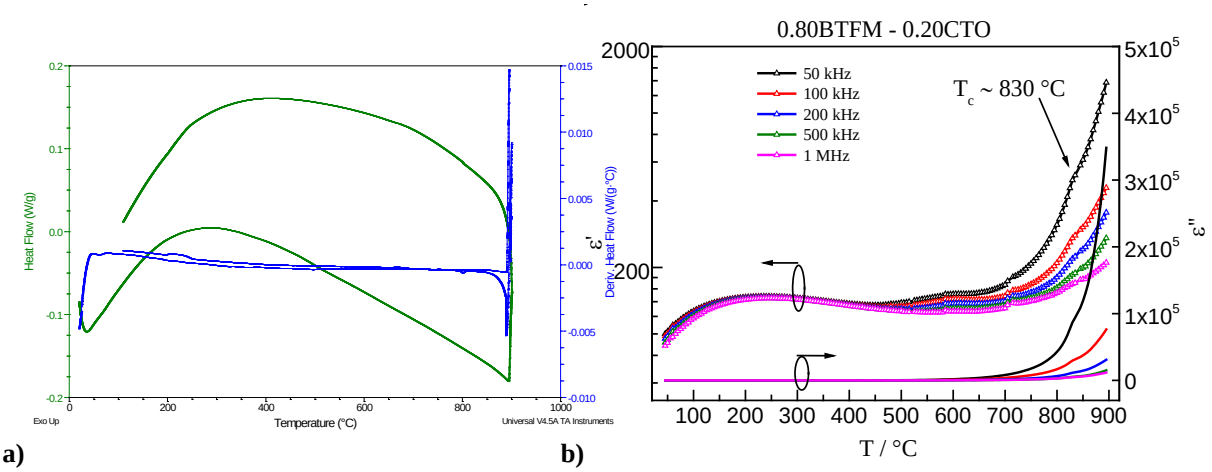

Figure 4.53 a) DTA data from 25 °C to 900 °C are shown in green and its derivative in blue for 0.8BTFM-0.2CTO. b) dielectric data from 25 °C to 900 °C at 50 kHz (black open triangles), 100 kHz (red open triangles), 200 kHz (blue open triangles) and 500 kHz (green open triangles). The black arrow at ~830 °C points out an anomaly in the data for 0.8BTFM-0.2CTO.

Figure 4.53 b) shows dielectric data from 25 °C to 900 °C for 0.8BTFM-0.2CTO at different frequencies and it is observed that there is an anomaly at 830 °C as pointed out with a black arrow and it is consistent with the ex-situ d_{33} measurement where the piezoelectric coefficient vanishes at T ~ 850 °C (Figure 4.52) for 0.8BTFM-0.2CTO. This might indicate a phase transition from a polar ($Pna2_1$) to a non-polar structure similar as in the case of $Bi(Ti_{3/8}Fe_{2/8}Mg_{3/8})O_3 – La(Mg_{1/2}Ti_{1/2})O_6$ - $LaFeO_3$ materials where the composition 0.72BTFM-0.28LFO undergoes a phase transition from the polar space group $Pmc2_1$ to the non-polar $Pmna$

[3]. However, further structural work is needed to confirm this structural transition. A similar behaviour has been observed for composition 0.75BTFM-0.25CTO and the results are shown in Appendix C.

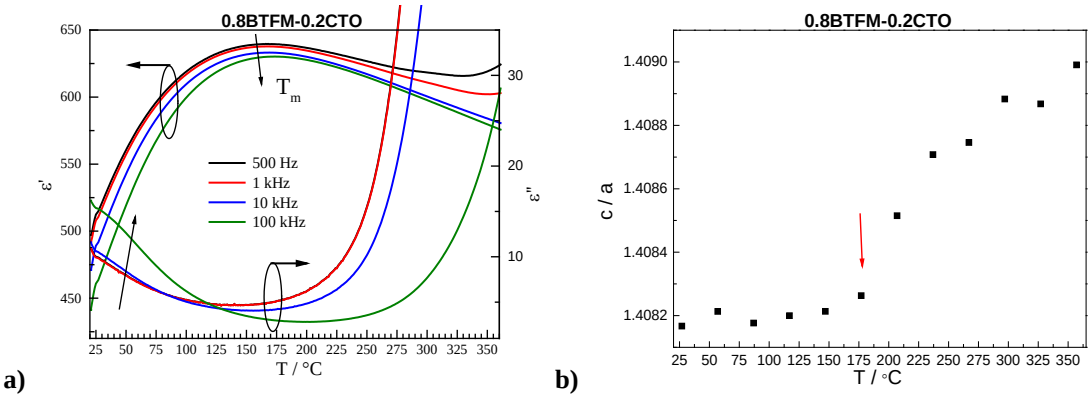

Figure 4.54 a) Dielectric data from 25 °C to 350 °C at 500 Hz (black line), 1 kHz (red line), 10 kHz (blue line) and 100 kHz (green line) for 0.8BTFM-0.2CTO. The black arrow at the top of the graph indicates the maximum at the dielectric, T_m ~ 175 °C. b) c/a versus temperature over the range from 25 °C to 350 °C. The red arrow points out an anomaly at T ~ 175 °C for 0.8BTFM-0.2CTO. The error bars are smaller than symbols.

Figure 4.54 a) shows a broad anomaly at the dielectric data for 0.8BTFM-0.2CTO and a maximum around T_m ~ 175 °C. This anomaly appears to be related to a structural change as observed in Figure 4.54 b) c/a versus temperature for 0.8BTFM-0.2CTO. A similar behaviour has been observed in the material $Bi_{0.5}La_{0.5}FeO_3$ (*Pnma*). In this study, the dielectric anomaly is related to changes in the FeO_6 octahedral tilt magnitudes along with a structural distortion of the octahedra with corresponding A-site displacement along the *c*-axis [18]. Nevertheless, further variable temperature structural work on 0.8BTFM-0.2CTO is needed to confirm this hypothesis.

Polarisation-electric field P((E)) and strain field measurements were performed at a frequency of 1 Hz on the selected composition 0.8BTFM-0.2CTO at 25 °C and at 250 °C, i.e. below and above the T_m ~ 175 °C respectively. The aim of carrying out a P(E) - strain field measurement at 250 °C was to check if it was possible to switch the polarisation as increasing the temperature decreases coercivity. P(E) measurements at 25 °C did not result in saturated loops as Figure 4.55 a) shows. A strain-field measurement was carried out at 25 °C but a butterfly loop

was not achieved. P(E) measurements at 250 °C resulted in a lossy hysteresis loop (Figure 4.55 c). However, a strain-field measurement on 0.8BTFM-0.2CTO at 250 °C displays a butterfly loop characteristic of piezoelectric behaviour as Figure 4.55 d) shows. This fact suggests that at room temperature it was not possible to obtain a butterfly loop before dielectric breakdown due to the high coercive field needed to apply. Nevertheless, at 250 °C a butterfly loop was achieved which is evidence for ferroelectric switching and piezoelectricity.

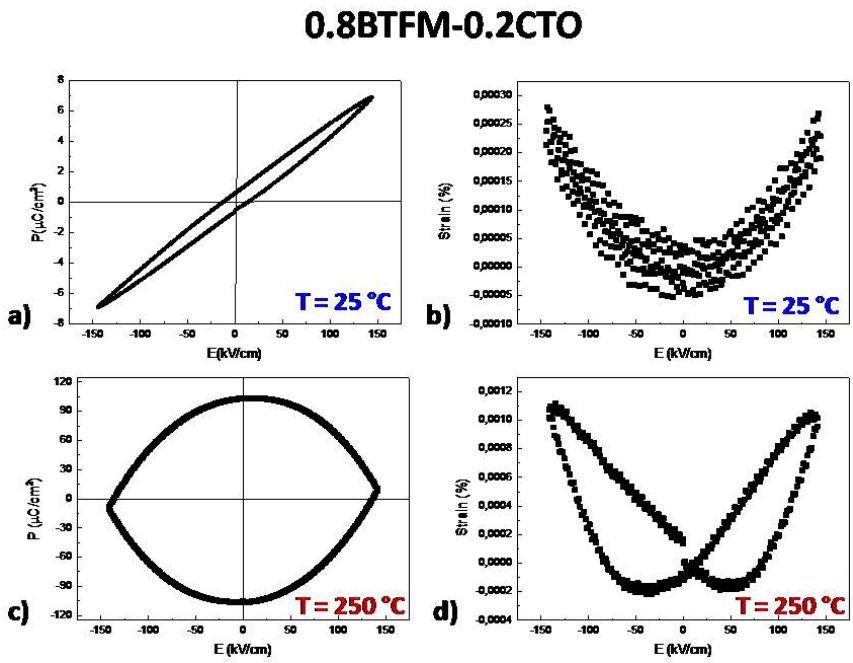

Figure 4.55 a) P(E) hysteresis loops at 25 °C for 0.8BTFM-0.2CTO at 1Hz corresponding to b) the strain-field loop at the same temperature. c) P(E) hysteresis loops at 250 °C for 0.8BTFM-0.2CTO at 1Hz corresponding to d) the strain-field loop at the same temperature.

P(E) measurements at room temperature and at 1 Hz were performed on other compositions with $O_{[001]}$ structure as Figure 4.56 a) and b) show for 0.7BTFM-0.3CTO and 0.75BTFM-0.25CTO respectively. It is observed that P(E) loops for both compositions are not saturated. However, they show a change in slope as the applied voltage is increased. This fact suggests non-linearity and as consequence of genuine domain wall motion [19] which is a necessity for ferroelectrics. The same behaviour has been observed for similar compounds as BTFM [20] and for BTFM -LMT-LFO [3] materials.

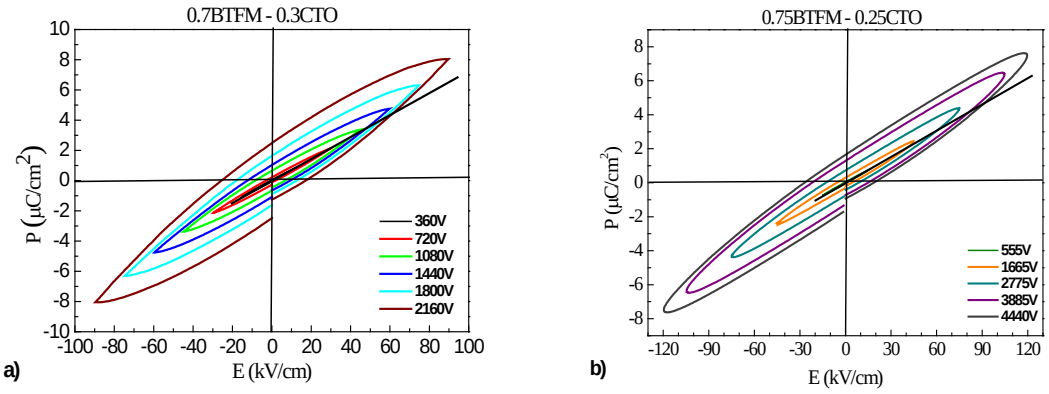

Figure 4.56 P(E) hysteresis loops at room temperature and frequency at 1 Hz for a) 0.7BTFM-0.3CTO and b) 0.75BTFM-0.25CTO. The legends at the right bottom show the voltages applied in each case. The black lines in a) and b) represent the slope of the P(E) hysteresis loop at the lowest voltage and is used to demonstrate nonlinearity.

4.3 Summary and conclusions

Here, a Bi-based system in the range $0.6 \leq x \leq 0.825$ has been synthesised at ambient pressure adopting a polar orthorhombic structure. It crystallises in the polar space group *Pna*2_1 as confirmed by the study of the reflection conditions (Section 4.1.3) and CBED results (Section 4.1.6). A six sites disordered model for the A-site has been built based on the charge density distribution using the MEM / Rietveld method [1] which is equivalent to a three sites disordered model for the A-site considering anisotropic atomic displacement for the A-site (Section 4.1.4.8). The polarisation of the $O_{[001]}$ phase is in the same direction as for one of the end-member of PZT, $PbTiO_3$ ($T_{[001]}$) [15] with respect to the primitive perovskite cell but the BO_6 octahedra are tilted to cause the expanded orthorhombic cell. There are other examples of Bi-based systems with tetragonal structure such as: Bi_2ZnTiO_6 [21] and $BiCoO_3$ [22] although they are just accessible via high pressure. $BiInO_3$ [23] crystallises in *Pna*2_1 but can be prepared just using the high pressure technique. Moreover, in the case of the system $Bi_{1-x}Ca_xFeO_3$ for x = 0.4 a T structure is formed but crystallises in the non-polar space group *I*4/*mcm* [24] while in the case of BTFM-CTO materials the $O_{[001]}$ crystallises in the polar space group *Pna*2_1. Therefore, we have a polar $O_{[001]}$ in the range $0.6 \leq x \leq 0.825$ and for $x \geq 0.95$ a polar R structure is formed with polarisation

along $[111]_p$. Thus, the mixed phase region ($O_{[001]}$ + $R_{[111]}$) $0.8375 \leq x \leq 0.925$ is formed by two polar phases with different polarisation directions as for PZT [15] and an MPB could be obtained where the electromechanical properties could be maximised.

The piezoelectric coefficient for the polar O phase for BTFM-CTO materials has been improved with d_{33} = 2.8 pC/N for 0.813BTFM-0.187CTO in comparison with the parent compound BTFM (d_{33} = 0.6 pC/N [16]). However, for composition 0.825BTFM-0.175CTO (close to mixed phase region ($O_{[001]}$ + $R_{[111]}$) as shown in Figures 3.8 and 3.9, Chapter 3) the piezoelectric coefficient increases sharply (d_{33} = 49 pC/N) and this is possibly due to polarisation rotation [12, 17]. However, this piezoelectric coefficient value is still not comparable with PZT (d_{33} = 223 pC/N [25]). Ex-situ d_{33} measurements at variable temperature suggest that *Tc* is around 850 °C because at this temperature the piezoelectric coefficient vanishes (Figure 4.52). As observed in impedance measurements from 25 °C to 900 °C for 0.8BTFM-0.2CTO (Figure 4.53b) there is an anomaly around *Tc* ~ 830 °C, confirming thus the ex-situ d_{33} measurements which indicate that *Tc* ~ 850 °C. In the case of the selected composition 0.8BTFM-0.2CTO, a broad anomaly at the dielectric data with a T_m ~ 175 °C is observed and consistent with the trend of c/a with temperature (Figure 4.54). For $Bi_{0.5}La_{0.5}FeO_3$ (*Pnma*) a similar behaviour has been observed where the dielectric anomaly is related to changes in the FeO_6 octahedral tilt magnitudes along with a structural distortion of the octahedra with corresponding A-site displacement along the *c*-axis [18]. Strain field loops on the selected composition 0.8BTFM-0.2CTO at room temperature do not show a butterfly shape characteristic of piezoelectric behaviour (Figure 4.55b)). However at 250 °C a butterfly loop is displayed (Figure 4.55d)). This fact suggests that at room temperature a butterfly loop is not achieved because of the high coercive field needed to apply so pellets break down before. Nevertheless, at 250 °C a butterfly loop could be achieved as the coercivity is decreased when increasing temperature. P(E) measurements did not result in saturated loops as shown in Figure 4.55 a), Figure 4.56 a) and

Figure 4.56 b) for selected compositions with O structure. This fact could be due to the high Curie temperature (*Tc* ~ 830 °C) of the polar O phase. Thus a large coercive field is needed to apply to reach a saturated loop but the pellet breaks down before. Nevertheless, electrical polarisation does not evolve as linear function of the driving field amplitude and this nonlinearity is a requisite for ferroelectrics and therefore domain wall motion [19]. This behaviour has been observed for similar materials as BTFM [20] and BTFM -LMT-LFO [3].

4.4 References

1. Takata, M., Umeda, B., Nishibori, E., Sakata, M., Saito, Y., Ohno, M. and Shinohara, H., *Nature*, 1995. **377**(6544): p. 46-49.
2. Louer D. and Boultif, A., *Zeitschrift Fur Kristallographie*, 2007: p. 191-196.
3. Dolgos M. R., Adem, U., Manjon-Sanz A., Wan X. M., Comyn T. P., Stevenson T., Bennett J., Bell A. J., Tran T. T., Halasyamani P. S., Claridge J. B. and Rosseinsky M. J., *Angewandte Chemie-International Edition*, 2012. **51**: p. 10770-10775.
4. Khomchenko V. A., Shvartsman, V. V.., Borisov P., Kleemann W., Kiselev D. A., Bdikin I. K., Vieira J. M. and Kholkin A. L., *Journal of Physics D-Applied Physics*, 2009. **42**: p. 045418.
5. Sasaki S., Prewitt, C. T., Bass J. D. and Schulze W. A., *Acta Crystallographica Section C-Crystal Structure Communications*, 1987. **43**: p. 1668-1674.
6. Bartkowiak M., Kearley, G. J., Yethiraj M. and Mulders A. M., *Physical Review B*, 2011. **83**: p. 064102(1-5).
7. Johnston K. E., Tang C. C., Parker J. E., Knight K. S., Lightfoot P. and Ashbrook S. E., *Journal of the American Chemical Society*, 2010. **132**: p. 8732-8746.
8. Kwei G. H., Lawson, A. C., Billinge S. J. L. and Cheong S. W., *Journal of Physical Chemistry*, 1993. **97**: p. 2368-2377.
9. Sakata, M. and Sato, M., *Acta Crystallographica Section A*, 1990. **46**: p. 263-270.
10. Capillas, C., Sururi T. E., de la Flor, G., Orobengoa, D., Perez-Mato, M., Aroyo, I., *Zeitschrift Fur Kristallographie*, 2011. **226**(2): p. 186-196.
11. http://www.iucr.org/resources/data/datasets/bond-valence-parameters.
12. Mandal, P., Manjon-Sanz, A., Corkett, A. J., Comyn, T. P, Dawson, K., Stevenson T., Bennett J., Henrichs, L. F., Bell, A. J., Nishibori, E., Takata, M., Marco, Z., Dolgos, M. R., Adem, U., Wan, X., Pitcher, M. J., Romani, S., T. Tran, T. T., Halasyamani, P. S., Claridge, J. B. and Rosseinsky, M. J., *Submitted to Advanced Materials* 2014.
13. Williams D. B. and Carter C.B., *Transmission electron microscopy: Diffraction II, Plenum Press*, New York 1996.
14. Stokes, H. T., Kisi, E. H., Hatch, D. M. and Howard, C. J., *Acta Crystallographica Section B-Structural Science*, 2002. **58**: p. 934-938.
15. Noheda, B., Cox, D. E., Shirane, G., Gonzalo, J. A., Cross, L. E. and Park, S. E., *Applied Physics Letters*, 1999. **74**(14): p. 2059-2061.
16. Dolgos, M., Adem, U., Wan, X., Xu, Z., Bell, A. J., Comyn, T. P., Stevenson, T., Bennett, J., Claridge, J. B. and Rosseinsky, M. J. *Chemical Science*, 2012. **3**: p. 1426-1435.
17. Guo, R., Cross, L. E., Park, S. E., Noheda, B., Cox, D. E. and Shirane, G., *Physical Review Letters*, 2000. **84**(23): p. 5423-5426.
18. Kavanagh, C. M., Goff, R. J., Daoud-Aladine, A., Lightfoot, P. and Morrison, F. D., *Chemistry of Materials*, 2012. **24**(23): p. 4563-4571.
19. Li, S. P., Cao, W. W. and Cross, L. E., *Journal of Applied Physics*, 1991. **69**(10): p. 7219-7224.
20. Bridges, M. A., Suchomel, M. R., Kuang, X., Sterianou, I., Sinclair, D. C. and Rosseinsky, M. J., *Angewandte Chemie-International Edition*, 2007. **46**: p. 8785 –8789.
21. Suchomel, M. R., Fogg, A. M., Mathieu, A., Hongjun, N., Claridge, J. B. and Rosseinsky, M. J., *Chemistry of Materials*, 2006. **18**(21): p. 4987-4989.
22. Belik, A. A., Iikubo, S., Kodama, K., Igawa, N., Shamoto, S., Niitaka, S., Azuma, M., Shimakawa, Y., Takano, M., Izumi, F. and Takayama-Muromachi, E., *Chemistry of Materials*, 2006. **18**(3): p. 798-803.

23. Belik, A. A., Stefanovich, S. Y., Lazoryak, B. I. and Takayama-Muromachi, E., *Chemistry of Materials*, 2006. **18**(7): p. 1964-1968.
24. Troyanchuk, I. O., Karpinsky, D. V., Bushinskii, M. V., Prokhnenko, O., Kopcevicz, M., Szymczak, R. and Pietosa, J, *Journal of Experimental and Theoretical Physics*, 2008. **107**(1): p. 83-89.
25. Jaffe, B., Piezoelectric Ceramics, *Academic Press: London*, New York, 1971.

CHAPTER 5 - Structural analysis and physical properties measurements on the mixed phase, orthorhombic ($O_{[001]}$) + rhombohedral ($R_{[111]}$) and the rhombohedral phase

This chapter focuses on the mixed phase region ($O_{[001]}$ + $R_{[111]}$) and the rhombohedral phase of BTFM-CTO materials. In Section 5.1.1, preliminary results of structural analysis on the mixed phase region are presented. Furthermore, the structural analysis of the known $R_{[111]}$ phase will be shown in Section 5.1.2. The promising results of the electromechanical properties measured on the mixed phase region will be presented and compared with the outcomes of the single phase $O_{[001]}$ and $R_{[111]}$ in Section 5.2.

5.1 Structural analysis of the mixed phase (orthorhombic + rhombohedral) and the rhombohedral phase

5.1.1 Le Bail fits on the mixed phase region at room temperature

In the compositional range $0.8375 \leq x \leq 0.925$, the powder X-ray diffraction (PXRD) patterns could not be indexed with either $O_{[001]}$ (Figures 3.10, 5.1, 5.4, 5.7 and 5.10) or $R_{[111\ ]}$ (Figures 3.11, 5.2, 5.5, 5.8 and 5.11) structures. However, when Le Bail fits were carried out in ($O_{[001]}$ + $R_{[111]}$) good fits were achieved with all the peaks indexed (Figures 3.12, 5.3, 5.6, 5.9 and 5.12) consistent with a mixed phase structure ($O_{[001]}$ + $R_{[111]}$). The Le Bail fits and lattice constants will be shown in Appendix A. Here, the mixed phase region spans $\Delta x \sim 0.08$ being the width comparable to those reported for the MPB region of PZT ($\Delta x \sim 0.01 - 0.15$ [1, 2]) and other lead-free MPB systems ($\Delta x \sim 0.08$ for NBT – KBT [3] and $\Delta x \sim 0.01$ for NBT – BTO [4]). All the compositions in the mixed phase region are SHG active and lie between two polar phases, confirming their polarity at room temperature. Thus, in the BTFM-CTO system there is a mixed phase region ($O_{[001]}$ + $R_{[111]}$) formed by two polar phases with different polarisation directions as Figure 5.13 shows and an MPB could be obtained where the electromechanical properties might be maximised as in PZT [5].

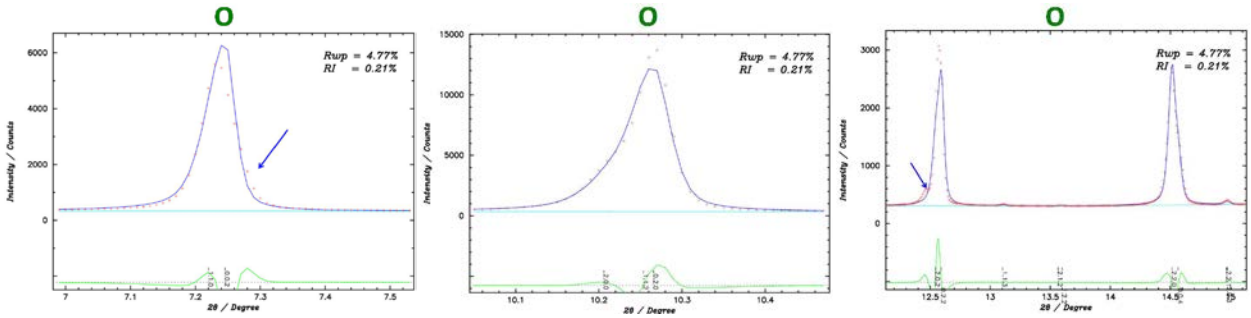

Figure 5.1 Enlargements of the Le Bail fit for 0.835BTFM-0.165CTO in the $O_{[001]}$ space group $Pna2_1$ at room temperature. The red points represent the observed data while the blue solid line represents the model. The difference green curve is below. The black tics represent positions of Bragg reflections. The blue arrows indicate the peaks with a poor fit.

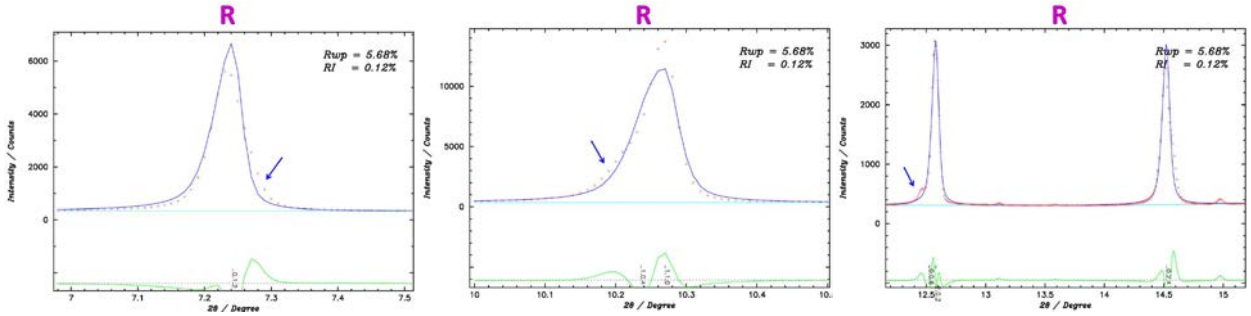

Figure 5.2 Enlargements of the Le Bail fit for 0.835BTFM-0.165CTO in the $R_{[111]}$ space group R3c at room temperature. The red points represent the observed data while the blue solid line represents the model. The difference green curve is below. The black tics represent positions of Bragg reflections. The blue arrows indicate the peaks with a poor fit.

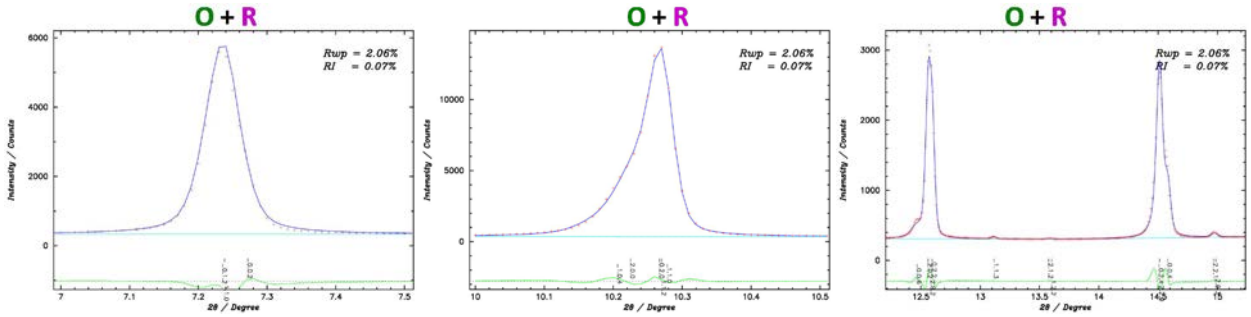

Figure 5.3 Enlargements of the Le Bail fit for 0.835BTFM-0.165CTO with one $O_{[001]}$ and one $R_{[111]}$ phase in space groups $Pna2_1$ and R3c respectively at room temperature. The red points represent the observed data while the blue solid line represents the model. The difference green curve is below. The black tics represent positions of Bragg reflections.

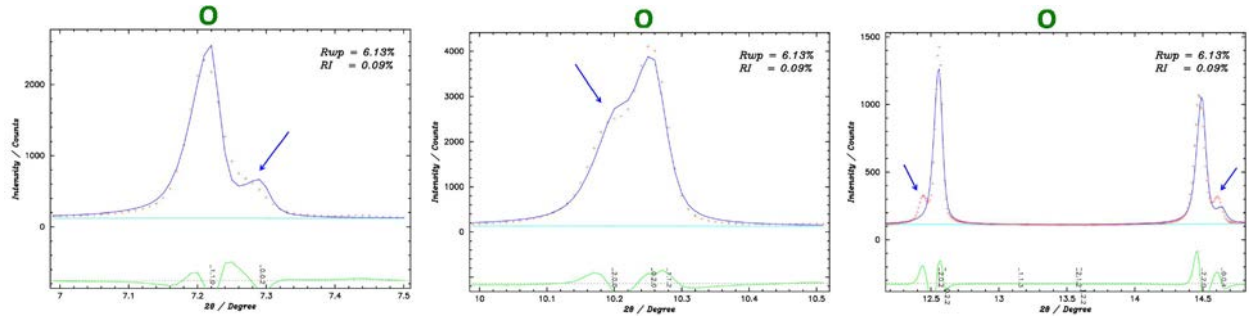

Figure 5.4 Enlargements of the Le Bail fit for 0.875BTFM-0.125CTO in the $O_{[001]}$ space group $Pna2_1$ at room temperature. The red points represent the observed data while the blue solid line represents the model. The difference green curve is below. The black tics represent positions of Bragg reflections. The blue arrows indicate the peaks with a poor fit.

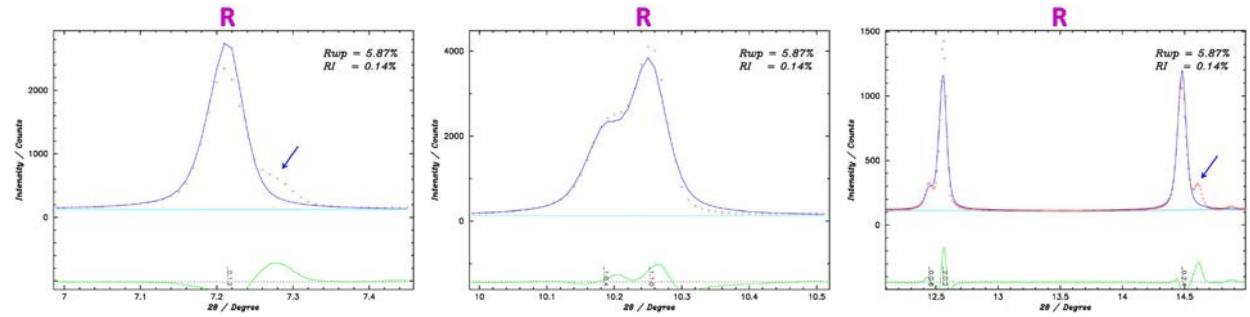

Figure 5.5 Enlargements of the Le Bail fit for 0.875BTFM-0.125CTO in the $R_{[111]}$ space group R3c at room temperature. The red points represent the observed data while the blue solid line represents the model. The difference green curve is below. The black tics represent positions of Bragg reflections. The blue arrows indicate the peaks with a poor fit.

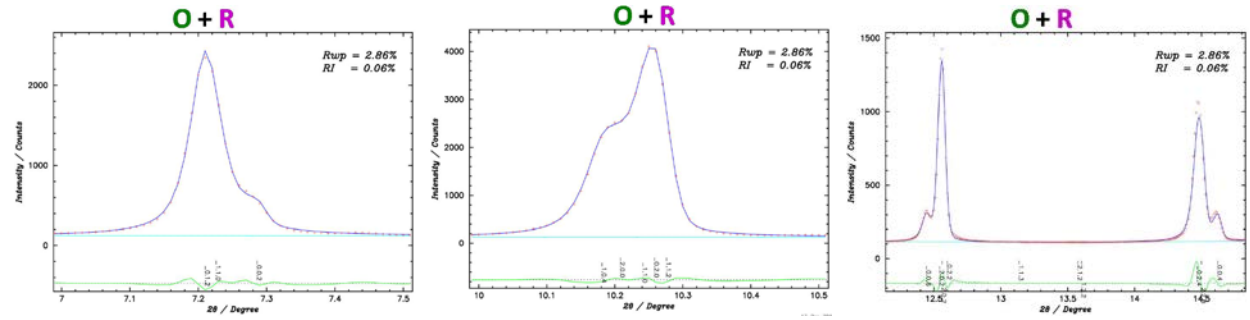

Figure 5.6 Enlargements of the Le Bail fit for 0.875BTFM-0.125CTO with one $O_{[001]}$ and one $R_{[111]}$ phase in space groups $Pna2_1$ and R3c respectively at room temperature. The red points represent the observed data while the blue solid line represents the model. The difference green curve is below. The black tics represent positions of Bragg reflections.

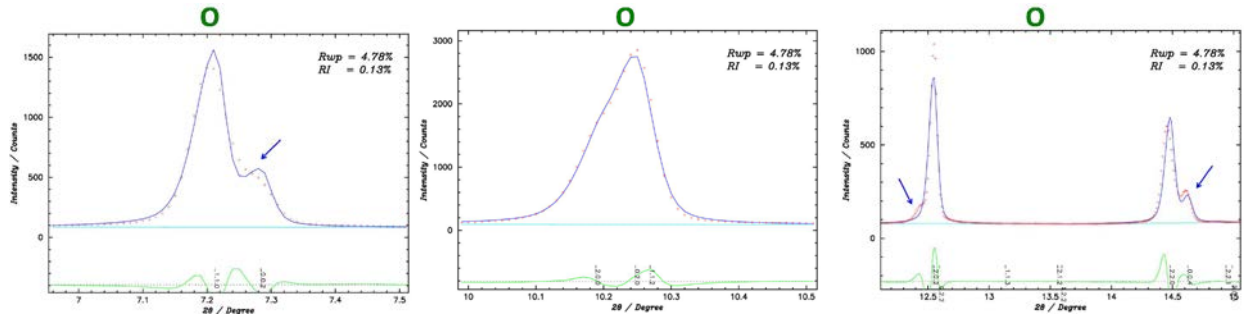

Figure 5.7 Enlargements of the Le Bail fit for 0.9BTFM-0.1CTO in the $O_{[001]}$ space group $Pna2_1$ at room temperature. The red points represent the observed data while the blue solid line represents the model. The difference green curve is below. The black tics represent positions of Bragg reflections. The blue arrows indicate the peaks with a poor fit.

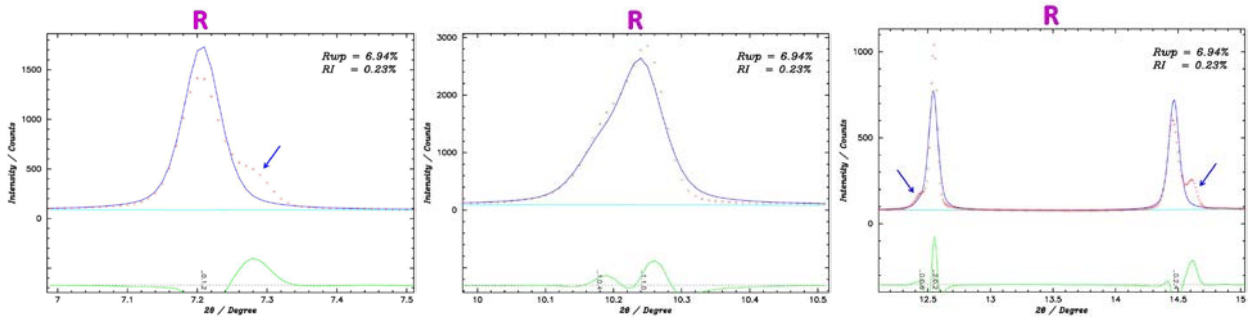

Figure 5.8 Enlargements of the Le Bail fit for 0.9BTFM-0.1CTO in the $R_{[111]}$ space group R3c at room temperature. The red points represent the observed data while the blue solid line represents the model. The difference green curve is below. The black tics represent positions of Bragg reflections. The blue arrows indicate the peaks with a poor fit.

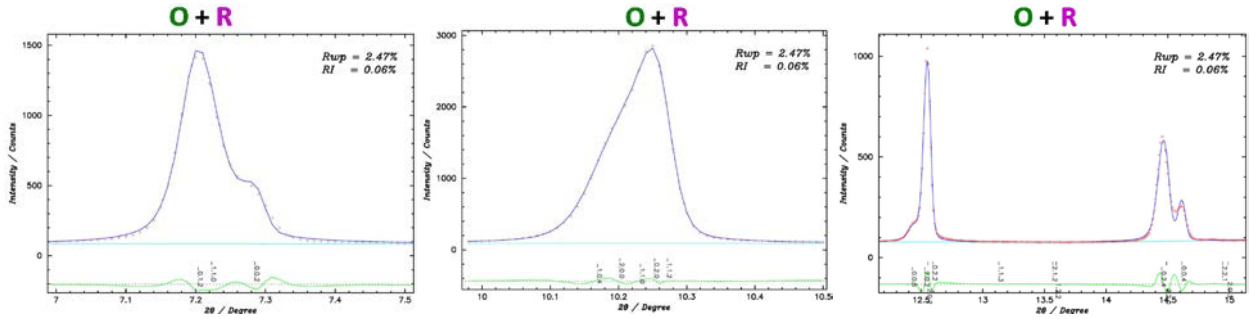

Figure 5.9 Enlargements of the Le Bail fit for 0.9BTFM-0.1CTO with one $O_{[001]}$ and one $R_{[111]}$ phase in space groups $Pna2_1$ and R3c respectively at room temperature. The red points represent the observed data while the blue solid line represents the model. The difference green curve is below. The black tics represent positions of Bragg reflections.

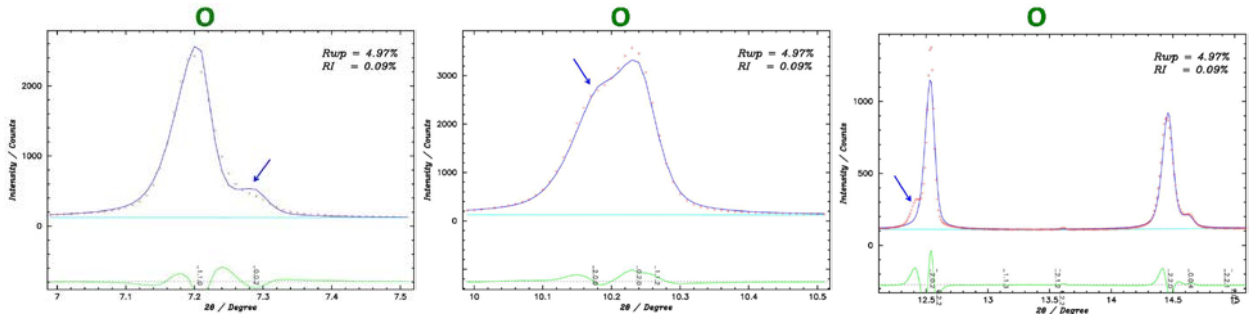

Figure 5.10 Enlargements of the Le Bail fit for 0.925BTFM-0.075CTO in the $O_{[001]}$ space group $Pna2_1$ at room temperature. The red points represent the observed data while the blue solid line represents the model. The difference green curve is below. The black tics represent positions of Bragg reflections. The blue arrows indicate the peaks with a poor fit.

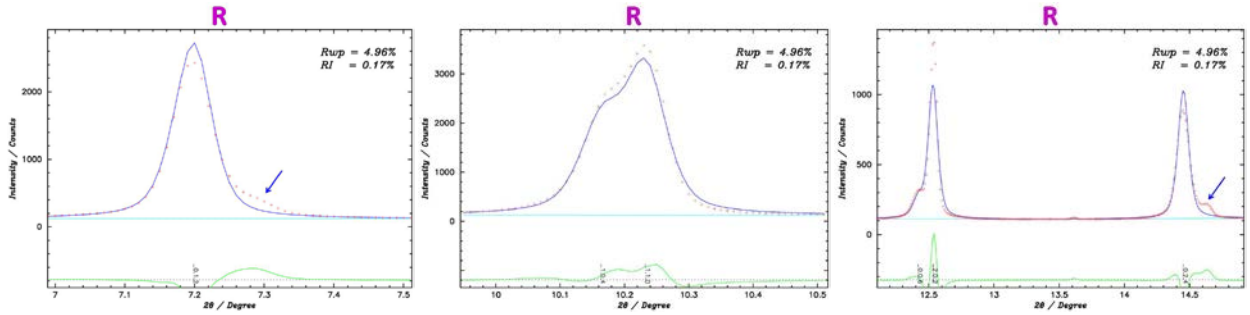

Figure 5.11 Enlargements of the Le Bail fit for 0.925BTFM-0.075CTO in the $R_{[111]}$ space group R3c at room temperature. The red points represent the observed data while the blue solid line represents the model. The difference green curve is below. The black tics represent positions of Bragg reflections. The blue arrows indicate the peaks with a poor fit.

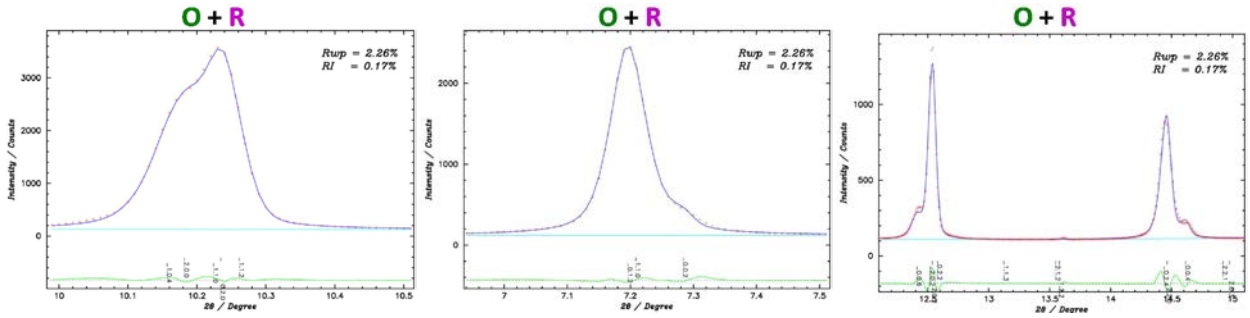

Figure 5.12 Enlargements of the Le Bail fit for 0.925BTFM-0.075CTO with one $O_{[001]}$ and one $R_{[111]}$ phase in space groups $Pna2_1$ and R3c respectively at room temperature. The red points represent the observed data while the blue solid line represents the model. The difference green curve is below. The black tics represent positions of Bragg reflections.

Table 5.1: Comparison of R_{wp} and R_I obtained from Le Bail fits performed on compositions in the mixed phase region as $O_{[001]}$, $R_{[111]}$ and $O_{[001]}$ +$R_{[111]}$.

Composition	Phase	R_{wp} / R_I / %
0.835BTFM-0.165CTO	Orthorhombic	4.77/0.21
	Rhombohedral	5.68/0.12
	Orthorhombic + Rhombohedral	2.06/0.07
0.875BTFM-0.125CTO	Orthorhombic	6.13/0.09
	Rhombohedral	5.87/0.14
	Orthorhombic + Rhombohedral	2.86/0.06
0.9BTFM-0.1CTO	Orthorhombic	4.78/0.13
	Rhombohedral	6.94/0.23
	Orthorhombic + Rhombohedral	2.47/0.06
0.925BTFM-0.175CTO	Orthorhombic	4.97/0.09
	Rhombohedral	4.96/0.17
	Orthorhombic + Rhombohedral	2.26/0.17

In Table 5.1 it was observed that for the Le Bail fits performed on compositions in the mixed phase region ($O_{[001]}$ + $R_{[111]}$), $0.8375 \leq x \leq 0.925$, the R_{wp} and R_I values obtained are lower than for single $O_{[001]}$ and $R_{[111]}$.

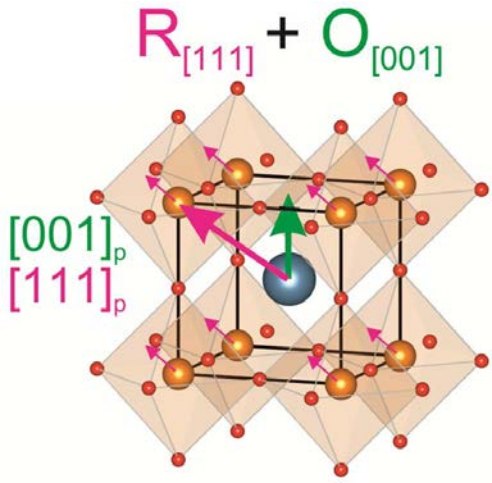

Figure 5.13 Schematic unit cell diagram showing the polarisation direction present in the $O_{[001]}$ + $R_{[111]}$ structure in the cubic perovskite sub cell, where the arrows indicate the polarisation direction of A-site cations (blue atoms) and B-site cations (orange atoms), with the oxide sublattice (red atoms) defining the shaded BO_6 octahedra. Figure adapted from [6].

However, the structural characterisation of this complex mixed phase region, $O_{[001]}$ + $R_{[111]}$, is expected to be challenging and will be the subject of future study. The same situation occurs with the structure of PZT at and near MPB which after many years of extensive study still remains the subject of controversy [7-13].

5.1.2 Rietveld analysis on the rhombohedral phase

Rietveld refinement was performed using synchrotron data at 27 °C on 0.95BTFM-0.05CTO in *R*3*c* as the parent compound BTFM [14]. The 2θ range of analysis was from 3° to 74°. The scale factor, peak shape parameters, lattice constants, atomic positions and atomic displacement parameters were refined.

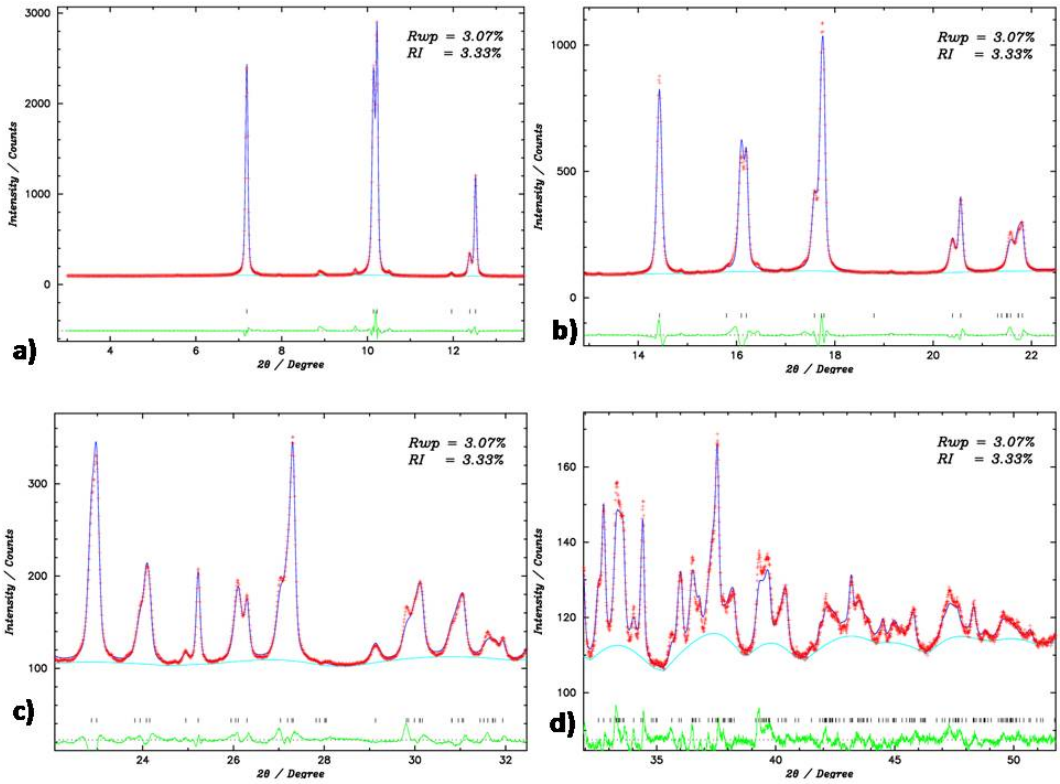

Figure 5.14 Rietveld refinement for 0.95BTFM-0.05CTO in R3c at 27 °C. The red crosses represent the observed data while the blue solid line represents the model. The difference green curve is below. The black tics represent positions of Bragg reflections.

Figure 5.14 shows Rietveld refinements for 0.95BTFM-0.05CTO in *R*3*c*. The reliability factors based on the weighted profiles, R_{wp}, and Bragg intensities, R_I are 3.07% and 3.23% respectively. The refined parameters are listed in Table 5.2.

Table 5.2: Atomic parameters for 0.95BTFM-0.05CTO from Rietveld refinement in R3c. The column one shows the different atoms; in columns two, three and four the atomic coordinates of each atom being x, y and z respectively; in column five the isotropic atomic displacement parameters, B, and in column six the occupancy of each atom.
Lattice constants: a = 5.5949(5) Å and c = 13.8708(3) Å.

Atoms	x	y	z	B	Occupancy
Bi/Ca	0	0.0243 (6)	0	1.09(2)	0. 316 /0. 016
Ti/Fe/Mg	0	0	0.2244(3)	0.2	0.41/0.23/0.36
O1	0.444(1)	0.0124(8)	0.9585 (3)	1.3(1)	1

The composition 0.95BTFM-0.05CTO was indexed in a rhombohedral unit cell with space group *R*3*c* as the parent compound BTFM [14] and with a polarisation along $[111]_p$ as Figure 5.15 shows.

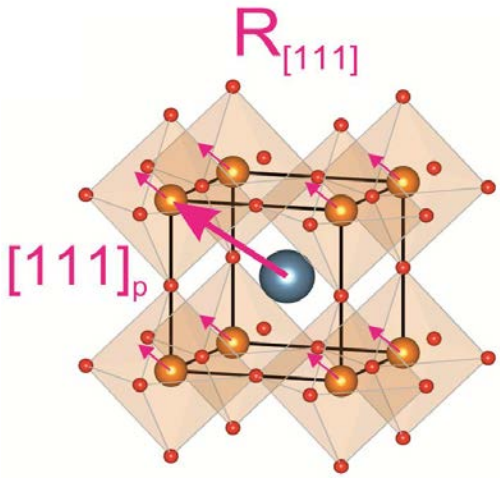

Figure 5.15 Schematic unit cell diagram showing the polarisation direction present in the $R_{[111]}$ structure in the cubic perovskite sub cell. Pink arrows indicate the polarisation direction of A-site cations (blue atom) and B-site cations (orange atoms), with the oxide sublattice (red atoms) defining the shaded BO_6 octahedra. Figure adapted from [6].

5.2 Physical properties of BTFM-CTO solid solutions

The piezoelectric behaviour of BTFM-CTO materials was examined. Discs were poled and longitudinal piezoelectric coefficients (d_{33}) were measured over the full range of compositions as Figure 5.16 a) shows. Compositions with $O_{[001]}$ structure ($0.65 \leq x \leq 0.825$) show small finite d_{33} values and they increase with BTFM content. Compositions with $R_{[111]}$ structure ($x \geq 0.95$) show an increase in d_{33} with decreasing x and small finite values. These finite d_{33} values observed in the $O_{[001]}$ and $R_{[111]}$ structures are consistent with their polarity shown by SHG measurements and polar structures. Most interestingly, high d_{33} values were obtained in the range $0.825 \leq x \leq 0.925$ being this fact consistent with the mixed phase structure. A maximum d_{33} of 53 pC/N has been obtained for 0.837BTFM-0.165CTO, this value is a quarter of that of PZT (223 pC/N [5]) and about two orders of magnitude greater than for the parent material BTFM (0.6 pC/N [15]). Thus, the aim of improving the electromechanical properties of BTFM has been achieved. However, in comparison with other lead-free piezoceramics the piezoelectric coefficient values obtained at the MPB for BTFM-CTO are smaller. In the case of NBT – BTO at the MPB d_{33} = 122 – 176 pC/N [16, 17], for NBT – KBT d_{33} = 140 – 190 pC/N [16], for NBT – KBT – BTO d_{33} = 170 pC/N [18] and for BFO – BTO d_{33} = 80 – 116 pC/N [19]. Although single phase $O_{[001]}$ and $R_{[111]}$ are polar, polarisation-electric field (P(E)) measurements did not result in saturated loops as Figures 5.16 b) and d) show for 0.8BTFM-0.2CTO and 0.95BTFM-0.05CTO respectively. This is due to the high coercive field which is beyond the range (150 – 200 kV/cm) accessed here. However, all the compositions in the mixed phase region show saturated P(E) loops (Figure 5.16 c)), Figure 5.17 and Figure 5.18 a). This fact agrees well with the enhanced d_{33} in the mixed phase region obtained.

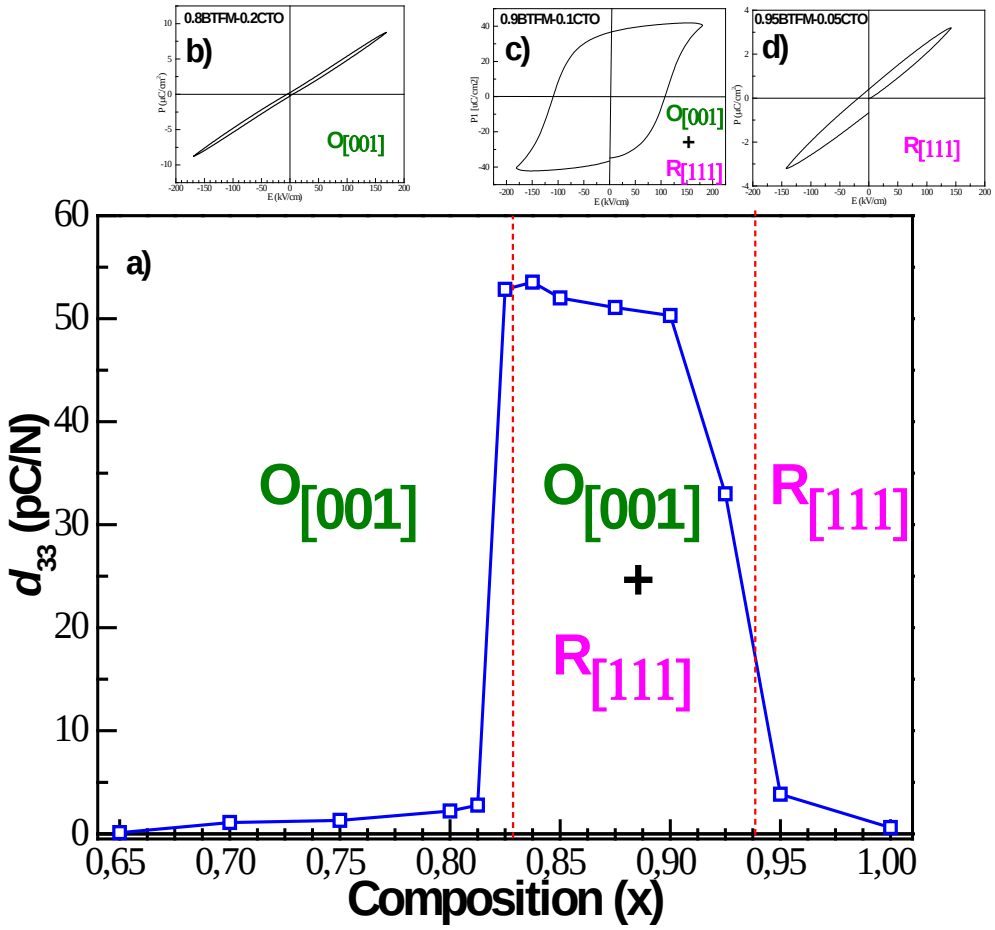

Figure 5.16 a) Variation of longitudinal piezoelectric coefficient (d_{33}) with BTFM content (x) on poled ceramic pellets of BTFM-CTO materials. Compositions in the range $0.65 \leq x \leq 0.825$ adopt $O_{[001]}$ structure, in the range $0.8375 \leq x \leq 0.925$ there is a mixed phase ($O_{[001]} + R_{[111]}$) and for $x \geq 0.95$ the $R_{[111]}$ structure is formed. (The red short dot lines indicate the boundaries around $0.825 > x > 0.837$ and $0.925 > x > 0.95$.The d_{33} values of all the compositions are listed in Appendix E. b), c) and d) P(E) loops under comparable measurement field for 0.8BTFM-0.2CTO ($O_{[001]}$), 0.9BTFM-0.1CTO ($O_{[001]} + R_{[111]}$) and 0.95BTFM-0.05CTO ($R_{[111]}$) respectively.

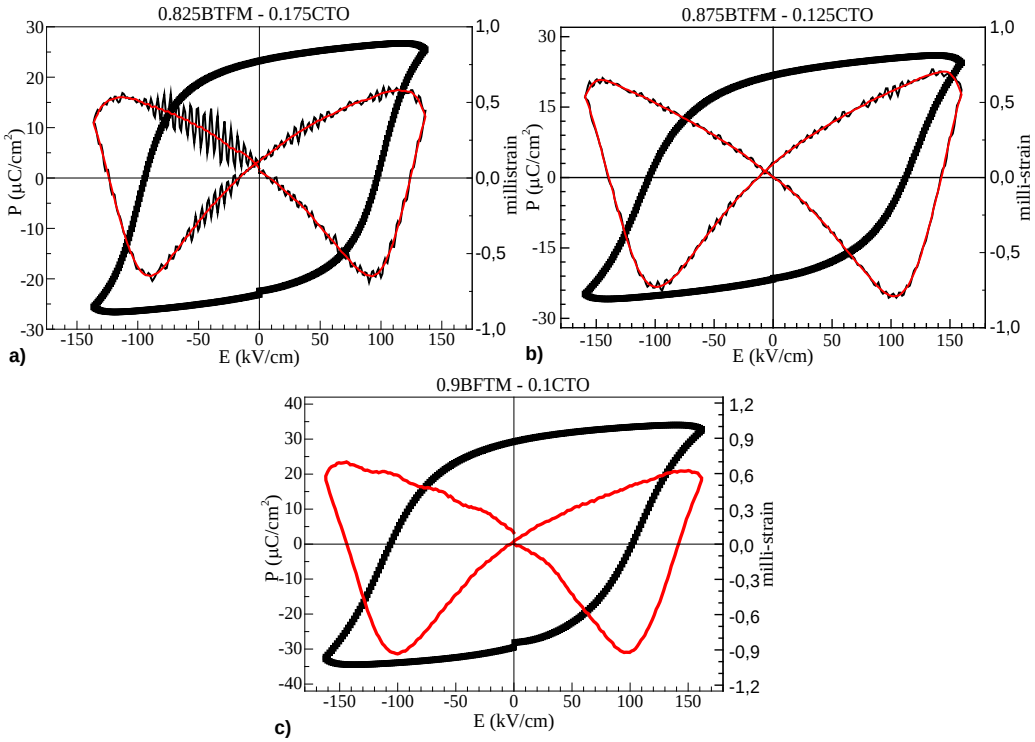

Figure 5.17 Room temperature P(E) (black) and strain-field loops (red) for selected compositions in the mixed phase region ($O_{[001]}$ + $R_{[111]}$): a) 0.825BTFM-0.175CTO; b) 0.875BTFM-0.125CTO and c) 0.9BTFM-0.1CTO at 1 Hz.

Figure 5.17 a), b) and c) show room temperature bipolar strain-field and *P*(*E)* data for the selected compositions 0.825BTFM-0.175CTO, 0.875BTFM-0.125CTO and 0.9BTFM-0.1CTO respectively in the mixed phase region ($O_{[001]}$ + $R_{[111]}$) at 1 Hz. More details about the experimental conditions are given in Section 2.4.1.2, Chapter 2. It is observed that saturated *P*(*E)* and strain-field loops with butterfly shape have been obtained confirming the ferroelectric behaviour of these compounds.

The composition 0.85BTFM-0.15CTO in the mixed phase region ($O_{[001]}$ + $R_{[111]}$) was selected for a detailed study of the electromechanical properties at room temperature. In Figure 5.18 a) a well saturated P(E) loop was obtained at a frequency of 1 Hz under different measurement fields being the maximum polarisation (P_{max}), remanent polarisation (P_{rem}) and coercive field (E_c) of 49 $\mu C/cm^2$, 44 $\mu C/cm^2$ and 110 kV/cm respectively. This P_{rem} value obtained for 0.85BTFM-0.15CTO is higher than the value observed for PZT ceramics (P_{rem} = 35

$\mu C/cm^2$) and other lead-free ceramics at the MPB [16, 20]. A room temperature strain-field measurement was performed at 1 Hz and the classic butterfly loop was obtained (Figure 5.18 b). In order to confirm the large observed polarisation, PUND measurements were carried out and a switchable polarisation of $P \sim 49\ \mu C/cm^2$ was obtained as Figure 5.18 c) shows. Thus, it was verified that the large polarisation is intrinsic. The well saturated P(E) loops and the butterfly strain-field data demonstrate the ferroelectric nature of this material. Because discs have low dielectric loss ($tan\delta \sim 0.03$ at 1 Hz) it was possible to perform measurements up to very high fields of ~ 200 kV/cm [6].

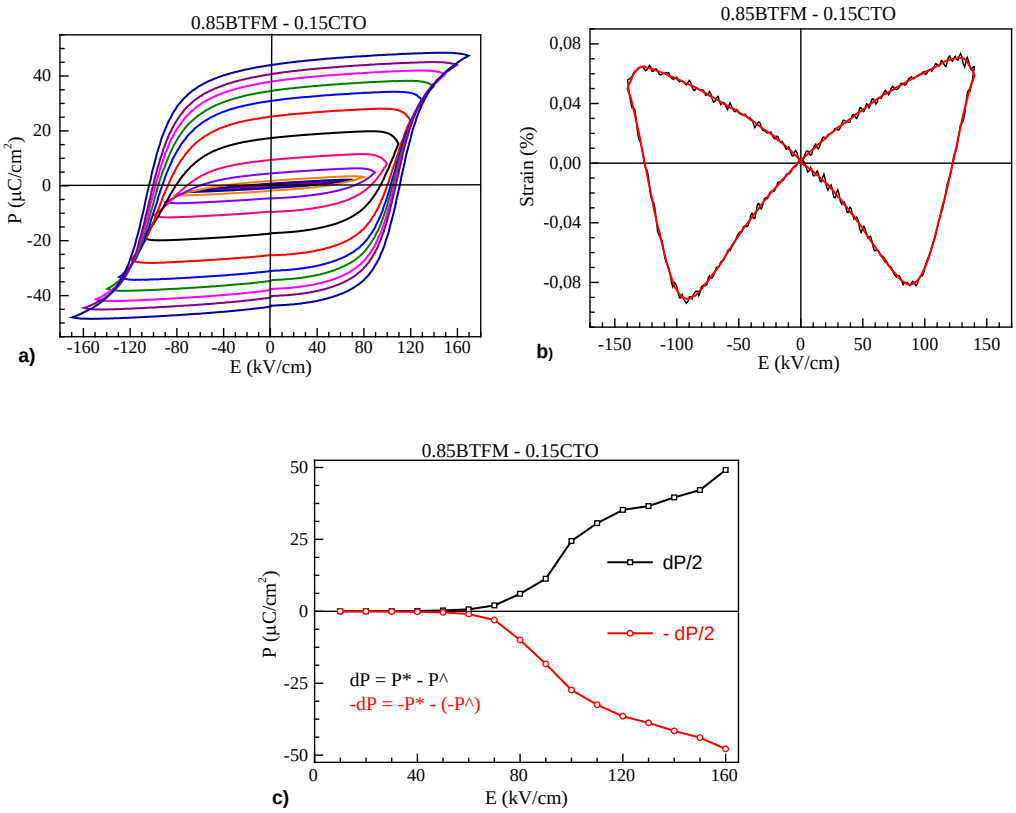

Figure 5.18 Room temperature electromechanical properties of the mixed phase region ($O_{[001]} + R_{[111]}$) composition 0.85BTFM-0.15CTO: a) Saturated P(E) hysteresis loop; b) butterfly strain-field loop and c) positive-up-negative-down (PUND) measurement. P contains remanent and non-remanent polarisations whereas P^ contains non-remanent polarisation contributions. dP (P* - P^) represents the remanent polarisation.*

The composition 0.825BTFM-0.175CTO (single phase $O_{[001]}$ before poling) which is close to the mixed phase region (Figure 5.16 a)) showed a d_{33} of 49 pC/N. However, as shown by the XRD of the poled pellet (Figure 4.51 in Section 4.2, Chapter 4) peaks corresponding to the $R_{[111]}$ phase appear indicating a polarisation rotation [7]. For composition 0.85BTFM-0.15CTO ($O_{[001]}$ + $R_{[111]}$) this fact is also evident from the change in intensities after poling as Figure 5.19 shows that the $O_{[001]}$ to $R_{[111]}$ phase transition can be driven via electric field.

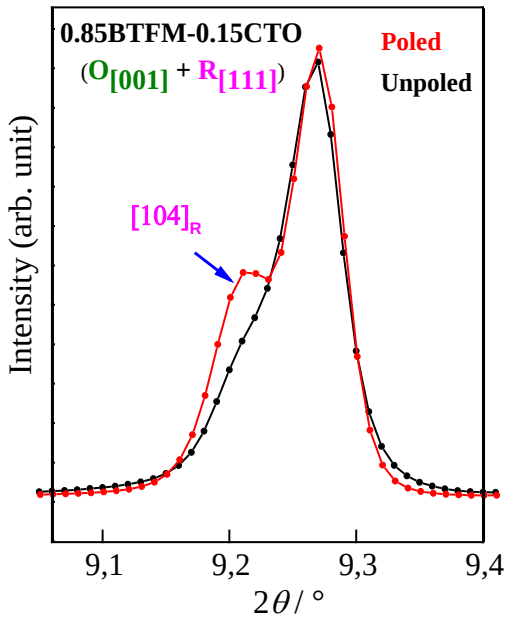

Figure 5.19 PXRD patterns for 0.85BTFM-0.15CTO showing the main perovskite peak collected on poled (red data) and unpoled (black data) pellets (λ ~ 0. 5 Å). The blue arrow corresponding to the poled pellet points out the intensity of the rhombohedral (104) reflection. Figure adapted from [6].

To examine the behaviour of the piezoelectric coefficient versus temperature an ex-situ d_{33} measurement from 25 °C to 900 °C was carried out on the selected composition 0.85BTFM-0.15CTO at the mixed phase region as Figure 5.20 a) shows (in Section 2.4.1.3, Chapter 2 more details about the experimental conditions are given). It was observed that d_{33} for 0.85BTFM-0.15CTO decreases sharply slightly above 250 °C showing that depolarisation occurs. However, the d_{33} becomes zero above 800 °C being 0.54 pC/N and 0.37 pC/N at 500 °C and 700 °C respectively as the inset shows. Figure 5.20 b) shows a pyroelectric current measurement

confirming that T_d ~ 275 °C. More details about the experimental conditions are given in Section 2.4.3 chapter 2. Figure 5.20 c) shows the integrated data of the subtraction of the unpoled current and poled current. It is observed that the lost polarisation obtained of ~ 46 $\mu C/cm^2$ is slightly less than the P_{max} of 0.85BTFM-0.15CTO as shown in Figure 5.18 a) .

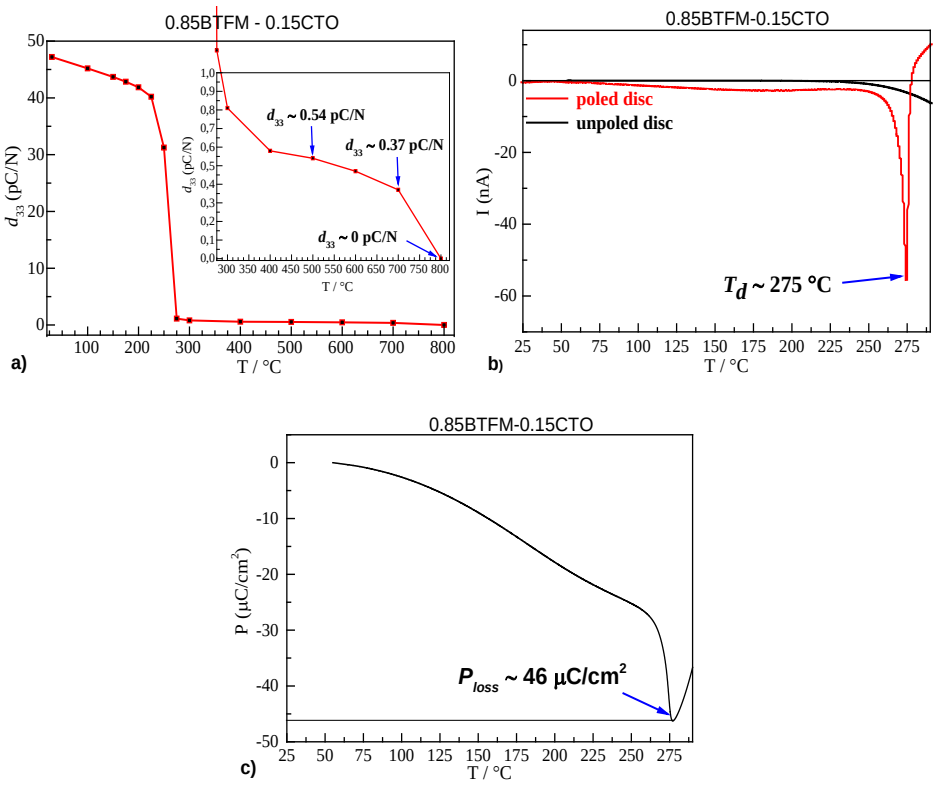

Figure 5.20 For 0.85BTFM-0.15CTO: a) Ex-situ d_{33} measurement from 25 °C to 800 °C. The inset at the top right shows an enlargement from ~ 300 °C to ~ 800 °C and the blue arrows point out d_{33} values at 500 °C, 700 °C, and 800 °C; b) pyroelectric coefficient measurement from 50 °C to 300 °C on a poled disc (red data) and an unpoled disc (black data), the blue arrow indicates the T_d ~ 275 °C and c) integrated data of the subtraction of the unpoled current and poled current, the blue arrow indicates the peak at 275 °C being the P_{loss} ~ 46 $\mu C/cm^2$.

Preliminary structural analysis below and above T_d on a selected composition in the mixed phase region suggests that below T_d the mixed phase region ($O_{[001]} + R_{[111]}$) is formed (Figure 5.21 a) and 5.21 b)). However, above T_d a phase transition might take place to a single O phase (Figure 5.21 c) and 5.21 d)). Nevertheless, further study is needed for a better understanding and is subject of future work.

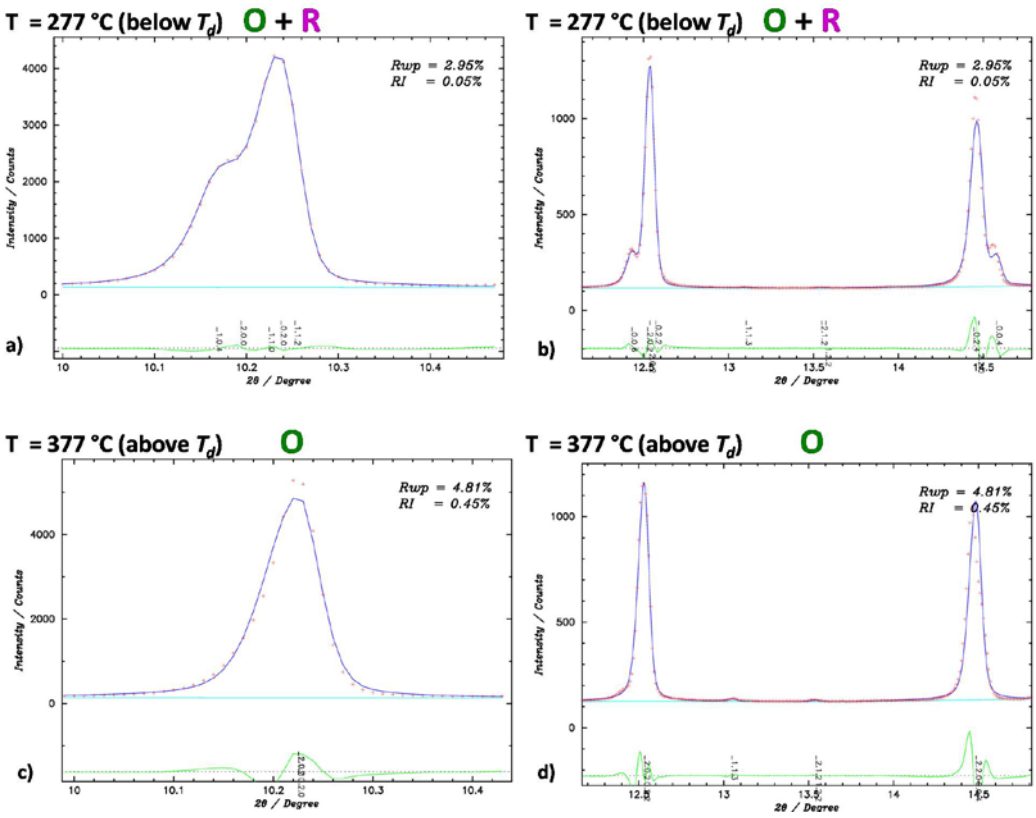

Figure 5.22 Enlargements of the Le Bail fit for 0.875BTFM-0.125CTO: a-b) with one $O_{[001]}$ and one $R_{[111]}$ phase in space groups $Pna2_1$ and R3c respectively at 277 °C (below T_d ~ 350 °C) while c-d) in the $O_{[001]}$ space group $Pna2_1$ at 377 °C (above T_d ~ 350 °C). The red points represent the observed data while the blue solid line represents the model. The difference green curve is below. The black tics represent positions of Bragg reflections.

Differential thermal analysis (DTA) were performed on compositions with $O_{[001]}$ + $R_{[111]}$ structure in order to detect any phase transitions from 25 °C to 900 °C. In Figure 5.22 a) for the selected composition 0.85BTFM-0.15CTO a weak anomaly can be observed at ~ 850 °C which might indicate a phase transition. Figure 5.22 b) shows dielectric data from 25 °C to 850 °C for 0.85BTFM-0.15CTO at different frequencies. A broad anomaly at the dielectric data for 0.85BTFM-0.15CTO and a maximum around T_m ~ 430 °C is observed. Moreover, a weak anomaly is observed at *Tc* ~ 830 °C as indicated with an arrow and matching with the anomaly observed at DTA data and ex-situ d_{33} measurements where the piezoelectric coefficient vanishes above 850 °C indicating thus a phase transition. However, as shown in Figure 5.22 b) the dielectric loss increases with temperature being complicated to detect clearly any phase

transition. DTA and impedance measurements on more compositions in the mixed phase region are shown in Appendix C.

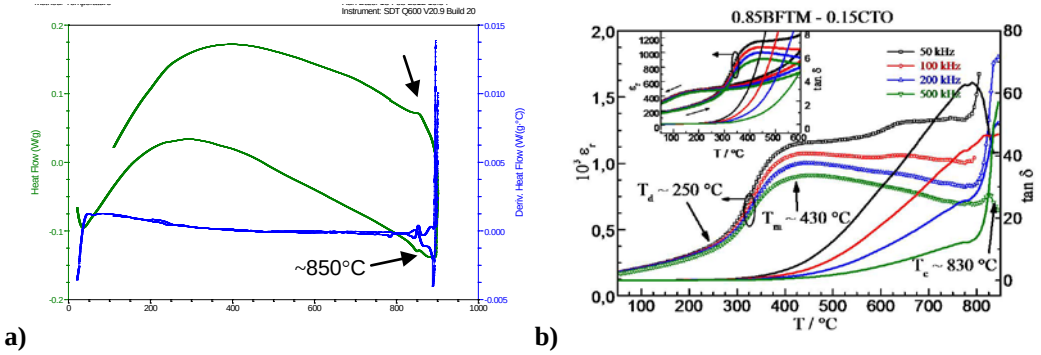

Figure 5.22 a) For 0.85BTFM-0.15CTO DTA data from 25 °C to 900 °C are shown in green and its derivative in blue. The black arrows point out a weak anomaly around 850 °C; b) dielectric data from 25 °C to 850 °C at 50 kHz (black open circles), 100 kHz (red open circles), 200 kHz (blue open circles) and 500 kHz (green open circles). The black arrow at ~ 250 °C indicates the T_d, the one at ~430 °C where the maximum at the dielectric data is achieved, Tm and the one at ~ 830 °C indicates Tc. The inset at the top left corner shows dielectric data from room temperature to 600 °C while heating (up) and cooling (down).

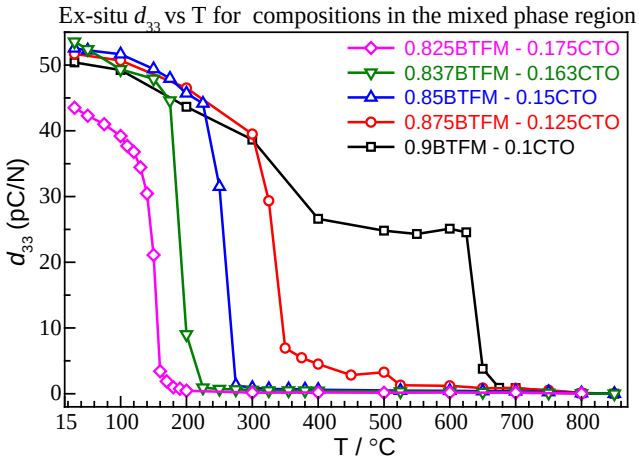

Figure 5.23 Ex-situ d_{33} measurements from 25 °C to 850 °C for compositions in the mixed phase region: 0.825BTFM-0.175CTO (pink open rhombuses), 0.837BTFM-0.163CTO (green open triangles), 0.85BTFM-0.15CTO (blue open triangles), 0.875BTFM-0.125CTO (red open circles) and 0.9BTFM-0.1CTO (black open squares).

Figure 5.23 shows the comparison of ex-situ d_{33} measurements from 25 °C to 850 °C for the compositions in the mixed phase region: 0.825BTFM-0.175CTO, 0.837BTFM-0.163CTO, 0.85BTFM-0.15CTO, 0.875BTFM-0.125CTO and 0.9BTFM-0.1CTO. It is observed that T_d increases with BTFM content (x) and in the case of 0.9BTFM-0.1CTO T_d ~ 650 °C. The disappearance of ex-situ d_{33} indicates a Curie temperature (*Tc*) of ~ 850 °C for all the

compositions. This high Curie and depolarisation temperatures (just in the case of 0.9BTFM-0.1CTO, T_d ~ 650 °C) observed in BTFM-CTO materials are attractive for applications [19, 21].

DTA was performed on 0.95BTFM-0.05CTO ($R_{[111]}$ structure) to detect any phase transitions from 25 °C to 900 °C. In Figure 5.24 a) two anomalies can be clearly observed at ~ 690 °C and ~ 850 °C as indicated with black arrows. Figure 5.24 b) shows dielectric data from 25 °C to 900 °C for 0.95BTFM-0.05CTO at different frequencies. Two distinct anomalies at ~ 670 °C and ~ 850 °C are observed matching with the anomalies observed in the DTA data which might indicate two phase transitions. In Figure 5.26, neutron diffraction data for 0.95BTFM-0.05CTO at 700 °C (top panel), 600 °C (middle panel) and 25 °C (bottom panel) were examined and compared. It is observed that data at 700 °C do not have the *R*3*c* ½$(111)_p$ tilting peak at ~ 2.4 Å as indicated by a black arrow while at 600 °C and 25 °C this peak appears. This situation is similar as for BTFM-BTO materials where for 0.75BTFM-0.25BTO the tilting peak was suppressed and was refined in *R*3*m* [22]. Thus, 0.95BTFM-0.05CTO might undergo two phase transitions possibly from the polar space group *R*3*c* to *R*3*m* and the non-polar space group $Pm\bar{3}m$. However, further structural work is needed to confirm this.

In the case of BTFM which also adopts an $R_{[111]}$ structure in *R*3*c* at room temperature, a sharp peak in permittivity around 730 °C is observed (Figure 3.1, Chapter 3) and data collected at 740 °C were refined in the space group $Pm\bar{3}m$ [14]. However a DTA measurement carried out on BTFM (Figure 5.25) shows two clear anomalies as for 0.95BTFM-0.05CTO indicating that this material with $R_{[111]}$ structure at room temperature undergoes two phase transitions. Nevertheless, further structural work is needed to confirm this.

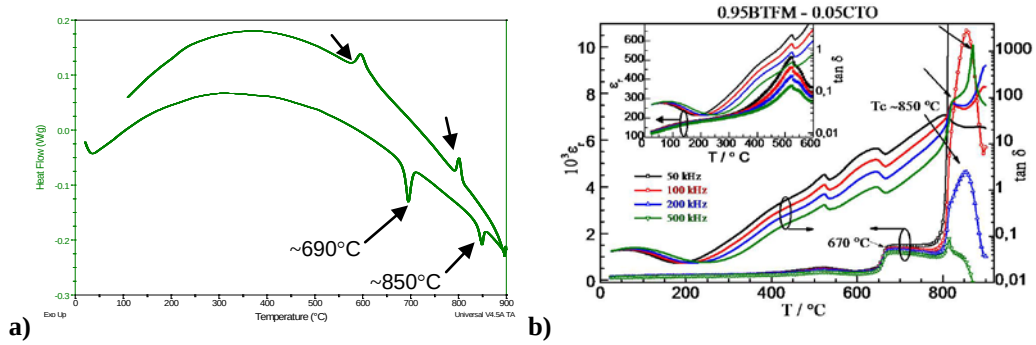

a) **b)**

Figure 5.24 a) DTA data from 25 °C to 900 °C are shown in green. The black arrows point out two anomalies around 690 °C and 850 °C; b) dielectric data from 25 °C to 900 °C at 50 kHz (black open circles), 100 kHz (red open circles), 200 kHz (blue open triangles) and 500 kHz (green open triangles). The black arrows at ~ 670 °C and ~ 850 °C indicate two anomalies in the data for 0.95BTFM-0.05CTO. The inset at the top left corner shows dielectric data from room temperature to 600 °C while heating (up).

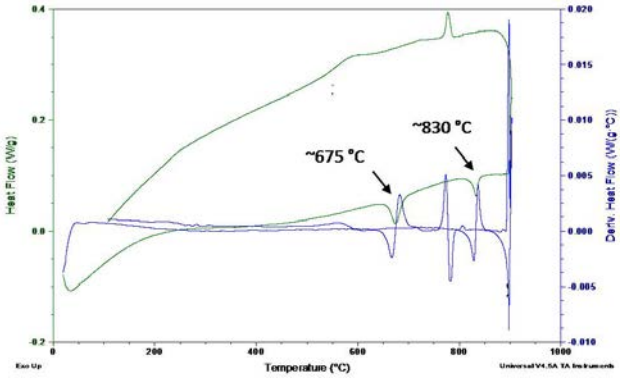

Figure 5.25 a) DTA data from 25 °C to 900 °C are shown in green and its derivative in blue. The black arrows point out two anomalies around ~ 675 °C and ~ 830 °C for BTFM.

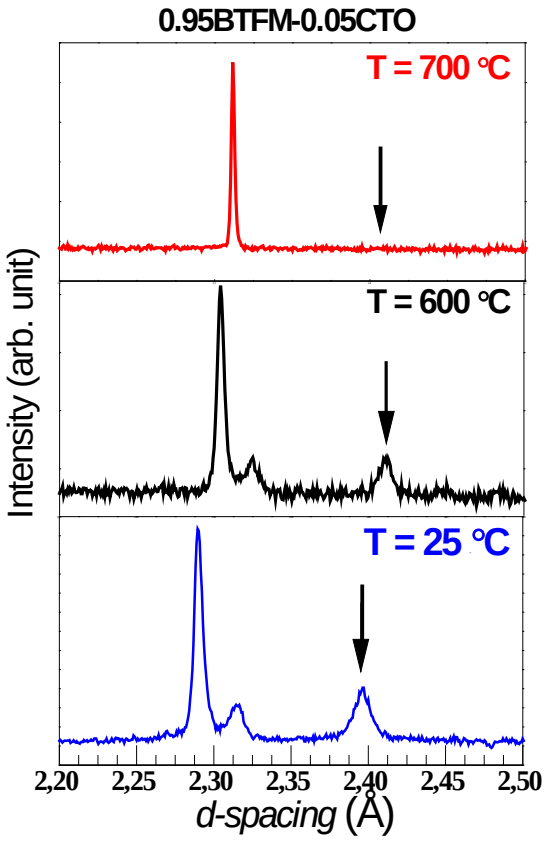

Figure 5.26 Neutron diffraction data for 0.95BTFM-0.05CTO at 700 °C (top panel), 600 °C (middle panel) and 25 °C (bottom panel). The black arrows in the neutron patterns show the presence/absence of a tilting peak.

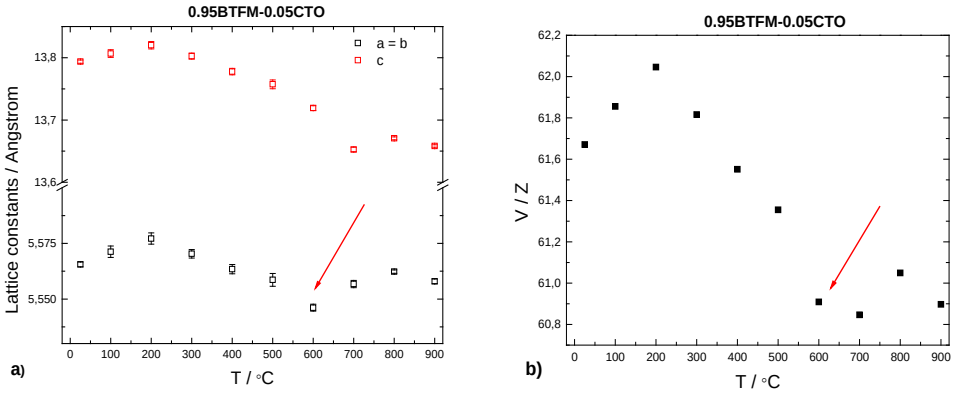

Figure 5.27 a) Lattice constants versus temperature from 25 °C to 900 °C; b) volume divided by Z where Z is the formula units in the unit cell for 0.95BTFM-0.05CTO using neutron data. The red arrows show an anomaly at ~600 °C.

Figure 5.27 a) shows the lattice constants obtained from a Le Bail analysis against neutron data (bank 2) for 0.95BTFM-0.05CTO. Figure 5.27 b) shows the volume versus temperature for 0.95BTFM-0.05CTO from 25 ° C to 900 °C. In Figure 5.27 a) and b) it is observed that the lattice constants and volume decrease with temperature suggesting negative thermal expansion.

Moreover, it is observed that there is an anomaly ~ 600 °C as indicated by red arrows and could match with the lost of the tilting peak ~ 700 °C. However, further structural work is needed to confirm this.

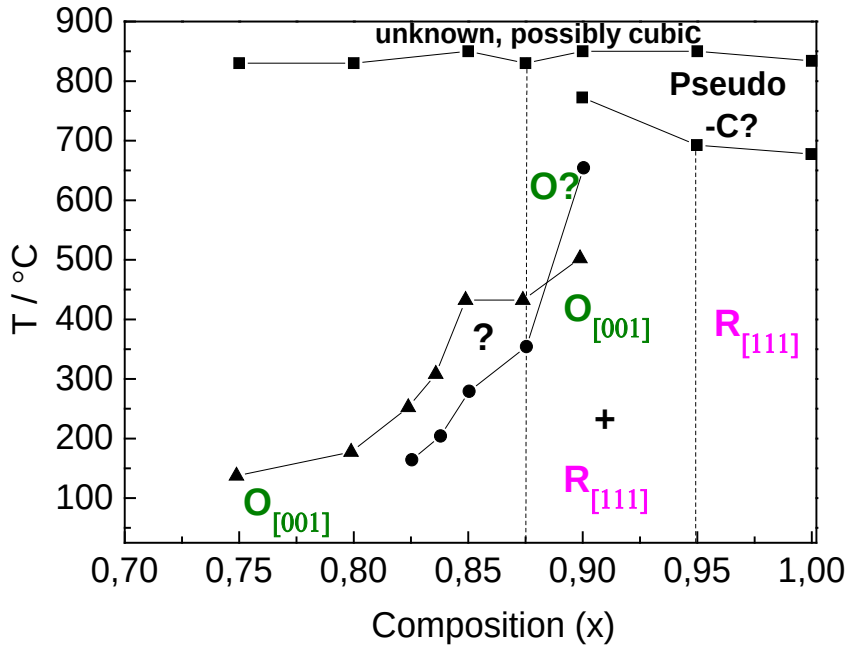

Figure 5.28 Preliminary phase diagram of xBTFM-(1-x)CTO materials. The black short dot lines indicate the phase boundaries. Black circles represent T_d obtained from pyrocurrent measurements, black triangles represent Tm obtained from dielectric data black squares represent while black squares represent temperatures obtained from DTA measurements. Where C refers to cubic.

Figure 5.28 shows a preliminary phase diagram of xBTFM-(1-x)CTO materials built versus temperature summarising the structural information obtained so far. The black short dot lines show the phase boundaries around 0.825 > x > 0.837 and 0.925 > x > 0.95. Black circles represent T_d obtained from pyrocurrent measurements, black triangles represent *Tm* obtained from dielectric data black squares represent while black squares represent temperatures obtained from DTA measurements. Where C refers to cubic though no crystallographic data are obtained for this phase. It can be observed that for 0.9BTFM-0.1CTO data obtained from T_d and *Tm* crossover and this fact might be because the dielectric loss is high at these temperatures.

5.3 Summary and conclusions

To summarise, a mixed phase region formed by two polar phases $O_{[001]}$ ($Pna2_1$) + $R_{[111]}$ ($R3c$) with different structures and polarisation directions has been achieved in BTFM-CTO materials in the compositional range $0.8375 \leq x \leq 0.925$ (Section 5.1.1). As predicted, the electromechanical properties are maximised in this mixed phase region. As Figure 5.16 a) shows, the d_{33} values are clearly enhanced at the mixed phase region in contrast with the small d_{33} values obtained for compositions in the single phase $O_{[001]}$ $0.6 \leq x < 0.825$ and $R_{[111]} \geq 0.95$ region. Moreover, well saturated loops along with butterflies loops have been obtained for all compositions at the mixed phase region as shown in Figures 5.17 in contrast the single phases $O_{[001]}$ and $R_{[111]}$ display non-saturated loops as Figure 5.16 b) and d) show for 0.8BTFM-0.2CTO and 0.95BTFM-0.05CTO respectively. A maximum d_{33} of 53 pC/N has been obtained for the 0.835BTFM-0.175CTO at the MPB region (Figure 5.16 a)). This value is about two orders higher than for the parent materials BTFM [22]. Therefore, the goal of improving the electromechanical properties of BTFM by making solid solutions with CTO has been accomplished. Nevertheless, in comparison with other lead-free piezoceramics the piezoelectric coefficient values obtained at the mixed phase region for BTFM-CTO are smaller.

Ex-situ d_{33} measurements performed on selected compositions at the mixed phase region show that T_d increases with BTFM content (Figure 5.23) and more interestingly in the case of 0.9BTFM-0.1CTO a high T_d of ~ 650 °C is obtained. The disappearance of ex-situ d_{33} at ~ 850 °C for all the compositions at the mixed phase region and based on the DTA and impedance measurements (Figures 5.22 a) and b)) suggest a high *Tc* of ~ 850 °C. This high T_d, just in the case of 0.9BTFM-0.1CTO, and *Tc* observed for BTFM-CTO materials is very attractive for possible applications [19, 21] .

For $x \geq 0.95$ the polar $R_{[111]}$ is adopted with space group *R*3*c* as the structural analysis on 0.95BTFM-0.05CTO shows in Section 5.1.2 being the electromechanical properties of this material similar as for the parent compound BTFM.

5.4 References

1. Arigur, P. and Benguigu, L, *Solid State Communications*, 1974. **15**(6): p. 1077-1079.
2. Soares, M. R., Senos, A. M. R. and Mantas, P. Q., *Journal of the European Ceramic Society*, 1999. **19**(10): p. 1865-1871.
3. Otonicar, M., Skapin, S. D., Spreitzer, M. and Suvorov, D., *Journal of the European Ceramic Society*, 2010. **30**(4): p. 971-979.
4. Daniels, J. E., Jo, W., Roedel, J. and Jones, J. L., *Applied Physics Letters*, 2009. **95**(3).
5. Jaffe, B., Piezoelectric Ceramics, *Academic Press*: London, New York, 1971.
6. Mandal, P., Manjon-Sanz, A., Corkett, A. J., Comyn, T. P, Dawson, K., Stevenson T., Bennett J., Henrichs, L. F., Bell, A. J., Nishibori, E., Takata, M., Marco, Z., Dolgos, M. R., Adem, U., Wan, X., Pitcher, M. J., Romani, S., T. Tran T. T., Halasyamani P. S., Claridge J. B. and Rosseinsky M. J., *Submitted to Advanced Materials* 2014.
7. Guo, R., Cross, L. E., Park, S. E., Noheda, B., Cox, D. E. and Shirane, G., *Physical Review Letters*, 2000. **84**(23): p. 5423-5426.
8. Fu, H. X. and Cohen, R. E., *Nature*, 2000. **403**(6767): p. 281-283.
9. Vanderbilt, D. and Cohen, M. H. *Physical Review B*, 2001. **63**(9): p. 094108.
10. Zhang, N., Yokota, H., Glazer, A. M., Ren, Z., Keen, D. A., Keeble, D. S., Thomas, A. and Ye, Z. G., *Nature Communications*, 2014. **5**: p. 5231-5239.
11. Zhang, Y., Xue, D., Wu, H., Ding, X., Lookman, T. and Ren, X., *Acta Materialia*, 2014. **71**(0): p. 176-184.
12. Cordero, F., Trequattrini, F., Craciun, F. and Galassi, C., *Journal of Physics Condensed Matter*, 2011. **23**(41).
13. Zhang, N., Yokota, H., Glazer, A. M., Ren, Z., Keen, D. A., Keeble, D. S., Thomas, A. and Ye, Z. G., *Nature Communications*, 2014. **5**: p. 5231-5231.
14. Craig, A. B., Allix, M., Suchomel, M. R. Xiaojun, K., Sterianou, I., Sinclair, D. C. and Rosseinsky, M. J., *Angewandte Chemie-International Edition*, 2007. **46**: p. 8785 –8789.
15. Dolgos, M. R., Adem, U., Manjon-Sanz, A., Wan, X., Comyn, T. P., Stevenson T., Bennett J., Bell, A. J., Tran, T. T., Halasyamani, P. S., Claridge, J. B. and Rosseinsky, M. J., *Angewandte Chemie-International Edition*, 2012. **51**: p. 10770-10775.
16. Roedel, J., Wook, J., Seifert, K. T. P., Anton, E. M, Granzow, T. and Damjanovic, D., *Journal of the American Ceramic Society*, 2009. **92**(6): p. 1153-1177.
17. Takenaka, T., Maruyama, K. and Sakata, K., *Japanese Journal of Applied Physics Part 1-Regular Papers Short Notes & Review Papers*, 1991. **30**(9B): p. 2236-2239.
18. Zhang, S., Shrout, T. R., Nagata, H., Hiruma, Y. and Takenaka, T. *Ieee Transactions on Ultrasonics Ferroelectrics and Frequency Control*, 2007. **54**(5): p. 910-917.
19. Leontsev, S. O. and Richard, E. E., *Science and Technology of Advanced Materials*, 2010. **11**(4) p. 044302-044315.
20. Shrout, T. R. and Zhang, S. J., *Journal of Electroceramics*, 2007. **19**(1): p. 113-126.
21. Zhang, S. and Yu, F., *Journal of the American Ceramic Society*, 2011. **94**(10): p. 3153-3170.
22. Dolgos, M., Adem, U., Wan, X., Xu, Z., Bell, A. J., Comyn, T. P., Stevenson, T., Bennett, J., Claridge, J. B. and Rosseinsky, M. J. *Chemical Science*, 2012. **3**: p. 1426-1435.

PUBLICATIONS FROM THIS THESIS

Dolgos, M. R., Adem, U., Manjon-Sanz, A., Wan, X., Comyn, T. P., Stevenson T., Bennett J., Bell, A. J., Tran, T. T., Halasyamani, P. S., Claridge, J. B. and Rosseinsky, M. J., *Angewandte Chemie-International Edition*, 2012. **51**: p. 10770-10775.

Mandal, P., Manjon-Sanz, A., Corkett, A. J., Comyn, T. P, Dawson, K., Stevenson T., Bennett J., Henrichs, L. F., Bell, A. J., Nishibori, E., Takata, M., Marco, Z., Dolgos, M. R., Adem, U., Wan, X., Pitcher, M. J., Romani, S., T. Tran T. T., Halasyamani P. S., Claridge J. B. and Rosseinsky M. J., *Submitted to Advanced Materials*, 2014.

Appendix A - Le Bail analysis at variable temperature for BTFM-CTO materials

Temperature dependence of the lattice parameters for x BTFM – (1-x) CTO materials were determined by Le Bail analysis using variable temperature (VT) synchrotron X-ray diffraction data. Initial parameters for the refinement were estimated using the peak positions of the data. The data range analysed was from 3° to 74°. In the range of compositions $0.6 \leq x \leq 0.8$, Le Bail analysis were carried out in the orthorhombic polar space group $Pna2_1$. In the range of compositions $0.85 \leq x \leq 0.9$, Le Bail analysis were performed as mixture of the phases $Pna2_1$ and the rhombohedral polar space group $R3c$. For the compositions 0.925BTFM-0.075CTO and 0.95BTFM-0.05CTO, Le Bail analysis were performed in $R3c$.

Figures A.1-A.8 show fitting results of Le Bail analysis refinements for 0.6BTFM-0.4CTO at VT from 100 K to 470 K. The x axis shows 2θ and the units are °. The y axis shows the intensity and the units are counts. The figures show the 2θ range from 3° to 40°. The red crosses represent the observed data while the blue solid line represents the model. The difference green curve is below. The black tics represent positions of Bragg reflections.

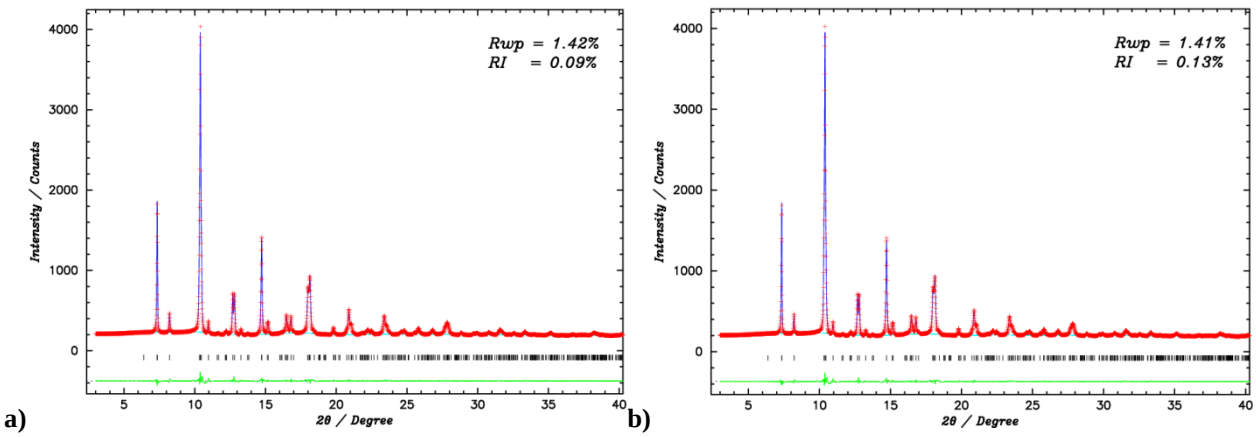

Figure A.1 a) LeBail fit for 0.6BTFM-0.4CTO at 100 K. b)Le Bail fit for 0.6BTFM-0.4CTO at 125 K.

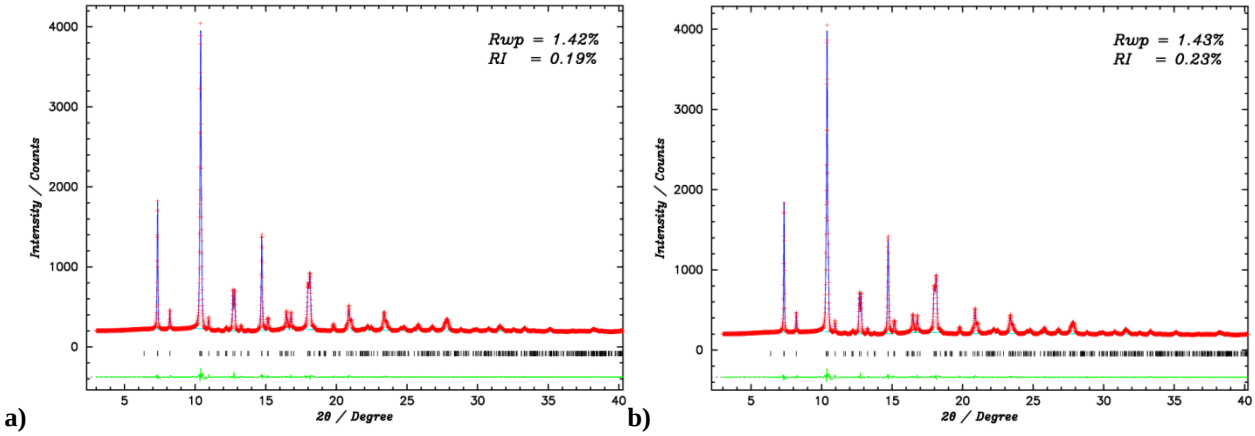

Figure A.2 a) Le Bail fit for 0.6BTFM-0.4CTO at 150 K. b) Le Bail fit for 0.6BTFM-0.4CTO at 175 K.

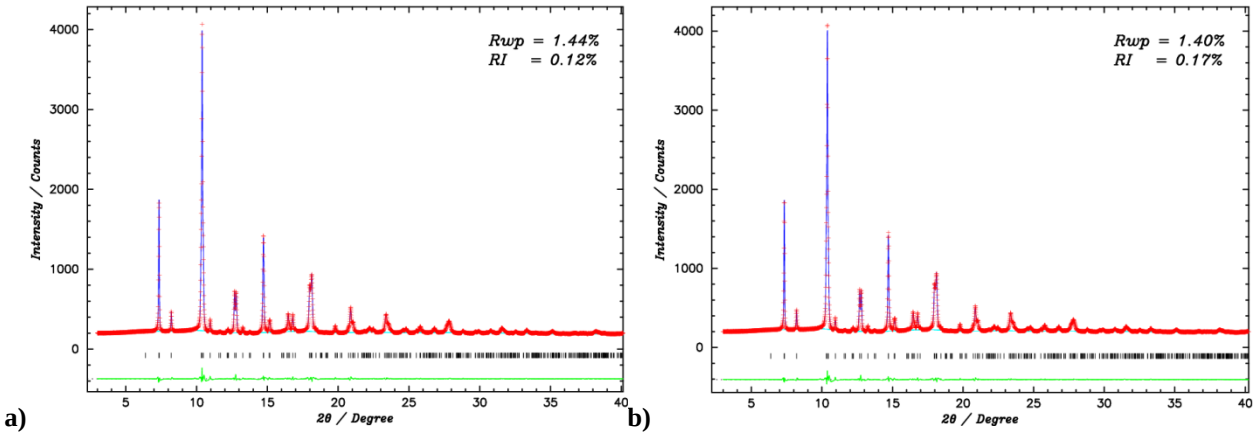

Figure A.3 a) Le Bail fit for 0.6BTFM-0.4CTO at 200 K. b) Le Bail fit for 0.6BTFM-0.4CTO at 225 K.

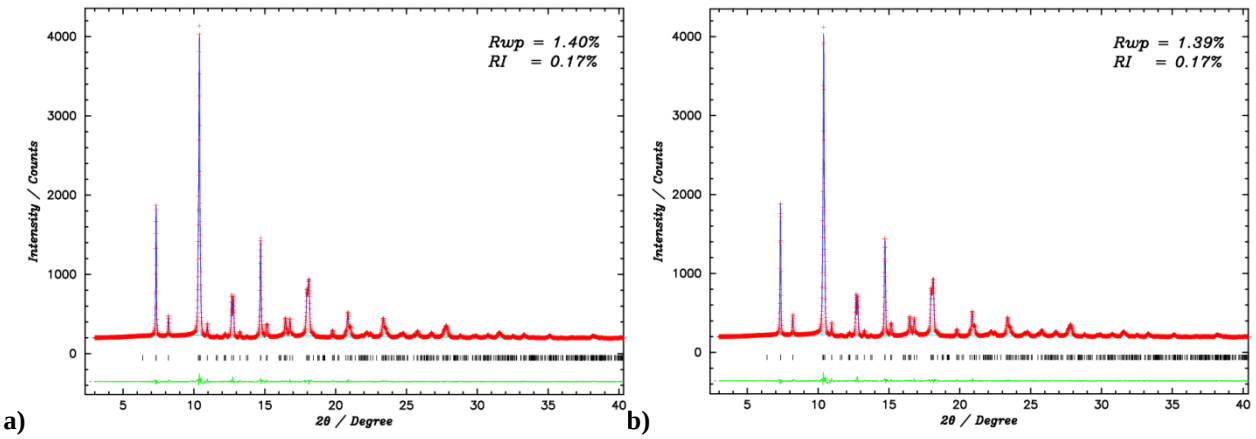

Figure A.4 a) Le Bail fit for 0.6BTFM-0.4CTO at 250 K. b) Le Bail fit for 0.6BTFM-0.4CTO at 275 K.

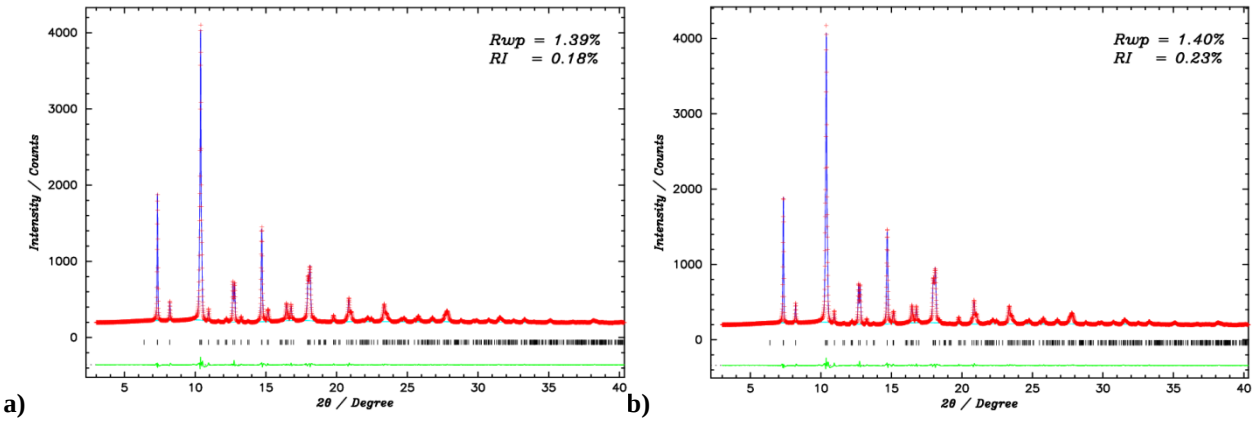

Figure A.5 a) Le Bail fit for 0.6BTFM-0.4CTO at 300 K. b) Le Bail fit for 0.6BTFM-0.4CTO at 325 K.

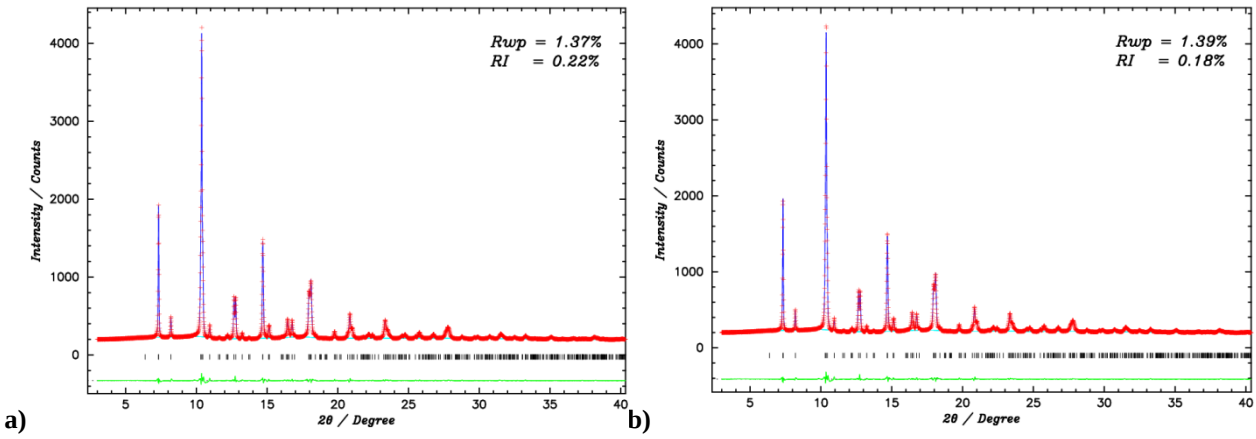

Figure A.6 a) Le Bail fit for 0.6BTFM-0.4CTO at 350 K. b) Le Bail fit for 0.6BTFM-0.4CTO at 375 K.

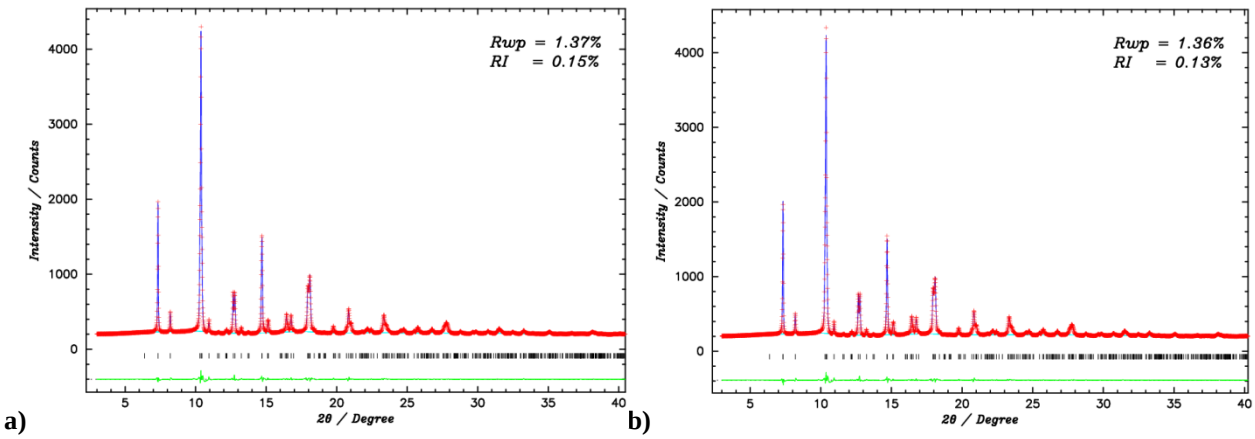

Figure A.7 a) Le Bail fit for 0.6BTFM-0.4CTO at 400 K. b) Le Bail fit for 0.6BTFM-0.4CTO at 425 K.

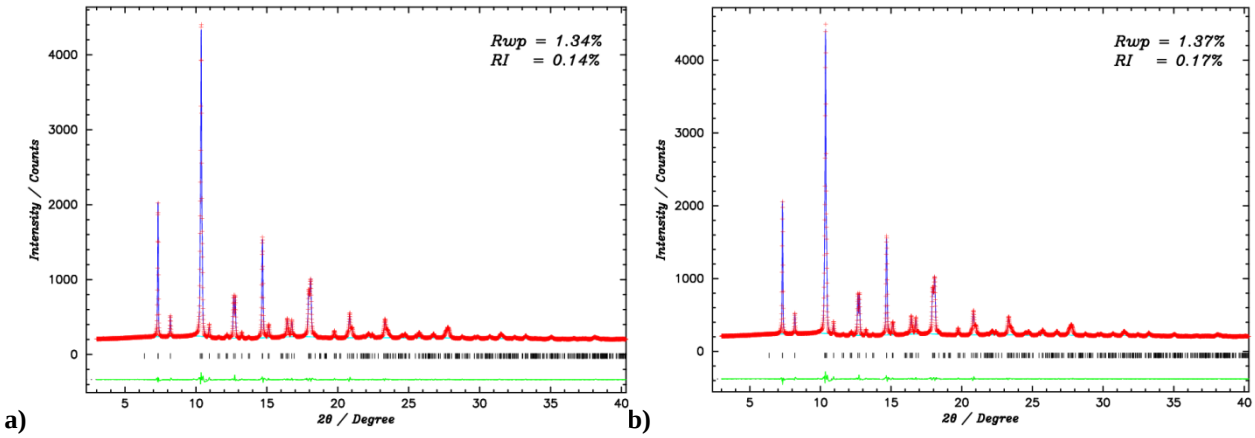

Figure A.8 a) Le Bail fit for 0.6BTFM-0.4CTO at 450 K. b) Le Bail fit for 0.6BTFM-0.4CTO at 470 K.

The lattice parameters *a*, *b* and *c*, the ratio *a* / *c*, the volume of the unit cell (*V*) and the reliability factors R_{wp} and R_I from 100 to 470 K for BTFM-CTO materials are listed in Tables A.1, A.2, A.3, A.4, A.5, A.6, A.7, A.8, A.9 and A.10. The volume of the unit cell is also expressed as *V* / *Z* in column number 7, where *Z* is the number of molecules or formula units *Z* in the unit cell. For the orthorhombic system, *Z* = 4 and for the rhombohedral system, *Z* = 6. The volume of the unit cell was calculated using Equation A.1.

$$V = \sqrt{abc(1 - \cos^2\alpha - \cos^2\beta - \cos^2\gamma + 2\cos\alpha\cos\beta\cos\gamma)} \qquad \text{Equation A.1}$$

where *V* is the volume of the unit cell, *a*, *b* and *c* are the lattice parameters and α, β and γ are the unit cell angles. For the orthorhombic structure $\alpha = \beta = \gamma = 90°$ while for the rhombohedral structure $\alpha = \beta = 90°$; $\gamma = 120°$.

Table A.1: Lattice parameters, volume of the unit cell and reliability factors for 0.6BTFM-0.4CTO at VT.

T* / *K	***a* / Å**	***b* / Å**	***c* / Å**	***a* / *c***	***V* / Å^3**	***R*$_{wp}$ / *R*$_I$/ %**
100	5.552(1)	5.4750(9)	7.800(1)	0.711821	205.34304	1.42/0.09
125	5.552(1)	5.4757(9)	7.800(1)	0.711803	205.4130	1.41/0.13
150	5.5539(9)	5.4767(9)	7.803(1)	0.711725	205.56565	1.42/0.19
175	5.5547(9)	5.4775(9)	7.804(1)	0.711716	205.65221	1.43/0.23
200	5.5563(8)	5.4794(8)	7.806(1)	0.711772	205.82746	1.44/0.12
225	5.5565(9)	5.4796(9)	7.807(1)	0.711719	205.86330	1.40/0.17
250	5.5574(9)	5.4805(8)	7.808(1)	0.711713	205.96843	1.40/0.17
275	5.5583(8)	5.4816(8)	7.810(1)	0.711697	206.08535	1.39/0.17
300	5.5594(9)	5.4828(8)	7.811(1)	0.711723	206.19625	1.39/0.18
325	5.5604(9)	5.4839(8)	7.812(1)	0.711714	206.31601	1.40/0.23
350	5.5615(9)	5.4854(8)	7.814(1)	0.711696	206.46280	1.37/0.22
375	5.5627(9)	5.4869(8)	7.816(1)	0.711687	206.60777	1.39/0.18
400	5.5637(8)	5.4883(8)	7.818(1)	0.711649	206.74388	1.37/0.15
425	5.5647(9)	5.4901(9)	7.819(1)	0.711671	206.88567	1.36/0.13
450	5.5662(8)	5.4924(8)	7.822(1)	0.711586	207.10917	1.34/0.14
470	5.5669(9)	5.4937(8)	7.823(1)	0.711598	207.20418	1.37/0.17

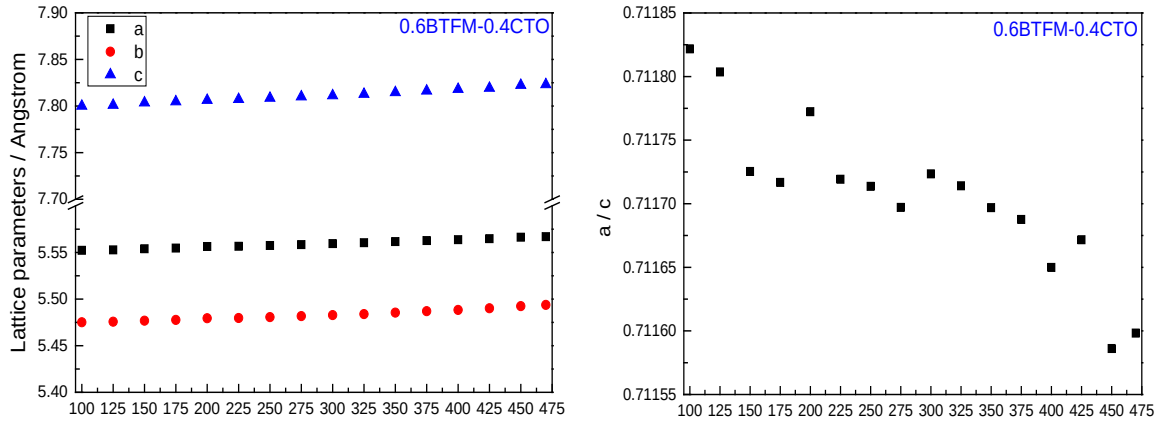

Figure A.9 a) Lattice parameters versus temperature, b) a / c versus temperature for 0.6BTFM-0.4CTO.

Figure A.9 a) shows the lattice parameters versus temperature for 0.6BTFM-0.4CTO. The y axis shows the lattice parameters and the units are Angstrom. At the y axis, there is a break from 5.6 to 7.7 for better visualization of the tendency of the lattice parameters versus temperature. The black squares represent the lattice parameter *a*, the red circles *b* and the blue triangles *c*. It is

observed that the lattice parameters increase with increasing temperature. Figure A.17 b) shows the ratio *a* / *c* versus temperature for 0.6BTFM-0.4CTO. The notation for x and y axis are the same as the Figures A.1-A.8. It is observed that the ratio *a* / *c* decreases linearly with temperature.

Figures A.10-A.17 show fitting results of Le Bail analysis for 0.65BTFM-0.35CTO at VT. The notation for x and y axis are the same as the Figures A.1-A.8. The figures show the 2θ range from 3° to 40°.

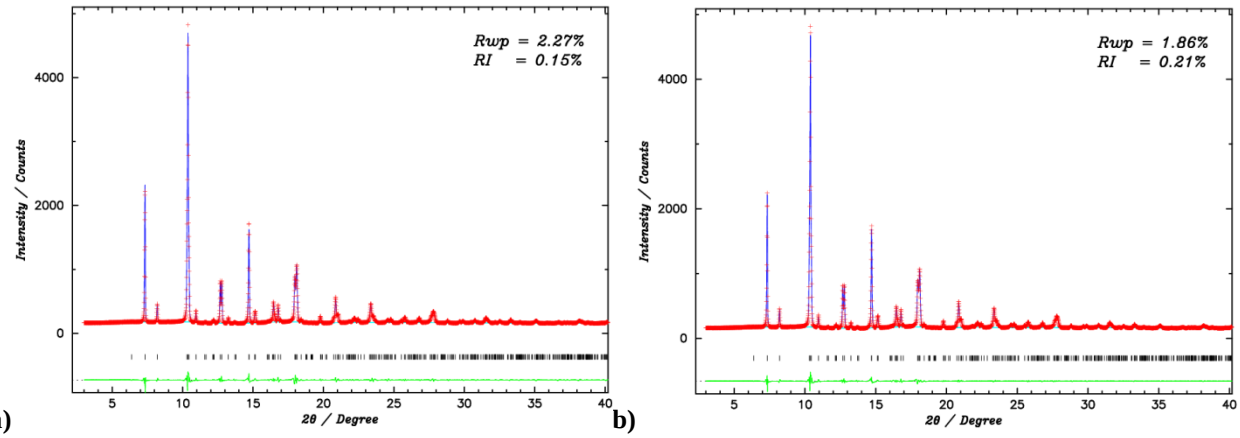

Figure A.10 a) Le Bail fit for 0.65BTFM-0.35CTO at 100 K. b) Le Bail fit for 0.65BTFM-0.35CTO at 125 K.

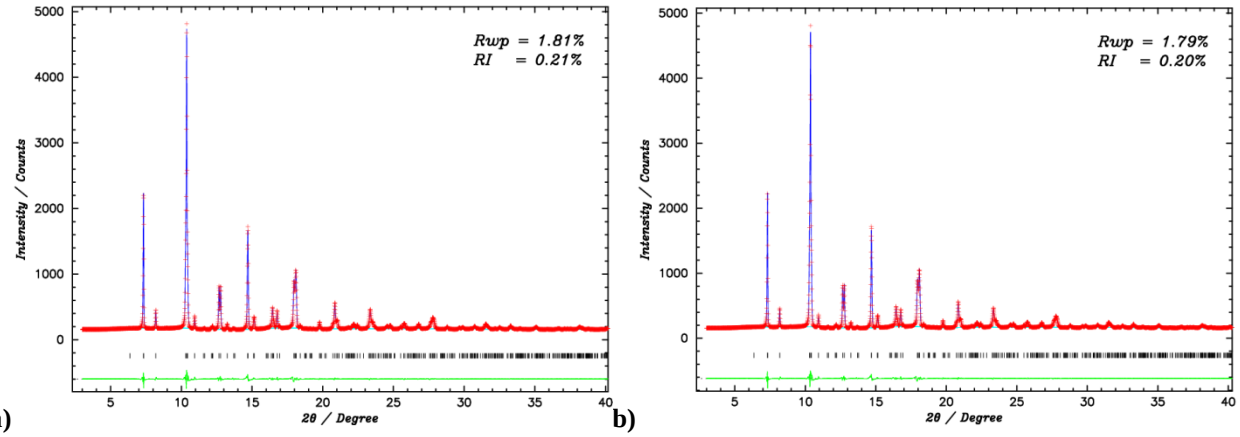

Figure A.11 a) Le Bail fit for 0.65BTFM-0.35CTO at 150 K. b) Le Bail fit for 0.65BTFM-0.35CTO at 175 K.

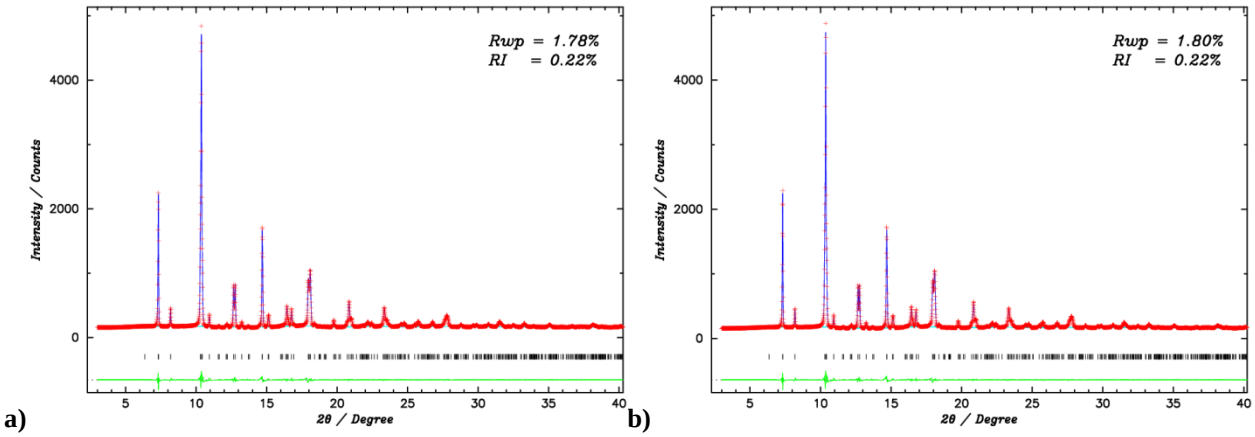

a) **b)**

Figure A.12 a) Le Bail fit for 0.65BTFM-0.35CTO at 200 K. b) Le Bail fit for 0.65BTFM-0.35CTO at 225 K.

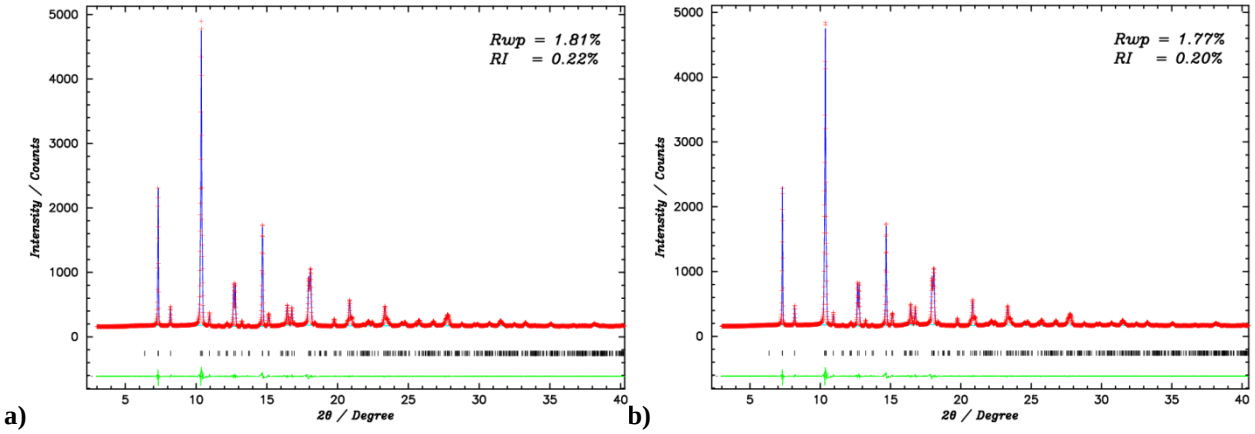

a) **b)**

Figure A.13 a) Le Bail fit for 0.65BTFM-0.35CTO at 250 K. b) Le Bail fit for 0.65BTFM-0.35CTO at 275 K.

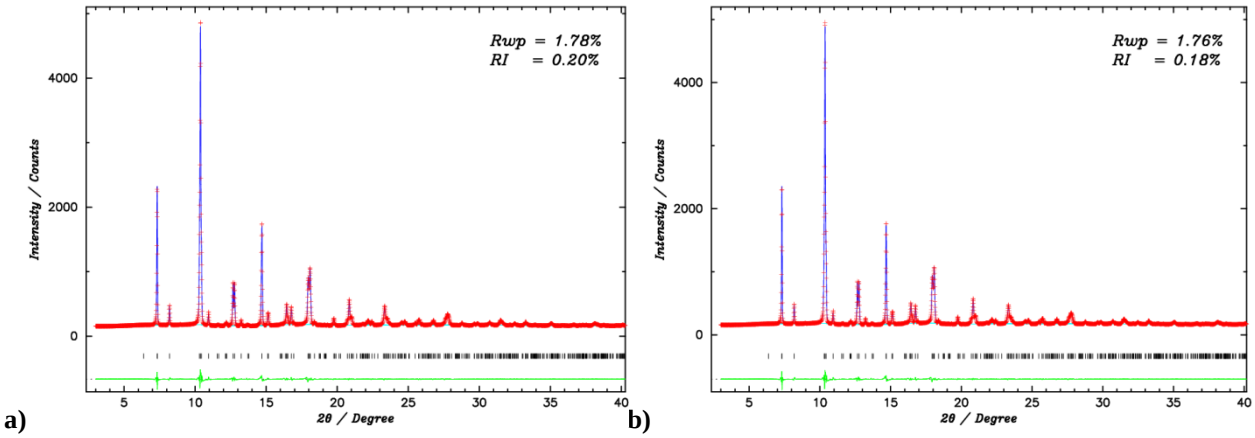

a) **b)**

Figure A.14 a) Le Bail fit for 0.65BTFM-0.35CTO at 300 K. b) Le Bail fit for 0.65BTFM-0.35CTO at 325 K.

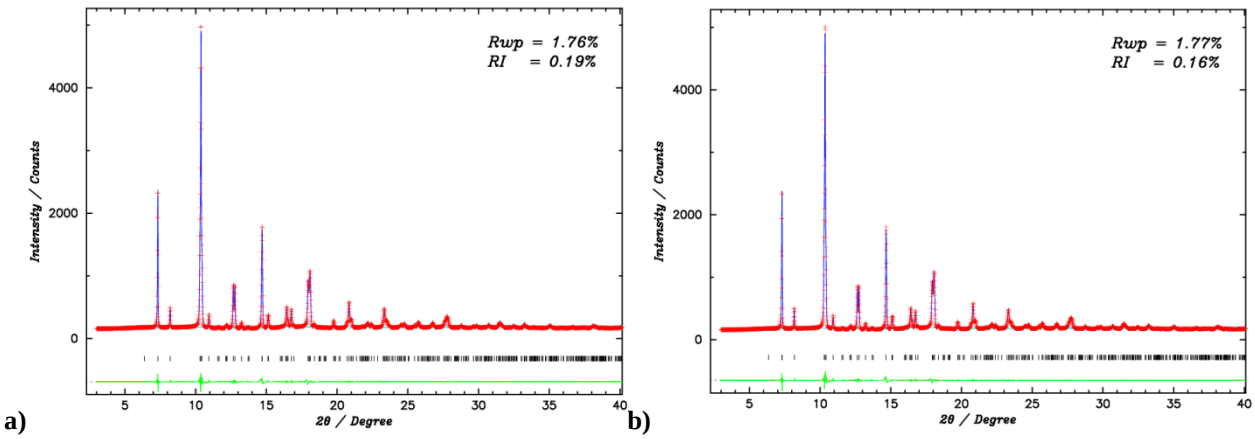

Figure A.15 a) Le Bail fit for 0.65BTFM-0.35CTO at 350 K. b) Le Bail fit for 0.65BTFM-0.35CTO at 375 K.

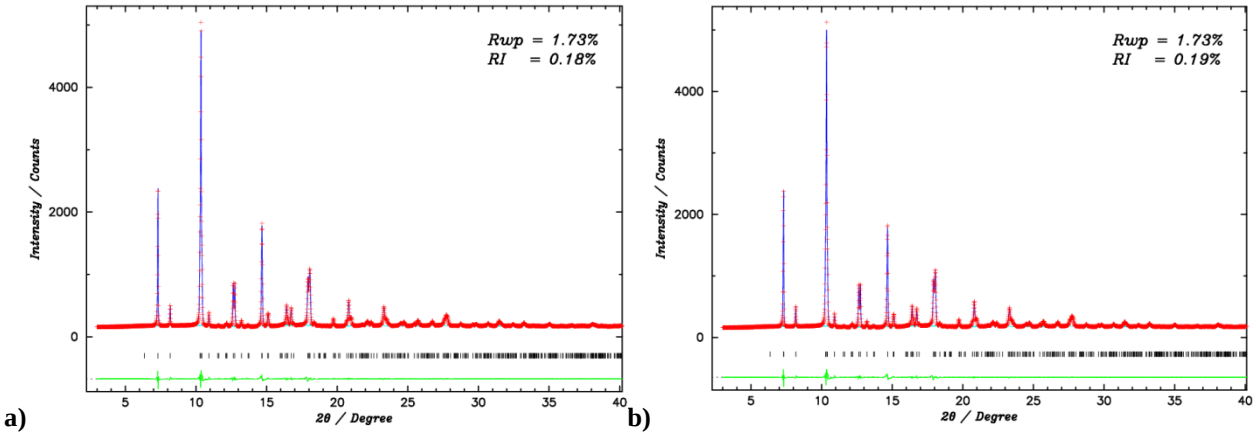

Figure A.16 a) Le Bail fit for 0.65BTFM-0.35CTO at 400 K. b) Le Bail fit for 0.65BTFM-0.35CTO at 425 K.

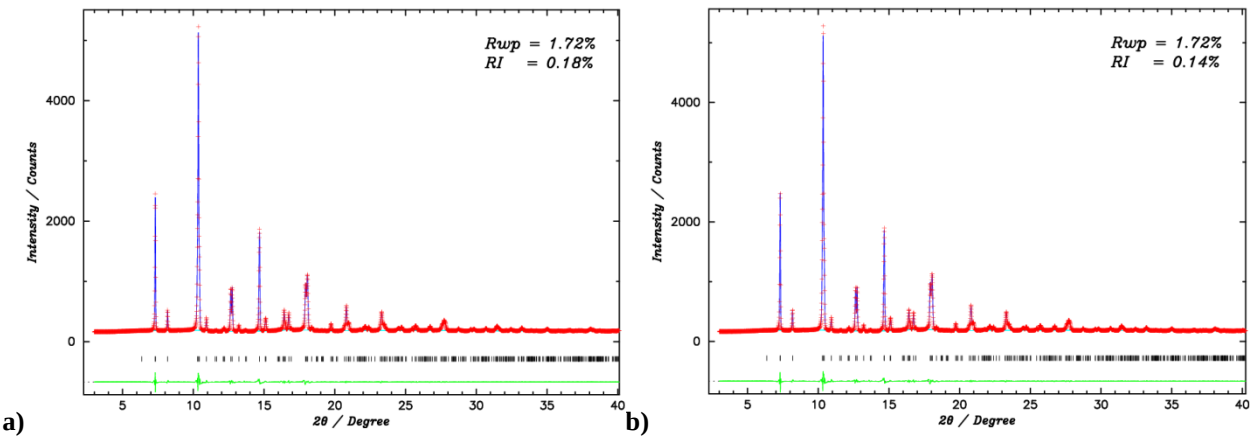

Figure A.17 a) Le Bail fit for 0.65BTFM-0.35CTO at 450 K. b) Le Bail fit for 0.65BTFM-0.35CTO at 470 K.

Table A.2: Lattice parameters, volume of the unit cell and reliability factors for 0.65BTFM-0.35CTO at VT.

T / K	a / Å	b / Å	c / Å	a / c	V / Å^3	R_{wp} / R_I / %
100	5.551(3)	5.479(1)	7.802(1)	0.7114	237.36660	2.27 / 0.15
125	5.5542(8)	5.4828(8)	7.8055(9)	0.71157	237.70411	1.86 / 0.21
150	5.5554(7)	5.4839(7)	7.807(1)	0.71157	237.8558477	1.81 /0.21
175	5.5563(7)	5.4850(7)	7.808(1)	0.71159	237.9767329	1.79 /0.20
200	5.5571(7)	5.4857(7)	7.809(1)	0.71159	238.0689399	1.78 /0.22
225	5.5579(7)	5.4865(7)	7.810(1)	0.71158	238.1816266	1.80 /0.22
250	5.5587(7)	5.4872(7)	7.812(1)	0.71156	238.2860438	1.81 /0.22
275	5.5597(7)	5.4881(7)	7.813(1)	0.711601	238.397092	1.77 /0.20
300	5.5606(7)	5.4889(7)	7.814(1)	0.711586	238.511279	1.78 /0.20
325	5.5617(7)	5.4900(7)	7.815(1)	0.711606	238.646574	1.76 /0.18
350	5.5627(7)	5.4911(7)	7.817(1)	0.71160	238.786194	1.76 /0.19
375	5.5637(7)	5.4923(7)	7.818(1)	0.71157	238.9300451	1.77 / 0.16
400	5.5649(7)	5.4937(7)	7.820(1)	0.711583	239.0924102	1.73 / 0.18
425	5.5661(7)	5.4953(7)	7.822(1)	0.71156	239.2700624	1.73 / 0.19
450	5.5672(7)	5.4969(7)	7.824(1)	0.711539	239.44231	1.72 / 0.18
470	5.5679(7)	5.4981(7)	7.825(1)	0.711485	239.5754128	1.72 / 0.14

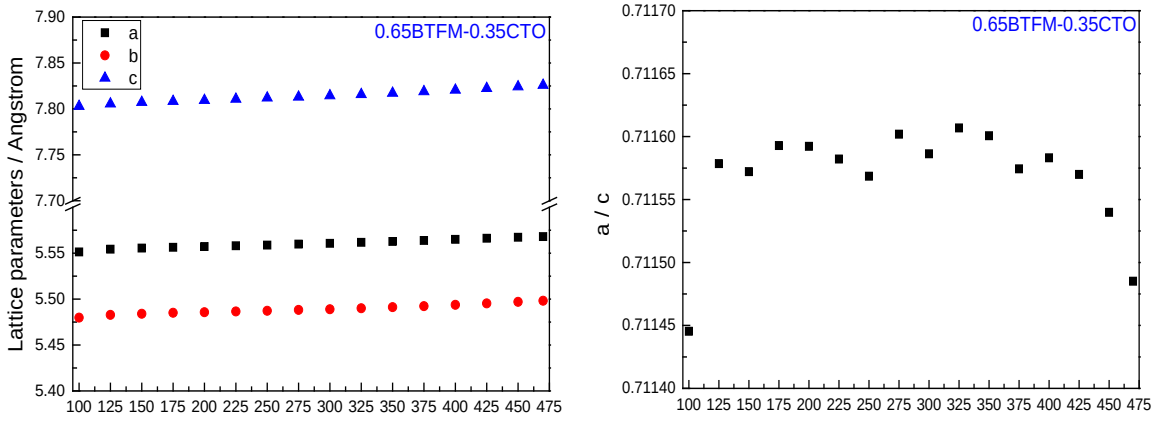

a) **b)**

Figure A.18 a) Lattice parameters versus temperature, b) a / c versus temperature for 0.65BTFM-0.35CTO.

Figure A.18 a) shows the lattice parameters versus temperature for 0.65BTFM-0.35CTO. The notation for x and y axis are the same as for Figure A.9 a). At the y axis, there is a break from 5.6 to 7.7 for better visualization of the tendency of the lattice parameters versus temperature. The black squares represent the lattice parameter *a*, the red circles *b* and the blue

triangles *c*. It is observed that the lattice parameters increase linearly with temperature. Figure A.18 b) shows the ratio *a* / *c* versus temperature for 0.65BTFM-0.35CTO. The notation for x and y axis are the same as for Figure A.9 b). It is observed that except for T = 100 K, the ratio a / c is constant with temperature. For T = 100 K, the reliability factors are much worse than the other temperatures so that can be the reason.

Figures A.19-A.26 show fitting results of Le Bail analysis for 0.7BTFM-0.3CTO at VT. The notation for x and y axis and the colours and marks are the same as for Figures A.1-A.8. The figures show the 2θ range from 3° to 40°.

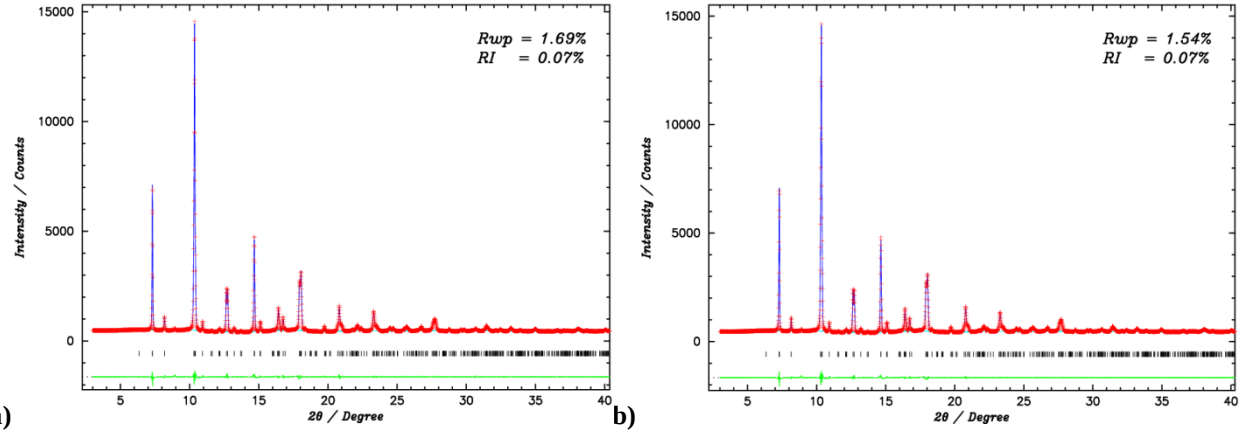

Figure A.19 a) Le Bail fit for 0.7BTFM-0.3CTO at 100 K. b) Le Bail fit for 0.7BTFM-0.3CTO at 125 K.

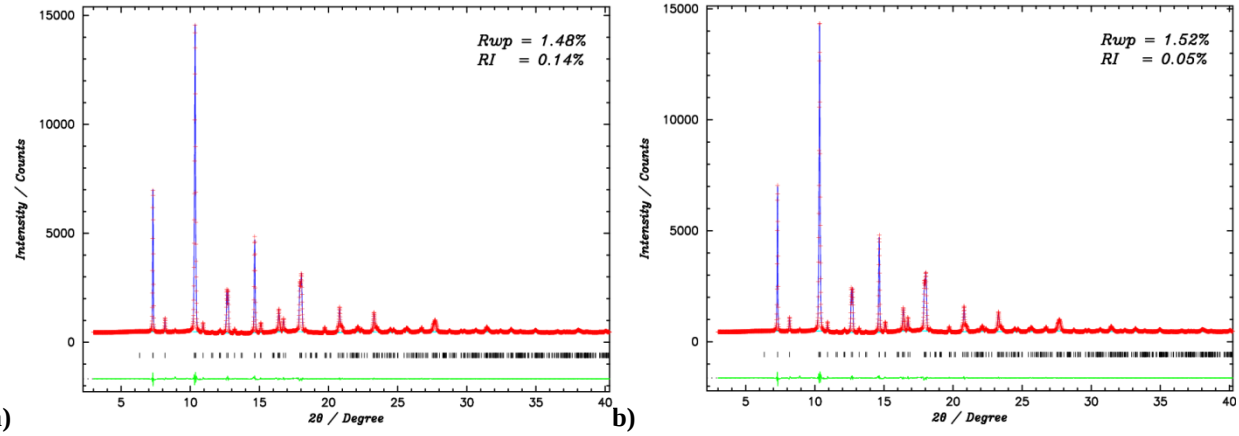

Figure A.20 a) Le Bail fit for 0.7BTFM-0.3CTO at 150 K. b) Le Bail fit for 0.7BTFM-0.3CTO at 175 K.

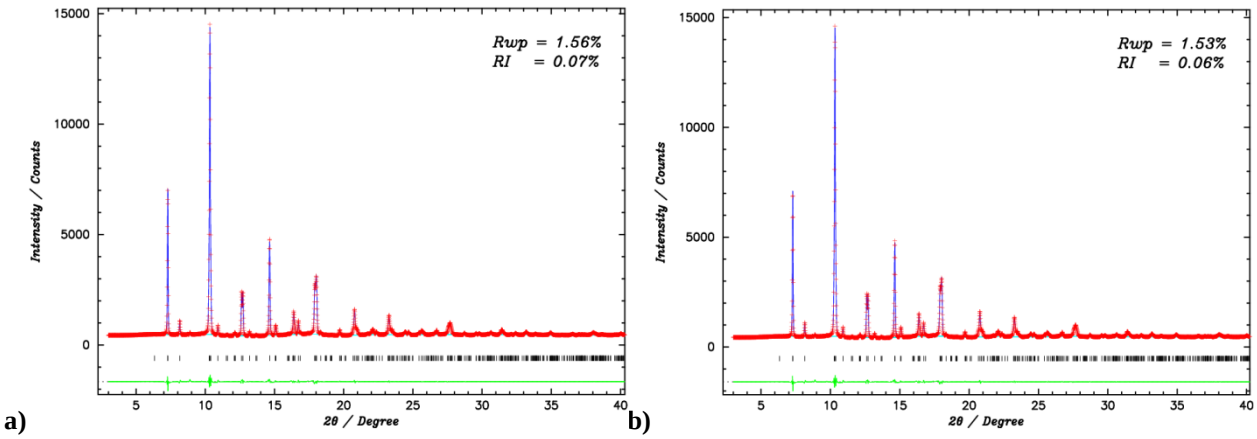

a) **b)**

Figure A.21 a) Le Bail fit for 0.7BTFM-0.3CTO at 200 K. b) Le Bail fit for 0.7BTFM-0.3CTO at 225 K.

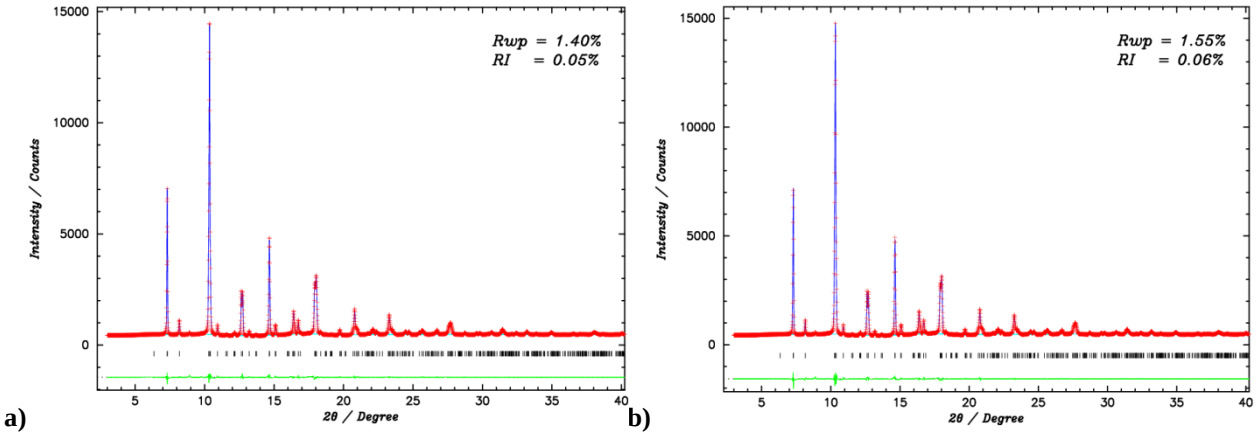

a) **b)**

Figure A.22 a) Le Bail fit for 0.7BTFM-0.3CTO at 250 K. b) Le Bail fit for 0.7BTFM-0.3CTO at 275 K.

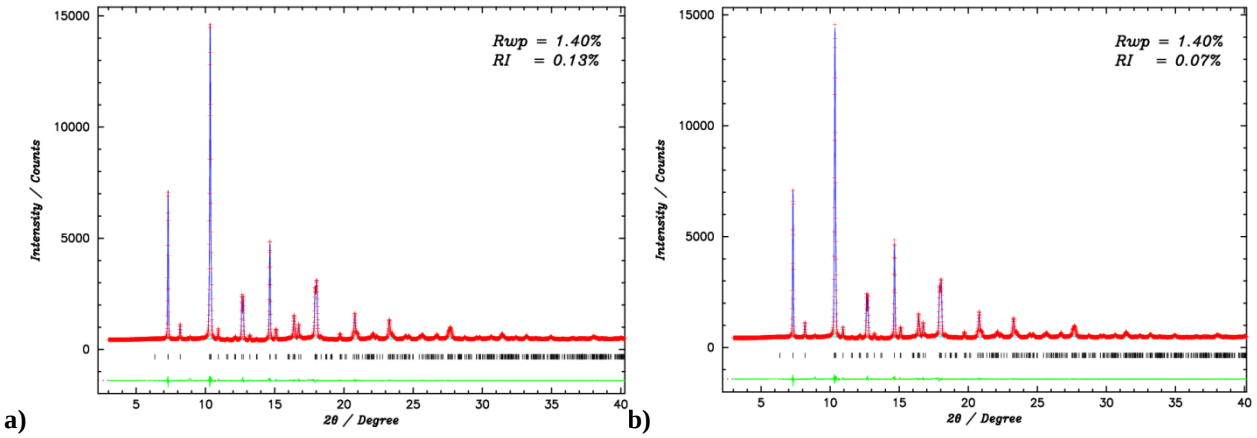

a) **b)**

Figure A.23 a) Le Bail fit for 0.7BTFM-0.3CTO at 300 K. b) Le Bail fit for 0.7BTFM-0.3CTO at 325 K.

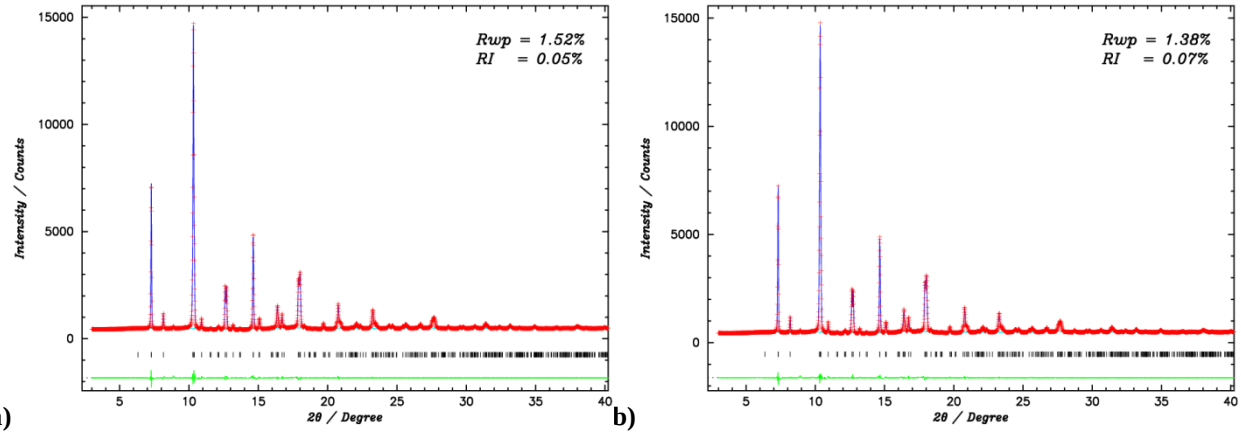

a) **b)**

Figure A.24 a) Le Bail fit for 0.7BTFM-0.3CTO at 350 K. b) Le Bail fit for 0.7BTFM-0.3CTO at 375 K.

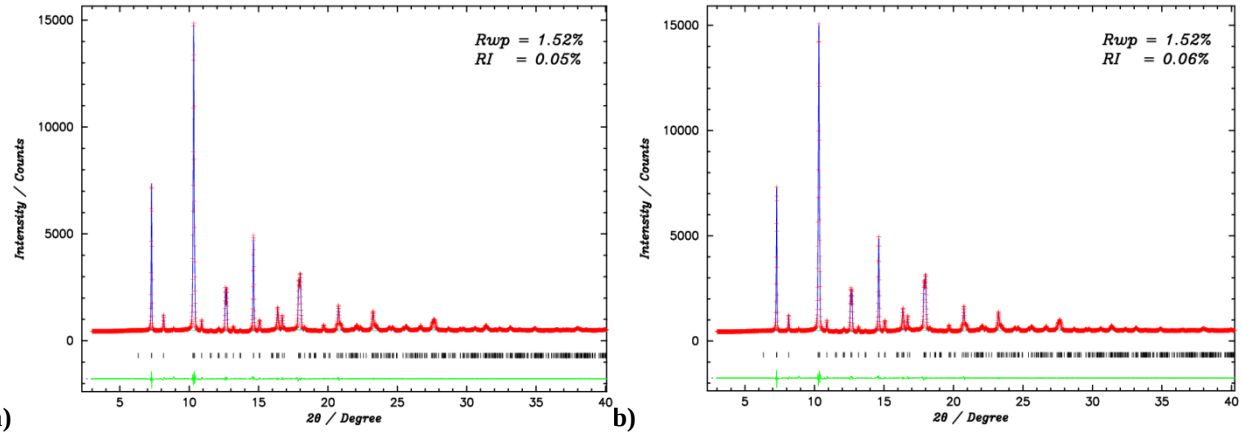

a) **b)**

Figure A.25 a) Le Bail fit for 0.7BTFM-0.3CTO at 400 K. b) Le Bail fit for 0.7BTFM-0.3CTO at 425 K.

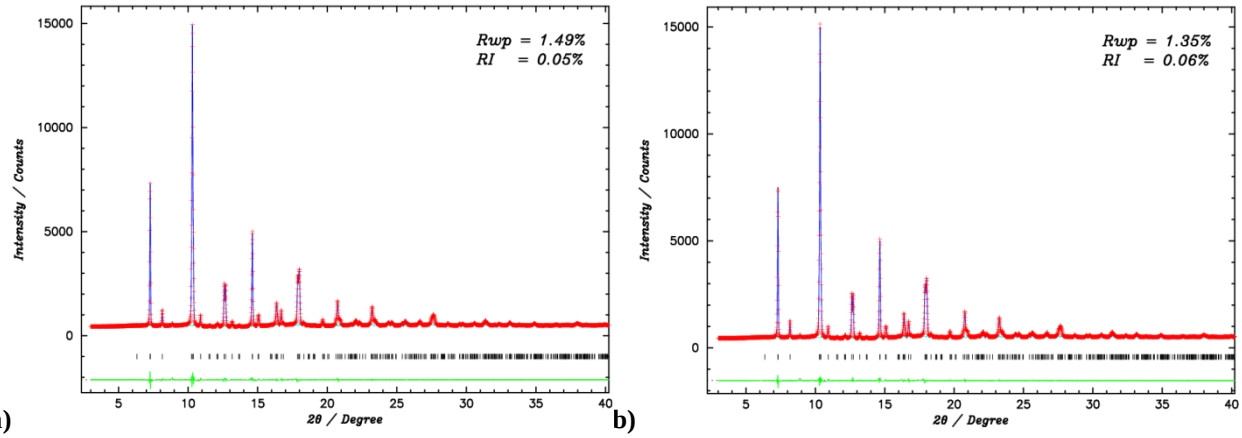

a) **b)**

Figure A.26 a) Le Bail fit for 0.7BTFM-0.3CTO at 450 K. b) Le Bail fit for 0.7BTFM-0.3CTO at 470 K.

Table A.3: Lattice parameters, volume of the unit cell and reliability factors for 0.7BTFM-0.3CTO at VT.

T / K	a / Å	b / Å	c / Å	a / c	V / Å^3	R_{wp} / R_I / %
100	5.5597(8)	5.4986(8)	7.8224(8)	0.71074	239.1444	1.69 /0.07
125	5.5622(7)	5.5013(7)	7.8254(8)	0.71079	239.45806	1.54 /0.07
150	5.5634(6)	5.5026(6)	7.828(1)	0.71066	239.66405	1.48 /0.14
175	5.5634(7)	5.5027(7)	7.8274(8)	0.71076	239.62888	1.52 /0.05
200	5.5644(7)	5.5037(7)	7.8285(8)	0.71078	239.75091	1.56 /0.07
225	5.5649(7)	5.5041(7)	7.8293(8)	0.710778	239.8137	1.53 /0.06
250	5.5664(6)	5.5053(6)	7.8331(9)	0.710622	240.04497	1.40 /0.05
275	5.5667(7)	5.5056(7)	7.8316(8)	0.710805	240.03096	1.55 /0.06
300	5.5681(6)	5.5065(6)	7.8356(9)	0.710622	240.2539	1.40 /0.13
325	5.5694(6)	5.5075(6)	7.8373(9)	0.710626	240.40142	1.40 /0.07
350	5.5697(7)	5.5078(7)	7.8353(8)	0.710843	240.36532	1.52 /0.05
375	5.5715(6)	5.5092(6)	7.8398(9)	0.710677	240.64313	1.38 /0.07
400	5.5718(7)	5.5094(7)	7.8379(8)	0.710871	240.60637	1.52 /0.05
425	5.5729(7)	5.5105(7)	7.8394(8)	0.710891	240.75047	1.52 /0.06
450	5.5741(7)	5.5117(7)	7.8410(8)	0.710887	240.90329	1.49 /0.05
470	5.5755(6)	5.5131(6)	7.8453(9)	0.710685	241.15632	1.35 /0.06

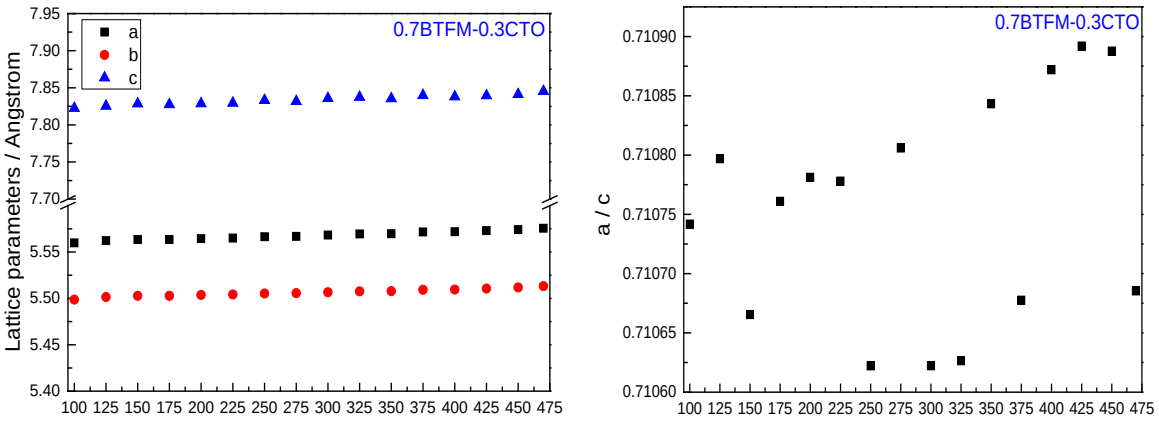

a) **b)**

Figure A.27 a) Lattice parameters versus temperature, b) a / c versus temperature for 0.7BTFM-0.3CTO.

Figure A.27 a) shows the lattice parameters versus temperature for 0.7BTFM-0.3CTO. The notation for x and y axis are the same as the Figure A.9 a). At the y axis, there is a break from 5.4 to 7.9 for better visualization of the tendency of the lattice parameters versus temperature. The color and marks are the same as the Figure A.9. It is observed that the lattice parameters increase

linearly with temperature. Figure A.27 b) shows the ratio *a* / *c* versus temperature for 0.7BTFM-0.3CTO. The units of x and y axis are the same as the Figure A.9 b). It is observed that there is not a clear tendency of the ratio *a* / *c* with temperature.

Figures A.28-A.35 show fitting results of Le Bail analysis for 0.75BTFM-0.25CTO at VT. The notation for x and y axis and the colours and marks are the same as for Figures A.1-A.8. The figures show the 2θ range from 3° to 40°.

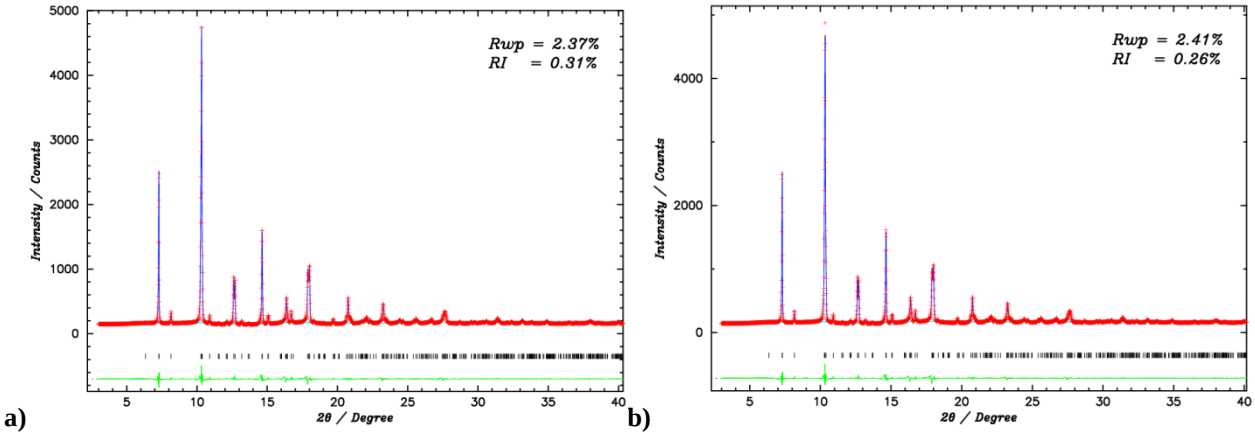

Figure A.28 a) Le Bail fit for 0.75BTFM-0.25CTO at 100 K. b) Le Bail fit for 0.75BTFM-0.25CTO at 125 K.

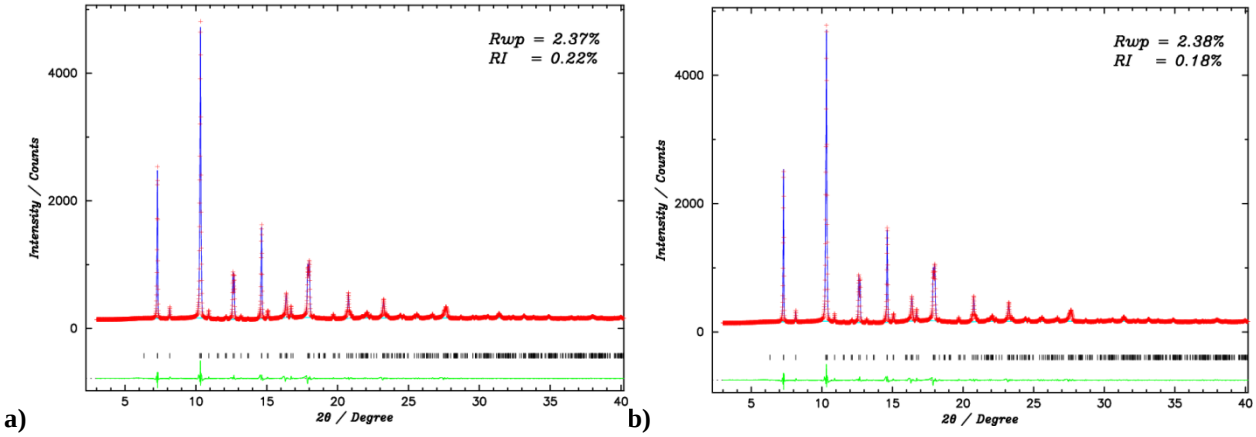

Figure A.29 a) Le Bail fit for 0.75BTFM-0.25CTO at 150 K. b) Le Bail fit for 0.75BTFM-0.25CTO at 175 K.

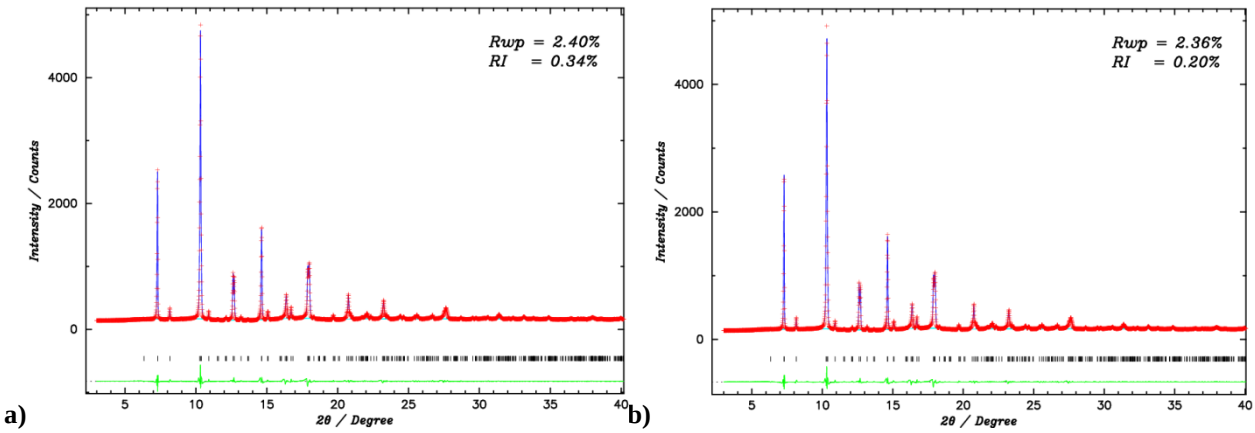

a) b)

Figure A.30 a) Le Bail fit for 0.75BTFM-0.25CTO at 200 K. b) Le Bail fit for 0.75BTFM-0.25CTO at 225 K.

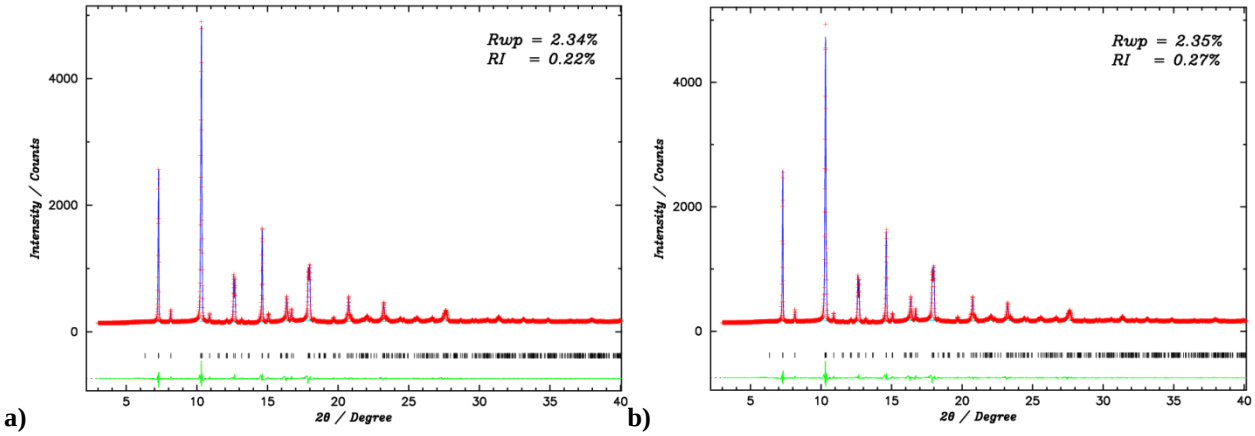

a) b)

Figure A.31 a) Le Bail fit for 0.75BTFM-0.25CTO at 250 K. b) Le Bail fit for 0.75BTFM-0.25CTO at 275 K.

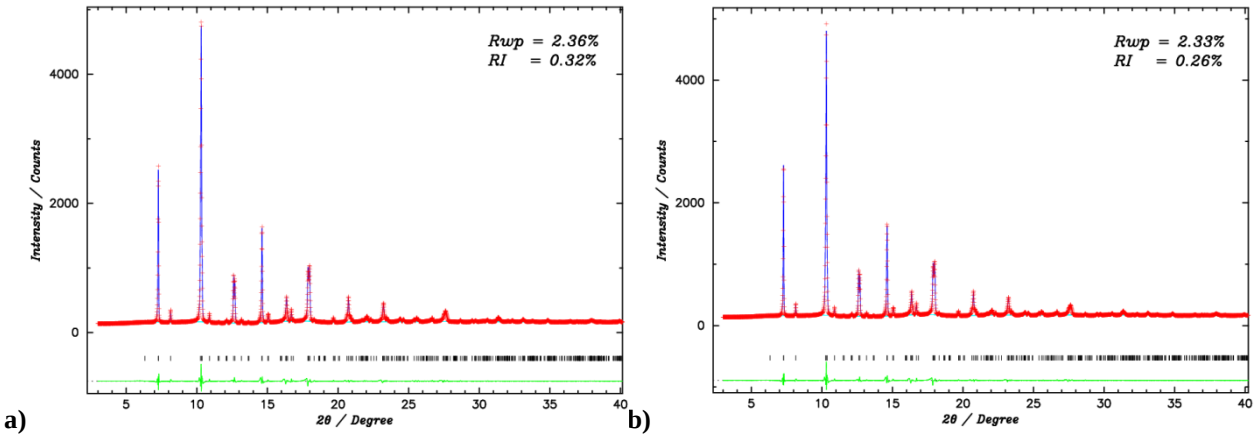

a) b)

Figure A.32 a) Le Bail fit for 0.75BTFM-0.25CTO at 300 K. b) Le Bail fit for 0.75BTFM-0.25CTO at 325 K.

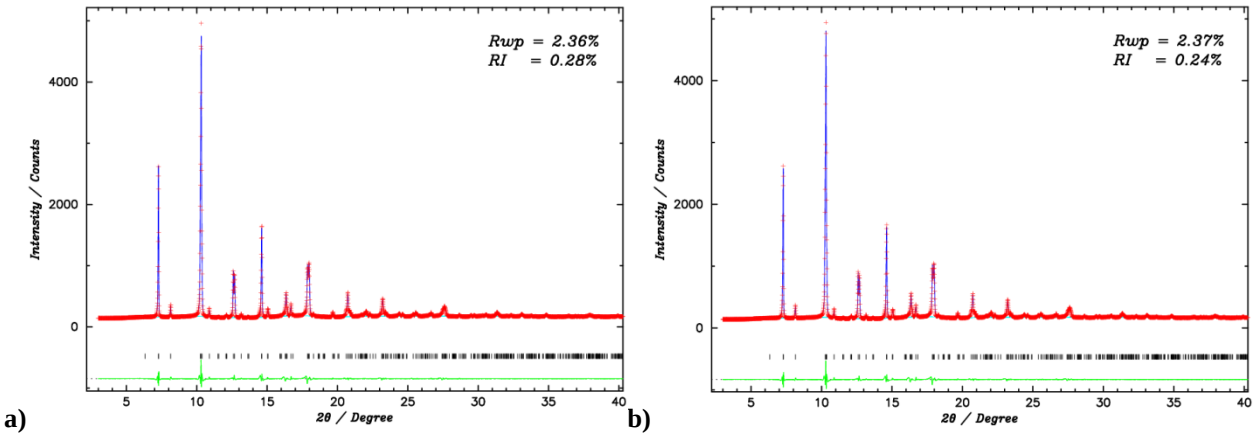

a) b)

Figure A.33 a) Le Bail fit for 0.75BTFM-0.25CTO at 350 K. b) Le Bail fit for 0.75BTFM-0.25CTO at 375 K.

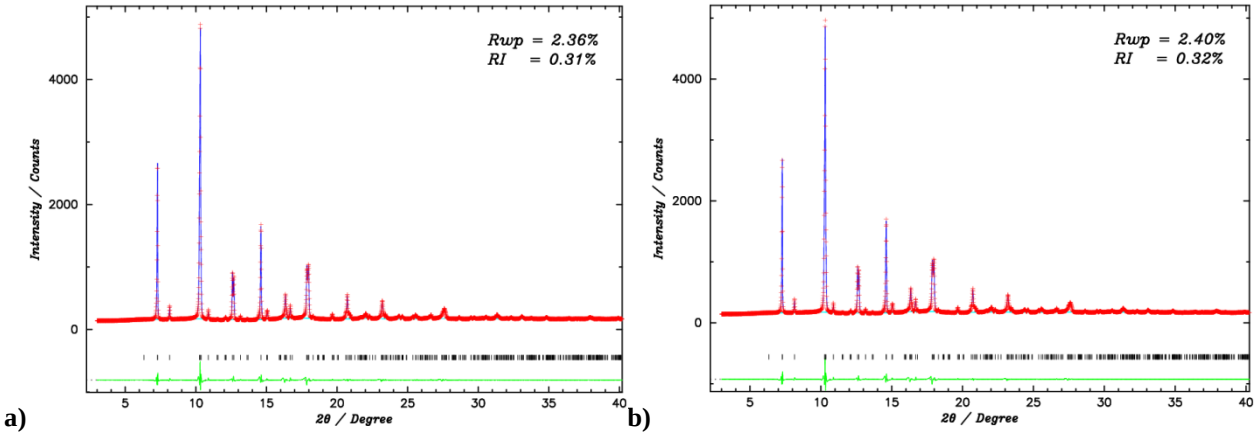

a) b)

Figure A.34 a) Le Bail fit for 0.75BTFM-0.25CTO at 400 K. b) Le Bail fit for 0.75BTFM-0.25CTO at 425 K.

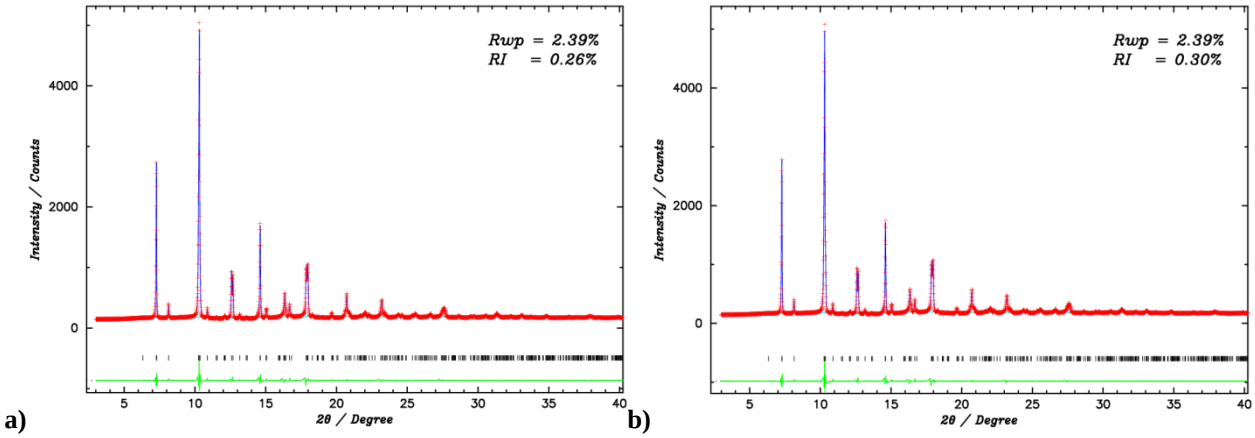

a) b)

Figure A.35 a) Le Bail fit for 0.75BTFM-0.25CTO at 450 K. b) Le Bail fit for 0.75BTFM-0.25CTO at 470 K.

Table A.4: Lattice parameters, volume of the unit cell and reliability factors for 0.75BTFM-0.25CTO at VT.

T* / *K	***a* / Å**	***b* / Å**	***c* / Å**	***a* / *c***	***V* / Å^3**	***R_{wp}* / *R_I*/ %**
100	5.5726(9)	5.5141(9)	7.838(1)	0.71089	240.88040	2.37 / 0.31
125	5.5730(9)	5.5150(9)	7.840(1)	0.710838	240.96912	2.41 / 0.26
150	5.5735(9)	5.5158(9)	7.841(1)	0.710806	241.06199	2.37 / 0.22
175	5.5741(9)	5.5166(9)	7.842(1)	0.710795	241.15138	2.38 / 0.18
200	5.5751(9)	5.517(1)	7.843(1)	0.710821	241.26128	2.40 / 0.34
225	5.5758(9)	5.5181(9)	7.844(1)	0.710783	241.3687	2.36 / 0.20
250	5.5768(9)	5.5190(9)	7.846(1)	0.710761	241.49853	2.34 / 0.22
275	5.5777(9)	5.5196(9)	7.847(1)	0.710765	241.60291	2.35 / 0.27
300	5.5787(9)	5.520(1)	7.848(1)	0.710765	241.72067	2.36 / 0.32
325	5.5797(9)	5.5210(9)	7.850(1)	0.710763	241.83959	2.33 / 0.26
350	5.5806(9)	5.521(1)	7.851(1)	0.710751	241.94448	2.36 / 0.28
375	5.5817(9)	5.522(1)	7.853(1)	0.710756	242.07049	2.37 / 0.24
400	5.5829(9)	5.522(1)	7.854(1)	0.710769	242.19602	2.36 / 0.31
425	5.5839(9)	5.523(1)	7.856(1)	0.71076	242.31519	2.40 / 0.32
450	5.5847(9)	5.524(1)	7.857(1)	0.710721	242.42756	2.39 / 0.26
470	5.5857(9)	5.525(1)	7.859(1)	0.710747	242.54660	2.39 / 0.30

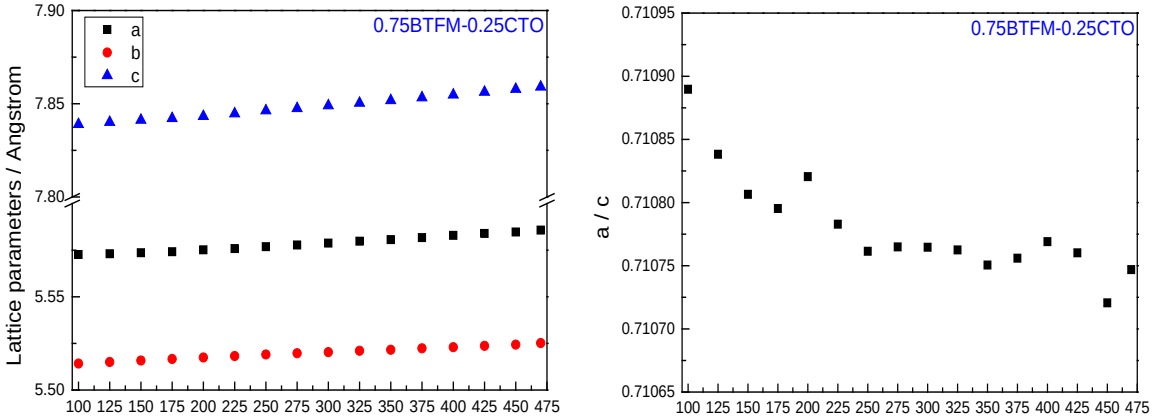

Figure A.36 a) Lattice parameters versus temperature, b) a / c versus temperature for 0.75BTFM-0.25CTO.

Figure A.36 a) shows the lattice parameters versus temperature for 0.75BTFM-0.25CTO. The notation for x and y axis are the same as the Figure A.9 a). At the y axis, there is a break from 5.6 to 7.8 for better visualization of the tendency of the lattice parameters versus temperature. The colour and marks are the same as the Figure A.9 a). It is observed that the

lattice parameters increase linearly with temperature. Figure A.36 b) shows the ratio a / c versus temperature for 0.75BTFM-0.25CTO. The notation for x and y axis are the same as the Figure A.9 b). It is observed that the ratio a / c decreases linearly with temperature.

Figures A.37-A.44 show fitting results of Le Bail analysis for 0.8BTFM-0.2CTO at VT. The notation for the axis x and y and the colour and marks are the same as for Figures A.1-A.8. The figures show the 2θ range from 3° to 40°.

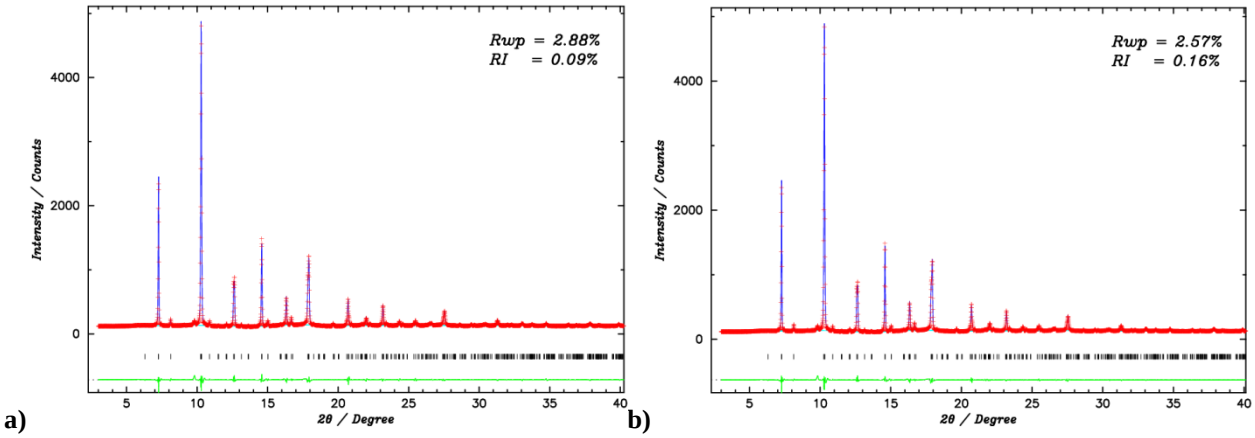

Figure A.37 a) Le Bail fit for 0.8BTFM-0.2CTO at 100 K. b) Le Bail fit for 0.8BTFM-0.2CTO at 125 K.

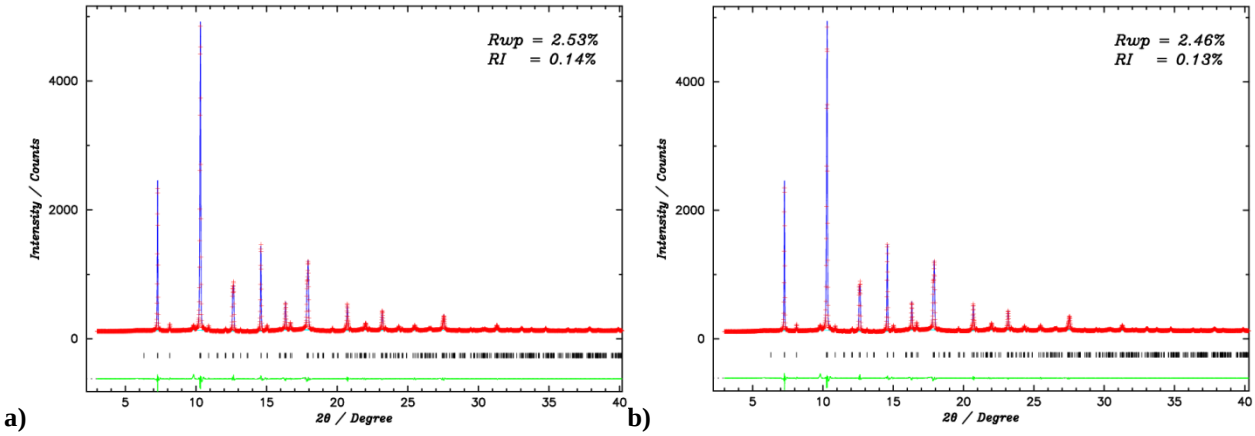

Figure A.38 a) Le Bail fit for 0.8BTFM-0.2CTO at 150 K. b) Le Bail fit for 0.8BTFM-0.2CTO at 175 K.

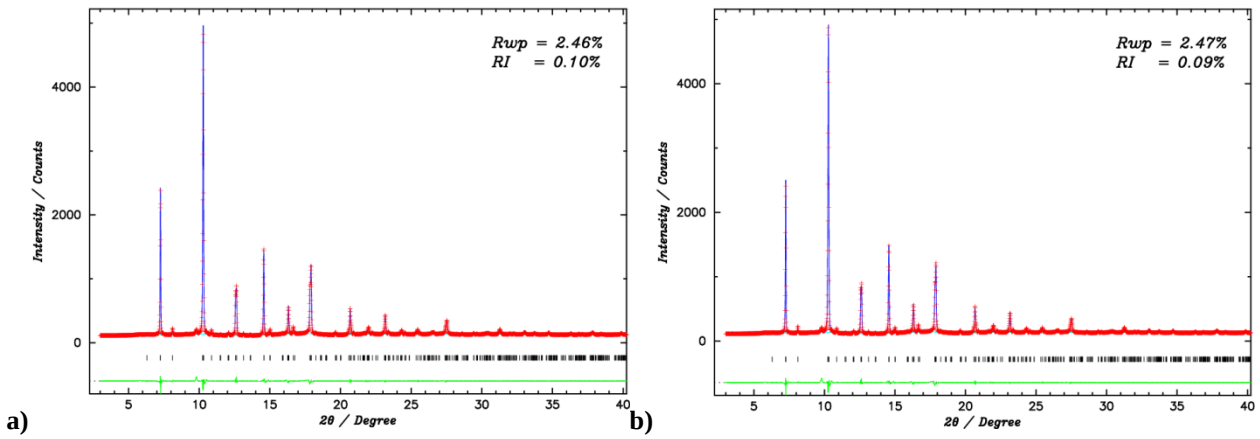

a) b)

Figure A.39 a) Le Bail fit for 0.8BTFM-0.2CTO at 200 K. b) Le Bail fit for 0.8BTFM-0.2CTO at 225 K.

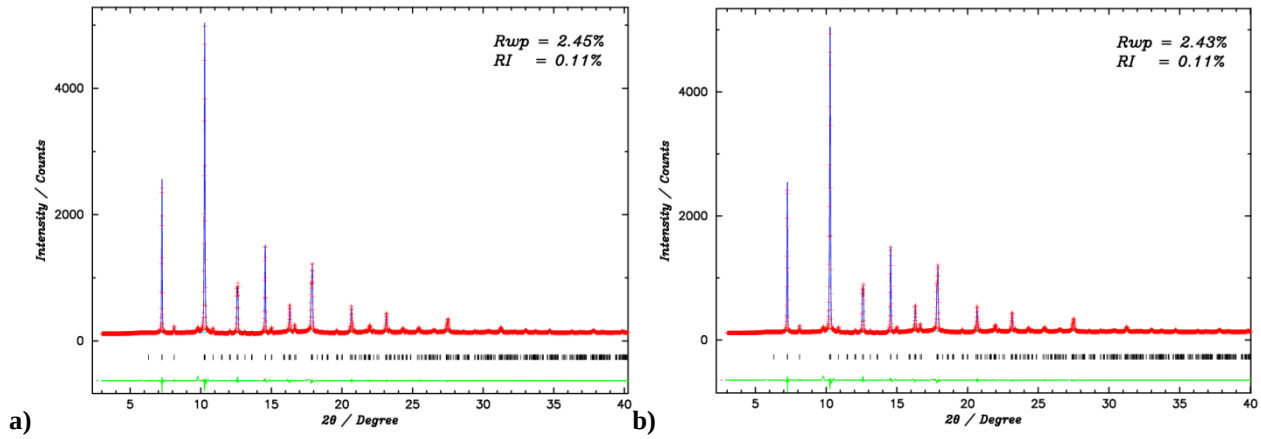

a) b)

Figure A.40 a) Le Bail fit for 0.8BTFM-0.2CTO at 250 K. b) Le Bail fit for 0.8BTFM-0.2CTO at 275 K.

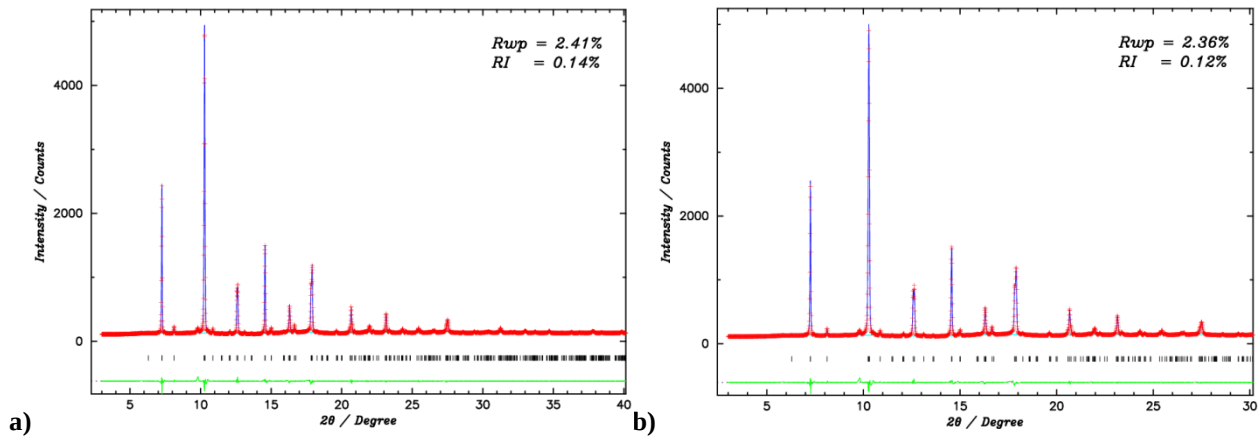

a) b)

Figure A.41 a) Le Bail fit for 0.8BTFM-0.2CTO at 300 K. b) Le Bail fit for 0.8BTFM-0.2CTO at 325 K.

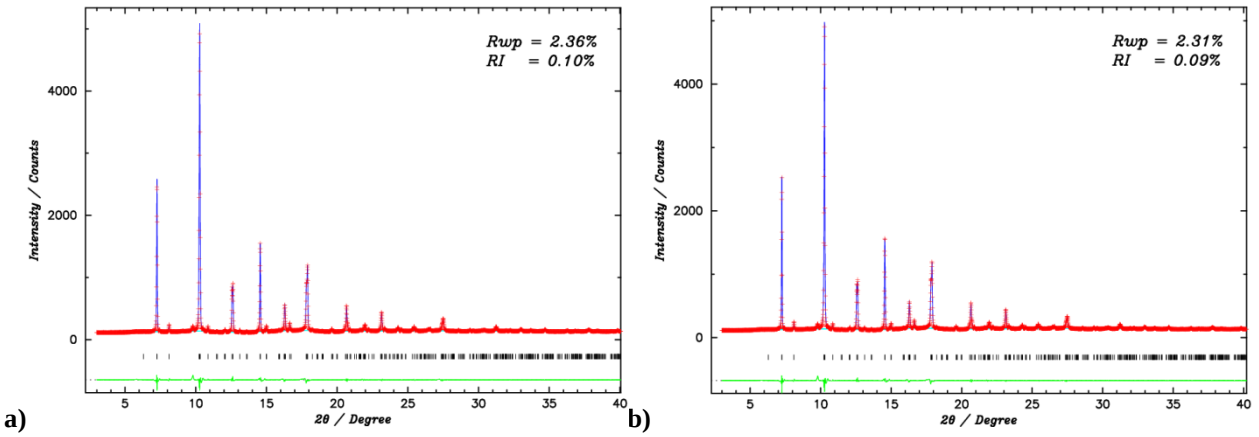

a) b)

Figure A.42 a) Le Bail fit for 0.8BTFM-0.2CTO at 350 K. b) Le Bail fit for 0.8BTFM-0.2CTO at 375 K.

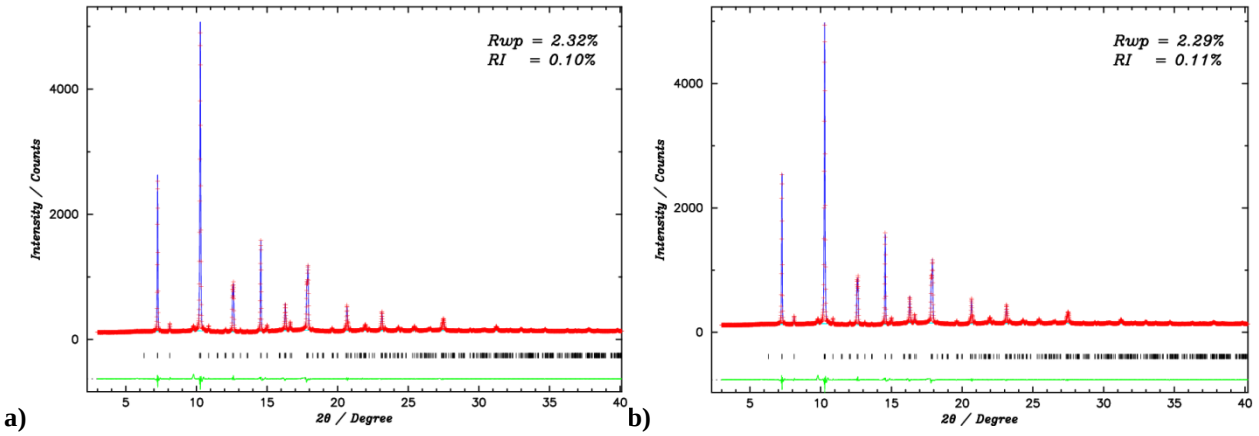

a) b)

Figure A.43 a) Le Bail fit for 0.8BTFM-0.2CTO at 400 K. b) Le Bail fit for 0.8BTFM-0.2CTO at 425 K.

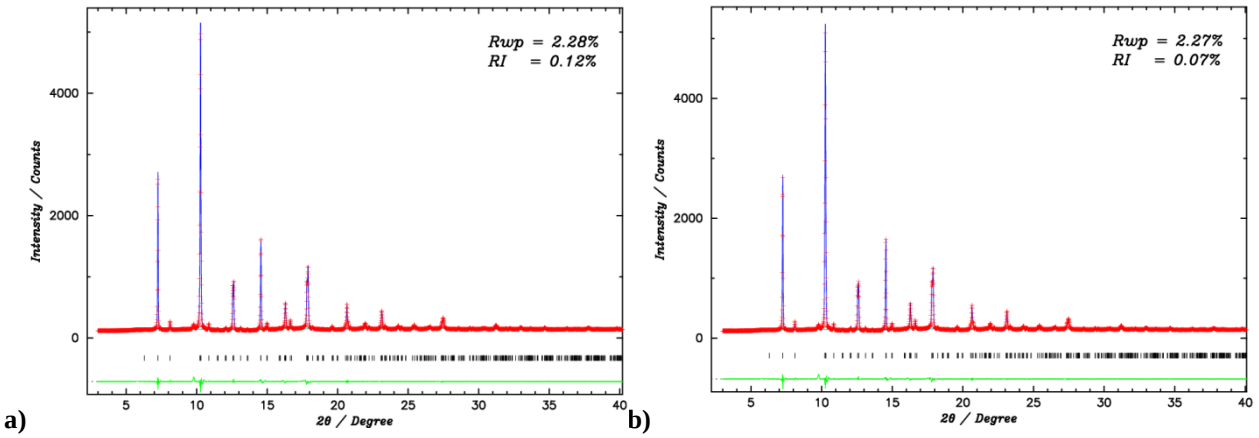

a) b)

Figure A.44 a) Le Bail fit for 0.8BTFM-0.2CTO at 450 K. b) Le Bail fit for 0.8BTFM-0.2CTO at 470 K.

Table A.5: Lattice parameters, volume of the unit cell and reliability factors for 0.8BTFM-0.2CTO at VT.

T / K	a / Å	b / Å	c / Å	a / c	V / Å^3	R_{wp} / R_I/ %
100	5.5780(9)	5.5386(9)	7.850(1)	0.710503	242.5517	2.88 / 0.09
125	5.5807(8)	5.5409(8)	7.856(1)	0.710297	242.9546	2.57 /0.16
150	5.5815(8)	5.5417(8)	7.857(1)	0.710340	243.04540	2.53 /0.14
175	5.5828(8)	5.5433(7)	7.860(1)	0.710269	243.25771	2.46 /0.13
200	5.5837(8)	5.5443(7)	7.861(1)	0.710256	243.38460	2.46 /0.10
225	5.5848(8)	5.5455(7)	7.863(1)	0.710256	243.53012	2.47 /0.09
250	5.5860(8)	5.5466(7)	7.864(1)	0.710258	243.68638	2.45 /0.11
275	5.5873(8)	5.5477(7)	7.866(1)	0.710262	243.84414	2.43 /0.11
300	5.5882(8)	5.5480(7)	7.867(1)	0.710302	243.92374	2.41 /0.14
325	5.5897(8)	5.5493(7)	7.870(1)	0.710260	244.12492	2.36 /0.12
350	5.5914(8)	5.5504(7)	7.872(1)	0.710267	244.32006	2.36 /0.10
375	5.5930(8)	5.5514(7)	7.874(1)	0.710267	244.50008	2.31 /0.09
400	5.5941(8)	5.5519(7)	7.875(1)	0.710303	244.60846	2.32 / 0.10
425	5.5956(8)	5.5529(7)	7.877(1)	0.710300	244.78616	2.29 / 0.11
450	5.5976(8)	5.5545(7)	7.881(1)	0.710266	245.04202	2.28 / 0.12
470	5.5986(8)	5.5552(7)	7.882(1)	0.710265	245.16120	2.27 / 0.07

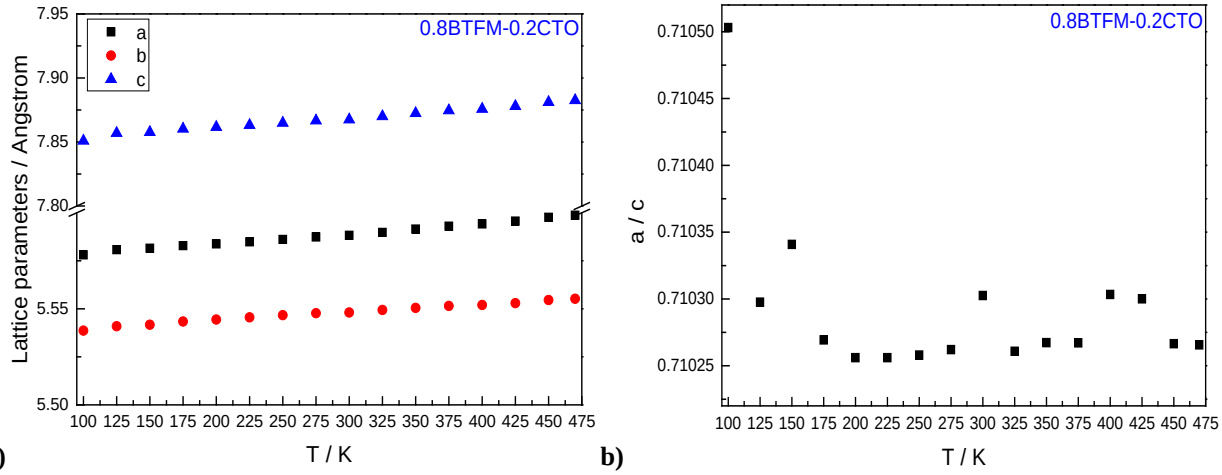

Figure A.45 a) Lattice parameters versus temperature, b) a / c versus temperature for 0.8BTFM-0.2CTO.

Figure A.45 a) shows the lattice parameters versus temperature for 0.8BTFM-0.2CTO. The notation of x and y axis are the same as the Figure A.9 a) . At the y axis, there is a break from 5.6 to 7.8 for better visualization of the tendency of the lattice parameters versus temperature. The color and marks are the same as the Figure A.9 a). It is observed that the lattice parameters

increases linearly with temperature. Figure A.45 b) shows the ratio *a* / *c* versus temperature for 0.8BTFM-0.2CTO. The notation of x and y axis are the same as the Figure A.9 b). It is observed that except for T = 100 K, the ratio a / c is more or less constant with temperature. For T = 100 K, the reliability factors are much worse than the other temperatures so that could be the reason.

Figures A.46-A.53 show fitting results of Le Bail analysis for 0.85BTFM-0.15CTO at VT. The notation of x and y axis are the same as the Figures A.1-A.8. The figures show the 2θ range from 3° to 40°. The red crosses represent the observed data while the blue solid line represents the model. The difference green curve is below. The above black tics represent Bragg reflection positions for the orthorhombic phase while the below black tics represent the rhombohedral phase.

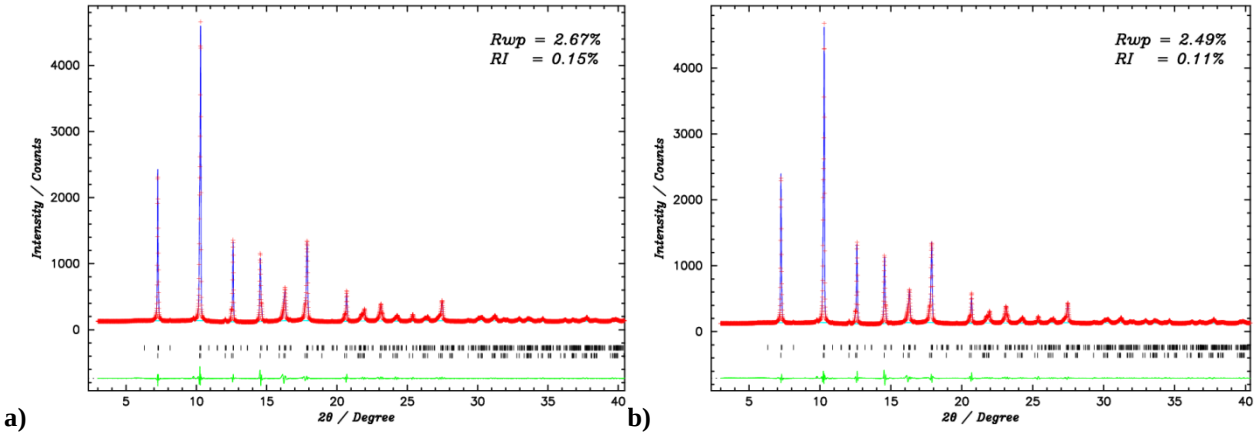

Figure A.46 a) Le Bail fit for 0.85BTFM-0.15CTO at 100 K. b) Le Bail fit for 0.85BTFM-0.15CTO at 125 K.

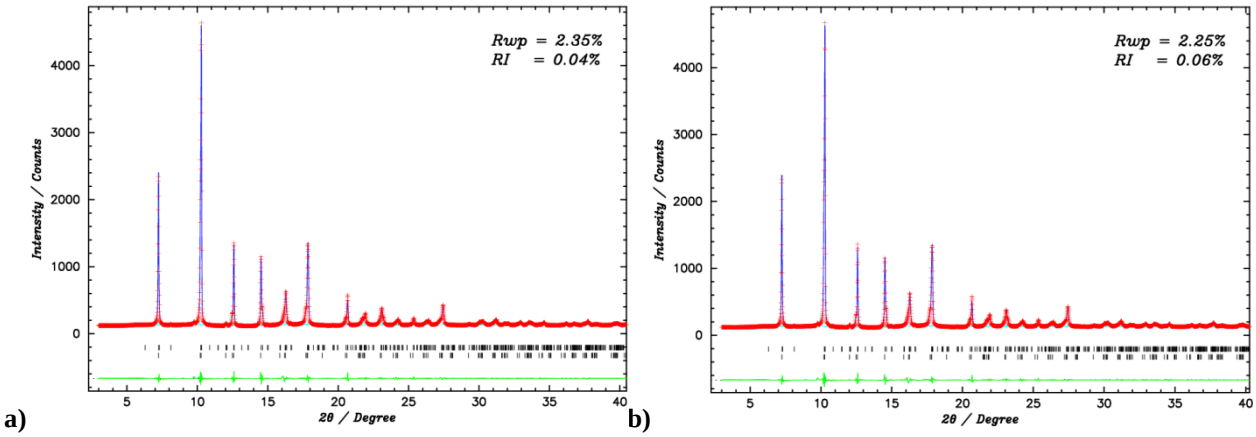

Figure A.47 a) Le Bail fit for 0.85BTFM-0.15CTO at 150 K. b) Le Bail fit for 0.85BTFM-0.15CTO at 175 K.

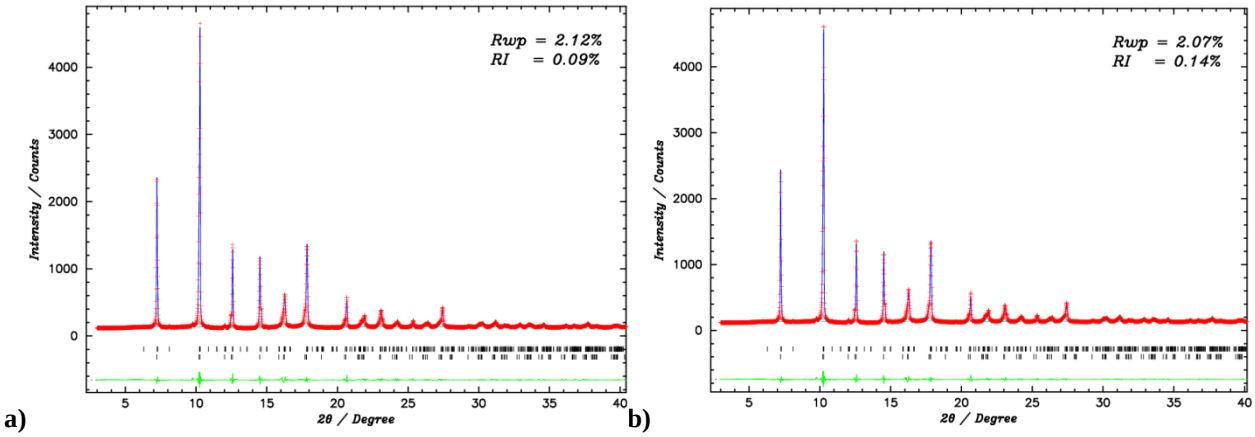

a) b)

Figure A.48 a) Le Bail fit for 0.85BTFM-0.15CTO at 200 K. b) Le Bail fit for 0.85BTFM-0.15CTO at 225 K.

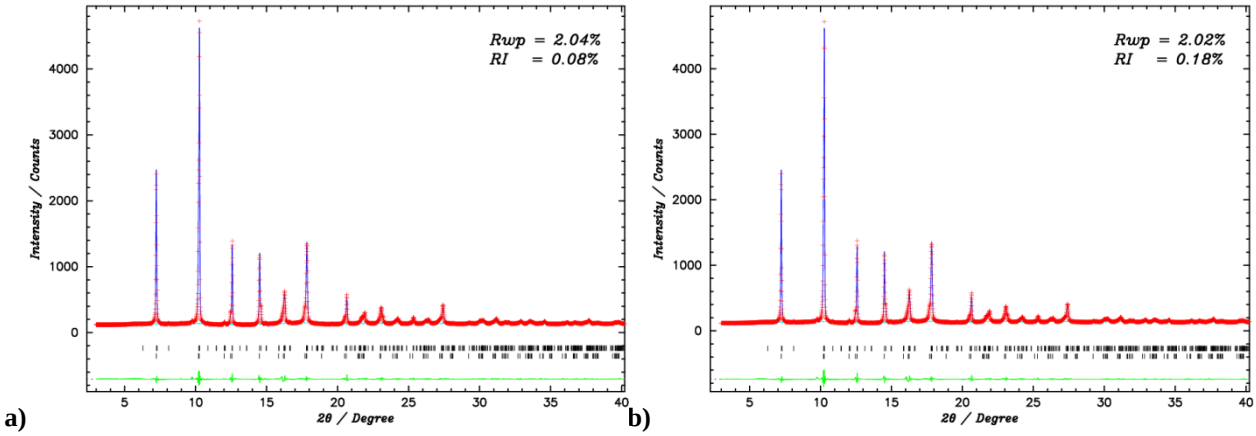

a) b)

Figure A.49 a) Le Bail fit for 0.85BTFM-0.15CTO at 250 K. b) Le Bail fit for 0.85BTFM-0.15CTO at 275 K.

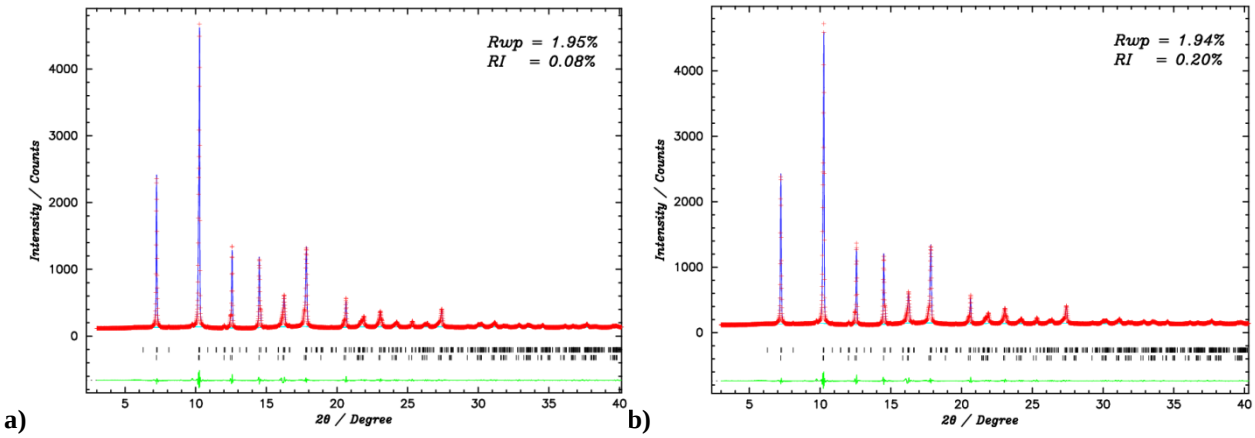

a) b)

Figure A.50 a) Le Bail fit for 0.85BTFM-0.15CTO at 300 K. b) Le Bail fit for 0.85BTFM-0.15CTO at 325 K.

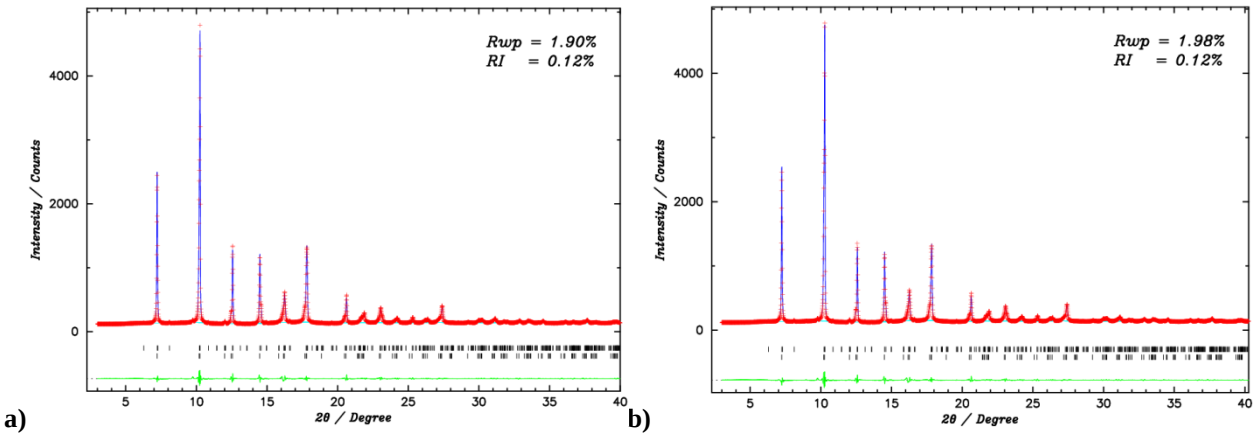

a) b)

Figure A.51 a) Le Bail fit for 0.85BTFM-0.15CTO at 350 K. b) Le Bail fit for 0.85BTFM-0.15CTO at 375 K.

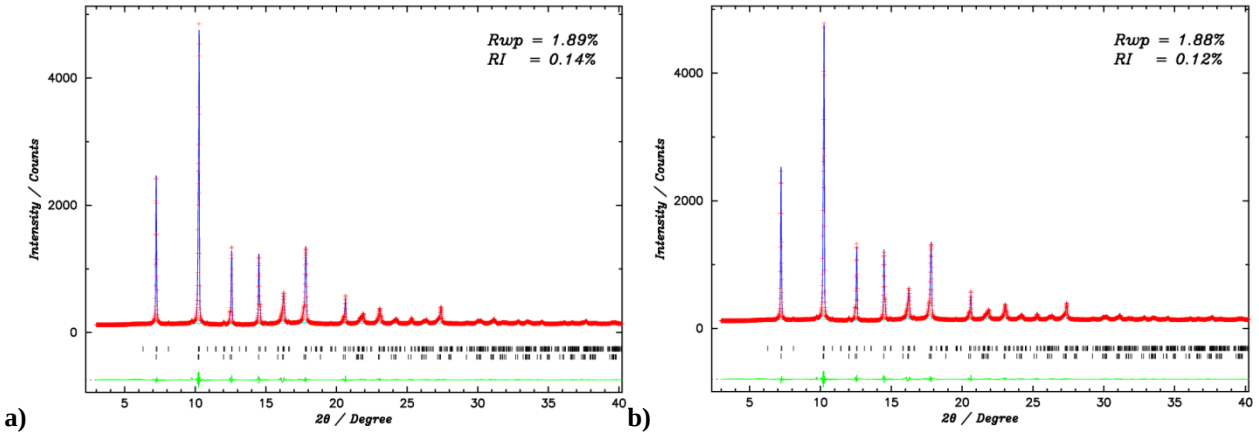

a) b)

Figure A.52 a) Le Bail fit for 0.85BTFM-0.15CTO at 400 K. b) Le Bail fit for 0.85BTFM-0.15CTO at 425 K.

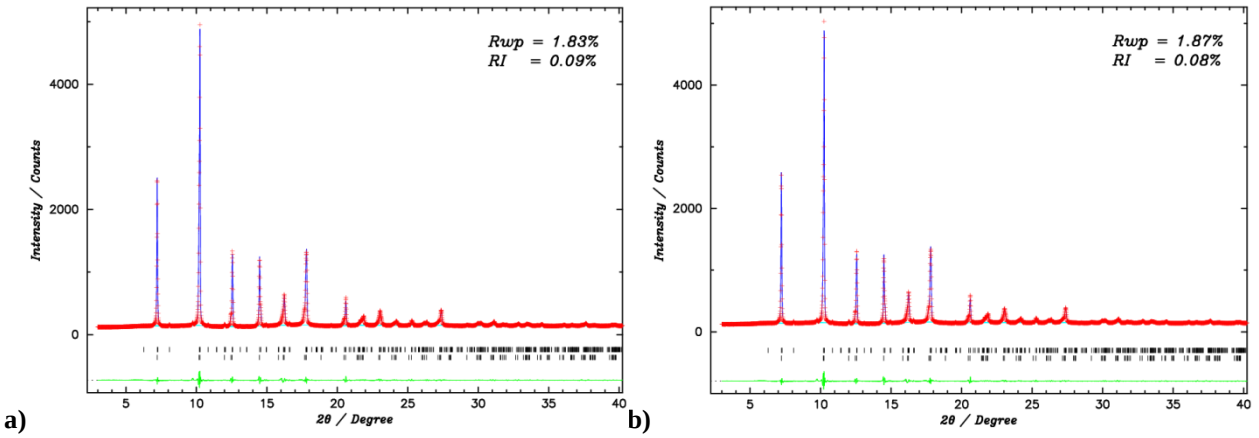

a) b)

Figure A.53 a) Le Bail fit for 0.85BTFM-0.15CTO at 450 K. b) Le Bail fit for 0.85BTFM-0.15CTO at 470 K.

Table A.6: Lattice parameters, volume of the unit cell and reliability factors for 0.85BTFM-0.15CTO at VT.

T* / *K	**Phase**	***a* / Å**	***b* / Å**	***c* / Å**	***a* / *c***	***V* / Å^3**	R_{wp} / R_I / %
100	O	5.592(1)	5.5703(9)	7.842(2)	0.713	244.31271	2.67 / 0.15
	R	5.570(1)	5.570(1)	13.777(3)	0.404	370.23694	
125	O	5.599(1)	5.5756(8)	7.850(2)	0.71327	245.07468	2.49/0.11
	R	5.581(2)	5.581(2)	13.786(4)	0.40483	371.92531	
150	O	5.6032(9)	5.5803(8)	7.855(1)	0.71326	245.63284	2.35/0.04
	R	5.588(2)	5.588(2)	13.794(4)	0.40509	373.05087	
175	O	5.6042(9)	5.5823(8)	7.858(1)	0.71315	245.84875	2.25/0.06
	R	5.589(2)	5.589(2)	13.796(4)	0.40513	373.31263	
200	O	5.6043(9)	5.5843(8)	7.861(1)	0.71289	246.03505	2.12/0.09
	R	5.589(2)	5.589(2)	13.796(3)	0.40514	373.29029	
225	O	5.6047(9)	5.5851(8)	7.8625(1)	0.71284	246.12393	2.07/0.14
	R	5.589(2)	5.589(2)	13.797(3)	0.40510	373.32010	
250	O	5.6056(8)	5.5861(8)	7.863(1)	0.71282	246.25123	2.04/0.08
	R	5.589(2)	5.589(2)	13.800(3)	0.40503	373.37646	
275	O	5.6060(9)	5.5863(8)	7.864(1)	0.71280	246.30017	2.02/0.18
	R	5.588(2)	5.588(2)	13.802(3)	0.40490	373.30072	
300	O	5.6068(9)	5.5875(7)	7.866(1)	0.71272	246.45673	1.95/0.08
	R	5.589(2)	5.589(2)	13.802(3)	0.40493	373.39867	
325	O	5.6081(9)	5.5880(7)	7.868(1)	0.71276	246.58093	1.94/0.20
	R	5.589(2)	5.5898(2)	13.806(3)	0.40487	373.59392	
350	O	5.6095(8)	5.5893(7)	7.870(1)	0.71270	246.77962	1.90 / 0.12
	R	5.591(2)	5.591(2)	13.808(3)	0.40491	373.82103	
375	O	5.6108(9)	5.5901(8)	7.872(1)	0.71268	246.93625	1.98 / 0.12
	R	5.591(2)	5.591(2)	13.811(3)	0.40485	373.96330	
400	O	5.6118(8)	5.5909(7)	7.875(1)	0.71261	247.08526	1.89 / 0.14
	R	5.592(2)	5.592(2)	13.812(3)	0.40491	374.16301	
425	O	5.6127(8)	5.5911(8)	7.876(1)	0.71256	247.18727	1.88 / 0.12
	R	5.5931(2)	5.5931(2)	13.812(3)	0.40492	374.21422	
450	O	5.6138(8)	5.5920(8)	7.879(1)	0.71243	247.36365	1.83 / 0.09
	R	5.594(2)	5.594(2)	13.814(3)	0.40493	374.38988	
470	O	5.6145(8)	5.5921(8)	7.881(1)	0.71233	247.46888	1.87 / 0.08
	R	5.593(2)	5.593(2)	13.814(3)	0.40490	374.36189	

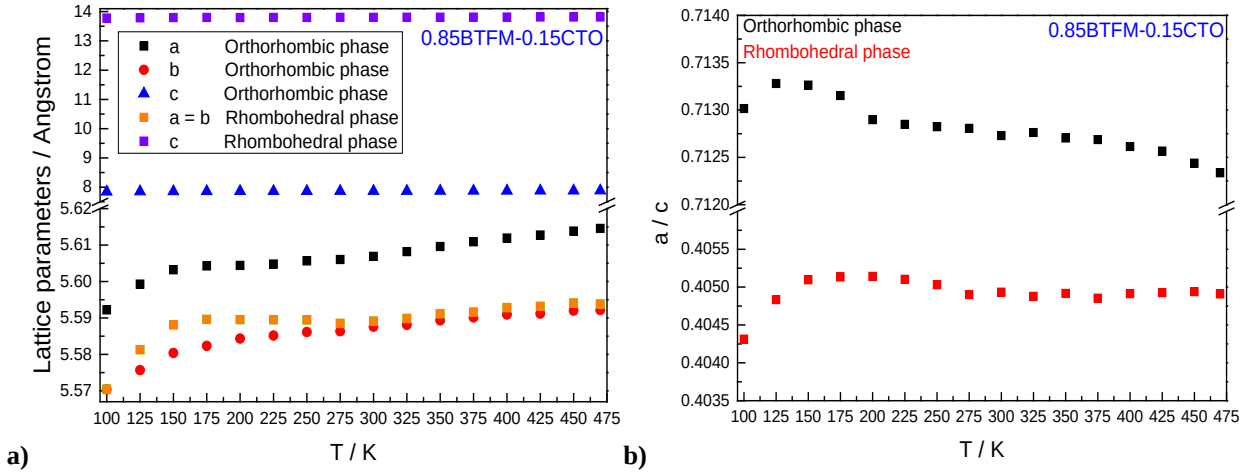

Figure A.54 a) Lattice parameters versus temperature, b) a / c versus temperature for 0.85BTFM-0.15CTO.

Figure A.54 a) shows the lattice parameters versus temperature for 0.85BTFM-0.15CTO. The notation of the x and y axis is the same as the Figure A.9 a). At the y axis, there is a break from 5.62 to 7.5 for better visualization of the tendency of the lattice parameters versus temperature. The black squares represent the lattice parameter *a*, the red circles *b* and the blue triangles *c* for the orthorhombic phase while the orange squares represent the lattice parameters *a* and *b* and the purple squares *c* for the rhombohedral phase. The lattice parameters *a* and *b* for the orthorhombic and rhombohedral structures increase with temperature. However, the lattice parameter *c* for both structures is constant with temperature. Figure A.54 b) shows the ratio *a* / *c* versus temperature for 0.85BTFM-0.15CTO. The notation of the x and y axis is the same as the Figure A.9 b). There is a break from 0.406 to 0.712. The black squares represent the orthorhombic phase while the red squares the rhombohedral phase. It is observed that the plots for the orthorhombic and rhombohedral phases follow a similar decreasing tendency of the ratio *a* / *c* with temperature.

Figures A.55-A.62 show fitting results of Le Bail analysis for 0.875BTFM-0.125CTO at VT. The notation of the x and y axis is the same as the Figures A.1-A.8. The figures show the 2θ range from 3° to 40°. The colours and marks are the same as the Figures A.46-4.53.

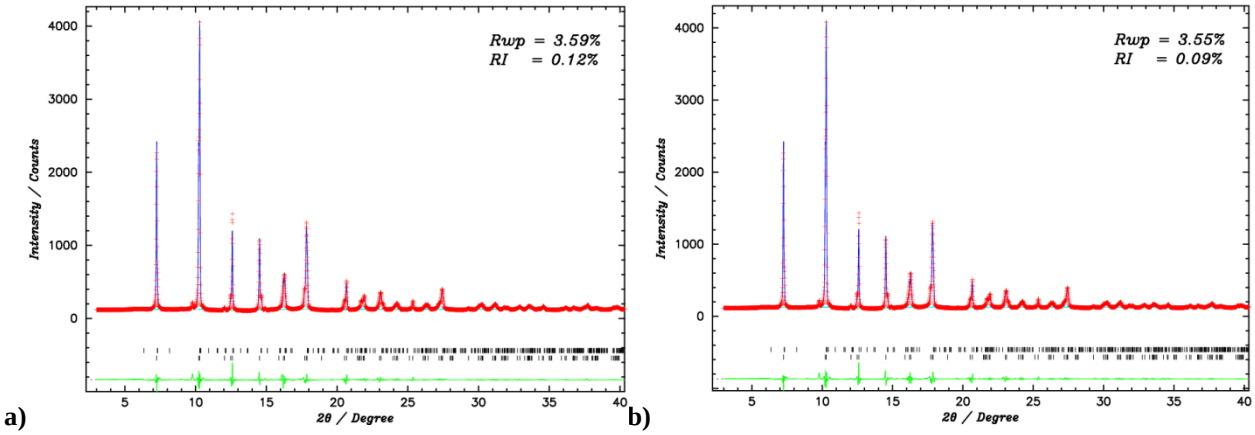

a) b)

Figure A.55 a) Le Bail fit for 0.875BTFM-0.125CTO at 100 K. b) Le Bail fit for 0.875BTFM-0.125CTO at 125 K.

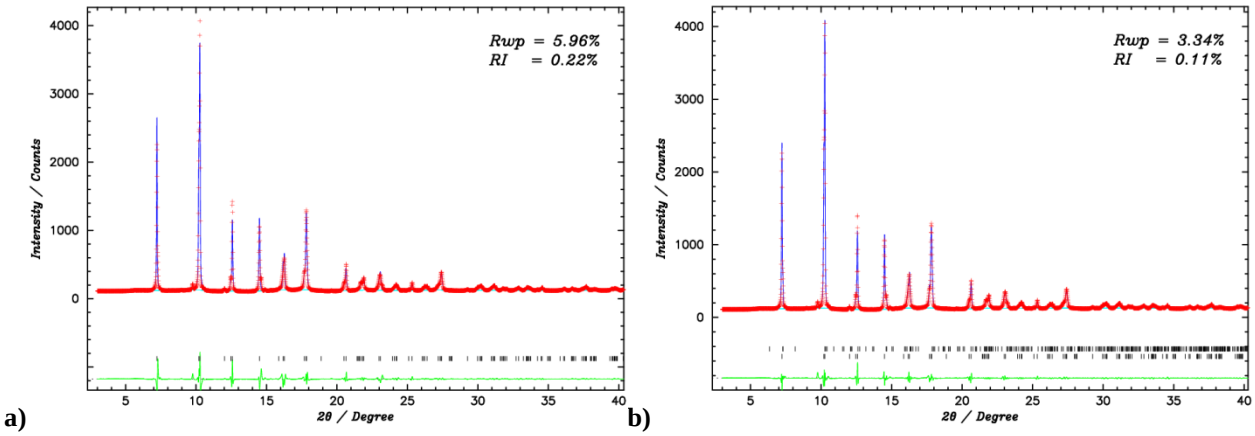

a) b)

Figure A.56 a) Le Bail fit for 0.875BTFM-0.125CTO at 150 K. b) Le Bail fit for 0.875BTFM-0.125CTO at 175 K.

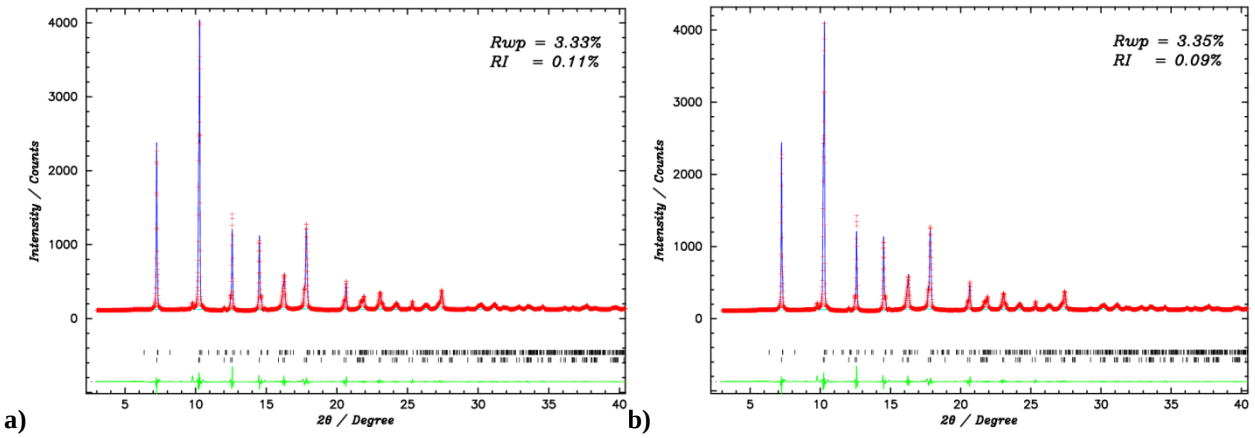

a) b)

Figure A.57 a) Le Bail fit for 0.875BTFM-0.125CTO at 200 K. b) Le Bail fit for 0.875BTFM-0.125CTO at 225 K.

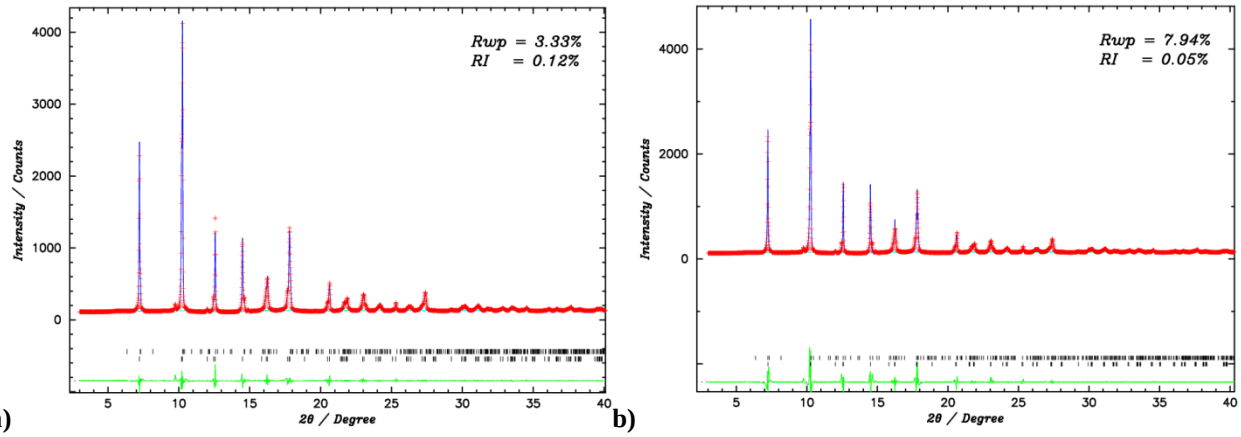

a) b)

Figure A.58 a) Le Bail fit for 0.875BTFM-0.125CTO at 250 K. b) Le Bail fit for 0.875BTFM-0.125CTO at 275 K.

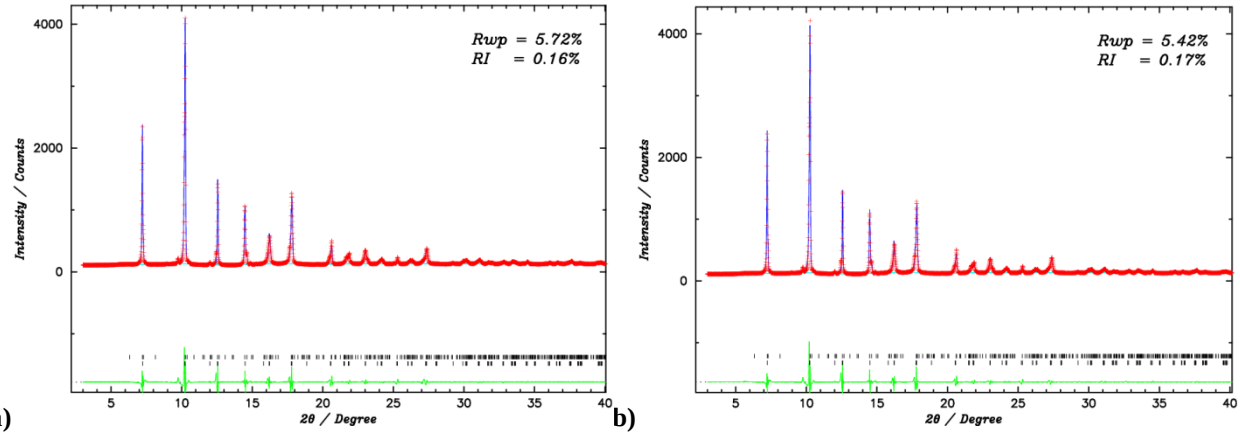

a) b)

Figure A.59 a) Le Bail fit for 0.875BTFM-0.125CTO at 300 K. b) Le Bail fit for 0.875BTFM-0.125CTO at 325 K.

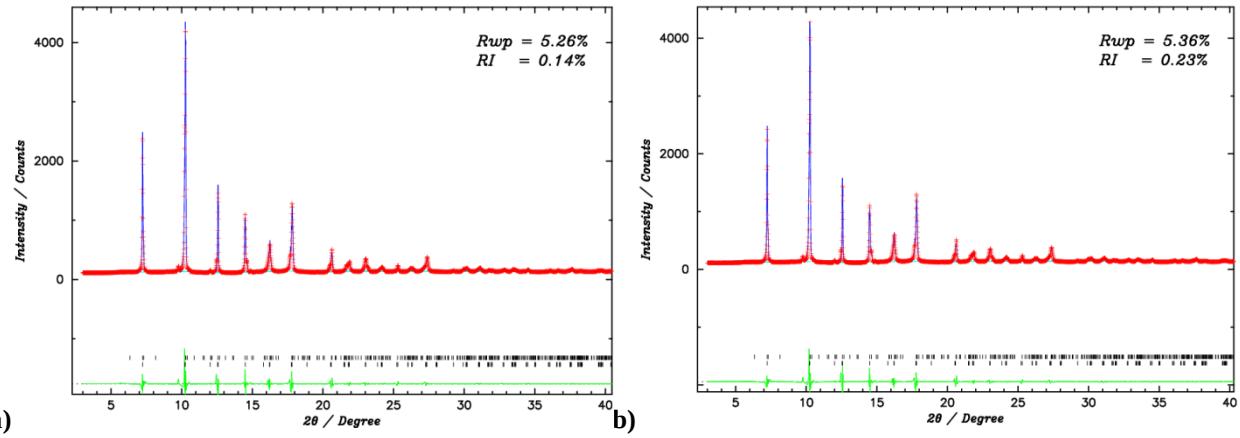

a) b)

Figure A.60 a) Le Bail fit for 0.875BTFM-0.125CTO at 350 K. b) Le Bail fit for 0.875BTFM-0.125CTO at 375 K.

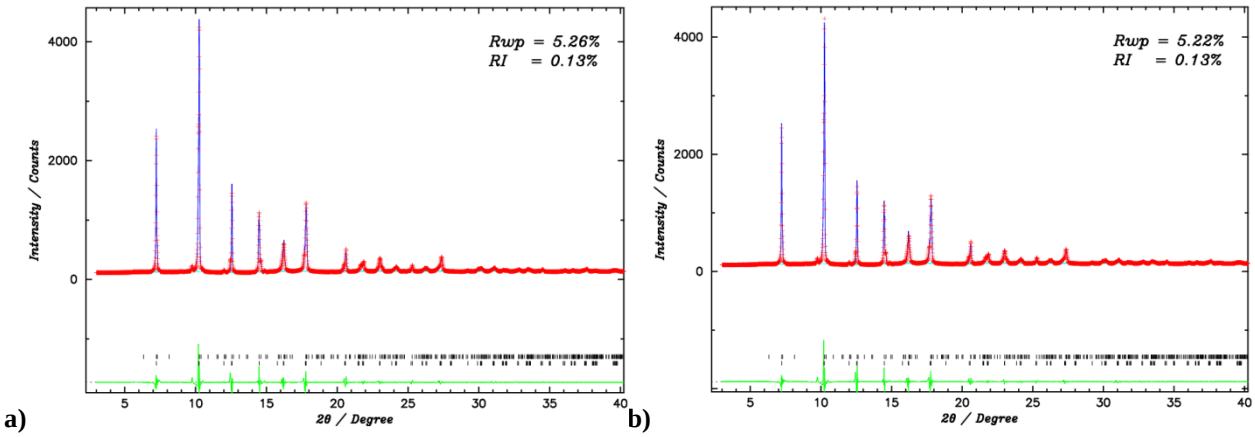

a) **b)**

Figure A.61 a) Le Bail fit for 0.875BTFM-0.125CTO at 400 K. b) Le Bail fit for 0.875BTFM-0.125CTO at 425 K.

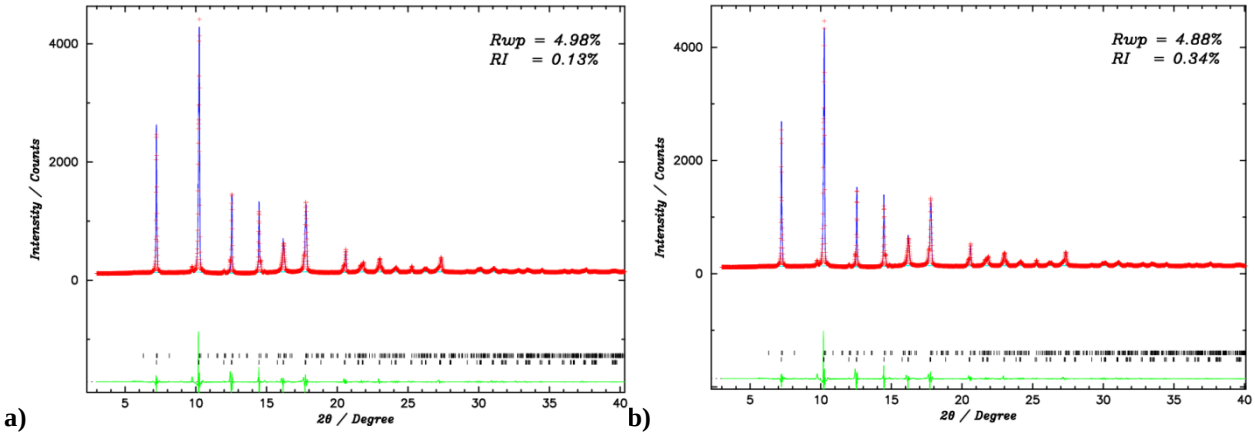

a) **b)**

Figure A.62 a) Le Bail fit for 0.875BTFM-0.125CTO at 450 K. b) Le Bail fit for 0.875BTFM-0.125CTO at 470 K.

Table A.7: Lattice parameters, volume of the unit cell and reliability factors for 0.875BTFM-0.125CTO at VT.

T* / *K	**Phase**	***a* / Å**	***b* / Å**	***c* / Å**	***a* / *c***	***V* / Å^3**	R_{wp} **/** R_I**/ %**
100	O	5.574(1)	5.535(3)	7.840(3)	0.71104	241.931	3.59/0.12
	R	5.573(1)	5.573(1)	13.795(3)	0.40405	371.185	
125	O	5.575(1)	5.499(2)	7.850(3)	0.71024	240.701	3.35/0.09
	R	5.574(1)	5.574(1)	13.795(3)	0.40406	371.24	
150	O	5.576(1)	5.495(2)	7.853(3)	0.71	240.694	5.96/0.22
	R	5.576(1)	5.576(1)	13.798(3)	0.40416	371.674	
175	O	5.577(1)	5.496(2)	7.856(3)	0.70996	240.836	3.34/0.11
	R	5.578(1)	5.578(1)	13.801(3)	0.40417	371.937	
200	O	5.578(1)	5.497(2)	7.857(3)	0.70998	240.948	3.33/0.11
	R	5.579(1)	5.579(1)	13.804(3)	0.40418	372.177	
225	O	5.579(1)	5.498(2)	7.857(3)	0.71003	241.051	3.35/0.09
	R	5.580(1)	5.580(1)	13.806(3)	0.4042	372.399	
250	O	5.580(1)	5.499(2)	7.859(3)	0.71008	241.207	3.33/0.12
	R	5.582(1)	5.582(1)	13.809(3)	0.40421	372.645	
275	O	5.588(2)	5.494(6)	7.939(6)	0.7039	243.767	7.94/0.05
	R	5.608(2)	5.608(2)	13.700(5)	0.40937	373.214	
300	O	5.589(2)	5.517(4)	7.934(3)	0.70454	244.708	5.72/0.16
	R	5.606(1)	5.606(1)	13.693(3)	0.40939	372.701	
325	O	5.588(2)	5.521(4)	7.930(3)	0.70472	244.73	5.42/0.17
	R	5.607(1)	5.607(1)	13.696(3)	0.40946	373.031	
350	O	5.590(1)	5.521(4)	7.929(2)	0.70496	244.77	5.26/0.14
	R	5.610(1)	5.610(1)	13.696(3)	0.40963	373.381	
375	O	5.590(2)	5.522(4)	7.928(3)	0.70508	244.767	5.36/0.23
	R	5.612(1)	5.612(1)	13.700(3)	0.40965	373.757	
400	O	5.590(1)	5.523(4)	7.930(2)	0.70494	244.893	5.26/0.13
	R	5.612(1)	5.612(1)	13.698(3)	0.40967	373.638	
425	O	5.589(1)	5.531(4)	7.930(2)	0.70476	245.225	5.22/0.13
	R	5.613(1)	5.613(1)	13.703(3)	0.40967	373.989	
450	O	5.588(1)	5.534(3)	7.927(2)	0.70491	245.174	4.98/0.13
	R	5.615(1)	5.615(1)	13.703(3)	0.40977	374.173	
470	O	5.590(1)	5.538(3)	7.928(2)	0.70507	245.475	4.88/0.34
	R	5.616(1)	5.616(1)	13.706(3)	0.40978	374.465	

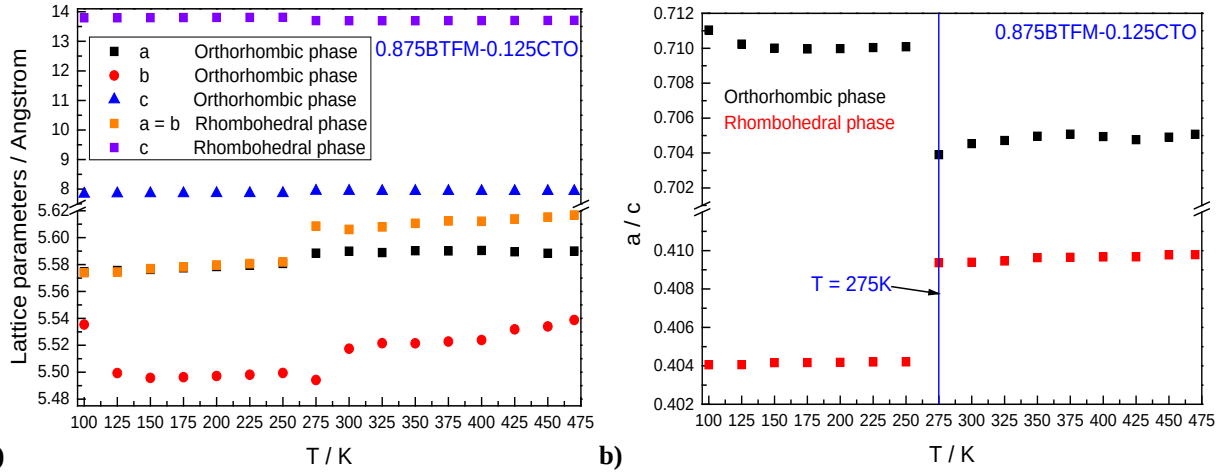

Figure A.63 a) Lattice parameters versus temperature, b) a / c versus temperature for 0.875BTFM-0.125CTO.

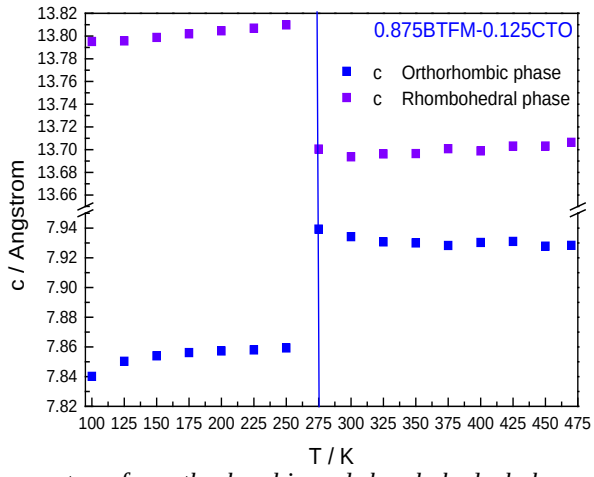

c) Comparison of the lattice parameter c for orthorhombic and rhombohedral phases versus temperature for 0.875BTFM-0.125CTO.

Figure A.63 a) shows the lattice parameters versus temperature for 0.875BTFM-0.125CTO. The notation of x and y axis are the same as the Figure A.9 a). At the y axis, there is a break from 5.62 to 7.5 for better visualization of the tendency of the lattice parameters versus temperature. The colours and marks are the same as the Figure A.54 a). The lattice parameters *a* and *b* for the orthorhombic and rhombohedral structures increase with temperature. At T = 250 K it is observed a sudden increasement of *a* and *b* for both phases. However, the lattice parameter *c* for both phases is constant with temperature. Figure A.63 b) shows the ratio *a* / *c* versus temperature for 0.875BTFM-0.125CTO. The notation of x and y axis are the same as the Figure A.9 b). There is a break from 0.412 to 0.701. The colours and marks are the same as the Figure A.54 b). The ratio *a* / *c* for both phases is constant until T = 250 K with temperature. At T = 250 K, for the

orthorhombic phase there is a sudden decreasement of the ratio a / c while for the rhombohedral phase there is a sudden increasement. Figure A.63 c) shows the lattice parameter c for orthorhombic and rhombohedral phases versus temperature for 0.875BTFM-0.125CTO. There is a break from 7.95 to 13.65. The blue squares represent c for the orthorhombic phase while the purple squares for the rhombohedral phase. At T = 250 K, for the orthorhombic phase there is a sudden increasement of the lattice parameter c while for the rhombohedral phase there is a sudden decreasement.

Figures A.64-A.71 show fitting results of Le Bail analysis for 0.9BTFM-0.1CTO at VT. The notation of x and y axis, the colours and marks are the same as for the Figures A.1-A.8. The figures show the 2θ range from 3° to 40°.

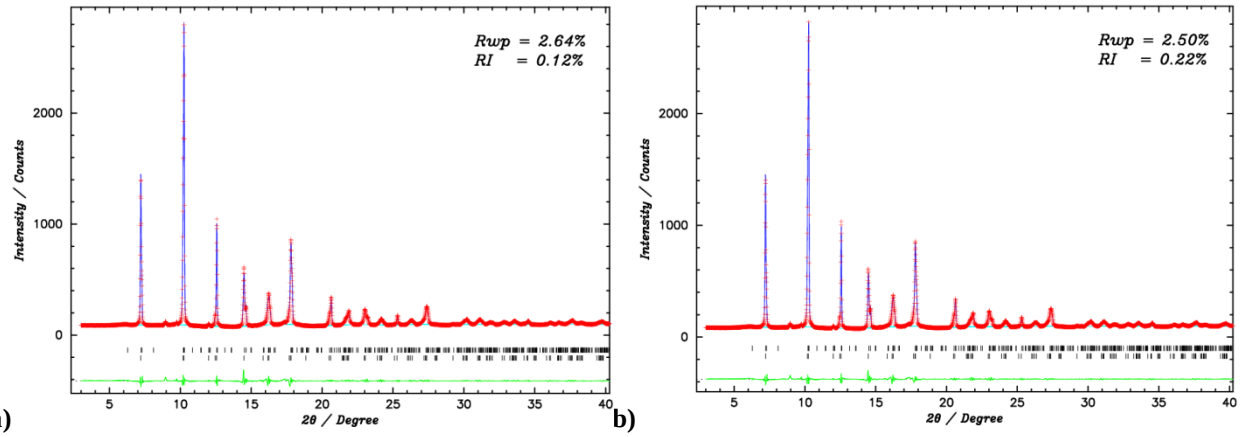

a) **b)**

Figure A.64 a) Le Bail fit for 0.9BTFM-0.1CTO at 100 K. b) Le Bail fit for 0.9BTFM-0.1CTO at 125 K.

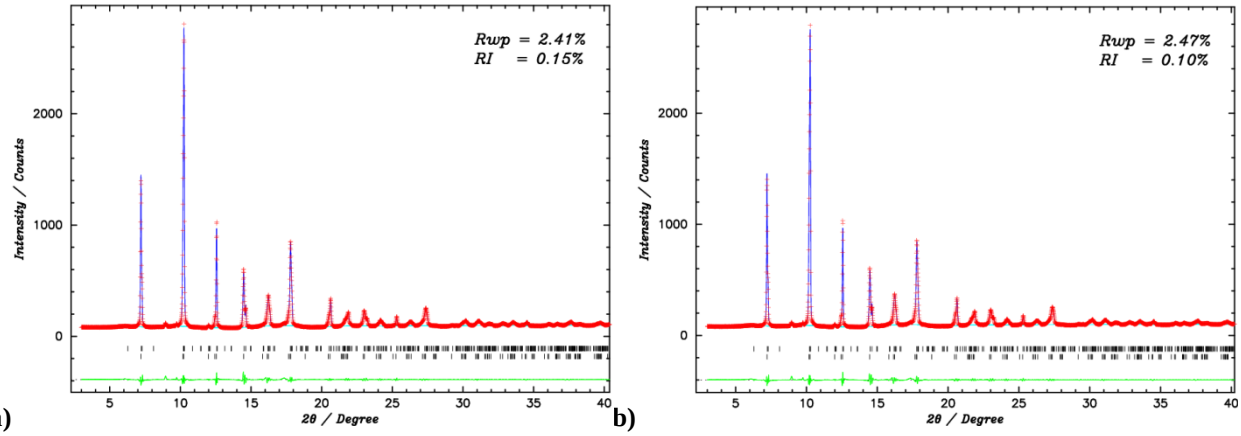

a) **b)**

Figure A.65 a) Le Bail fit for 0.9BTFM-0.1CTO at 150 K. b) Le Bail fit for 0.9BTFM-0.1CTO at 175 K.

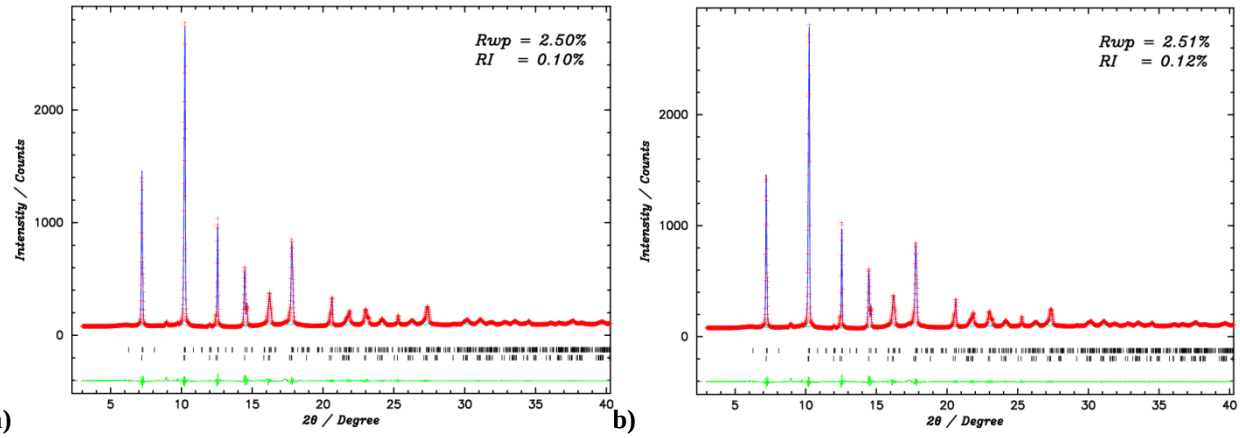

a) **b)**

Figure A.66 a) Le Bail fit for 0.9BTFM-0.1CTO at 200 K. b) Le Bail fit for 0.9BTFM-0.1CTO at 225 K.

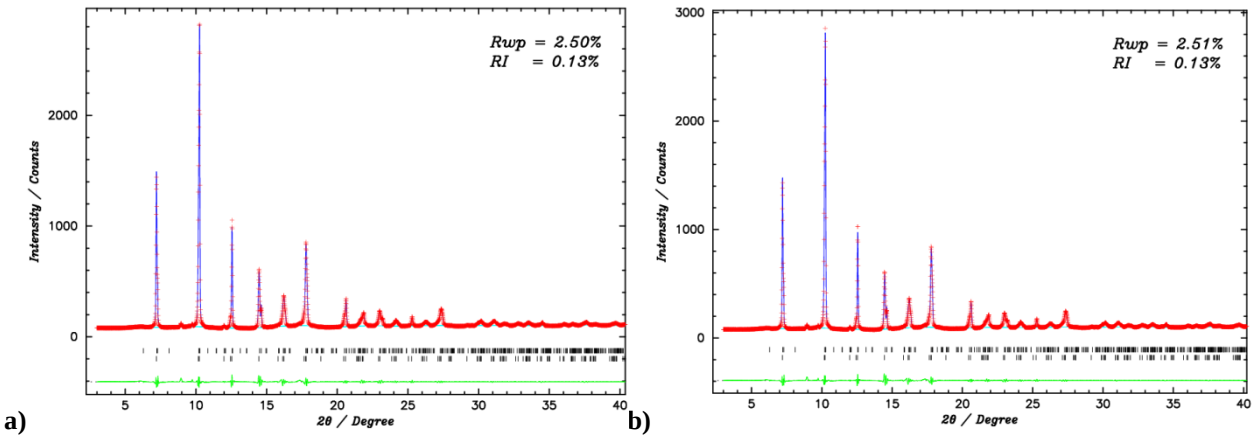

a) **b)**

Figure A.67 a) Le Bail fit for 0.9BTFM-0.1CTO at 250 K. b) Le Bail fit for 0.9BTFM-0.1CTO at 275 K.

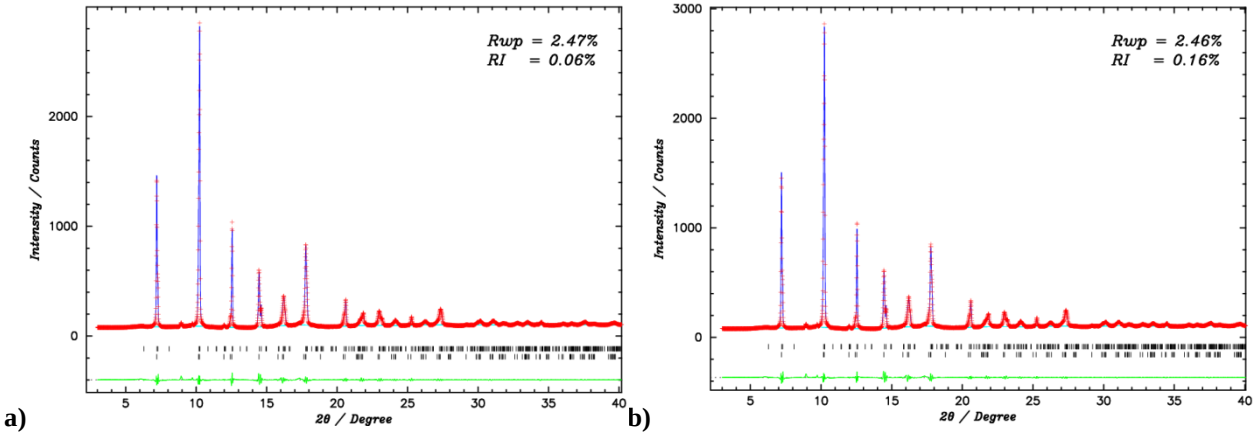

a) **b)**

Figure A.68 a) Le Bail fit for 0.9BTFM-0.1CTO at 300 K. b) Le Bail fit for 0.9BTFM-0.1CTO at 325 K.

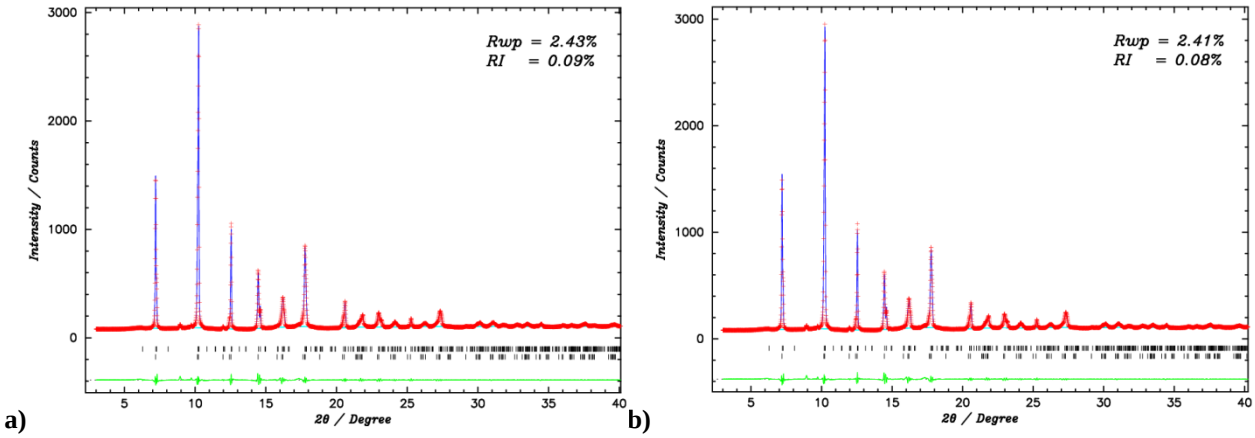

a) **b)**

Figure A.69 a) Le Bail fit for 0.9BTFM-0.1CTO at 350 K. b) Le Bail fit for 0.9BTFM-0.1CTO at 375 K.

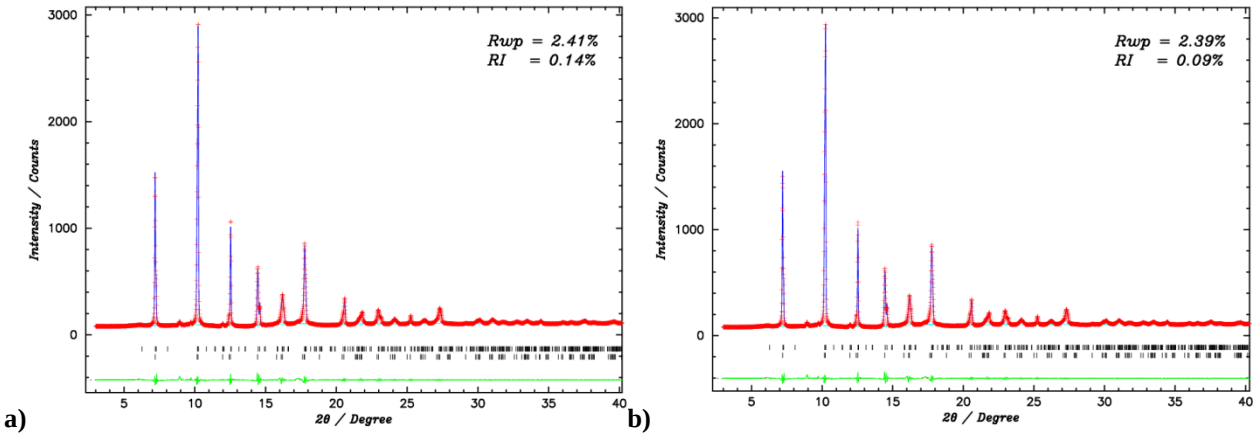

a) **b)**

Figure A.70 a) Le Bail fit for 0.9BTFM-0.1CTO at 400 K. b) Le Bail fit for 0.9BTFM-0.1CTO at 425 K.

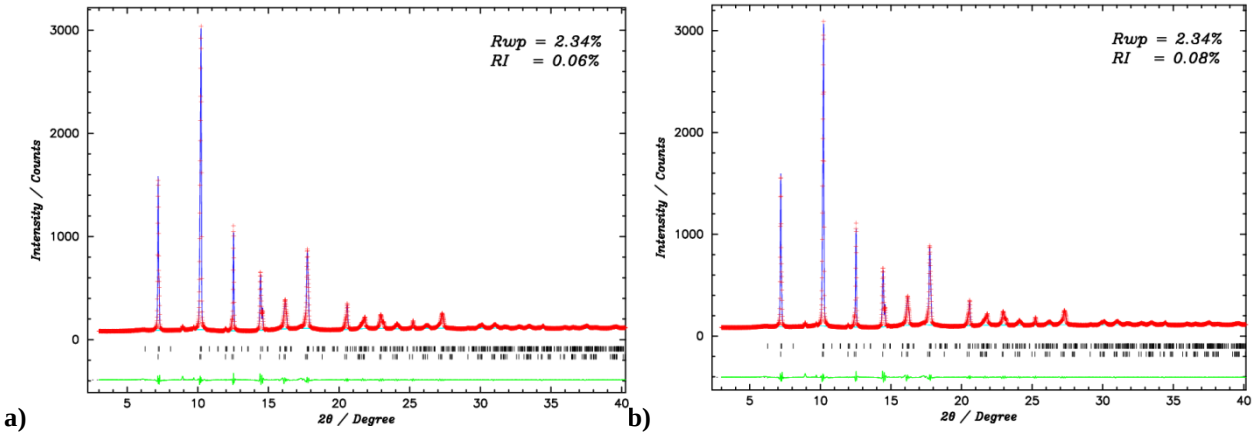

a) **b)**

Figure A.71 a) Le Bail fit for 0.9BTFM-0.1CTO at 450 K. b) Le Bail fit for 0.9BTFM-0.1CTO at 470 K.

Table A.8: Lattice parameters, volume of the unit cell and reliability factors for 0.9BTFM-0.1CTO at VT.

T* / *K	**Phase**	***a* / Å**	***b* / Å**	***c* / Å**	***a* / *c***	***V* / Å^3**	R_{wp} **/** R_I **/ %**
100	O	5.601(1)	5.574(1)	7.836(1)	0.71478	244.7	2.64/0.12
	R	5.584(2)	5.584(2)	13.790(5)	0.40495	372.455	
125	O	5.604(1)	5.576(1)	7.839(1)	0.71487	244.961	2.50/0.22
	R	5.587(1)	5.587(1)	13.799(4)	0.40491	373.081	
150	O	5.607(1)	5.578(1)	7.843(1)	0.7149	245.31	2.41/0.15
	R	5.590(1)	5.590(1)	13.818(4)	0.40456	374	
175	O	5.608(1)	5.580(1)	7.845(1)	0.7149	245.527	2.47/0.10
	R	5.592(1)	5.592(1)	13.824(4)	0.40453	374.47	
200	O	5.609(1)	5.581(1)	7.846(1)	0.71492	245.699	2.50/0.10
	R	5.593(1)	5.593(1)	13.828(4)	0.4045	374.727	
225	O	5.610(1)	5.582(1)	7.847(1)	0.71494	245.798	2.51/0.12
	R	5.594(1)	5.594(1)	13.829(4)	0.4045	374.819	
250	O	5.611(1)	5.583(1)	7.848(1)	0.71496	245.934	2.50/0.13
	R	5.595(1)	5.595(1)	13.831(4)	0.4045	374.989	
275	O	5.612(1)	5.585(1)	7.850(1)	0.71494	246.119	2.51/0.13
	R	5.596(1)	5.596(1)	13.836(4)	0.40445	375.254	
300	O	5.618(1)	5.587(1)	7.853(1)	0.71541	246.522	2.47/0.06
	R	5.598(1)	5.598(1)	13.840(4)	0.4045	375.672	
325	O	5.615(1)	5.587(1)	7.854(1)	0.71488	246.441	2.46/0.16
	R	5.598(1)	5.598(1)	13.841(4)	0.40444	375.646	
350	O	5.616(1)	5.589(1)	7.857(1)	0.71484	246.705	2.43/0.09
	R	5.600(1)	5.600(1)	13.844(4)	0.40453	376.061	
375	O	5.618(1)	5.591(1)	7.860(1)	0.71478	246.915	2.41 / 0.08
	R	5.601(1)	5.601(1)	13.847(4)	0.40453	376.331	
400	O	5.619(1)	5.592(1)	7.862(1)	0.71471	247.057	2.41 / 0.14
	R	5.602(1)	5.602(1)	13.850(4)	0.40453	376.521	
425	O	5.620(1)	5.594(1)	7.865(1)	0.71464	247.317	2.39 / 0.09
	R	5.604(1)	5.604(1)	13.853(4)	0.40458	376.863	
450	O	5.622(1)	5.596(1)	7.868(1)	0.71455	247.611	2.34 / 0.06
	R	5.606(1)	5.606(1)	13.858(4)	0.40457	377.303	
470	O	5.623(1)	5.597(1)	7.870(1)	0.71448	247.786	2.34 / 0.08
	R	5.607(1)	5.607(1)	13.860(4)	0.40459	377.499	

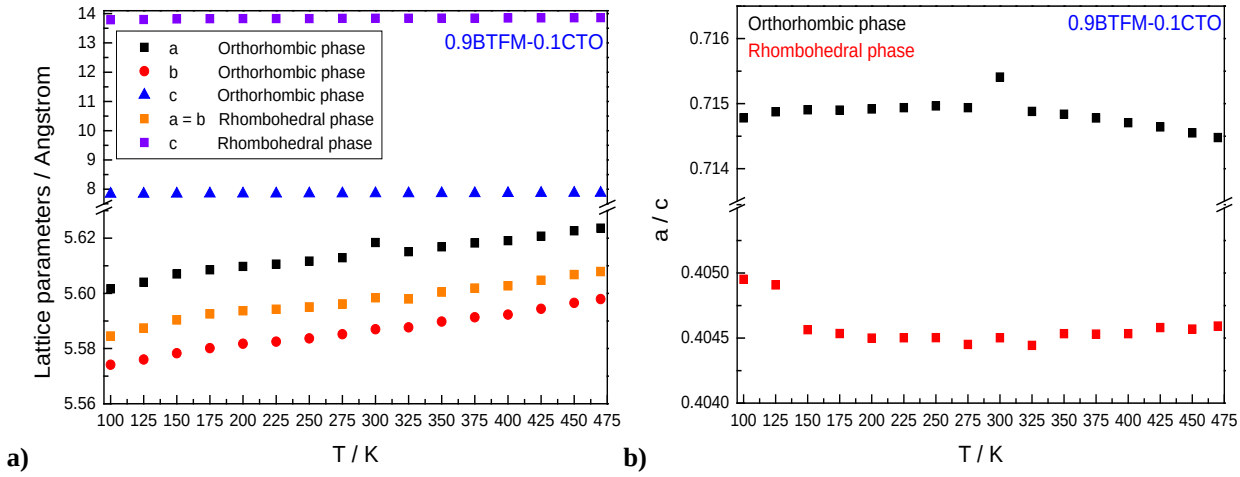

Figure A.72 a) Lattice parameters versus temperature, b) a / c versus temperature for 0.9BTFM-0.1CTO.

Figure A.72 a) shows the lattice parameters versus temperature for 0.9BTFM-0.1CTO. The notation of x and y axis are the same as the Figure A.9 a). At the y axis, there is a break from 5.63 to 7.5 for better visualization of the tendency of the lattice parameters versus temperature. The colours and marks are the same as the Figure A.54 a). The lattice parameters *a* and *b* for the orhtorhombic and rhombohedral phases increase with temperature. However, the lattice parameter *c* for both structures is constant with temperature. Figure A.72 b) shows the ratio *a* / *c* versus temperature for 0.9BTFM-0.1CTO. The notation of x and y axis are the same as the Figure A.9 b). There is a break from 0.404 to 0.7165. The colours and marks are the same as the Figure A.54 b). It is observed that the plots for the orthorhombic and rhombohedral phases follow a similar linear tendency of the ratio *a* / *c* with temperature.

Figures 3.73-3.80 show fitting results of Le Bail analysis for 0.925BTFM-0.075CTO at VT. The notation of x and y axis, the colours and marks are the same as for the Figures 3.1-3.8. The figures show the 2θ range from 3° to 40°.

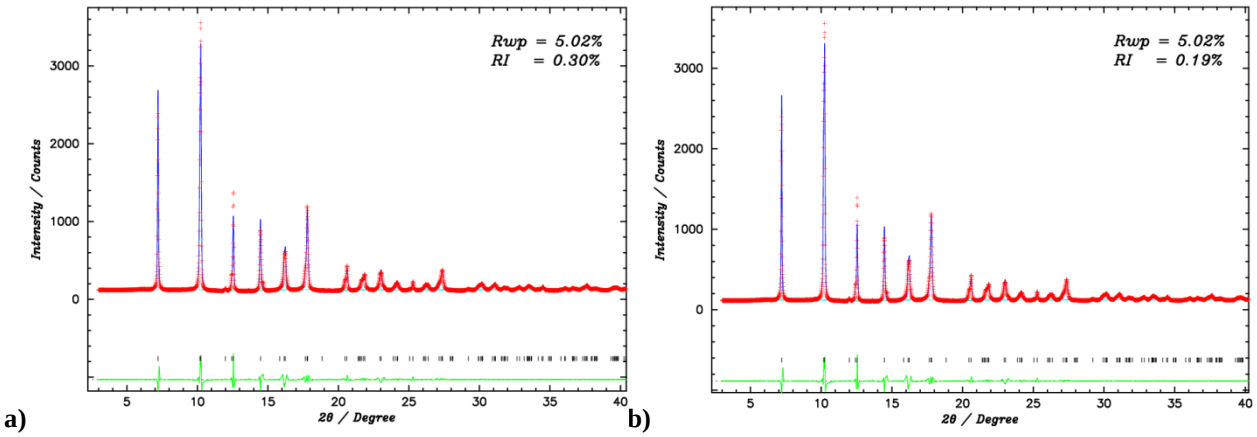

a) b)

Figure A.73 a) Le Bail fit for 0.925BTFM-0.075CTO at 100 K. b) Le Bail fit for 0.925BTFM-0.075CTO at 125 K.

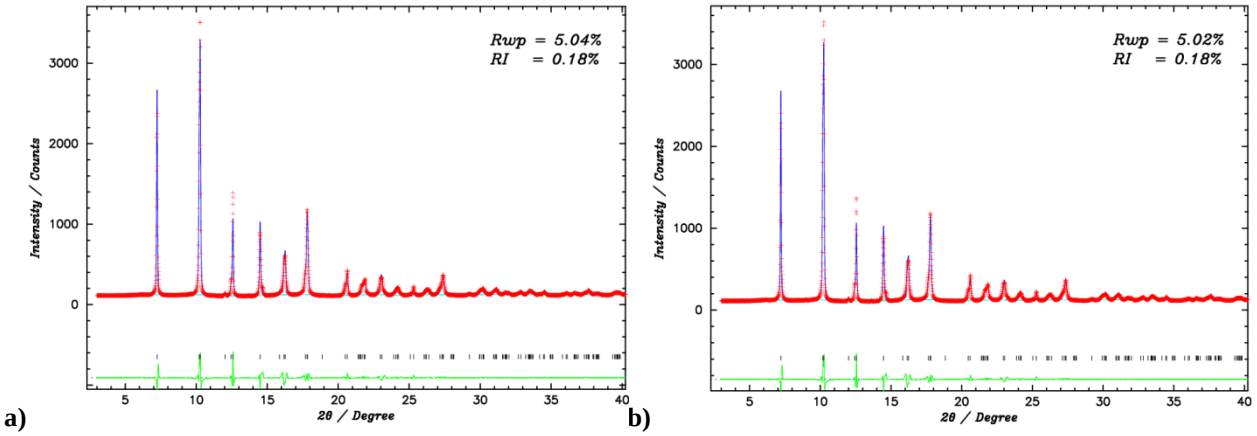

a) b)

Figure A.74 a) Le Bail fit for 0.925BTFM-0.075CTO at 150 K. b) Le Bail fit for 0.925BTFM-0.075CTO at 175 K.

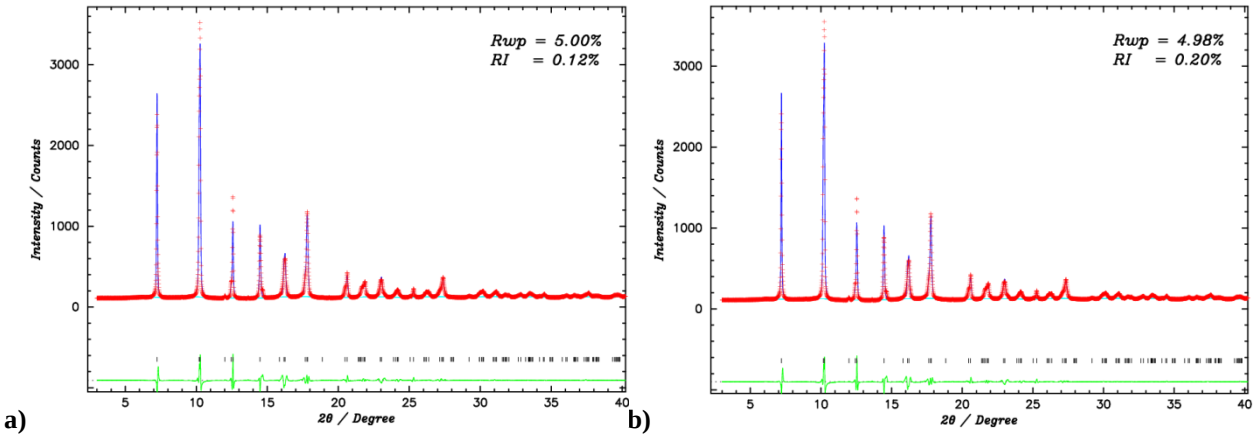

a) b)

Figure A.75 a) Le Bail fit for 0.925BTFM-0.075CTO at 200 K. b) Le Bail fit for 0.925BTFM-0.075CTO at 225 K.

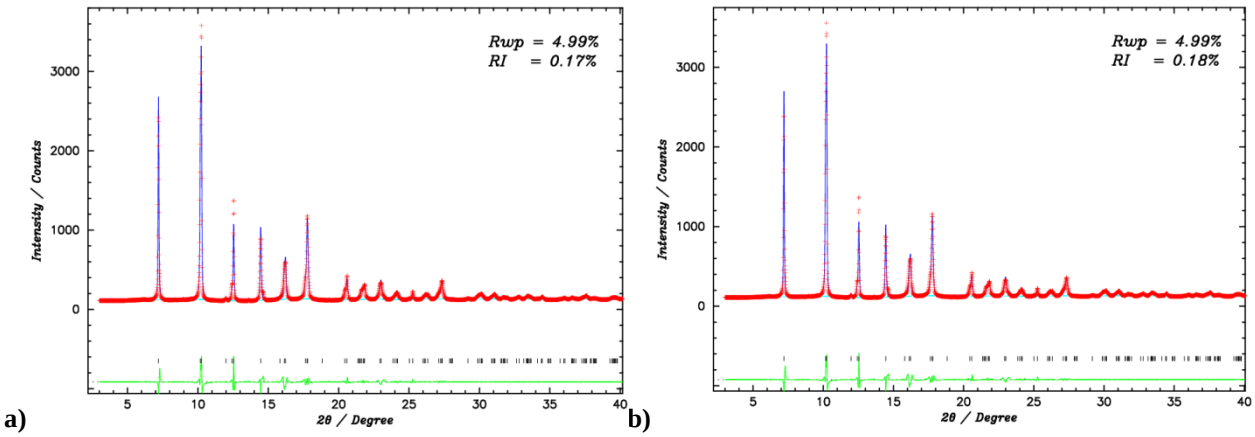

a) b)

Figure A.76 a) Le Bail fit for 0.925BTFM-0.075CTO at 250 K. b) Le Bail fit for 0.925BTFM-0.075CTO at 275 K.

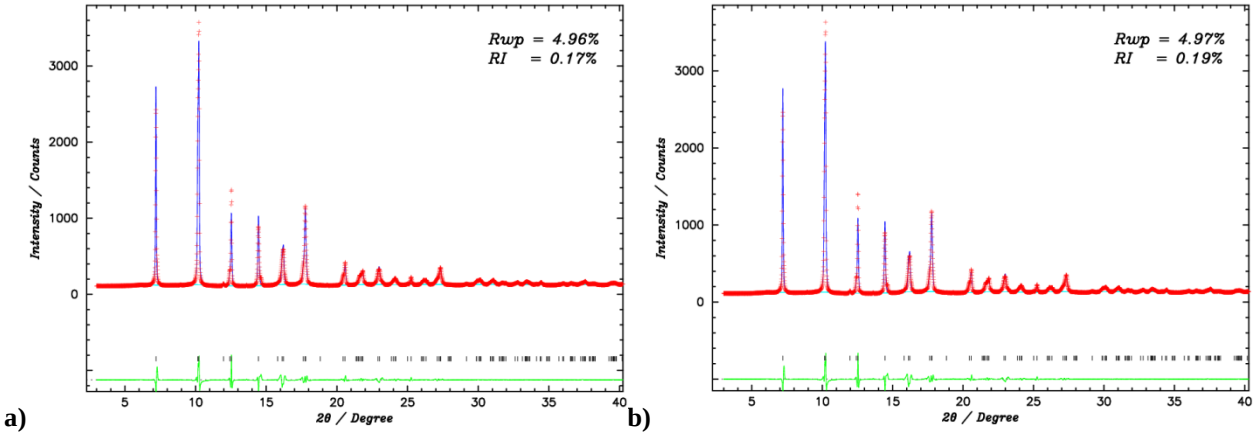

a) b)

Figure A.77 a) Le Bail fit for 0.925BTFM-0.075CTO at 300 K. b) Le Bail fit for 0.925BTFM-0.075CTO at 325 K.

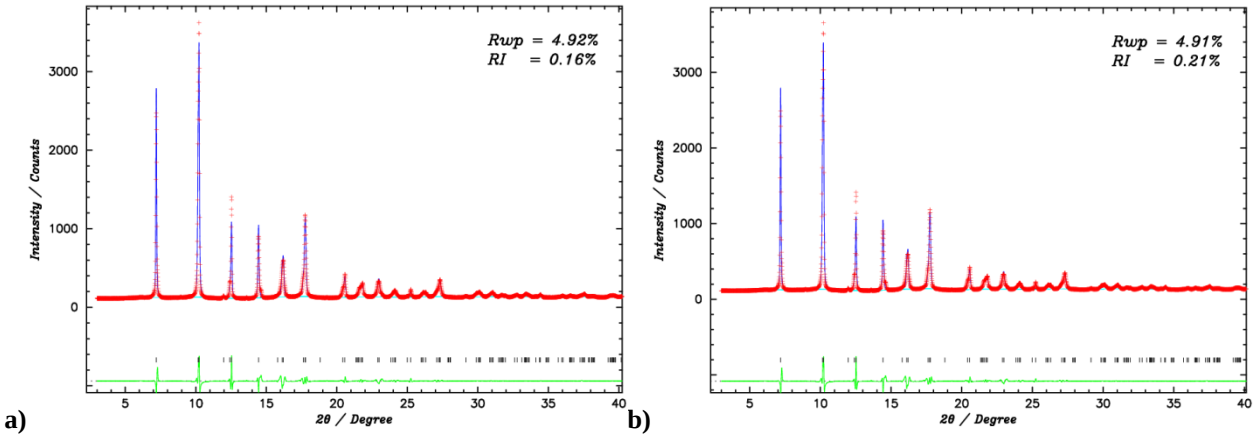

a) b)

Figure A.78 a) Le Bail fit for 0.925BTFM-0.075CTO at 350 K. b) Le Bail fit for 0.925BTFM-0.075CTO at 375 K.

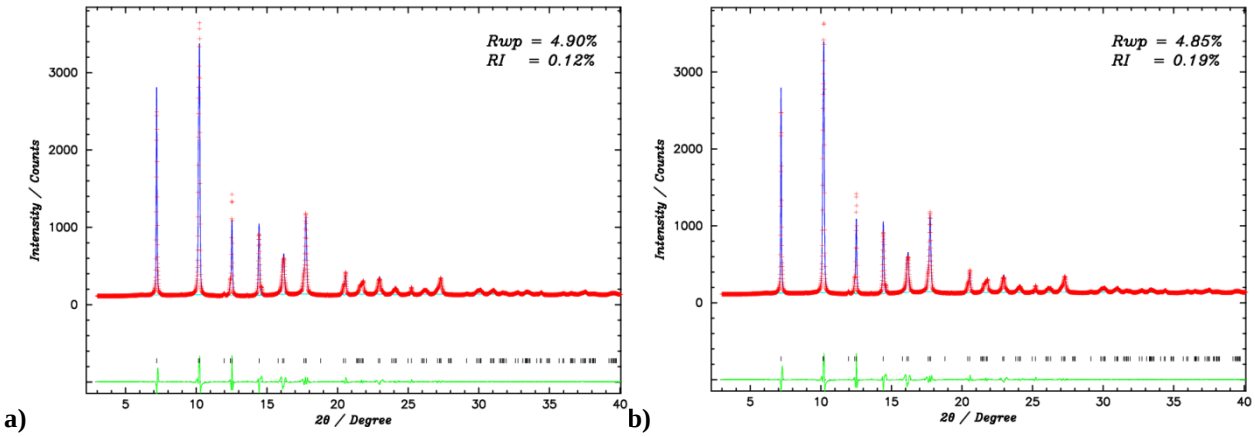

a) **b)**

Figure A.79 a) Le Bail fit for 0.925BTFM-0.075CTO at 400 K. b) Le Bail fit for 0.925BTFM-0.075CTO at 425 K.

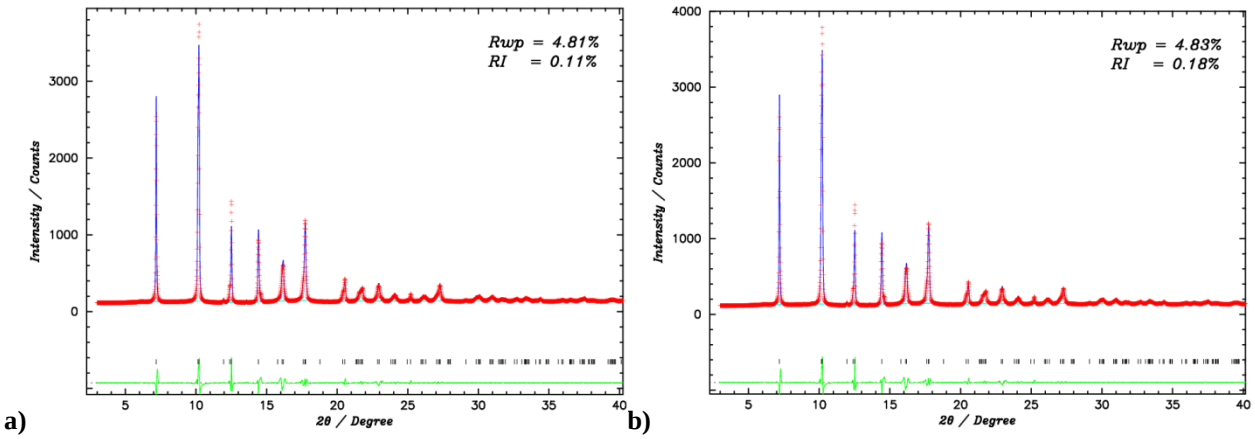

a) **b)**

Figure A.80 a) Le Bail fit for 0.925BTFM-0.075CTO at 450 K. b) Le Bail fit for 0.925BTFM-0.075CTO at 470 K.

Table A.9: Lattice parameters, volume of the unit cell and reliability factors for 0.925BTFM-0.075CTO at VT.

T* / *K	***a* / Å**	***b* / Å**	***c* / Å**	***a* / *c***	***V* / Å^3**	***R*$_{wp}$ / *R*$_I$/ %**
100	5.582(1)	5.582(1)	13.815(6)	0.40409	372.91525	5.02/0.30
125	5.583(1)	5.583(1)	13.817(5)	0.40408	373.03221	5.02/0.19
150	5.584(1)	5.584(1)	13.820(6)	0.404078	373.29965	5.04/0.18
175	5.585(1)	5.585(1)	13.823(6)	0.404071	373.4961	5.02/0.18
200	5.587(1)	5.587(1)	13.827(6)	0.40409	373.90215	5.00/0.12
225	5.587(1)	5.587(1)	13.829(6)	0.40406	373.96732	4.98/0.20
250	5.589(1)	5.589(1)	13.832(6)	0.40407	374.24105	4.99/0.17
275	5.590(1)	5.590(1)	13.835(6)	0.40407	374.49854	4.99/0.18
300	5.592(1)	5.592(1)	13.838(6)	0.40408	374.78030	4.96/0.17
325	5.593(1)	5.593(1)	13.842(6)	0.40409	375.05442	4.97/0.19
350	5.595(1)	5.5951(1)	13.845(6)	0.40410	375.37687	4.92/0.16
375	5.596(1)	5.596(1)	13.849(6)	0.40410	375.66664	4.91/0.21
400	5.598(1)	5.598(1)	13.852(6)	0.40413	376.00978	4.90/0.12
425	5.599(1)	5.599(1)	13.855(6)	0.40414	376.25323	4.85/0.19
450	5.601(1)	5.601(1)	13.859(6)	0.40417	376.60211	4.81/0.11
470	5.602(1)	5.602(1)	13.861(6)	0.40417	376.82666	4.83/0.18

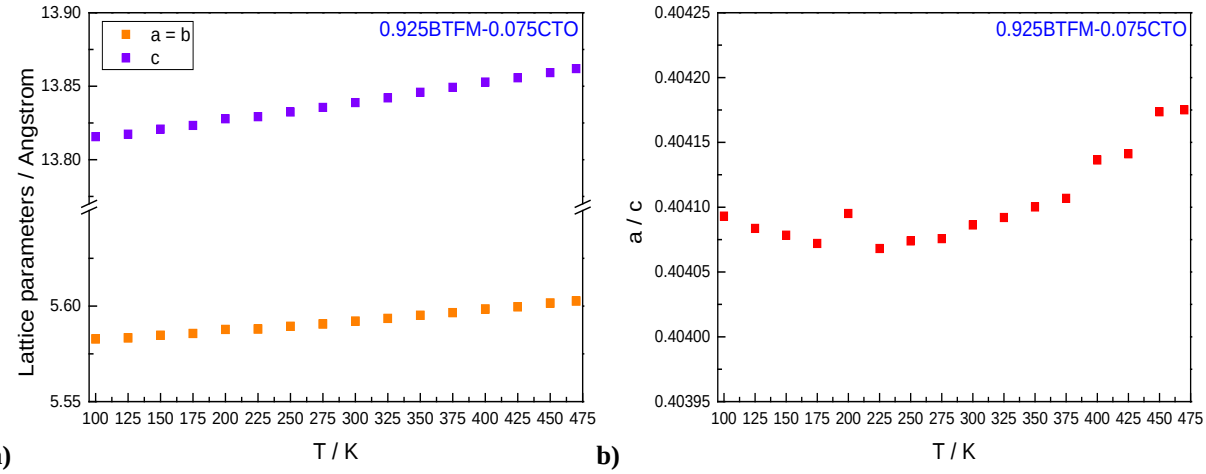

Figure A.81 a) Lattice parameters versus temperature, b) a / c versus temperature for 0.925BTFM-0.075CTO.

Figure A.81 a) shows the lattice parameters versus temperature for 0.925BTFM-0.075CTO. The notation of x and y axis are the same as the Figure A.9 a). At the y axis, there is a break from 5.65 to 13.77 for better visualization of the tendency of the lattice parameters versus temperature. The orange squares represent the lattice parameters *a* and *b* and the purple squares *c*. the lattice

parameters *a*, *b* and *c* increase with temperature. Figure A.81 b) shows the ratio *a* / *c* versus temperature for 0.925BTFM-0.075CTO. The notation of x and y axis are the same as the Figure A.9 b). It is observed that the ratio a / c increases with temperature.

Figures A.82-A.89 show fitting results of Le Bail analysis for 0.95BTFM-0.05CTO at VT. The notation of x and y axis, the colours and marks are the same as for the Figures A.1-A.8. The figures show the 2θ range from 3° to 40°.

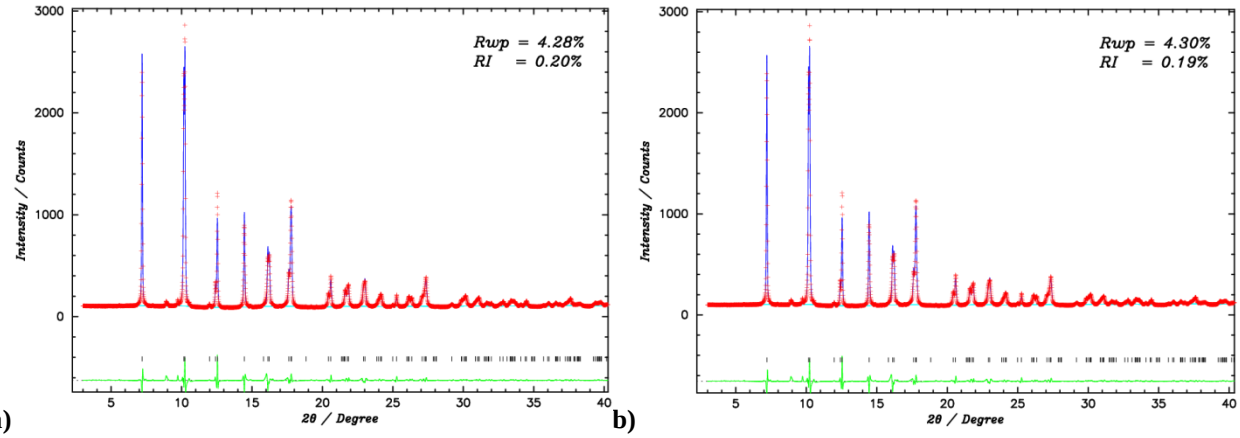

a) **b)**

Figure A.82 a) Le Bail fit for 0.95BTFM-0.05CTO at 100 K. b) Le Bail fit for 0.95BTFM-0.05CTO at 125 K.

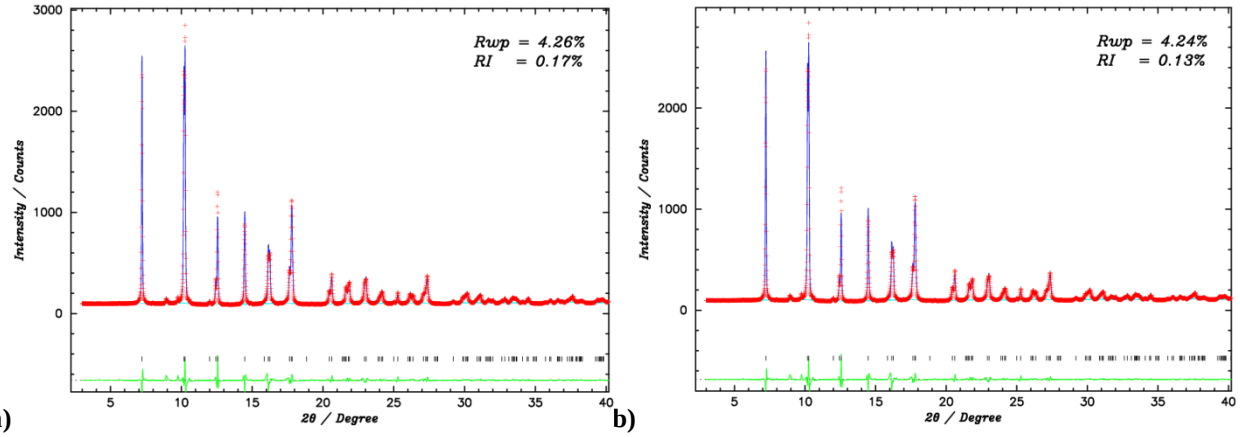

a) **b)**

Figure A.83 a) Le Bail fit for 0.95BTFM-0.05CTO at 150 K. b) Le Bail fit for 0.95BTFM-0.05CTO at 175 K.

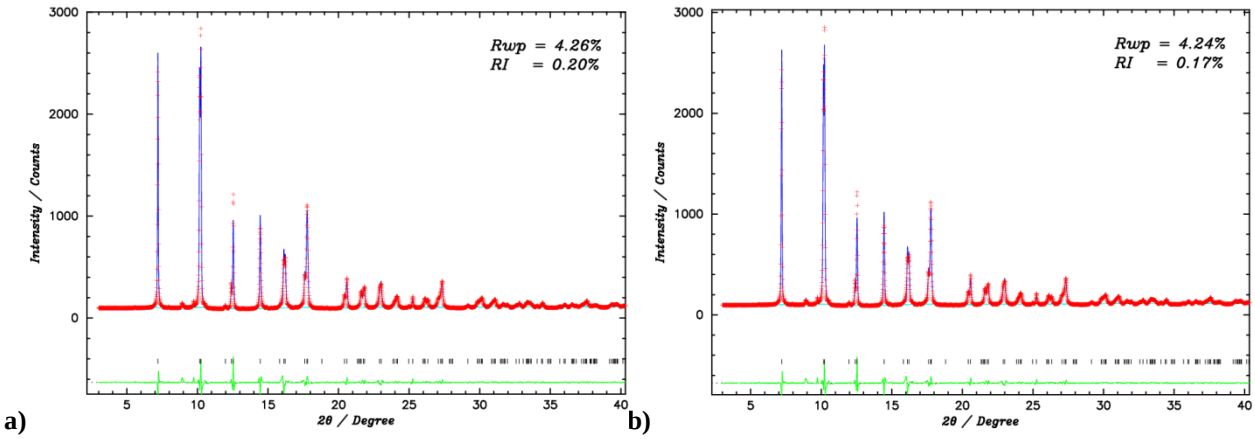

a) b)

Figure A.84 a) Le Bail fit for 0.95BTFM-0.05CTO at 200 K. b) Le Bail fit for 0.95BTFM-0.05CTO at 225 K.

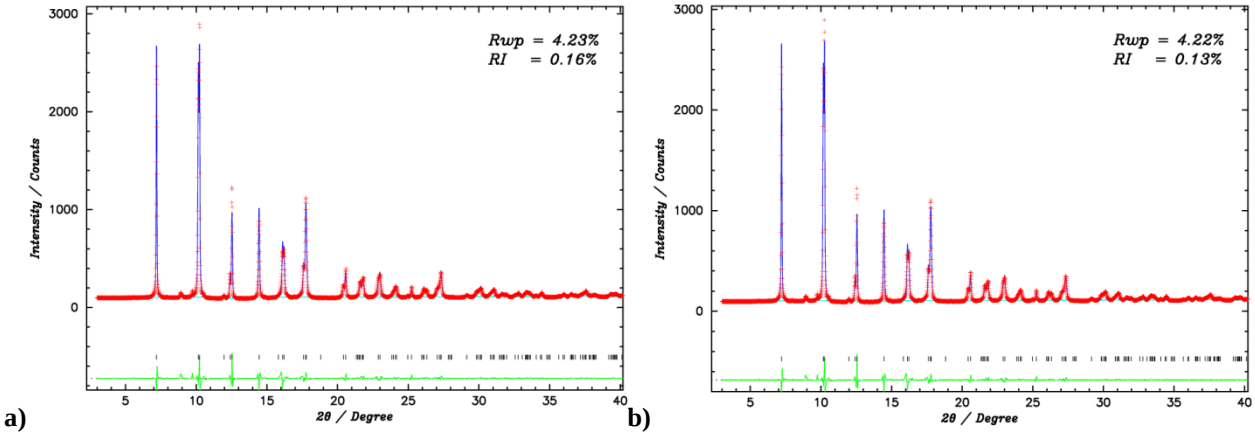

a) b)

Figure A.85 a) Le Bail fit for 0.95BTFM-0.05CTO at 250 K. b) Le Bail fit for 0.95BTFM-0.05CTO at 275 K.

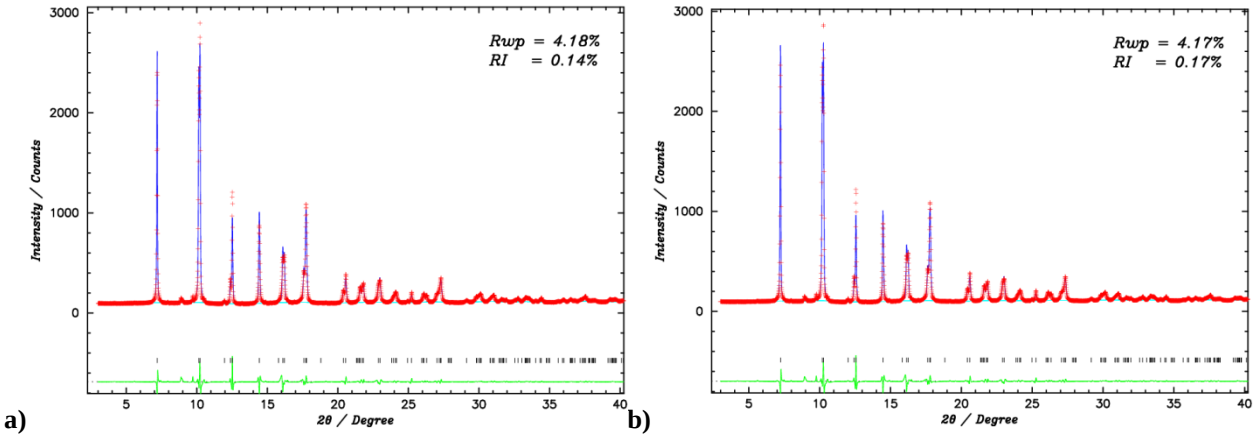

a) b)

Figure A.86 a) Le Bail fit for 0.95BTFM-0.05CTO at 300 K. b) Le Bail fit for 0.95BTFM-0.05CTO at 325 K.

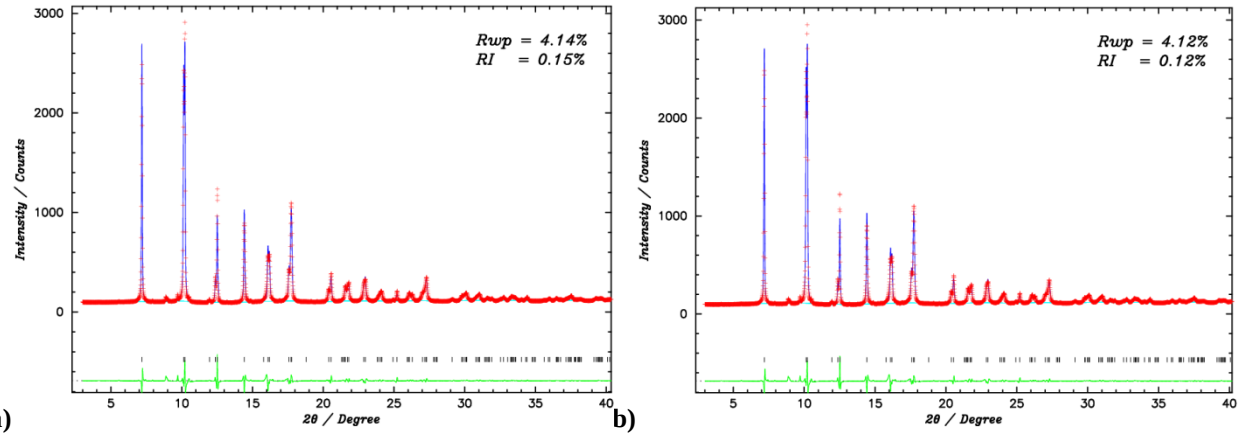

a) **b)**

Figure A.87 a) Le Bail fit for 0.95BTFM-0.05CTO at 350 K. b) Le Bail fit for 0.95BTFM-0.05CTO at 375 K.

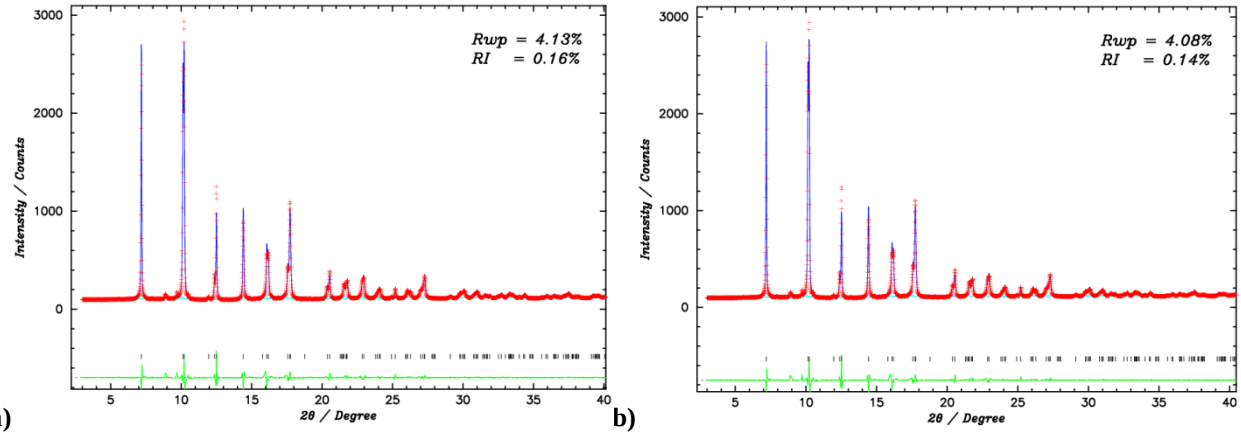

a) **b)**

Figure A.88 a) Le Bail fit for 0.95BTFM-0.05CTO at 400 K. b) Le Bail fit for 0.95BTFM-0.05CTO at 425 K.

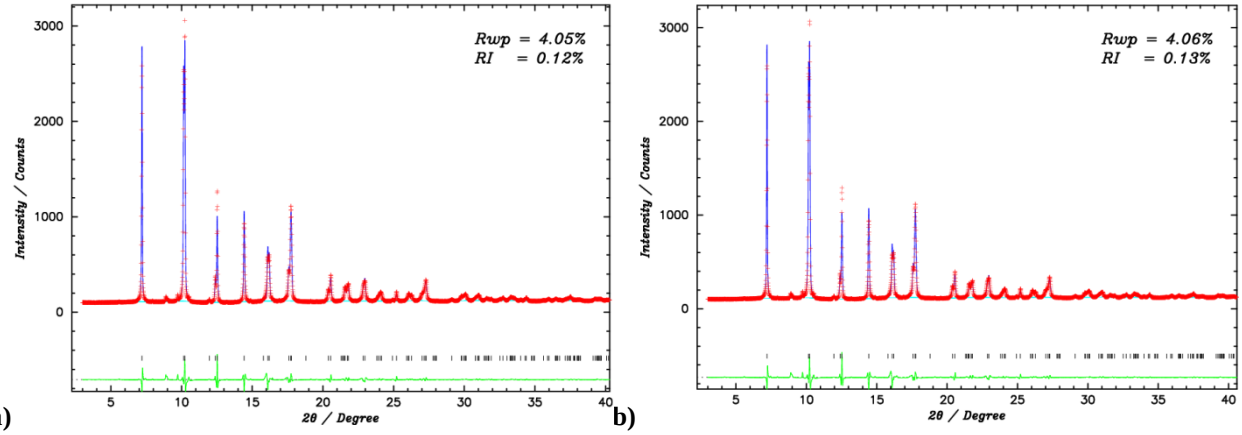

a) **b)**

Figure A.89 a) Le Bail fit for 0.95BTFM-0.05CTO at 450 K. b) Le Bail fit for 0.95BTFM-0.05CTO at 470 K.

Table A.10: Lattice parameters, volume of the unit cell and reliability factors for 0.95BTFM-0.05CTO at VT.

T* / *K	***a* / Å**	***b* / Å**	***c* / Å**	***a* / *c***	***V* / Å^3**	***R_{wp}* / *R_I*/ %**
100	5.587(1)	5.587(1)	13.850(3)	0.40341	374.49183	4.28/0.20
125	5.588(1)	5.588(1)	13.853(3)	0.40340	374.67181	4.30/0.19
150	5.589(1)	5.589(1)	13.855(3)	0.40339	374.87738	4.26/0.17
175	5.590(1)	5.590(1)	13.859(3)	0.40337	375.15003	4.24/0.13
200	5.591(1)	5.591(1)	13.862(3)	0.40336	375.4021	4.26/0.20
225	5.593(1)	5.593(1)	13.866(3)	0.40336	375.66391	4.24/0.17
250	5.594(1)	5.594(1)	13.869(3)	0.40336	375.92234	4.23/0.16
275	5.595(1)	5.595(1)	13.872(3)	0.40335	376.19573	4.22/0.13
300	5.597(1)	5.597(1)	13.876(3)	0.40336	376.49809	4.18/0.14
325	5.598(1)	5.598(1)	13.879(3)	0.40336	376.77066	4.17/0.17
350	5.600(1)	5.600(1)	13.883(3)	0.40336	377.07713	4.14/0.15
375	5.601(1)	5.601(1)	13.887(3)	0.40336	377.39156	4.12/0.12
400	5.603(1)	5.603(1)	13.890(3)	0.40337	377.65317	4.13/0.16
425	5.604(1)	5.604(1)	13.894(3)	0.40337	377.98093	4.08/0.14
450	5.606(1)	5.606(1)	13.897(3)	0.40339	378.28338	4.05/0.12
470	5.607(1)	5.607(1)	13.900(3)	0.40339	378.52698	4.06/0.13

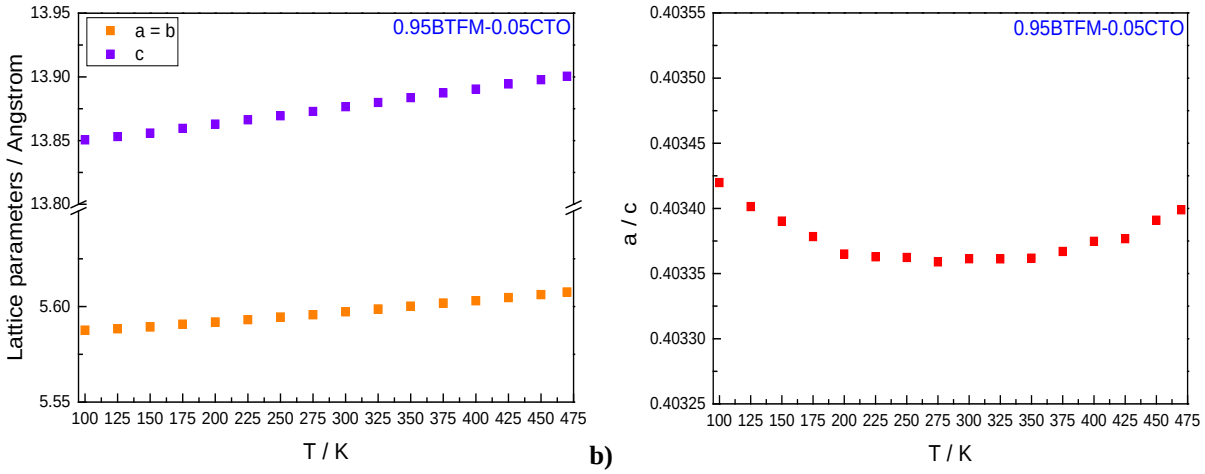

Figure A.90 a) Lattice parameters versus temperature, b) a / c versus temperature for 0.95BTFM-0.05CTO.

Figure A.90 a) shows the lattice parameters versus temperature for 0.95BTFM-0.05CTO. The notation of the x and y axis are the same as the Figure A.9 a). At the y axis, there is a break from 5.65 to 13.8 for better visualization of the tendency of the lattice parameters versus temperature. The colours and marks are the same as Figure A.81 a). It is observed that the lattice

parameters *a*, *b* and *c* increase with temperature. Figure A.90 b) shows the ratio *a* / *c* versus temperature for 0.95BTFM-0.05CTO. The colours and marks are the same as Figure A.81 a).

Figures A.91-A.96 show fitting results of Le Bail analysis for 0.8BTFM-0.2CTO at VT. The notation of the x and y axis, the colours and marks are the same as for the Figures A.1-A.8. The figures show the 2θ range from 3° to 40°.

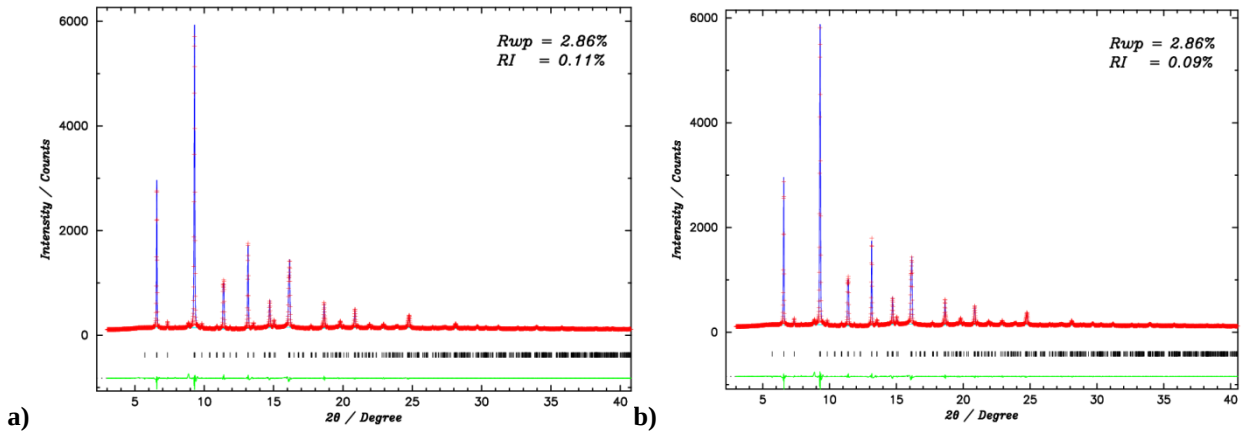

Figure A.91 a) Le Bail fit for 0.8BTFM-0.2CTO at 300 K. b) Le Bail fit for 0.8BTFM-0.2CTO at 330 K.

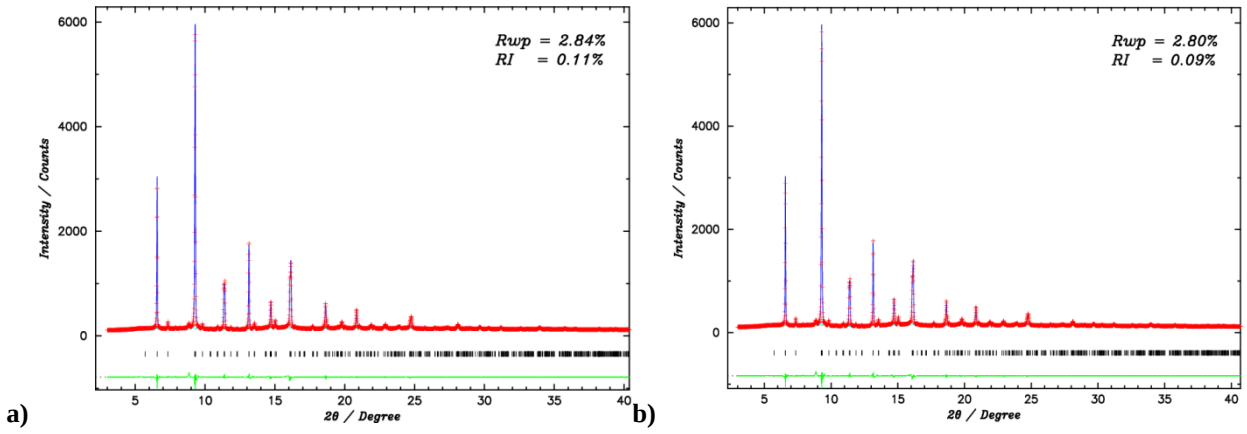

Figure A.92 a) Le Bail fit for 0.8BTFM-0.2CTO at 360 K. b) Le Bail fit for 0.8BTFM-0.2CTO at 390 K.

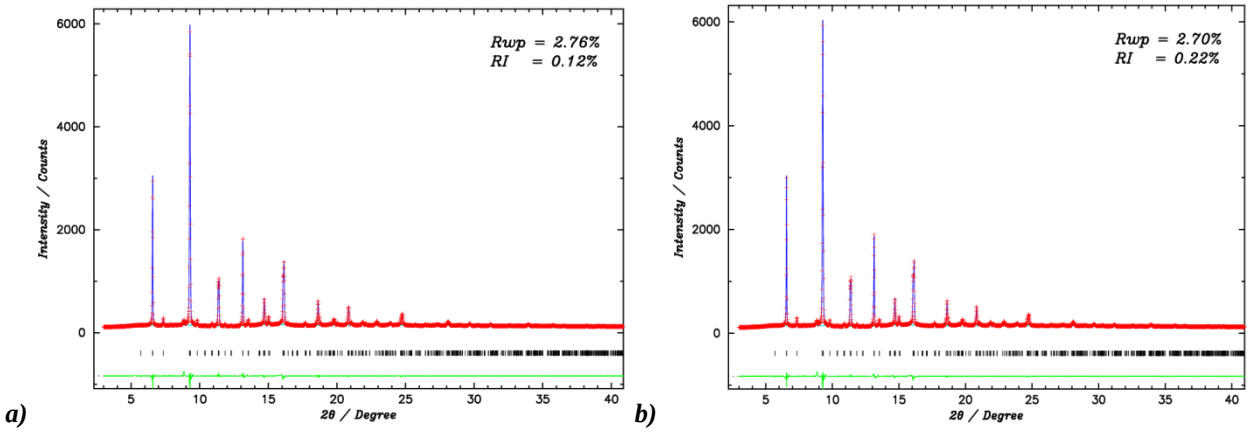

Figure A.93 a) Le Bail fit for 0.8BTFM-0.2CTO at 420 K. b) Le Bail fit for 0.8BTFM-0.2CTO at 450 K.

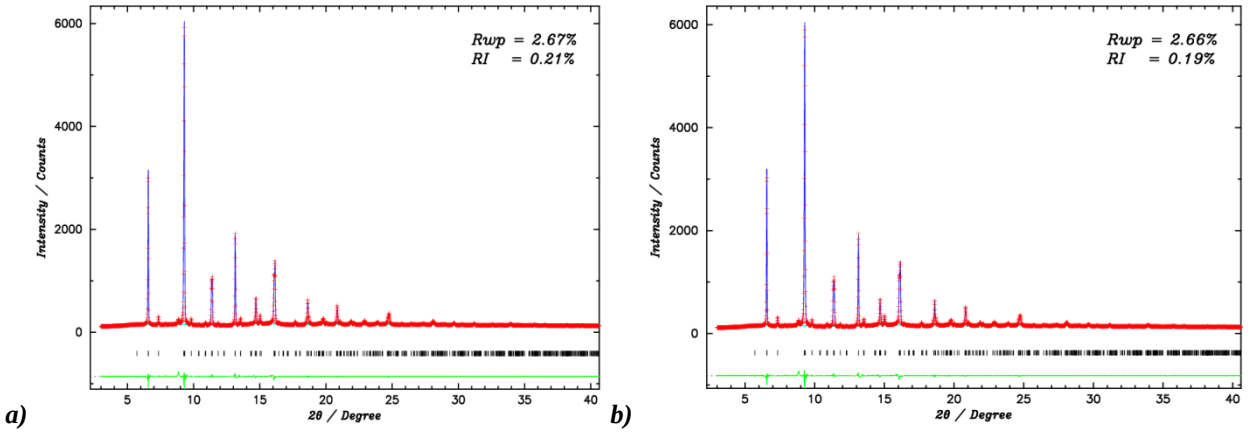

Figure A.94 a) Le Bail fi for 0.8BTFM-0.2CTO at 480 K. b) Le Bail fit for 0.8BTFM-0.2CTO at 510 K.

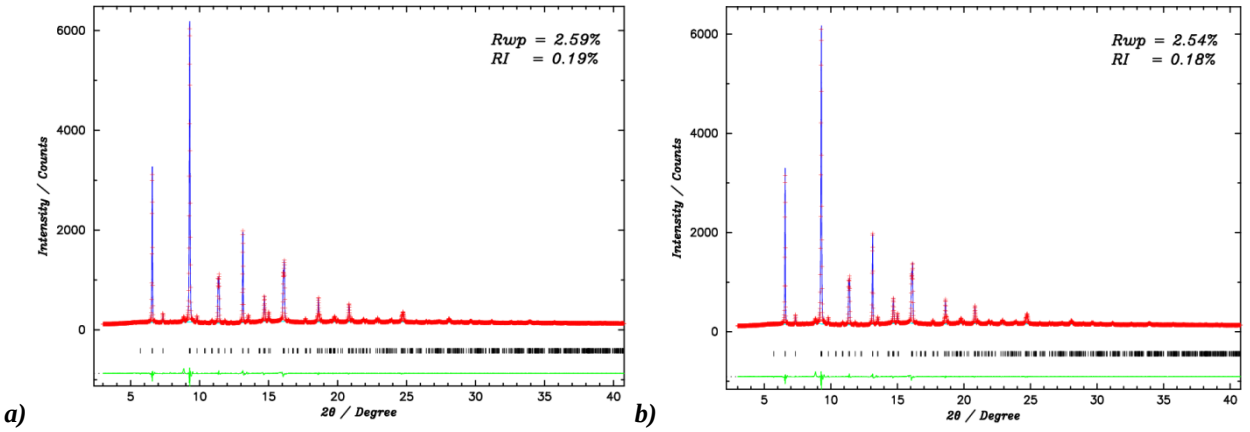

Figure A.95 a) Le Bail fit for 0.8BTFM-0.2CTO at 540 K. b) Le Bail fit for 0.8BTFM-0.2CTO at 570 K.

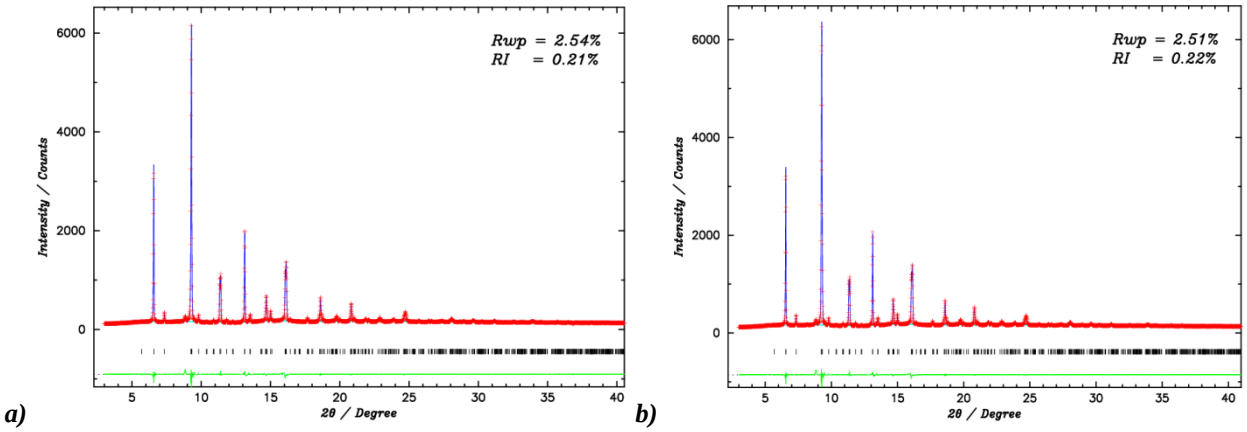

Figure A.96 a) Le Bail fit for 0.8BTFM-0.2CTO at 600 K. b) Le Bail fit for 0.8BTFM-0.2CTO at 630 K.

Table A.11: Lattice parameters, volume of the unit cell and reliability factors for 0.8BTFM-0.2CTO at VT.

***T* / K**	***a* / Å**	***b* / Å**	***c* / Å**	***c* / *a***	R_{wp} / R_I / %
300	5.5843(9)	5.5441(9)	7.863(2)	1.40817	2.86/ 0.11
330	5.5858(9)	5.5453(9)	7.866(1)	1.40821	2.86/0.09
360	5.5879(9)	5.5467(8)	7.868(2)	1.40818	2.84/ 0.11
390	5.5892(9)	5.5472(8)	7.870(2)	1.4082	2.78/ 0.11
420	5.5905(9)	5.5480(8)	7.872(2)	1.40821	2.76/ 0.11
450	5.5924(9)	5.5493(8)	7.875(2)	1.40826	2.71/ 0.19
480	5.5943(9)	5.5507(8)	7.879(2)	1.40852	2.67/ 0.21
510	5.5955(9)	5.5512(8)	7.882(2)	1.40871	2.66/0.19
540	5.5969(9)	5.5519(8)	7.884(2)	1.40875	2.59/0.19
570	5.5981(9)	5.5528(8)	7.887(2)	1.40888	2.54/0.18
600	5.5995(9)	5.5536(8)	7.889(2)	1.40887	2.54/ 0.22
630	5.6005(8)	5.5548(8)	7.891(2)	1.40899	2.51/ 0.22

Appendix B - Le Bail fits outcomes for 0.825BTFM-0.175CTO for all the non-centrosymmetric orthorhombic space groups in the six different settings

Table B1: Setting abc

Space group	Rwp	Number of reflections
*P*222 (16)	0.02132	434
*Pmm*2 (25)	0.02132	434
$P222_1$ (17)	0.02132	430
$P2_12_12$ (18)	0.02132	426
$P2_12_12_1$ (19)	0.02135	422
*Pma*2 (28)	0.02136	401
$Pmn2_1$ (31)	0.02143	397
$Pmc2_1$ (26)	0.02144	398
$Pna2_1$ (33)	0.02151	375
*Pnn*2 (34)	0.02163	375
*Pnc*2 (30)	0.02164	376
*Amm*2 (38)	0.02822	218
*Ama*2 (40)	0.02826	201
$I2_12_12_1$ (24)	0.03776	217
*I*222 (23)	0.03776	217
*Imm*2 (44)	0.03776	217
*Ima*2 (46)	0.03778	201
*Pba*2 (32)	0.06768	375
$Pca2_1$ (29)	0.06769	375
*Pcc*2 (27)	0.06772	376
*Aem*2 (39)	0.07082	205
*Aea*2 (41)	0.07084	188
*Iba*2 (45)	0.0754	188
*C*222 (21)	0.10995	219
*Cmm*2 (35)	0.10995	219
$C222_1$ (20)	0.11001	215
$Cmc2_1$ (36)	0.11016	199
*Ccc*2 (37)	0.11025	190
*Fmm*2 (42)	0.11285	111
*F*222 (22)	0.11285	111
*Fdd*2 (43)	0.28841	95

Table B2: Setting acb

Space group	Rwp	Number of reflections
*P*222 (16)	0.02132	434
$P2_12_12$ (18)	0.02132	426
*Pmm*2 (25)	0.02132	434
$P222_1$ (17)	0.02133	430
$P2_12_12_1$ (19)	0.02135	422
$Pmc2_1$ (26)	0.02136	398
*Pnc*2 (30)	0.02152	376
$Pmn2_1$ (31)	0.02332	397
*Pma*2 (28)	0.02335	401
$Pna2_1$ (33)	0.02347	375
*Pnn*2 (34)	0.02352	375
*Amm*2 (38)	0.02822	218
*Ama*2 (40)	0.0299	201
$I2_12_12_1$ (24)	0.03776	217
*I*222 (23)	0.03776	217
*Imm*2 (44)	0.03776	217
*Ima*2 (46)	0.03785	201
*Pcc*2 (27)	0.06769	376
$Pca2_1$ (29)	0.06834	375
*Pba*2 (32)	0.06836	375
*Aem*2 (39)	0.07082	205
*Aea*2 (41)	0.0715	188
*Iba*2 (45)	0.07545	188
*C*222 (21)	0.11003	219
*Cmm*2 (35)	0.11003	219
$C222_1$ (20)	0.11008	215
$Cmc2_1$ (36)	0.11017	199
*Ccc*2 (37)	0.11028	190
*Fmm*2 (42)	0.11285	111
*F*222 (22)	0.11285	111
*Fdd*2 (43)	0.28332	95

Table B3: Setting bac

Space group	Rwp	Number of reflections
*P*222 (16)	0.02132	434
*Pmm*2 (25)	0.02132	434
$P222_1$ (17)	0.02132	430
$P2_12_12$ (18)	0.02132	426
$P2_12_12_1$ (19)	0.02135	422
$Pmn2_1$ (31)	0.02147	408
*Pnn*2 (34)	0.02163	375
*Imm*2 (44)	0.03776	217
$I2_12_12_1$ (24)	0.03776	217
*I*222 (23)	0.03776	217
*Pma*2 (28)	0.06767	408
*Pba*2 (32)	0.06768	375
$Pmc2_1$ (26)	0.06768	408
*Pcc*2 (27)	0.06772	376
*Pnc*2 (30)	0.06772	375
$Pna2_1$ (33)	0.06782	371
$Pca2_1$ (29)	0.06782	372
*Iba*2 (45)	0.0754	188
*Ima*2 (46)	0.07541	204
*C*222 (21)	0.10995	219
*Cmm*2 (35)	0.10995	219
$C222_1$ (20)	0.11001	215
*Amm*2 (38)	0.11003	219
$Cmc2_1$ (36)	0.11007	206
*Ama*2 (40)	0.11015	206
*Ccc*2 (37)	0.11025	190
*Aem*2 (39)	0.11054	203
*Aea*2 (41)	0.11066	190
*F*222 (22)	0.11285	111
*Fmm*2 (42)	0.11285	111
*Fdd*2 (43)	0.28841	95

Table B4: Setting bca

Space group	Rwp	Number of reflections
*P*222 (16)	0.02132	434
*Pmm*2 (25)	0.02132	434
$P222_1$ (17)	0.02132	430
$P2_12_12$ (18)	0.02135	426
$P2_12_12_1$ (19)	0.02135	422
*Pma*2 (28)	0.02136	398
$Pca2_1$ (29)	0.02147	365
$Pna2_1$ (33)	0.02153	361
*Pba*2 (32)	0.02167	362
$Pmn2_1$ (31)	0.02332	397
$Pmc2_1$ (26)	0.02335	401
*Pnc*2 (30)	0.02365	368
*Pcc*2 (27)	0.02366	372
*Pnn*2 (34)	0.02372	364
$C222_1$ (20)	0.02822	214
*Cmm*2 (35)	0.02822	218
*C*222 (21)	0.02822	218
$Cmc2_1$ (36)	0.0299	201
*Ccc*2 (37)	0.03022	188
$I2_12_12_1$ (24)	0.03776	217
*Imm*2 (44)	0.03776	217
*I*222 (23)	0.03776	217
*Ima*2 (46)	0.03785	201
*Iba*2 (45)	0.03793	185
*Amm*2 (38)	0.11003	219
*Ama*2 (40)	0.11017	199
*Aem*2 (39)	0.11054	203
*Aea*2 (41)	0.11068	183
*F*222 (22)	0.11285	111
*Fmm*2 (42)	0.11285	111
*Fdd*2 (43)	0.38355	94

Table B5: Setting cab

Space group	Rwp	Number of reflections
*P*222 (16)	0.02132	434
*Pmm*2 (25)	0.02132	434
$P2_12_12$ (18)	0.02132	426
$P222_1$ (17)	0.02133	430
$P2_12_12_1$ (19)	0.02135	422
$Pmn2_1$ (31)	0.02147	408
*Pnn*2 (34)	0.02352	375
*Imm*2 (44)	0.03776	217
$I2_12_12_1$ (24)	0.03776	217
*I*222 (23)	0.03776	217
$Pmc2_1$ (26)	0.06767	408
*Pma*2 (28)	0.06768	408
*Pcc*2 (27)	0.06769	376
$Pca2_1$ (29)	0.0678	372
*Pnc*2 (30)	0.06832	375
*Pba*2 (32)	0.06836	375
$Pna2_1$ (33)	0.06844	371
*Ima*2 (46)	0.07541	204
*Iba*2 (45)	0.07545	188
*Amm*2 (38)	0.10995	219
*C*222 (21)	0.11003	219
*Cmm*2 (35)	0.11003	219
*Ama*2 (40)	0.11007	206
$C222_1$ (20)	0.11008	215
$Cmc2_1$ (36)	0.11015	206
*Aem*2 (39)	0.11025	203
*Ccc*2 (37)	0.11028	190
*Aea*2 (41)	0.11037	190
*F*222 (22)	0.11285	111
*Fmm*2 (42)	0.11285	111
*Fdd*2 (43)	0.28332	95

Table B6: Setting cba

Space group	Rwp	Number of reflections
*P*222 (16)	0.02132	434
*Pmm*2 (25)	0.02132	434
$P222_1$ (17)	0.02132	430
$P2_12_12$ (18)	0.02135	426
$P2_12_12_1$ (19)	0.02135	422
$Pmc2_1$ (26)	0.02136	401
$Pmn2_1$ (31)	0.02143	397
*Pma*2 (28)	0.02144	398
*Pba*2 (32)	0.02167	362
$Pna2_1$ (33)	0.02352	361
$Pca2_1$ (29)	0.02354	365
*Pnc*2 (30)	0.02356	368
*Pcc*2 (27)	0.02366	372
*Pnn*2 (34)	0.02372	364
$C222_1$ (20)	0.02822	214
*Cmm*2 (35)	0.02822	218
*C*222 (21)	0.02822	218
$Cmc2_1$ (36)	0.02826	201
*Ccc*2 (37)	0.03022	188
$I2_12_12_1$ (24)	0.03776	217
*Imm*2 (44)	0.03776	217
*I*222 (23)	0.03776	217
*Ima*2 (46)	0.03778	201
*Iba*2 (45)	0.03793	185
*Amm*2 (38)	0.10995	219
*Ama*2 (40)	0.11016	199
*Aem*2 (39)	0.11025	203
*Aea*2 (41)	0.11046	183
*F*222 (22)	0.11285	111
*Fmm*2 (42)	0.11285	111
*Fdd*2 (43)	0.38355	94

Appendix C - DTA measurements and dielectric data for BTFM-CTO materials

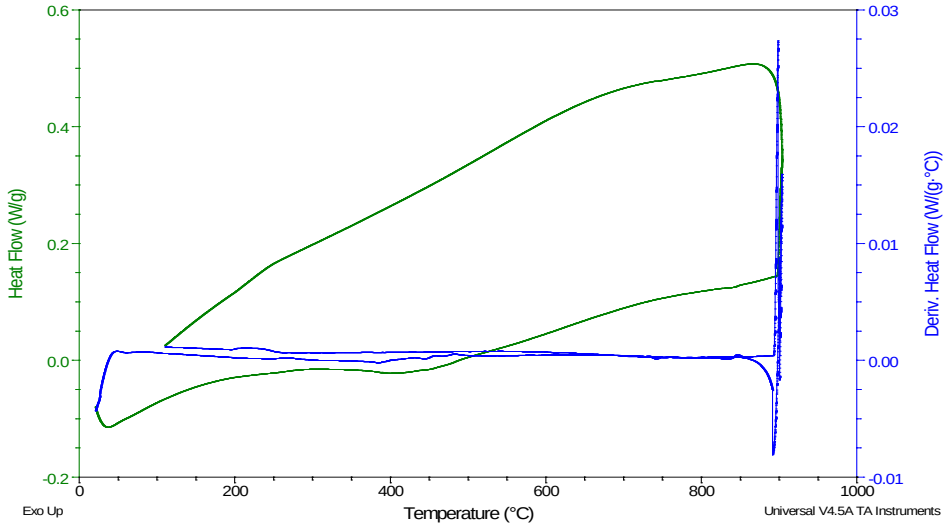

Figure C1 a) DTA data from 25 °C to 900 °C are shown in green and its derivative in blue for 0.7BTFM-0.3CTO.

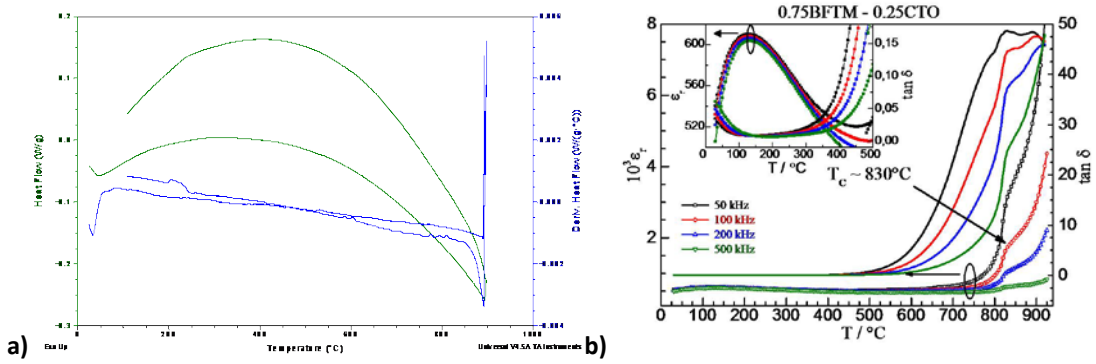

Figure C2 a) DTA data from 25 °C to 900 °C are shown in green and its derivative in blue for 0.75BTFM-0.25CTO; b) dielectric data from 25 °C to 900 °C at 50 kHz (black open circles), 100 kHz (red open circles), 200 kHz (blue open circles) and 500 kHz (green open circles). The inset at the top left corner shows dielectric data from room temperature to 500 °C while heating (up). The black arrow at ~830 °C points out an anomaly in the data for 0.75BTFM-0.25CTO.

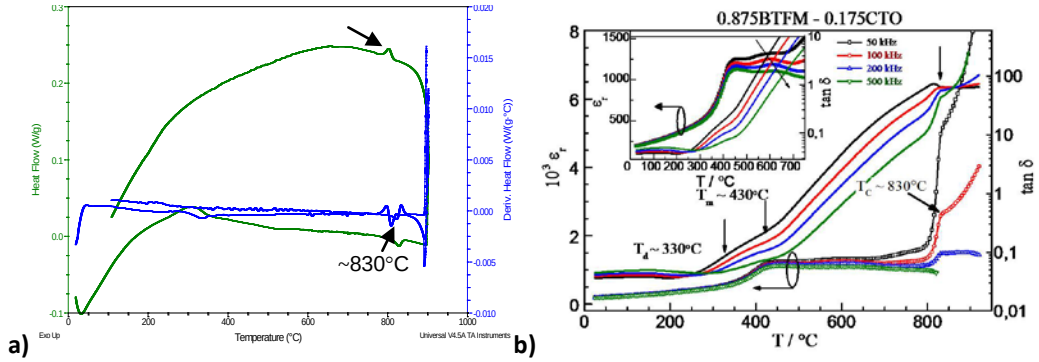

Figure C3 a) DTA data from 25 °C to 900 °C are shown in green and its derivative in blue. The black arrows point out a weak anomaly around 830 °C; b) dielectric data from 25 °C to 900 °C at 50 kHz (black open circles), 100 kHz (red open circles), 200 kHz (blue open circles) and 500 kHz (green open circles). The inset at the top left corner shows dielectric data from room temperature to 750 °C while heating (up). The black arrow at ~330 °C indicates T_d while the one at ~430 °C, Tm and Tc ~ 830 °C for 0.875BTFM-0.125CTO.

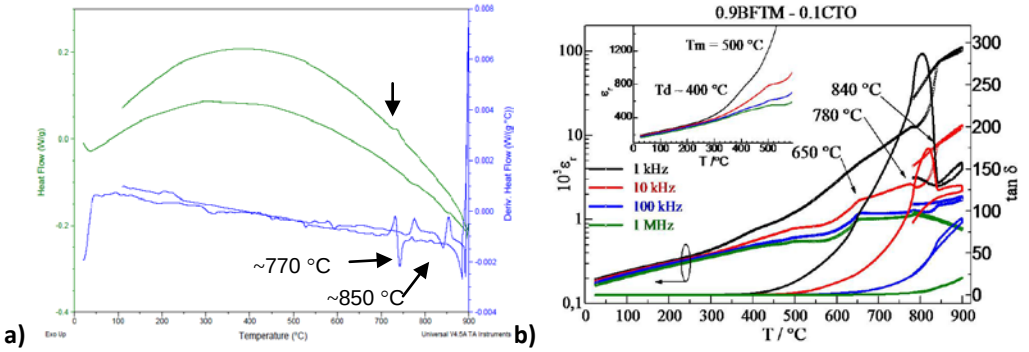

Figure C4 a) DTA data from 25 °C to 900 °C are shown in green and its derivative in blue. The black arrows point out two weak anomalies around 770 °C and 850 °C; b) dielectric data from 25 °C to 900 °C at 1 kHz (black open circles), 10 kHz (red open circles), 100 kHz (blue open circles) and 1 MHz (green open circles). The inset at the top left corner shows dielectric data from room temperature to 600 °C while heating (up).T_d ~ 400 °C and Tm ~ 500 °C. The black arrows at ~650 °C, 780 °C and 840 °C indicate three anomalies that take place at 10 kHz data for 0.9BTFM-0.1CTO.

Appendix D- Comparison of the dielectric loss for a MnO_2 doped and undoped sample of 0.8BTFM-0.2CTO

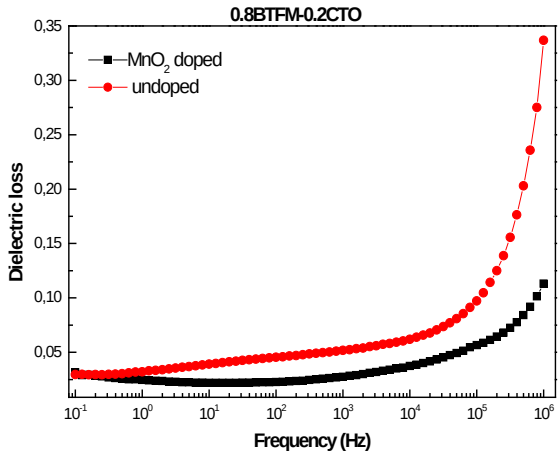

Figure D Comparison of dielectric loss over frequency for MnO_2 doped (black data) and undoped (red data) for 0.8BTFM-0.2CTO. For the doped sample the dielectric loss is reduced.

Appendix E- Longitudinal piezoelectric coefficient (d_{33}) values for compositions in the mixed phase region (O + R), 0.8375 ≤ x ≤ 0.925 and rhombohedral phase x ≥ 0.95

Table E Longitudinal piezoelectric coefficient (d_{33}) values for compositions in the mixed phase region (O + R), 0.8375 ≤ x ≤ 0.925 and rhombohedral phase x ≥ 0.95.

COMPOSITION	d_{33} **(pC/N)**
0.835BTFM-0.165CTO	53.6
0.85BTFM-0.15CTO	52
0.875BTFM-0.125CTO	51.1
0.9BTFM-0.1CTO	50.3
0.925BTFM-0.1CTO	1.7
0.95BTFM-0.05CTO	3.8
BTFM	0.6